

**UNIVERSIDADE DE SÃO PAULO
INSTITUTO DE FÍSICA DE SÃO CARLOS**

Carlos Maciel de Oliveira Bastos

**Realistic g-factor and k.p parameters in III-V
semiconductors and prediction of semiconductors layered
materials**

São Carlos

2019

Carlos Maciel de Oliveira Bastos

**Realistic g-factor and k.p parameters in III-V
semiconductors and prediction of semiconductors layered
materials**

Thesis presented to the Graduate Program
in Physics at the Instituto de Física de São
Carlos, Universidade de São Paulo, to obtain
the degree of Doctor in Science.

Concentration area: Basic Physics

Advisor: Prof. Dr. Guilherme Matos Sipahi
Co-Advisor: Prof. Dr. Juarez Lopes Ferreira
da Silva

Corrected version
(Original version available on the Program Unit)

São Carlos
2019

AUTHORIZE THE REPRODUCTION AND DISSEMINATION OF TOTAL OR PARTIAL COPIES OF THIS THESIS, BY CONVENCIONAL OR ELECTRONIC MEDIA FOR STUDY OR RESEARCH PURPOSE, SINCE IT IS REFERENCED.

Cataloguing data reviewed by the Prof. Bernhard Gross Library and Information, with information provided by the author.

Bastos, Carlos Maciel de Oliveira

Realistic g-factor and k.p parameters in III-V semiconductors and prediction of semiconductors layered materials / Carlos Maciel de Oliveira Bastos ; advisor Guilherme Matos Sipahi ; co-advisor Juarez Lopes Ferreira Da Silva - corrected version – São Carlos, 2019.

145 p.

Thesis (Doctorate - Graduate Program in Basic Physics) – Instituto de Física de São Carlos, Universidade de São Paulo-Brazil, 2019.

1. k.p method. 2. Density functional theory. 3. Semiconductors. 4. 2D materials. I. Sipahi, Guilherme Matos, advisor. II. Da Silva, Juarez Ferreira Lopes, co-advisor. III. Title.

To my parents, Vera and Gonzaga. And my wife Luciana.

ACKNOWLEDGEMENTS

Initially I acknowledge my family: my parents Vera and Gonzaga, my brother Júnior and my wife Luciana for their support and encouragement.

I would like to express my deep gratitude to my supervisors Professor Guilherme Matos Sipahi and Professor Juarez Lopes Ferreira da Silva, for their guidance, useful critiques and enthusiastic encouragement in this PhD project. I would like also to acknowledge all the other IFSC professors who contributed with their excellent training to the success of this work. I wish to thank Profs. Luiz Nunes de Oliveira, Victor Lopez Richard and Matheus Paes Lima for being part of my PhD qualification committee, and providing helpful feedback to this thesis and its physics discussions.

My grateful thanks to my IFSC coworkers and friends: Paulo Faria Junior, Tiago Campos, Denis Candido, Marcelo Sandoval and Caio Oliveira for their advice and hours of rich physics discussions. Equally, I thank the IQSC coworkers: Naidel Caturello, Diego Guedes Sobrinho, Fernando Sabino, Rafael Besse, Luís Cabral, Israel Rosalino and Augusto Silva for the numerous scientific conversations and the QTNano group meetings for rich scientific debates about DFT that contributed to this PhD project.

I would also like to extend my thanks to the technicians of the IFSC, in special to Ailton, Cristina, Luciano, Neuza, Ricardo, Silvio, Sonia, Lhaís and Italo for their help in offering me the resources and infrastructure to develop this PhD project. My thanks for the CAPES, CNPq and FAPESP which offered the financial support and infrastructure for this PhD project, and in special, this study was financed in part by the Coordenação de Aperfeiçoamento de Pessoal de Nível Superior-Brasil (CAPES)-Finance Code 001.

Finally, I wish to thank the people with whom I interacted socially and scientifically throughout the years, in special the "barrilada" and "bandejão" groups and all my friends whose names I will omit since they are a large number of people.

'One Bourbon, One Scotch, One Beer.'
John Lee Hooker

ABSTRACT

BASTOS, C. M. O. **Realistic g-factor and k.p parameters in III-V semiconductors and prediction of semiconductors layered materials.** 2019. 145p. Thesis (Doctor in Science) - Instituto de Física de São Carlos, Universidade de São Paulo, São Carlos, 2019.

Semiconductor devices have today an important impact on the contemporary world, with a large number of applications ranging from LEDs to mobile phone chips. The development of new electronic devices needs the control of the electronic structure achieved with new experimental techniques. For this reason, a fundamental issue on this area is the understanding of the electronic structure of the materials that compose such devices. An example is the fact that spintronic devices need a disequilibrium between the *spin-up* and *spin-down* distributions, with a difference of few millielectronvolts between them. Today, only a small group of theoretical methods can achieve the precision needed to guide the development of these new devices. In addition, with the control of growth temperatures and pressures, it is possible to obtain metastable phases of the same material, increasing the spectrum of possible choices. In this PhD project, we propose a theoretical approach that combines two of the most used methods used in the electronic structure calculations, the density functional theory and the **k·p** method, connecting them via a *fitting* method that was developed and tuned during its execution period. To test our approach and the *fitting* method, we have applied it to the *zincblende* GaAs phase, comparing our theoretical predictions with experimental data, proving the effectiveness of our approach. Extending the application to other III-V zincblende phase semiconductors, we reviewed the **k·p** parameters, the effective masses and the effective g-factors for these materials. In addition, we investigated transition metal dichalcogenides, which form stratified materials and may form two-dimensional structures, and are possibly semiconductor materials. We investigated three polymorphic phases of 27 materials, predicting their structural, electronic and elastic properties. We also investigated an important trend we found between the charge transferred from the metal to the chalcogen and the energy required to isolate a single layer, proposing a mechanism that explains this effect. In conclusion, we proposed a new theoretical approach, which we applied to III-V semiconductors, and investigated the existence of new semiconductor materials among transition metal dichalcogenides. This PhD project contributes to the increasing of the accuracy of theoretical approaches, with consequences for the development of new semiconductor devices and for the understanding of physical phenomena involving these materials.

Keywords: k.p method. Density functional theory. Semiconductors. 2D materials.

RESUMO

BASTOS, C. M. O. **Fator-g e parâmetros $k\cdot p$ realísticos em semicondutores III-V e a predição de materiais semicondutores estratificados.** 2019. 145p. Tese (Doutorado em Ciências) - Instituto de Física de São Carlos, Universidade de São Paulo, São Carlos, 2019.

Os dispositivos semicondutores têm grande impacto no mundo atual, com um grande número de aplicações indo desde os LEDs até os chips presentes nos celulares. O desenvolvimento de novos dispositivos eletrônicos necessita do controle da estrutura eletrônica, que vem sendo alcançado com novas técnicas experimentais. Por este motivo, um ponto fundamental desta área é o entendimento da estrutura eletrônica dos materiais que os compõem. Um exemplo desta necessidade é o fato de que dispositivos *spintrônicos* necessitam do desbalanço entre os *spin-up* e *spin-down*, com uma diferença de poucos milieletrons entre eles. Hoje, apenas um pequeno grupo de métodos teóricos que consegue alcançar a precisão necessária para guiar o desenvolvimento desses novos dispositivos. Além disso, com o controle das temperaturas e pressões de crescimento, é possível obter fases metaestáveis de um mesmo material, aumentando o espectro de possíveis escolhas. Neste projeto de doutorado, nós propomos uma abordagem teórica que combina dois dos principais métodos usados nos cálculos de estrutura eletrônica, a teoria do funcional da densidade e o método $k\cdot p$, que são conectados através de um método de *fitting* que foi desenvolvido e aprimorado durante seu período de execução. Para testar nossa abordagem e o método de *fitting*, nós aplicamos ao GaAs na fase *zincblende* e comparamos as nossas predições teóricas com dados experimentais, comprovando a eficiência de nossa abordagem. Estendendo a aplicação aos demais semicondutores III-V na fase *zincblende*, nós revisamos os parâmetros $k\cdot p$, massas efetivas e os fatores-g efetivos nesses materiais. Além disso, investigamos os dicalcogenetos de metais de transição, que formam materiais estratificados e podem formar estruturas bidimensionais, e possivelmente materiais semicondutores. Nós investigamos três fases polimórficas de 27 materiais, prevendo suas propriedades estruturais, eletrônicas e elásticas. Também investigamos uma importante tendência que encontramos entre a carga transferida do metal para o calcogênio e a energia necessária para isolar uma única camada, propondo um mecanismo para explicar esse efeito. Concluindo, nós propusemos uma nova abordagem teórica, que aplicamos aos semicondutores III-V, além de investigarmos a existência de novos materiais semicondutores entre os dicalcogenetos de metais de transição. Este projeto de doutorado contribui para o aumento da precisão de abordagens teóricas, com consequências para o desenvolvimento de novos dispositivos semicondutores e para o entendimento de fenômenos físicos envolvendo esses materiais.

Keywords: Método $k\cdot p$. Teoria do funcional da densidade. Semicondutores. Materiais 2D.

LIST OF ABBREVIATIONS AND ACRONYMS

BO	Born-Oppenheimer
DFT	Density functional theory
HK	Hohenberg-Kohn
SE	Schrödinger equation

CONTENTS

1	INTRODUCTION	17
1.1	Semiconductor materials and electronic structure	17
1.2	g-factor and k.p parameters	18
1.3	Layered materials and transition metal dichalcogenides	19
1.4	Outline	20
2	THEORETICAL BACKGROUND	23
2.1	The k.p method	23
2.2	Density functional theory and hybrid functionals	26
2.2.1	Hohenberg–Kohn and Kohn–Sham formalism	26
2.2.2	Exchange-correlation functionals and hybrid functionals	30
2.2.3	Hybrid exchange-correlation functionals	31
2.2.4	Van der Waals energy	32
2.3	Computational implementation	33
3	PUBLISHED PAPERS	35
4	CONCLUSION	69
	REFERENCES	71
	APPENDIX	77
	APPENDIX A – COLLABORATION PUBLISHED PAPERS	79
	APPENDIX B – SUPPORTING INFORMATION	101

1 INTRODUCTION

1.1 Semiconductor materials and electronic structure

Few categories of materials had a higher impact in the last century as the semiconductors. The number of applications for such are huge, from LEDs to solar cells, from transistors that compose the computer chips to sensors used on a myriad of different fields. Each smart phone posses a huge amount of electronic components: GaAs-based antennae, WiFi and GPS circuits, flash memories, and arm chips, among others. Finally, the development of faster microchips depends on the research of new semiconductor technologies, materials and/or arrangements of structures formed by these materials, opening new research fields, such as nanotechnology.

Although electronic devices exist since the late 1800's, the use of semiconductor devices after the 1940's lead to a revolution in their making, see e.g., rectifiers,¹ diodes,² p-n junction transistors,³ field effect transistors (FETs),² photo-detectors,⁴ and light-emission diodes (LEDs),^{5,6} among others. Recently, more efficient photovoltaic technologies^{7,8} were achieved through the use of semiconductor materials in the development of solar cells, by solving the issues of the mismatches between the spectra of available photon energies and the gaps of the semiconductors. Other example of recent application of semiconductors is the development of spintronic devices⁹ which are based in spin-polarized transport, e.g., the Datta-Das spin field transistor (SFET) based on InGaAs heterostructures.¹⁰

Semiconductors are materials with moderately good conductivity, usually showing resistivities lying in the range of 10^{-2} - $10^{-9}\Omega$ cm.¹¹ Conductivity however, may depend heavily on external factors, e.g., temperature and chemical purity.³ Semiconductors appear in diverse chemical alloys and/or crystalline structures, allowing them to be classified by using the chemical character of the system in different ways. Elemental semiconductors^{11,12} are compounds of one chemical element, e.g., Si and Ge. Binary compounds are formed by a combination of III and V (such as GaAs), II and VI (ZnS), I and VII (CuCl) and IV and VI (PbS) elements of the periodic table appearing in a large number of different compositions and crystalline structures.¹¹ Other possible classes are: oxide semiconductors, e.g., Cu_2O , that have oxygen in their composition; magnetic semiconductors,¹³ such as EuS and $\text{Ga}_{1-x}\text{Mn}_x\text{As}$ that possess magnetic ions in their composition and may exhibit different magnetic properties like ferromagnetism or antiferromagnetism; organic semiconductors, such as poly-acetylene $[\text{CH}_2]_n$,¹³ and also, layered semiconductors,¹⁴ e.g., MoS_2 . Finally, there is another semiconductor material not classified in any of the previous classes: SbSI, a semiconductor that exhibits ferroelectricity at low temperatures.¹³

The synthesis of a large number of semiconductor materials have been possible

due to the development of more versatile growth techniques. With these techniques it is possible to substitute one element for other with similar properties, grow alloys with different stoichiometry, grow compounds with different crystalline phases and find materials with different physical properties, making them viable to the application in industrial scale. Among the growth techniques, we highlight the four more common: i) Czochralski method,¹⁵ ii) Chemical vapor deposition (CVD),¹⁶ iii) molecular beam epitaxy (MBE)¹⁷ and iv) vapor phase epitaxy (VPE).¹⁸

In opposition of direct technological applications, semiconductor materials are also used to investigate a new physical phenomena. Recently, nanowires of III-V semiconductors in contact of superconductor were used to investigate Majorana fermions.¹⁹ Moreover, many semiconductor materials are topological insulators (TIs), or can be used to build heterostructures that present topological properties.^{20,21} Actually, new results indicates that some 2D TMDCs are topological insulators depending on the crystalline phases.²²

1.2 g-factor and k.p parameters

With improvement of the semiconductor materials fabrication processes and experimental techniques, more accuracy and precision are required in theoretical predictions. For example, with the advent of spintronic devices is only possible with the control of the imbalance between spin-up and spin-down in the band structure within few units of meV.⁹ However, there are actually a small number of theoretical techniques allowing the prediction of the electronic structure with the required accuracy and precision.

Band structure determination accommodates a range of methods that may be classified roughly as atomistic or effective models. On the side of atomistic models there are the first principle methods, as the density functional theory (DFT) where all atomic interaction is included with none or a small number of external parameters, e.g., Hartree–Fock method, density functional theory, among others. A direct consequence of the atomistic character is that the computational cost increases with the number of atoms considered in the calculation, limiting it to a small number of atoms typically on the order of hundreds. Due to the approximations used in traditional exchange-correlation functionals, the DFT method does not predict correctly the band gap of semiconductors. In the last twenty years however, new functional approximations were proposed to increase the precision and accuracy of theoretical properties in comparison with experimental values, with a reasonable computational cost. Examples of these new functionals are PBE0,^{23,24} HSE06,^{25,26} and B3LYP.²⁷

On the effective models side, there are methods such as $\mathbf{k} \cdot \mathbf{p}$, semiempirical methods, tight-binding, among others. In this approach the interaction is described by an effective Hamiltonian. Due this characteristic, the method requires a large number of external parameters, that can be obtained from experiment or directly from preexistent band

structures, e.g., calculated with DFT.²⁸ The $\mathbf{k} \cdot \mathbf{p}$ and the other effective methods show a small computational cost when compared with first principle methods, allowing to calculate properties of structures larger than thousands atoms and, specially, to simulate heterostructures.

In this work, we propose a framework combining two theoretical methods, in order to increase the precision and stability of the electronic structure: i) density functional theory (DFT) and ii) $\mathbf{k} \cdot \mathbf{p}$ method. In this framework, we obtain the band structure from DFT method, using a modified hybrid functionals to overcome the band gap determination issue and obtain a band structure that presents the experimental band gap and spin-orbit splitting in the Γ point. From these band structures, we apply with a fitting method developed in order to extract the $\mathbf{k} \cdot \mathbf{p}$ parameters.

As an example of the application of our framework, we obtain reliable III-V semiconductors $\mathbf{k} \cdot \mathbf{p}$ parameters and using these parameters, we estimate the effective g-factors in agreement with experimental values (for materials having experimental data in the literature). Effective g-factors are crucial to the development of spintronic devices that use magnetic fields.⁹

A second use for our framework is the investigation and discovery of new semiconductor material candidates. As an example we can apply it to two dimensional materials, a new class of materials in which the atoms are positioned in one or a small number of layers in an arrangement that precludes the chemical bond in the direction perpendicular to the planes of the layers. Stacked arrangements of materials of this particular class hold by itself a large number of compounds and crystalline phases.

1.3 Layered materials and transition metal dichalcogenides

In the last five years, layered and bidimensional semiconductors received a large attention from the research community leading to an impressive number of published papers.²⁹⁻³¹ Among these materials, the transition metal dichalcogenides (TMDCs), composed by transition metals (M) and chalcogen (X) with stoichiometric formula MX_2 , have been the most highlighted by promising a huge impact on our technology.^{32,33} For example, since the interlayer provides a convenient accommodation for other chemical elements, such as Li^+ ,³⁴ the energy storage using bulk TMDCs obtained energy densities of $1.6-2.4 \text{ mWhcm}^{-3}$ *. Other example consists of the gas sensor for NO_2 using MoS_2 monolayer, providing a precision of 1 ppm.³⁵ Other applications of TMDCs monolayers include photonic devices,³⁶ high sensitivity biosensors,³⁷ transistors,³⁸ etc. Furthermore, the monolayers can be used like the 3D materials, such as III-V semiconductors, to grow heterostructures.²⁹ These are classified as two types: i) vertical heterostructures, in which a layer is deposited on top of another layer with a different compound; ii) lateral het-

* For comparison, an alkaline battery has $\sim 0.1 \text{ mWhcm}^{-3}$

erostructures, in which the same layer accommodate regions of two or more compounds.³⁹ Like in 3D semiconductors, the promise is that the vertical and lateral heterostructures would increase the range of applications of TMDC materials.

A wide number of TMDC materials can be composed by combining a transition metal with a chalcogen element. These materials may also present a large number of polymorphic phases. These phases are generally metastable but can be obtained by changing the initial conditions in the growth process. Due to the huge number of possibilities and the metastability of most phases, the majority of these materials have not been synthesized and their electronic properties are unknown.

We extended the framework used in the III-V semiconductors to investigate the TMDCs. In this subproject, we evaluated the TMDs composed by Ti, Zr, Hf, V, Nb, Ta, Cr, Mo and W, combined with S, Se and Te in three polymorphic phases, resulting in 81 different materials. As the structural parameters, e.g. lattice parameters, are unknown for the most part of TMDs materials, we performed an extensive study of the structural and electronic properties using DFT. We applied general hybrid functionals to obtain band gaps closer to the experimental values, since most of TMDs band gaps are unknown. Although not adjusted to experimental values, as the HSE $_{\alpha}$ functional, the HSE06 hybrid functional was used to evaluate the band structures, identifying the semiconductors TMDs. As the literature presents a small number of effective Hamiltonians for these materials, a possible extension of this thesis is the development of $\mathbf{k}\cdot\mathbf{p}$ Hamiltonians, applying the same techniques used in the III-V semiconductors.

1.4 Outline

In chapter 2 we present a brief review of the theoretical methods used in this thesis. Initially, we describe the $\mathbf{k}\cdot\mathbf{p}$ method (section 2.1), followed by a description of the DFT method (section 2.2). In this section we present the Hohenberg–Kohn theorems and the Kohn–Sham formalism; the exchange–correlation and hybrid functionals; and the Van der Waals corrections, paramount to the correct evaluation of layered materials, such as the TMDs. In chapter 3, we present the three papers that include the most significant results of this project: two on III-V semiconductors and one on TMDs. Finally, in chapter 4, we present our general conclusions and perspectives. In the Appendices we include two other articles in which our contribution was essential and all the Supporting Information of the three main articles.

In the first paper, “Stability and accuracy control of $\mathbf{k}\cdot\mathbf{p}$ parameters”, published in Semiconductor Science and Technologies, in 2016, we propose the framework used to obtain the $\mathbf{k}\cdot\mathbf{p}$ parameters through the fitting of a hybrid-DFT band structure whose functional was modified to give the experimental gap, fully developed in this PhD project. The fitting procedure developed to determine the $\mathbf{k}\cdot\mathbf{p}$ parameters from the DFT band

structure is explained in details, using the bulk GaAs as a benchmark. In this paper, we also proposed a data analysis procedure using the root mean squared deviation (RMSD) to assess the accuracy of the $\mathbf{k}\cdot\mathbf{p}$ parameters. In this procedure, we used data comprising different regions from Γ point to a given percent of the first Brillouin Zone, obtaining a set of $\mathbf{k}\cdot\mathbf{p}$ parameters for each region. With the RMSD analyses it is possible to identify the importance of the non-parabolic regions in the stability of the 8-band parameters. In the Supporting Information (see appendix B), the same methodology was applied to the 6-band $\mathbf{k}\cdot\mathbf{p}$ Hamiltonian for GaAs.

In the second paper, “A comprehensive study of g-factors, elastic, structural and electronic properties of III-V semiconductors using hybrid-density functional theory” published in the Journal of Applied Physics, in 2018, we applied the framework to all III-V semiconductor materials. For this work, instead of adjust the HSE hybrid functional to provide the experimental gap value, we modified it to adjust the experimental spin-orbit splitting too, using the normalized-root-mean-squared-deviation (NRMSD) to find the optimal HSE parameter that describes both, band gap energy and spin-orbit splitting at Γ point. In order to guarantee that the modifications in the functional parameters, optimized to obtain a correctly electronic structure, lead to realistic structural parameters, we evaluated the lattice parameters and elastic constants, comparing with the results in the literature. Our results are in complete agreement with the experimental values, showing that the modifications do not change significantly the structural parameters. Therefore, after apply our method and RMSD analysis to obtain the $\mathbf{k}\cdot\mathbf{p}$ parameters, we calculated the effective masses and estimated the effective g-factor using the Roth’s formula.

In the third paper, “Ab initio investigation of structural stability and exfoliation energies in transition metal dichalcogenides based on Ti-, V-, and Mo-group elements”, published in the Physical Review Materials, in 2019, we investigated the TMDs. Initially, we extended the same framework used in the III-V semiconductors to investigate this new class of semiconductor materials. In this work, we predicted the structural and electronic properties, classifying the materials as metals, semimetals or semiconductors. We also evaluated the exfoliation energy, quantifying the easiness of separation for a monolayer. As a correlation between exfoliation energy and effective Bader charge, i.e., transfer charge between metal and chalcogen, was identified, we proposed a new mechanism that contributes to lower the exfoliation energy in some TMDs. In principle, the same methodology applied to the III-V semiconductors to generate effective Hamiltonians can be used for TMDs, but in this moment, literature presents a very small number of $\mathbf{k}\cdot\mathbf{p}$ Hamiltonian for TMDs materials.

Finally, we collaborated in two other papers during this project. The first, “Realistic multiband $k \cdot p$ approach from ab initio and spin-orbit coupling effects of InAs and InP in wurtzite phase”, was published in the Physical Review B, in 2016, and presents a new $\mathbf{k}\cdot\mathbf{p}$

Hamiltonian for wurtzite III-Vs that includes the spin-orbit splitting in the Γ point. We used the same framework used in III-V semiconductors, but with a modified fitting method, due to large number of $\mathbf{k}\cdot\mathbf{p}$ fitting parameters. The Second paper, “Size-Induced Phase Evolution of MoSe₂ Nanoflakes Revealed by Density Functional Theory” was published in The Journal of Physical Chemistry C, in 2018, in which we investigated the formation of TMDs nanoflakes, whose polymorphic phase depend on the size effect explained by using the Peierls distortion. Both papers are complementary to the main papers either applying the framework to III-V $\mathbf{k}\cdot\mathbf{p}$ parameters or understanding the structural and electronic properties of TMDs.

2 THEORETICAL BACKGROUND

Theoretical studies in the condensed matter systems require a description of the dynamic involving many-particles, e. g. the interaction between electrons-electrons or electron-nuclei. With the description of these interactions one can obtain the structural and dynamical properties of a system and determine its electronic structure, allowing the determination of structural properties as atoms organization, magnetic moment, phonons, cohesive energy, among others. Also, electronic excitation spectrum enable to know dynamical properties, e.g., vibrational states in molecules and optical processes.

These theoretical methods can be classified in general as two different approaches: atomistic and effective models. In the first, one solves the many-body Hamiltonian including the fundamental interactions. This approach requires extremely demanding computational resources and several approximations, which in principle, do not include adjusting parameters. This class of methods is also called first principles or *ab initio*. the second approach consists in building a suitable Hamiltonian model. Starting with the available information of system, it is possible to identify the relevant aspects and build an effective Hamiltonian

Here, we present a brief review of two methods, one from each class, used in this project: i) $\mathbf{k}\cdot\mathbf{p}$ method, an effective method; ii) and density functional theory, that is in principle an *ab initio* method. Both methods, however, start from the electronic Hamiltonian, i.e., the fundamental Hamiltonian considering the Born–Oppenheimer approximation, which allows the separation of the fundamental Hamiltonian in a nuclei and an electronic Hamiltonians.

In the Born Oppenheimer approximation (more details in the reference⁴⁰), the system Hamiltonian for N electrons and M nuclei can be separated in the electronic (H_e) and nuclei (H_n) parts,

$$H = H_e + H_n, \quad (2.1)$$

being the electronic Hamiltonian

$$H_e = - \sum_i^N \frac{\hbar^2}{2m} \nabla_{\mathbf{r}_i}^2 + \sum_{i<j}^N \frac{e^2}{|\mathbf{r}_i - \mathbf{r}_j|} - \sum_i^N \sum_j^P \frac{Z_j e}{|\mathbf{r}_i - \mathbf{R}_j|}. \quad (2.2)$$

2.1 The $\mathbf{k}\cdot\mathbf{p}$ method

In this brief review, we present a method description. The detailed calculations of matrix elements and symmetry analyses can be found in the reference.⁴¹ Using the effective Hamiltonian approach, we adopt the picture of one electron in an effective potential

generated by all other electrons and nuclei, written as

$$H = -\frac{\hbar^2}{2m} \nabla_{\mathbf{r}_i}^2 + V_{ef}(\mathbf{r}). \quad (2.3)$$

where $V_{ef}(\mathbf{r})$ is the effective potential generated by all other electrons and the nuclei. This Hamiltonian is non-relativistic, but some relativistic effects can be added *ad hoc*. Depending on the system, when modeling semiconductors, the relativistic effects may be crucial, e.g., breaking of symmetry that can separate the spins up and down. In this work, we consider the spin-orbit potential in the Hamiltonian,

$$H = -\frac{\hbar^2}{2m} \nabla_{\mathbf{r}_i}^2 + V_{ef}(\mathbf{r}) + \frac{i\hbar^2}{4m_0^2 c^2} (\nabla V_{ef} \times \nabla_{\mathbf{r}_i}) \cdot \boldsymbol{\sigma}. \quad (2.4)$$

As crystal is a system in which one considers the electrons to be subject to a periodic potential. By consequence, the wave function must obey the Bloch theorem and, therefore, can be written as

$$\Psi(\mathbf{r}) = e^{i\mathbf{k}\cdot\mathbf{r}} u_{n,\mathbf{k}}(\mathbf{r}). \quad (2.5)$$

Applying the wave function in the Schrödinger equation (SE),

$$E\Psi(\mathbf{r}) = H\Psi(\mathbf{r}), \quad (2.6)$$

i.e,

$$E \left(e^{i\mathbf{k}\cdot\mathbf{r}} u_{n,\mathbf{k}}(\mathbf{r}) \right) = -\frac{\hbar^2}{2m} \nabla_{\mathbf{r}_i}^2 \left(e^{i\mathbf{k}\cdot\mathbf{r}} u_{n,\mathbf{k}}(\mathbf{r}) \right) + V_{ef}(\mathbf{r}) \left(e^{i\mathbf{k}\cdot\mathbf{r}} u_{n,\mathbf{k}}(\mathbf{r}) \right) - \frac{i\hbar^2}{4m_0^2 c^2} (\nabla V_{ef} \times \nabla_{\mathbf{r}_i}) \cdot \boldsymbol{\sigma} \left(e^{i\mathbf{k}\cdot\mathbf{r}} u_{n,\mathbf{k}}(\mathbf{r}) \right), \quad (2.7)$$

and applying the operators and simplifying the expression, we obtain

$$E u_{n,\mathbf{k}}(\mathbf{r}) = \left[\frac{\hbar^2}{2m} k^2 - \frac{\hbar^2}{m} i\mathbf{k} \nabla_{\mathbf{r}_i} + \frac{\hbar^2}{2m} \nabla_{\mathbf{r}_i}^2 \right] u_{n,\mathbf{k}}(\mathbf{r}) + \left[V_{ef}(\mathbf{r}) + \frac{\hbar^2}{4m_0^2 c^2} \mathbf{k} \cdot (\boldsymbol{\sigma} \times \nabla V_{ef}) - \frac{i\hbar^2}{4m_0^2 c^2} (\nabla V_{ef} \times \nabla_{\mathbf{r}_i}) \cdot \boldsymbol{\sigma} \right] u_{n,\mathbf{k}}(\mathbf{r}). \quad (2.8)$$

In order to simplify the notation, let's define $\mathbf{p} = -i\hbar\nabla$, and

$$E u_{n,\mathbf{k}}(\mathbf{r}) = \left[\frac{\hbar^2}{2m} k^2 + \frac{\hbar}{m} \mathbf{k} \cdot \mathbf{p} + \frac{p^2}{2m} + V_{ef}(\mathbf{r}) \right] u_{n,\mathbf{k}}(\mathbf{r}) + \left[\frac{\hbar^2}{4m_0^2 c^2} \mathbf{k} \cdot (\boldsymbol{\sigma} \times \nabla V_{ef}) + \frac{\hbar}{4m_0^2 c^2} (\nabla V_{ef} \times \mathbf{p}) \cdot \boldsymbol{\sigma} \right] u_{n,\mathbf{k}}(\mathbf{r}). \quad (2.9)$$

As this equation has the same structure of the Schrödinger equation, we can identify the Hamiltonian as

$$H(\mathbf{k}) = \frac{p^2}{2m} + \frac{\hbar^2}{2m} k^2 + \frac{\hbar}{m} \mathbf{k} \cdot \mathbf{p} + V_{ef}(\mathbf{r}) + \frac{\hbar}{4m_0^2 c^2} (\nabla V_{ef} \times \mathbf{p}) \cdot \boldsymbol{\sigma} + \frac{\hbar^2}{4m_0^2 c^2} \mathbf{k} \cdot (\boldsymbol{\sigma} \times \nabla V_{ef}). \quad (2.10)$$

It is important to notice that this expression includes the periodic information from Bloch Theorem. The last term, i. e., the spin-orbit dependent of \mathbf{k} , is small and can be neglected in a first approximation. However, even small as this term is, as it contributes to the break of spin-degeneracy in \mathbf{k} -points other than the Γ point, it was taken into account in the wurtzite Hamiltonian from our paper published in PRB (see appendix A).

To solve the Schrodinger equation, we used the perturbation theory proposed by Löwdin. The first step of this scheme is to define a expansion point \mathbf{k}_0 and break the Hamiltonian in two terms,

$$[H(\mathbf{k}_0) + H(\mathbf{k})] u_{n,\mathbf{k}}(\mathbf{r}) = E_n(\mathbf{k}) u_{n,\mathbf{k}}(\mathbf{r}), \quad (2.11)$$

with

$$H(\mathbf{k}_0) = \frac{p^2}{2m} + V_{ef}(\mathbf{r}) + \frac{\hbar}{m} \mathbf{k}_0 \cdot \mathbf{p} + \frac{\hbar^2 k_0^2}{2m} \quad (2.12)$$

and

$$H(\mathbf{k}) = \frac{\hbar}{m} (\mathbf{k} - \mathbf{k}_0) \cdot \mathbf{p} + \frac{\hbar^2}{2m} (k^2 - k_0^2) + \frac{\hbar}{4m_0^2 c^2} (\nabla V_{ef} \times \mathbf{p}) \cdot \boldsymbol{\sigma}. \quad (2.13)$$

With the choice of the Luttinger–Kohn set basis

$$|n\mathbf{k}\rangle = e^{i(\mathbf{k}-\mathbf{k}_0)\cdot\mathbf{r}} u_{n,\mathbf{k}_0}(\mathbf{r}), \quad (2.14)$$

the expected energy values can be obtained from

$$\langle n\mathbf{k}_0 | E_n | n\mathbf{k} \rangle = \langle n\mathbf{k}_0 | (H(\mathbf{k}_0) + H(\mathbf{k})) | n\mathbf{k} \rangle \quad (2.15)$$

i.e.,

$$\begin{aligned} \langle n\mathbf{k}_0 | E_n | n\mathbf{k} \rangle &= \langle n\mathbf{k}_0 | \left[\frac{p^2}{2m} + V_{ef}(\mathbf{r}) \right] | n\mathbf{k} \rangle + \langle n\mathbf{k}_0 | \frac{\hbar}{m} \mathbf{k}_0 \cdot \mathbf{p} | n\mathbf{k} \rangle \\ &+ \langle n\mathbf{k}_0 | \frac{\hbar^2 k_0^2}{2m} | n\mathbf{k} \rangle + \langle n\mathbf{k}_0 | \frac{\hbar}{m} \mathbf{k} \cdot \mathbf{p} | n\mathbf{k} \rangle \\ &+ \langle n\mathbf{k}_0 | \frac{\hbar^2}{2m} k^2 | n\mathbf{k} \rangle + \langle n\mathbf{k}_0 | \frac{\hbar}{4m_0^2 c^2} (\nabla V_{ef} \times \mathbf{p}) \cdot \boldsymbol{\sigma} | n\mathbf{k} \rangle. \end{aligned} \quad (2.16)$$

In the next step, the Löwdin formalism classify the states in the system into in two classes: A and B. Class A contains the states that we want to evaluate and may also contain states that strongly interact with them. Class B contains all the other states. From this point on we will refer to $|\alpha\rangle$ and $|\beta\rangle$ as the states from classes A and B, respectively. Therefore,

$$|n\mathbf{k}\rangle = \sum_{\alpha}^A C_{\alpha n}(\mathbf{k}) |\alpha\rangle + \sum_{\beta}^B C_{\beta n}(\mathbf{k}) |\beta\rangle. \quad (2.17)$$

As pointed before, the choice of class A states depends on the energy range of interest and how the states in this range interact with other states. The order of the perturbation

theory term also depends on the physical effects we want to describe. To increase the accuracy of the band structure evaluated with the method, there are traditionally two ways: i) increase the order of the perturbation or ii) increase the number of the states chosen in class A.

The Hamiltonian is then written using the matrix elements of class A states in the form

$$\begin{aligned} \langle \alpha | H | \alpha' \rangle = & E_{\alpha\alpha'} + \langle \alpha | \frac{\hbar}{m} \mathbf{k} \cdot \mathbf{p} | \alpha' \rangle + \langle \alpha | \frac{\hbar}{4m_0^2 c^2} (\nabla V_{ef} \times \mathbf{p}) \cdot \sigma | \alpha' \rangle \\ & + \sum_{\beta} \frac{\langle \alpha | \frac{\hbar}{m} \mathbf{k} \cdot \mathbf{p} | \beta \rangle \langle \beta | \frac{\hbar}{m} \mathbf{k} \cdot \mathbf{p} | \alpha' \rangle}{E_{\alpha} - E_{\beta}} + \dots, \end{aligned} \quad (2.18)$$

with

$$E_{\alpha\alpha'} = E(0) \delta_{\alpha\alpha'} + \frac{\hbar^2 k^2}{2m_0} \delta_{\alpha\alpha'}. \quad (2.19)$$

An inspection of the matrix elements show that the interactions of elements in class A are fully taken into account. Class B elements are not calculated and only their interaction with elements of class A are take into account.

Although the expression of the effective mass matrix elements is defined, usually the sum of class B states is unfeasible and the matrix elements are parameterized using the Löwdin expansion together with group theory and crystal symmetries.⁴¹ As in principle, the $\mathbf{k} \cdot \mathbf{p}$ method does not allow the evaluation of the parameters, they must be obtained from other sources. The focus of this PhD project was the development of a framework, including a fitting method to determine these parameters, known as $\mathbf{k} \cdot \mathbf{p}$ parameters.

2.2 Density functional theory and hybrid functionals

2.2.1 Hohenberg–Kohn and Kohn–Sham formalism

In 1964, Pierre Hohenberg and Walter Kohn published two theorems,⁴² that are considered as the starting point of the modern density functional theory, the so-called the Hohenberg–Kohn (HK) theorems. They found a mathematical proof that stationary many-body systems can be characterized by their ground state densities. Initially, let us consider the Hamiltonian for N electrons interacting within BO approximation, *

$$H_e = - \sum_i^N \frac{\hbar^2}{2m} \nabla_{\mathbf{r}_i}^2 + \sum_{i < j}^N \frac{e^2}{|\mathbf{r}_i - \mathbf{r}_j|} - \sum_i^N \sum_j^P \frac{Z_j e}{|\mathbf{r}_i - \mathbf{R}_j|}. \quad (2.20)$$

The last term of the equation 2.20 is the interaction between electrons and nuclei. As this term depends on the nuclei position, it is called external potential.

Let us find the solution of the SE

$$\hat{H}_e |\psi_k\rangle = E_k |\psi_k\rangle. \quad (2.21)$$

* For simplicity, we do not consider the presence of electromagnetic external fields and we consider $T = 0$. Both considerations can be extended to treat general cases.

For simplicity, we will consider only the non-degenerate ground state[†] $|\psi_0\rangle$. The SE depends on the external potential, the wave functions and indirectly on the density of the ground state (the squared modulus of its wave function). Therefore, the solution of SE can be interpreted as a mapping among the external potential, the wave functions and the density of the ground state, i.e.,

$$\begin{aligned}\mathcal{V} &= \{v_{ext} \text{ corresponding to } |\psi_0\rangle \text{ and is non-degenerated } (v'_{ext} \neq v_{ext} + cte)\}, \\ \mathcal{G} &= \{|\psi_0\rangle \text{ ground state corresponding to one element of } \mathcal{V}, \text{ with } |\psi'_0\rangle \neq e^{i\theta}|\psi_0\rangle\}, \\ \mathcal{N} &= \{\rho_0 \text{ with } \rho_0 = |\langle\psi_0|\psi_0\rangle|^2 \text{ and } \psi \in \mathcal{G}\}.\end{aligned}$$

Let us consider the mapping, $A : \mathcal{V} \rightarrow \mathcal{G}$ and $B : \mathcal{G} \rightarrow \mathcal{N}$ as illustrated in Fig. 1.

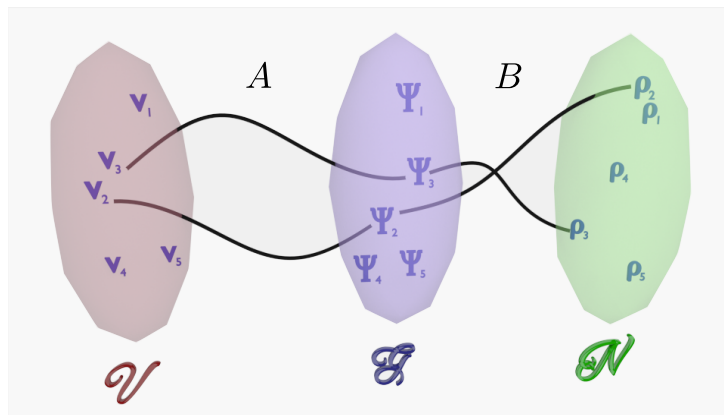


Figure 1 – Mapping between external potential (\mathcal{V}), wave functions (\mathcal{G}) and the density of ground state (\mathcal{N}).

Source: By the author.

Hohenberg and Kohn showed that the map A is unique, i.e., it is impossible to obtain the same $|\psi_0\rangle$ using two different potentials. Although, it is impossible to obtain the same ρ_0 from two different wave functions, i.e., the map B is unique too. Based in this arguments HK formulated and obtained a mathematical proof for two theorems,[‡]

The ground state is a unique functional of the ground state density.

$$|\psi_0\rangle = |\psi[\rho_0]\rangle. \quad (2.22)$$

This theorem is a directly consequence of the correspondence between the external potential, the wave function of the ground state[§], and the electronic density.

There is a minimum for $E[\rho]$: if ρ is the ground state density corresponding to v_{ext} , one has for all densities $\rho'_0(\mathbf{r}) \neq \rho_0(\mathbf{r})$

$$E[\rho_0] < E[\rho'_0] \iff E_0 = \min E[\rho] \text{ with } \rho \in \mathcal{N} \quad (2.23)$$

[†] The restriction on non-degenerate ground states is not crucial and can be removed.

[‡] The mathematical proofs of the theorems can be found in the ref. 40

[§] for wave functions which are solution of the SE

This theorem is the consequence of the variational principle and the unique relation between ρ and $|\psi_0\rangle$. The domain of the function $E[\rho]$ is restricted only to the densities in \mathcal{N} , i.e., only the ground state densities which are solution of the SE. Despite of the wonderful advance of the HK theorems, this formalism does not have an immediate practical application due to the fact that the explicit forms of some functionals are unknown, e.g., the functional of kinetic energy.

In 1965, Walter Kohn and Lu Sham proposed one way to find the density for an interacting system using an effective non-interacting system in which the explicit density functional form is known: the exact mapping called Kohn–Sham formalism (KS).⁴³ Consider a non-interacting system with an external potential V_s ,

$$\hat{H}_s = \hat{T}_s + \hat{V}_s, \quad (2.24)$$

where \hat{T}_s is the kinetic energy. Using the HK theorems, the ground state which is the solution of the SE of the Hamiltonian 2.24 is a unique functional of the ground state density $|\Phi[\rho]\rangle$. As the system is non-interacting, the wave function can be build using the Slater determinant, the explicit form of the Coulomb potential and kinetic energy are known and the energy functional is determined by

$$\hat{H}_s = E_s|\Phi_0\rangle \rightarrow E_s[\rho] = \langle \Phi[\rho] | \hat{T}_s[\rho] | \Phi[\rho] \rangle + \int v_s(\mathbf{r})\rho(\mathbf{r})d\mathbf{r}. \quad (2.25)$$

Here, it is important to notice that the wave function $|\Phi[\rho]\rangle$ from the non-interact system is not identical to the one obtained for the interacting system case.

However, there is one external potential v_s in which the ground state density $\rho_0(\mathbf{r})$ is also the ground state density of the interacting system with a potential v_{ext} . Sure, v_s and v_{ext} differ but have the same ground state density. Therefore, the ground state density of an interacting system can be represented using a non-interacting system. This representation is called Kohn–Sham system and its wave function ϕ_i^{KS} are called Kohn–Sham orbitals. In other words, a Kohn–Sham system can be understood as a mapping between an interacting and a non-interacting systems, with the same ground state density of the interacting system, i.e.,

$$\rho_0(\mathbf{r}) \equiv \rho_0^s(\mathbf{r}) = \sum_i |\phi_i^{KS}|^2. \quad (2.26)$$

Here, it is important to note that the electronic densities obtained from non-interacting and KS systems have the same numeric values but are fundamentally different. The first is a straightforward result of a non-interacting system, while the second is a highly non-trivial representation of the interacting system.

In order to find the v_s that reflects the nature of the interacting system, Kohn and Sham build the wave function using the Kohn–Sham orbitals, and evaluate the total

energy, which were decomposed in three terms, given by

$$E[\rho] = T_s[\rho] + E_H[\rho] + E_{xc}[\rho]. \quad (2.27)$$

In the first term, the interacting kinetic energy was split in two parts: i) the single-particle contribution, that represents most of the kinetic energy and whose functional form is known; and ii) the interacting particles contribution. This contribution was included in the exchange-correlation term (last term of equation 2.28). Second and third terms have origin in the Coulomb interaction, which due to the anti-symmetric character of the wave function, build using the Slater determinant, is splitted in two terms, the Hartree ($E_H[\rho]$) and exchange terms. The exchange term is combined with electronic correlation that is not present in the non-interacting system. This term is called the exchange-correlation term ($E_{xc}[\rho]$). The second term, the Hartree term has its functional form exactly known and given by

$$E_H[\rho] = \frac{1}{2} \int d\mathbf{r}' \frac{\rho(\mathbf{r}')}{|\mathbf{r} - \mathbf{r}'|}. \quad (2.28)$$

Note that the integral is performed over all electrons, including the one that interacts with the effective potential.

In the Kohn–Sham formalism, the exchange-correlation term ($E_{xc}[\rho]$) absorbs the complicated many-body effects that are not contained in T_s and E_H . This term does not have an exact explicit functional form and requires approximations to be solved. As a consequence of the approximations, the self-interaction in Hartree term is not cancelled. In order to include a correction, another potential is included in the exchange-correlation functional aiming to cancel the self-interaction. Therefore, the exchange-correlation energy is composed by four components: i) exchange term, ii) electronic correlation, iii) correction to kinetic energy and iv) self-interacting energy correction, i.e.,

$$E_{xc}[\rho(\mathbf{r})] = E_x[\rho(\mathbf{r})] + E_c[\rho(\mathbf{r})] + (T[\rho(\mathbf{r})] - T_s[\rho(\mathbf{r})]) + E_{si}[\rho(\mathbf{r})]. \quad (2.29)$$

This decomposition of the total energy is valid for densities that are simultaneously interacting and non-interacting, i.e., the electronic density for an interacting system can be obtained using the non-interacting system. The terms T_s and E_H which are exactly functional forms of the density and can be evaluated straightforward. Its components usually dominate over the exchange-correlation energy. Therefore, an approximate account of E_{xc} allows a sufficiently accurate description of most many-particle systems.

With the energy partition, the ground state can be obtained using the variational method [¶], which results in the following equation,

$$\{T_s[\rho] + v_H[\rho] + v_{xc}[\rho]\} \phi_i^{KS}(\mathbf{r}) = \epsilon_i \phi_i^{KS}(\mathbf{r}), \quad (2.30)$$

[¶] The mathematical demonstration can be found in the reference 40

where $\phi_i^{KS}[\rho](\mathbf{r})$ are the Kohn–Sham orbitals. The equation 2.30 is called Kohn–Sham equation and it is traditionally solved by a self consistent method. This method starts with some trial density $\rho^{(1)}(\mathbf{r})$, allowing the construction of a tentative potential

$$v_s^{(1)}(\mathbf{r}) = v_H[\rho](\mathbf{r}) + v_{ext}[\rho^{(1)}](\mathbf{r}) + v_{xc}[\rho^{(1)}](\mathbf{r}), \quad (2.31)$$

assuming that the explicit functional $v_{xc}[\rho^{(1)}](\mathbf{r})$ is known. The solution of the equation 2.30 using the potential $v_s^{(1)}(\mathbf{r})$ then provides some $\phi_i^{KS(2)}$ that leads to an improved density $\rho^{(2)}$ via

$$\rho^{(2)}(\mathbf{r}) = \sum_i |\phi_i^{KS(2)}(\mathbf{r})|^2. \quad (2.32)$$

The density $\rho^{(2)}$ can be used in its turn to obtain improved potentials. This interactive procedure is repeated until the convergence criteria is reached, e.g., until the difference between the densities obtained in two successive iterations falls below some predefined accuracy criterion. In practice, the control of this self-consistent procedure is non-trivial.

2.2.2 Exchange-correlation functionals and hybrid functionals

In the KS formalism, in principle, the only term that requires approximation is the exchange-correlation functional. This term can be analyzed through a model derived from the homogeneous electron gas (HGE). The HGE is an infinite system with interacting electrons uniformly distributed in the space. Analyzing the Coulomb interaction in HGE, due to the fact that it is a long range interaction, the HGE’s energy density. This problem is solved by adding a homogeneous background of positive charges,⁴⁰ canceling the divergence in the long range interaction. As the net charge, in any volume in space, is zero, the long-range Coulomb force is zero and, consequently, a finite density is obtained. Using the HGE one can derive the approximation for the analytical exchange energy functional. For the correlation term, the energy functional can be obtained in two distinct regimes: high and low density. The correlation energy functional between these two regimes is obtained through interpolation.

For real systems, e.g. solids and molecules, however, the electron densities are inhomogeneous. Nonetheless, the HEG can be used to estimate the exchange and correlation in systems with inhomogeneous electron densities. In a local density approximation (LDA), one considers the inhomogeneous system having locally the same density of a HEG ($\rho_{\text{HGE}} = \rho_{\text{inhom}}$). Other corrections included in the exchange-correlation term, e.g the interacting part of the kinetic energy, are based on the same local concept for exchange and correlation terms. As LDA is a first principles functional of ρ , it does not depend on any free parameter introducing some physical scale or experimental data and is treated locally as an HEG. Therefore, it is expected that LDA would be appropriate to treat systems that share some properties with the HEG, e.g., metals.

A different class of exchange-correlation functionals based in HGE is the Generalized Gradient Approximation (GGA), which includes the information from density and the gradient of density. In contrast with LDA, their construction is not unique, and different parametrizations are possible, e.g., Perdew–Wang (PW91)⁴⁴ and Perdew–Burke–Ernzerhof (PBE),⁴⁵ among others. As both, LDA and GGA, use HGE, both share the same deficiency that is none of these approximations can be described in an one particle system, i.e. for one electron, the exchange term does not reduce to a pure Coulomb self-interaction. Consequently, considering many particles, the self-interaction error propagate for all particles. As suggested by Zunger and Perdew,⁴⁶ this error is responsible for the fact that DFT does not predict correctly the energy gap in semiconductors.

2.2.3 Hybrid exchange-correlation functionals

The main problem of the local and semi-local exchange correlation approximations is the lack of inclusion of non-local effects, i.e., the exchange correlation considers only the local effects. In order to include some non-local effects, a new class of functionals, so called hybrid functional, was proposed. Hybrid functionals mix the exact exchange energy, generally evaluated from Hartree–Fock method, with (semi)local exchange energy. The first hybrid functional was proposed by Perdew *et. al.*, is known as the PBE0 functional and is composed by mixing 75 % of the PBE exchange energy with 25 % of the non-local Fock exchange of the Hartree–Fock (HF) method. The correlation energy is also used the PBE functional, i.e., $E_{\text{XC}}^{\text{PBE0}} = E_{\text{c}}^{\text{PBE}} + \alpha E_{\text{x}}^{\text{HF}} + (1 - \alpha)E_{\text{c}}^{\text{PBE}}$, where $\alpha = 0.25$.²³ The mixing of 0.25 for the non-local Fock exchange was obtained by Perdew *et. al.* from the adiabatic perturbation theory.²³

Another hybrid functional, HSE, was proposed by Heyd, Scuseria and Ernzerhof,^{25,26,47} and was derived from PBE0 by using a screening function to split the semilocal PBE exchange and non-local Fock term into two parts, namely, a short- (SR) and long-range (LR) exchange contributions. Heyd *et.al.* showed that the non-local Fock LR contribution cancels with part of the PBE LR exchange, numerically. Thus, the hybrid HSE functional is given by the following equation,

$$E_{\text{XC}}^{\text{HSE}} = E_{\text{c}}^{\text{PBE}} + E_{\text{x}}^{\text{PBE,LR}}(\omega) + \alpha E_{\text{x}}^{\text{HF,SR}}(\omega) + (1 - \alpha)E_{\text{c}}^{\text{PBE,SR}}(\omega) , \quad (2.33)$$

in which it was introduced a new parameter, ω , that measures the intensity of the Coulomb screening, i. e., the extension of the non-local Fock interactions.

For example, if $\omega = 0 \text{ \AA}^{-1}$, the SR is equivalent to the full Fock operator and the LR contribution will become zero, while for $\omega \rightarrow \infty$, the range of SR terms decreases, recovering asymptotically the PBE functional. As defined in the PBE0 functional, the parameter α controls the amount of PBE exchange replaced by the non-local Fock exchange, and hence, in principle, it can range from 0 to 1. The most popular parametrization for the

HSE functional is called HSE06, with $\alpha = 0.25$ and $\omega = 0.206 \text{ \AA}^{-1}$, values from the same evaluation made by Perdew in PBE0 and fitted from a large number of systems.^{26,48}

2.2.4 Van der Waals energy

Due to the small influence of the Van der Waals interactions in the total energy determination, its correction is usually neglected in the development of most of the correlation functionals. However, for layered and 2D materials as graphene and transition metal dichalcogenides (TMDs), this correction is fundamental. The interaction among different layers is described through Van der Waals potentials. These are composed by three terms,

$$V_{dW} = V_{\text{dip-dip}}(\mathbf{r}) + V_{\text{dip-ind}}(\mathbf{r}) + V_{\text{london}}(\mathbf{r}) \quad (2.34)$$

where $V_{\text{dip-dip}}(\mathbf{r})$, $V_{\text{dip-ind}}(\mathbf{r})$ and $V_{\text{london}}(\mathbf{r})$ are dipole-dipole, dipole-induced dipole and London potential. The dipole-dipole term is the electrostatic potential between permanent dipoles in a polar system. This interaction is a part of the Coulomb potential in Kohn–Sham equation and does not need approximations. In the dipole-induced dipole term, the interaction occurs between polar and non-polar systems, similar to dipole-dipole interaction, this potential is incorporated in the Coulomb potential too. The London potential is interpreted as the interaction between an instantaneous dipole moment, caused by a fluctuation of the electron distribution that produces interactions between two bodies. A classical expression of this potential function between two heterogeneous bodies is given by

$$V_{\text{London}}(\mathbf{r}) = -\frac{3}{2} \frac{\alpha_A \alpha_B}{R_{AB}^6} \frac{I_A I_B}{I_A + I_B} \quad (2.35)$$

where I is the ionization potential. The London interaction is composed by a pure electron correlation between two bodies, and cannot be incorporated in the one-body mean-field approximation. This interaction is not incorporated in KS calculation using conventional (semi-)local functionals and needs to be introduced via a new term.

In the literature, various types of dispersion corrections have been suggested. These London dispersion corrections are generally classified into five types: i) classical dispersion corrections, ii) corrections determined through perturbation theories, iii) linear-response theories, iv) Van der Waals (dispersion) functionals and v) semiempirical dispersion-corrected functionals. Here, we focus only the semiempirical dispersion-correction, which was used in this project. This correction is based in the empirical classical form to London interaction, given by,

$$E_{\text{disp}}^{\text{London}} = - \sum_{i>j} \frac{C_6^{ij}}{R_{ij}^6} f_{\text{damped}}(R_{ij}) \quad (2.36)$$

where, C_6^{ij} is a parametrized interatomic dispersion coefficient and f_{damped} is a damping function for cutting off unnecessary short-range interactions. In the DFT-D functionals, there are three versions, DFT-D1, DFT-D2, and DFT-D3, based on the level of dispersion

corrections. This type of dispersion correction is efficient because it consists in an energy correction done *a posteriori*, i.e., the London dispersion energy is included after the end of the Kohn–Sham cycles. Due *a posteriori* inclusion in the total energy, this method has small computational cost when compared with other Van der Waals corrections, e.g., random phase approximation (RPA).

2.3 Computational implementation

In the development of this PhD project, we used well known packages as well as we implemented some computational codes. To perform the DFT calculations, we used the Vienna ab initio simulation package (VASP)^{49,50} to solve the Kohn–Sham equation, using a plane-waves basis and the project-augmented waves (PAW) method.⁵¹ The Kohn–Sham orbitals are expanded in a plane-wave basis which are limited with a cut-off energy. The relativistic effects are included as fully relativistic for core-electrons and as scalar relativistic for valence electrons. Spin-orbit coupling is included using the second-variation method.⁵² With VASP we evaluated the structural, elastic and electronic properties of all systems calculated in this project. Due to VASP code versatility, it is possible to easily change the internal parameters in the hybrid-density functional HSE, and include the corrections as spin-orbit coupling and Van der Waals energy, among others, which are already implemented in the code.

Another important code used in this project is the fitting method that connects the $\mathbf{k}\cdot\mathbf{p}$ Hamiltonians and the band structures from the DFT calculations. We initially implemented this code in Mathematica, using the non-linear minimization library implemented in its libraries. This implementation was efficient for a sparse matrix Hamiltonian, as 6 and 8 bands $\mathbf{k}\cdot\mathbf{p}$ Hamiltonian for zincblende, and was used in most of the papers of this PhD project. However, for a dense matrix Hamiltonian, as the 8-band $\mathbf{k}\cdot\mathbf{p}$ Hamiltonian for wurtzite systems used in the collaborative paper published in the PRB (appendix A), the implementation of the Mathematica library was not very efficient, requiring a large amount of RAM memory.

Consequently, we reimplemented the code in python, using the `scipy`⁵³ and `lmfit`⁵⁴ libraries. This implementation reduced the amount of time and machine resources required for the calculation. Also, as python has a free license, the access of the code became more extensive. Other improvements, such as adding modularization to the code were also implemented. With the last version of the code it was possible to evaluate a dense matrix $\mathbf{k}\cdot\mathbf{p}$ Hamiltonian, including large $\mathbf{k}\cdot\mathbf{p}$ Hamiltonian as the 14-band zincblende one. We intend to make the code available to the community. Finally, some simple codes were implemented, e.g., extracting the bands of VASP output files and energy rigid shifts, among others.

3 PUBLISHED PAPERS

Stability and accuracy control of $\mathbf{k} \cdot \mathbf{p}$ parameters

Carlos M O Bastos^{1,4}, Fernando P Sabino¹, Paulo E Faria Junior^{1,2},
Tiago Campos¹, Juarez L F Da Silva³ and Guilherme M Sipahi^{1,2}

¹ São Carlos Institute of Physics, University of São Paulo, PO Box 369, 13560-970, São Carlos, SP, Brazil

² Department of Physics, State University of New York at Buffalo, 14260, Buffalo, New York, USA

³ São Carlos Institute of Chemistry, University of São Paulo, PO Box 780, 13560-970, São Carlos, SP, Brazil

E-mail: cmobastos@ifsc.usp.br

Received 26 April 2016

Accepted for publication 26 July 2016

Published 1 September 2016



CrossMark

Abstract

The $\mathbf{k} \cdot \mathbf{p}$ method is a successful approach to obtain band structure, optical and transport properties of semiconductors and it depends on external parameters that are obtained either from experiments, tight binding or *ab initio* calculations. Despite the widespread use of the $\mathbf{k} \cdot \mathbf{p}$ method, a systematic analysis of the stability and the accuracy of its parameters is not usual in the literature. In this work, we report a theoretical framework to determine the $\mathbf{k} \cdot \mathbf{p}$ parameters from state-of-the-art hybrid density functional theory including spin-orbit coupling, providing a calculation where the gap and spin-orbit energy splitting are in agreement with the experimental values. The accuracy of the set of parameters is enhanced by fitting over several directions at once, minimizing the overall deviation from the original data. This strategy allows us to systematically evaluate the stability, preserving the accuracy of the parameters, providing a tool to determine optimal parameters for specific ranges around the Γ -point. To prove our concept, we investigate the zinc blende GaAs that shows results in excellent agreement with the most reliable data in the literature.

 Online supplementary data available from stacks.iop.org/sst/31/105002/mmedia

Keywords: $\mathbf{k} \cdot \mathbf{p}$ parameters, DFT-HSE, band structure, electronic states

(Some figures may appear in colour only in the online journal)

1. Introduction

A deep knowledge of the band structure (electronic states) of semiconductors is one of the first steps towards the understanding of a wide range of physical systems and phenomena, such as topological insulators [1–3], Majorana fermions [4–7] and polytypic nanowhiskers [8, 9] or technologies such as spintronics [10, 11]. The band structure of a given material of interest can be obtained using experimental information [12, 13] or based on theoretical calculations using different level of approximations developed along the years [14], i.e., the effects of particular interactions can be studied in details. For example, the role of the spin-orbit coupling (SOC) can be studied in

detail using different approximations, which is crucial as SOC plays a critical role in the systems mentioned above.

The theoretical approaches to calculate the band structure for a given material can be separated in two lines, namely, (i) first-principles methods based on density functional theory (DFT) [15, 16] or quantum-chemistry methods such as the Hartree-Fock; (ii) phenomenological approaches such as the $\mathbf{k} \cdot \mathbf{p}$ [17, 18] or tight-binding [19–21] methods. For crystalline materials, both first-principles and phenomenological approaches can be applied and their results can be compared with experiments, and hence, their accuracy can be established. However, the use of first-principles methods for modeling confined systems such as quantum-dots, nanowires, etc, requires supercells with thousand or even million atoms, which are forbidden because of its computational cost. In

⁴ Author to whom any correspondence should be addressed.

contrast, the $\mathbf{k} \cdot \mathbf{p}$ method has a lower computational cost because the interactions between the particles are described by an effective potential set up by a set of parameters. The determination of such parameters is of seminal importance.

The $\mathbf{k} \cdot \mathbf{p}$ Hamiltonian is constructed using the framework of perturbation theory [22, 23] and group theory analysis to reduce the number of matrix elements that are replaced by effective parameters. The number of parameters depend on the number of selected bands and on the symmetry of the described crystal. In zinc blende crystals, there is a relation allowing to calculate the effective mass parameters using the effective masses themselves [24], but for wurtzite crystal symmetry this is no longer true [25].

The effective masses can be determined experimentally using, for example, cyclotron resonance [26, 27], Hall effect [28] or optical measurements [29, 30], or theoretically, fitting a parabolic dispersion very close to Γ -point of *ab initio* band structure calculations [31, 32]. These procedures are only able to produce the effective mass parameters, leaving to other techniques the task of setting the values for the interband coupling parameters, such as the well known Kane parameter, P . This parameter is usually extracted from the effective g factor [33].

Parameters for most of the standard compounds may be found on the literature [33–36]. For example, [33] presents a compilation of parameters for almost all binary, ternary and quaternary zinc blende compounds and also for wurtzite III-nitrides, however, those parameters were obtained by mixing experimental and theoretical data, i.e., no systematic procedure was employed. The reference provides parameters for the usual 6×6 (Luttinger–Kohn [37]) and 8×8 (Kane [17] and Rashba–Sheka–Pikus [38]) band models. As we go further into the $\mathbf{k} \cdot \mathbf{p}$ models, there exist only few reliable sources of parameters for models with a higher number of bands, e.g., for 14×14 [39, 40], 20×20 [41], 24×24 [42], 34×34 [43] and 40×40 [44] bands.

In this paper, we developed a new framework to determine the $\mathbf{k} \cdot \mathbf{p}$ parameters from preexistent band structures that works with any crystal symmetry. Fitting a set of functions

derived from the secular equation of the $\mathbf{k} \cdot \mathbf{p}$ Hamiltonian to a preexistent band structure we were able to extract all the $\mathbf{k} \cdot \mathbf{p}$ parameters at once, including the interband coupling parameters. Furthermore, we performed the fitting using several different directions of the first Brillouin zone (FBZ), thus finding all the parameters in a consistent way. As a proof of concept we use a zinc blende GaAs band structure obtained by the hybrid DFT calculation with the Heyd–Scuseria–Ernzerhof (HSE) functional. Since GaAs is the most studied material it will be easy to compare our results with the reported values in the literature. Furthermore, using our method we are able to predict the best set of parameters for a specific region of the FBZ. We show that, in the GaAs case, our parameters are in good agreement with the literature. We also address the accuracy of the Kane model by defining an strategy to evaluate its limits of validity. In conclusion, our method is neither limited to the crystal phase nor the Hamiltonian and opens up the possibility to study novel semiconductor systems.

The paper is organized as follows: in section 2 we present the the 8×8 $\mathbf{k} \cdot \mathbf{p}$ Hamiltonian. The process to obtain DFT-HSE band structure for GaAs is shown in section 3. In section 4 we show the developed method for a general Hamiltonian specify the expressions for the 8×8 Hamiltonian. The application of the method to zinc blende GaAs band structure is presented in section 5. We proceed to the analysis of optimal parameters in section 6, comparing our results with the literature in section 7. Finally, our conclusions are shown in section 8.

2. The $\mathbf{k} \cdot \mathbf{p}$ method

In this paper, we employed the 8×8 $\mathbf{k} \cdot \mathbf{p}$ Hamiltonian proposed by Kane [17], that extends the 6×6 Hamiltonian proposed by Luttinger–Kohn [37], in which the first-order contribution of the \mathbf{k} -dependent spin–orbit term and also the second order contribution of $\mathbf{k} \cdot \mathbf{p}$ between conduction (CB) and valence bands (VBs) are neglected. Further details on the $\mathbf{k} \cdot \mathbf{p}$ Hamiltonian are discussed in the supplemental material. The 8×8 Kane Hamiltonian shows as

$$\begin{pmatrix} Q & S & R & 0 & i\frac{S}{\sqrt{2}} & -i\sqrt{2}R & -iP_- & 0 \\ S^\dagger & T & 0 & R & i\frac{(T-Q)}{\sqrt{2}} & i\sqrt{\frac{3}{2}}S & \sqrt{\frac{2}{3}}P_z & -\frac{1}{\sqrt{3}}P_- \\ R^\dagger & 0 & T & -S & -i\sqrt{\frac{3}{2}}S^\dagger & i\frac{(T-Q)}{\sqrt{2}} & -\frac{i}{\sqrt{3}}P_+ & -i\sqrt{\frac{2}{3}}P_z \\ 0 & R^\dagger & -S^\dagger & Q & -i\sqrt{2}R^\dagger & -i\frac{S^\dagger}{\sqrt{2}} & 0 & -P_+ \\ -i\frac{S^\dagger}{\sqrt{2}} & -i\frac{(T-Q)^\dagger}{\sqrt{2}} & i\sqrt{\frac{3}{2}}S & i\sqrt{2}R & \frac{Q+T}{2} + \Delta_{so} & 0 & -\frac{i}{\sqrt{3}}P_z & -i\sqrt{\frac{2}{3}}P_- \\ i\sqrt{2}R^\dagger & -i\sqrt{\frac{3}{2}}S^\dagger & -i\frac{(T-Q)^\dagger}{\sqrt{2}} & i\frac{S}{\sqrt{2}} & 0 & \frac{Q+T}{2} + \Delta_{so} & \sqrt{\frac{2}{3}}P_+ & -\frac{1}{\sqrt{3}}P_z \\ -iP_- & \sqrt{\frac{2}{3}}P_z & \frac{i}{\sqrt{3}}P_- & 0 & \frac{i}{\sqrt{3}}P_z & \sqrt{\frac{2}{3}}P_- & E_c & 0 \\ 0 & -\frac{1}{\sqrt{3}}P_+ & i\sqrt{\frac{2}{3}}P_z & -P_- & i\sqrt{\frac{2}{3}}P_+ & -\frac{1}{\sqrt{3}}P_z & 0 & E_c \end{pmatrix}, \quad (1)$$

where the terms are given by

$$\begin{aligned}
Q &= -\frac{\hbar^2}{2m_0} [(\tilde{\gamma}_1 + \tilde{\gamma}_2)(k_x^2 + k_y^2) - (\tilde{\gamma}_1 - 2\tilde{\gamma}_2)k_z^2], \\
R &= -\frac{\hbar^2}{2m_0} \sqrt{3} [\tilde{\gamma}_2(k_x^2 - k_y^2) + 2i\tilde{\gamma}_3 k_x k_y], \\
E_c &= E_g + \frac{\hbar^2}{2m_0} \tilde{\epsilon} k^2, \\
P_z &= P k_z, \\
T &= -\frac{\hbar^2}{2m_0} [(\tilde{\gamma}_1 - \tilde{\gamma}_2)(k_x^2 + k_y^2) + (\tilde{\gamma}_1 + 2\tilde{\gamma}_2)k_z^2], \\
S &= i\frac{\hbar^2}{2m_0} [2\sqrt{3}\tilde{\gamma}_3 k_z (k_x - ik_y)], \\
P_{\pm} &= \frac{1}{\sqrt{2}} P (k_x \pm ik_y), \\
k^2 &= k_x^2 + k_y^2 + k_z^2
\end{aligned} \tag{2}$$

with the following parameters:

- $\tilde{\gamma}_1, \tilde{\gamma}_2, \tilde{\gamma}_3, \tilde{\epsilon}$: second order effective mass parameters of VB and CB. These parameters are adimensional⁵.
- P : first order interaction term between states in the CB and the VB. An energy equivalent, $E_p = 2m_0 P^2 / \hbar^2$, may be used to analyze the effects of this parameter.
- Δ_{so} : first order SOC interaction term (energy difference between HH/LH and SO bands at Γ -point).
- E_g : energy band gap between the CB and HH/LH bands at the Γ -point.

The Kane Hamiltonian basis set is composed by the topmost six states of VB and the first two states of CB, in the following order: $|\text{HH}\uparrow\rangle, |\text{LH}\uparrow\rangle, |\text{LH}\downarrow\rangle, |\text{HH}\downarrow\rangle, |\text{SO}\uparrow\rangle, |\text{SO}\downarrow\rangle, |\text{CB}\uparrow\rangle, |\text{CB}\downarrow\rangle$. HH, LH, SO and CB stand for the heavy hole, light hole, split-off hole and CB states, respectively. \uparrow and \downarrow are used to distinguish the total angular momentum projections. The states description using the original atomic orbital basis is given by:

$$\begin{aligned}
|\text{HH}\uparrow\rangle &= \frac{1}{\sqrt{2}} |(X + iY)\uparrow\rangle, \\
|\text{HH}\downarrow\rangle &= \frac{i}{\sqrt{2}} |(X - iY)\downarrow\rangle, \\
|\text{LH}\uparrow\rangle &= \frac{i}{\sqrt{6}} |(X + iY)\downarrow - 2Z\uparrow\rangle, \\
|\text{LH}\downarrow\rangle &= \frac{1}{\sqrt{6}} |(X - iY)\uparrow + 2Z\downarrow\rangle, \\
|\text{SO}\uparrow\rangle &= \frac{1}{\sqrt{3}} |(X + iY)\downarrow + Z\uparrow\rangle, \\
|\text{SO}\downarrow\rangle &= \frac{i}{\sqrt{3}} |-(X - iY)\uparrow + Z\downarrow\rangle, \\
|\text{CB}\uparrow\rangle &= |S\uparrow\rangle, \\
|\text{CB}\downarrow\rangle &= |S\downarrow\rangle,
\end{aligned} \tag{3}$$

⁵ The tilde is used, as in $\tilde{\gamma}_1$, to refer to the Kane model parameters in opposition to the Luttinger parameters, defined in [37], that are noted without it, as in γ_1 .

where $|X\rangle, |Y\rangle$ and $|Z\rangle$ are the p-type like states (p_x, p_y and p_z) and $|S\rangle$ the s-like ones and \uparrow and \downarrow represent their spins.

3. GaAs hybrid DFT-HSE band structure

The *ab initio* GaAs band structure was obtained through the use of hybrid DFT calculations within the HSE [45] exchange-correlation functional where the energy is given by the following equation

$$\begin{aligned}
E_{\text{xc}}^{\text{HSE}} &= \alpha E_{\text{x}}^{\text{SR}}(\mu) + (1 - \alpha) E_{\text{x}}^{\text{PBE,SR}} \\
&+ E_{\text{x}}^{\text{PBE,LR}} + E_{\text{c}}^{\text{PBE}}.
\end{aligned} \tag{4}$$

In the HSE formulation, the exchange energy is partitioned into two terms, namely, short range (SR) and long range (LR) terms. A screening nonlocal Fock operator is employed to obtain the SR term, in which the μ parameter ($\mu = 0.206 \text{ \AA}^{-1}$) determines the intensity of the screening [46], while the LR term is described by the semilocal Perdew–Burke–Ernzerhof (PBE) [47] functional. The parameter α defines the percentage of the nonlocal SR exchange term, and it is 0.25 in the HSE06 functional. However, this particular value was obtained for typical molecules, based on the analysis of the adiabatic connection formula and the lowest order of Görling–Levy perturbation theory [47], and consequently does not yield a correct band gap (although better than PBE) for most of the materials [46–48]. Therefore, the α parameter can be assumed as a fitting parameter, which can be adjusted to reproduce particular bulk properties, e.g., energy band gap, lattice parameter, etc. We have fitted α to yield the fundamental experimental GaAs band gap [23, 33] (i.e., 1.519 eV).

To solve the Kohn–Sham equation, we employed the projected augmented wave (PAW) method [49, 50], as implemented in Vienna *ab initio* simulation package (VASP) [51, 52], and the PAW projectors provided within VASP to describe the following valence states, $4s^2 4p^3$ for As and $3d^{10} 4s^2 4p^1$ for Ga. To describe the valence electronic states, we employed the scalar relativistic approximation, in which the SOC effects for the valence states were taken into account by perturbation theory employing 38 empty states. For the total energy and band structure calculations, we employed a cutoff energy of 455 eV, while a cutoff energy of 607 eV was used to obtain the equilibrium volume by the minimization of the stress tensor. For the Brillouin zone integration, we employed a \mathbf{k} -point mesh of $8 \times 8 \times 8$, which yields accurate results.

GaAs crystallize in the well known zinc blende structure with space group T_d and one formula unit per primitive unit cell, in which every Ga atom is surrounded by four As atoms (tetrahedral symmetry), and vice versa. Using the fact that the band gap of a semiconductor increases almost linearly by increasing the percentage of the α (nonlocal Fock term) parameter [48] we set $\alpha = 0.317$, finding a GaAs band gap of 1.521 eV, which deviates by 0.14% from the experimental

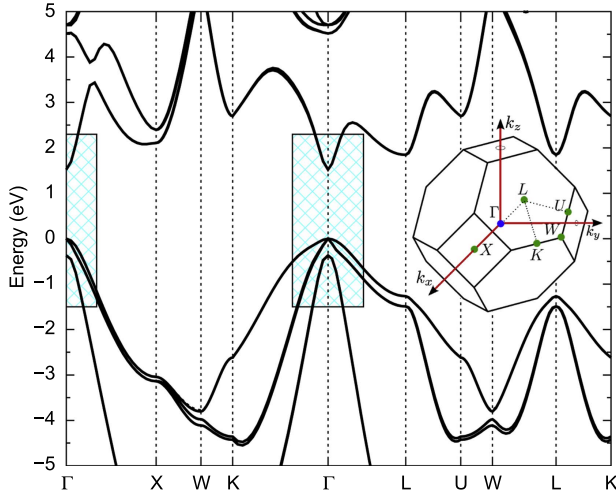


Figure 1. Band structure for GaAs zinc blende with the respective FBZ and the high symmetry points. The highlighted regions indicate the approximate region where Kane Hamiltonian is valid.

result. We obtained an equilibrium lattice parameter of 5.652 Å, which deviates by 0.03% compared with the experimental results (5.654 Å) [53]. However, we would like to point out that using $\alpha = 0$ yields $a_0 = 5.733$ Å. Furthermore, total calculations at the same lattice constant without the SOC for the valence states increase the band gap to 1.627 eV.

Figure 1 presents the band structure with SOC for the valence states on the usual high-symmetry Brillouin lines. Both the VBM and the CBM are located at the Γ -point, as expected [33]. In the absence of SOC (not shown here), the highest VB is composed by a sixfold degenerate state (each band being twofold degenerate in spin) at Γ -point. However, when the SOC is considered this degeneracy is broken in a twofold degenerate, split-off band, and a fourfold degenerate band that still remains the highest VB. The energy difference between these states are $\Delta_{so} = 0.369$ eV which is 8% bigger than the experimental value, 0.341 eV [33]. Even though the band gap was fitted to yield the experimental result, the Δ_{so} parameter was not fitted in our calculations, which explains this difference. For \mathbf{k} -points other than Γ , SOC still breaks the degeneracy of the highest VB, creating the heavy and light holes bands. A closer look will show that in less symmetric points, e.g. along the $\Gamma - K$ line, the degeneracy is further broken, creating bands with no degeneracy. The present results are consistent with the literature, including SOC or not.

To ensure high quality data for the fitting along the desired $\Gamma - X$, $\Gamma - L$ and $\Gamma - K$ lines, we calculated a large number of \mathbf{k} -points along each line. Because of the perturbation theory used in the $\mathbf{k} \cdot \mathbf{p}$ method, we expect to fit the parameters only at a defined region around the Γ -point. In order to reduce the high computational cost of the hybrid DFT-HSE+SOC approach, we restricted \mathbf{k} -points to 100 samples up to 50% of the FBZ.

4. The fitting method

Along the years, $\mathbf{k} \cdot \mathbf{p}$ parameters are usually being derived from effective masses using experimental data [36, 54–57] or from theoretical band structure calculations [32, 58–63]. Although this procedure is relatively simple, it is not always possible to find analytical solutions relating $\mathbf{k} \cdot \mathbf{p}$ parameters to the effective masses. Alternatively, the determination of the parameters may rely on the fitting of previously calculated band structures [31, 60, 64–69]. However, details about the fitting approach are not usually described by the authors.

Although we consider a fitting that is based on the resolution of the secular equation, as in previous works [59, 68, 70], we used it in a different way. The secular equation is used to reduce the complexity of the fitting. Using the property that the eigenvalues are roots of the secular equation and, by consequence, assuming that we can collect expressions for any of the coefficients that must also be zero, we extract a new set of n equations (n being the order of the original matrix) that are used in our fitting. With this procedure, we make explicit the couplings among the different bands, simplifying the expressions to be solved. The functions determined for each direction are used together to provide the fitting that minimizes the euclidean distance of the full set of equations to the previously calculated data at once. Because we determine all the distances in a single step, we guarantee that no direction is assigned more importance than any other. In fact, the addition of other directions to the fitting provides a way to increase the accuracy.

The general form of any $\mathbf{k} \cdot \mathbf{p}$ matrix with n energy bands is given by

$$\begin{pmatrix} \alpha_{11}(\mathbf{k}, \{p\}) & \dots & \alpha_{1i}(\mathbf{k}, \{p\}) & \dots & \alpha_{1n}(\mathbf{k}, \{p\}) \\ \vdots & \ddots & \vdots & \ddots & \vdots \\ \alpha_{i1}^\dagger(\mathbf{k}, \{p\}) & \dots & \alpha_{ii}(\mathbf{k}, \{p\}) & \dots & \alpha_{in}(\mathbf{k}, \{p\}) \\ \vdots & \ddots & \vdots & \ddots & \vdots \\ \alpha_{1n}^\dagger(\mathbf{k}, \{p\}) & \dots & \alpha_{in}^\dagger(\mathbf{k}, \{p\}) & \dots & \alpha_{nn}(\mathbf{k}, \{p\}) \end{pmatrix}, \quad (5)$$

where the matrix elements, $\alpha_{ij}(\mathbf{k}, \{p\})$ are functions that represent each matrix element with \mathbf{k} being the wave vector and $\{p\}$, the set of $\mathbf{k} \cdot \mathbf{p}$ parameters to be determined.

The secular equation of the Hamiltonian (5) may be written as a general polynomial for the eigenvalues ϵ

$$\begin{aligned} & c_{n-1}(\alpha_{11}(\mathbf{k}, \{p\}), \dots, \alpha_{nn}(\mathbf{k}, \{p\}))\epsilon^{n-1}(\mathbf{k}) \\ & + \dots + c_1(\alpha_{11}(\mathbf{k}, \{p\}), \dots, \alpha_{nn}(\mathbf{k}, \{p\}))\epsilon(\mathbf{k}) \\ & + c_0(\alpha_{11}(\mathbf{k}, \{p\}), \dots, \alpha_{nn}(\mathbf{k}, \{p\})) = -\epsilon^n(\mathbf{k}), \end{aligned} \quad (6)$$

where c_i are the polynomial coefficients, functions of the matrix elements $\alpha_{ij}(\mathbf{k}, \{p\})$. Since these coefficients are functions of \mathbf{k} and $\{p\}$, we can denote them as $c_i(\mathbf{k}, \{p\})$, rewriting the above equation as

$$\sum_{i=0}^{n-1} c_i(\mathbf{k}, \{p\})\epsilon^i(\mathbf{k}) = -\epsilon^n(\mathbf{k}). \quad (7)$$

The analytical forms of these coefficients are used as the fitting functions on our approach, and will be identified as

analytical functions, denoted by the super-index A :

$$\begin{cases} c_0^A(\mathbf{k}, \{p\}) \\ c_1^A(\mathbf{k}, \{p\}) \\ \vdots \\ c_{n-1}^A(\mathbf{k}, \{p\}). \end{cases} \quad (8)$$

The next step is to find a similar relation for the eigenvalues obtained from the preexistent band structures, from now on called *reference band structure*. Assuming that the eigenvalues satisfy the secular equation, we can write a system of equations to determine the polynomial coefficients as a function of the wave vector \mathbf{k} :

$$\begin{pmatrix} 1 & \epsilon_1(\mathbf{k}) & \dots & \epsilon_1^i(\mathbf{k}) & \dots & \epsilon_1^{n-1}(\mathbf{k}) \\ \vdots & \vdots & \ddots & \vdots & \ddots & \vdots \\ 1 & \epsilon_i(\mathbf{k}) & \dots & \epsilon_i^i(\mathbf{k}) & \dots & \epsilon_i^{n-1}(\mathbf{k}) \\ \vdots & \vdots & \ddots & \vdots & \ddots & \vdots \\ 1 & \epsilon_n(\mathbf{k}) & \dots & \epsilon_n^i(\mathbf{k}) & \dots & \epsilon_n^{n-1}(\mathbf{k}) \end{pmatrix} \times \begin{pmatrix} c_0(\mathbf{k}) \\ c_1(\mathbf{k}) \\ \vdots \\ c_i(\mathbf{k}) \\ \vdots \\ c_{n-1}(\mathbf{k}) \end{pmatrix} = - \begin{pmatrix} \epsilon_1^n(\mathbf{k}) \\ \vdots \\ \epsilon_i^n(\mathbf{k}) \\ \vdots \\ \epsilon_n^n(\mathbf{k}) \end{pmatrix}, \quad (9)$$

where $\epsilon_i(\mathbf{k})$ represents the i th energy band.

Therefore, using eigenvalues from the *reference band structure*, we can solve this system to obtain the coefficients c_i as functions of $\epsilon_i(\mathbf{k})$. This form of the coefficients will be called *numerical functions*, denoted by the super-index N :

$$\begin{cases} c_0^N[\epsilon_1(\mathbf{k}), \epsilon_2(\mathbf{k}), \dots, \epsilon_n(\mathbf{k})] \\ c_1^N[\epsilon_1(\mathbf{k}), \epsilon_2(\mathbf{k}), \dots, \epsilon_n(\mathbf{k})] \\ \vdots \\ c_{n-1}^N[\epsilon_1(\mathbf{k}), \epsilon_2(\mathbf{k}), \dots, \epsilon_n(\mathbf{k})]. \end{cases} \quad (10)$$

Since we want to use the $\mathbf{k} \cdot \mathbf{p}$ to describe our *reference band structure*, we should now consider that both numerical and analytical forms of the coefficients are equivalent, leading to the equality

$$\begin{cases} c_0^A(\mathbf{k}, \{p\}) = c_0^N[\epsilon_1(\mathbf{k}), \epsilon_2(\mathbf{k}), \dots, \epsilon_n(\mathbf{k})] \\ c_1^A(\mathbf{k}, \{p\}) = c_1^N[\epsilon_1(\mathbf{k}), \epsilon_2(\mathbf{k}), \dots, \epsilon_n(\mathbf{k})] \\ \vdots \\ c_{n-1}^A(\mathbf{k}, \{p\}) = c_{n-1}^N[\epsilon_1(\mathbf{k}), \epsilon_2(\mathbf{k}), \dots, \epsilon_n(\mathbf{k})]. \end{cases} \quad (11)$$

Having both, analytical and numerical functions, we can perform the fitting procedure to extract the $\mathbf{k} \cdot \mathbf{p}$ parameters that best describe the *reference band structure*. The fitting was done using the nonlinear least squares method, implemented on MathematicaTM using the NonLinearModelFit routine [71]. Several different minimization methods were tested: Newton, QuasiNewton, LevenbergMarquardt, Gradient, Conjugate Gradient. As the results were similar for all tested methods, we chose the conjugate gradient method due

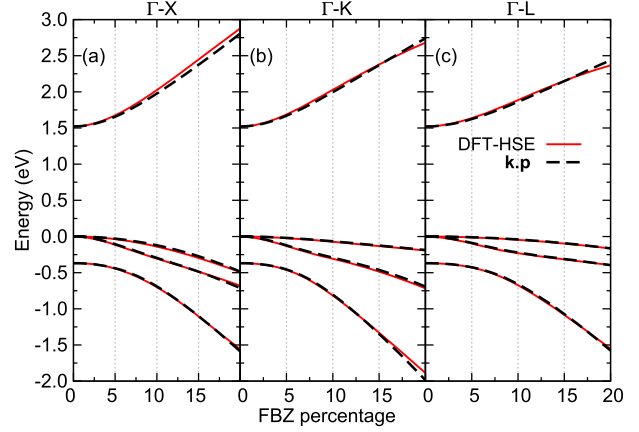


Figure 2. Comparison between the band structure obtained by diagonalization of the $\mathbf{k} \cdot \mathbf{p}$ Hamiltonian with the 20% region parameter set (dashed lines) and the band structure obtained by hybrid DFT-HSE+SOC (solid lines). We show three directions of the FBZ: (a) $\Gamma - X$, (b) $\Gamma - K$ and (c) $\Gamma - L$. The x-axis shows percentage in the specific direction.

to its relatively low memory requirements for a large-scale problem and simplicity of its iteration [72].

The fitting method described above is general, and it can be applied for any given system, even for $\mathbf{k} \cdot \mathbf{p}$ Hamiltonians larger than 8×8 and any direction in the FBZ. For the particular case of semiconductors with zinc blende structures, we can sample the FBZ along the three most relevant high-symmetry directions, namely, $\Gamma - X$, $\Gamma - K$, and $\Gamma - L$. The number of \mathbf{k} -point lines play an important role, e.g., the direction $\Gamma - L$ can yield only the $\tilde{\gamma}_1$ and $\tilde{\gamma}_3$ parameters, and hence, additional directions are required to identify the $\tilde{\gamma}_2$ parameter.

For the case of the Hamiltonian given in equation (1), the secular equation can always be factorized in the separate components, reducing the dimension of the problem by half. The factorized secular equation reads as

$$[c_0^N(\mathbf{k}, \{p\}) + c_1^N(\mathbf{k}, \{p\})\epsilon + c_2^N(\mathbf{k}, \{p\})\epsilon^2 + c_3^N(\mathbf{k}, \{p\})\epsilon^3 + \epsilon^4]^2 = 0, \quad (12)$$

where $\{p\} = \{\tilde{\gamma}_1, \tilde{\gamma}_2, \tilde{\gamma}_3, \Delta_{\text{so}}, P, E_g, \tilde{\epsilon}\}$. In specific directions the secular equation may be further factorized.

Solving the system (12), we obtain the following relations for the numerical coefficients

$$\begin{aligned} c_{\text{HH}}^N(k_{\text{TX}}) &= -\epsilon_{\text{HH}}(k_{\text{TX}}), \\ c_2^N(k_{\text{TX}}) &= -\epsilon_{\text{CB}}(k_{\text{TX}}) - \epsilon_{\text{LH}}(k_{\text{TX}}) - \epsilon_{\text{SO}}(k_{\text{TX}}), \\ c_1^N(k_{\text{TX}}) &= \epsilon_{\text{CB}}(k_{\text{TX}})\epsilon_{\text{LH}}(k_{\text{TX}}) + \epsilon_{\text{CB}}(k_{\text{TX}})\epsilon_{\text{SO}}(k_{\text{TX}}) \\ &\quad + \epsilon_{\text{LH}}(k_{\text{TX}})\epsilon_{\text{SO}}(k_{\text{TX}}), \\ c_0^N(k_{\text{TX}}) &= \epsilon_{\text{CB}}(k_{\text{TX}})\epsilon_{\text{LH}}(k_{\text{TX}})\epsilon_{\text{SO}}(k_{\text{TX}}). \end{aligned} \quad (13)$$

Notice that in the previous expressions, $\epsilon_1, \epsilon_2, \epsilon_3$ and ϵ_4 were replaced by the average of the eigenvalues of the bands at the specific k -point: $\epsilon_{\text{CB}}, \epsilon_{\text{HH}}, \epsilon_{\text{LH}}$ and ϵ_{SO} .

The parameters Δ_{so} and E_g can be directly found from the Γ -point energies and used as input to the fitting approach. Since, we adjusted simultaneously the expressions for all the

different bands in all chosen directions of the FBZ, the overall quality of the parameters for the multiband Hamiltonian is guaranteed.

5. $\mathbf{k} \cdot \mathbf{p}$ parameters for zinc blende GaAs

In figure 2, we show the results of the fitting, using 20% of the FBZ superposed to the original DFT-HSE+SOC calculation. For this particular range, we have found the following set of parameters: $\gamma_1 = 1.31$, $\gamma_2 = -0.72$, $\gamma_3 = 0.03$ and $e = -2.50$ in units of $\hbar^2/2m_0$; $P = 9.75$ eV Å. A first inspection shows that the most important features of the band structure are preserved. The band structure for this range of wave vectors has essentially two different regions, one up to 8% of the FBZ and a second from 8% to 20%. The HH and LH bands present nearly parabolic behavior in both regions, but the effective masses if calculated only inside each region, would be clearly different. The nonparabolicity, or band scattering, around 8% and the quasi linear behavior of the CB and the split-off hole bands after the nonparabolicity are in good agreement with the *reference band structure*. Finally, a simple visual inspection of this results shows that the difference between the curves is smaller than 8% at the borders of the region.

To avoid using visual estimation of the agreement of curves, it is necessary to find a procedure that numerically determines how close the DFT-HSE+SOC and the $8 \times 8 \mathbf{k} \cdot \mathbf{p}$ band structures are with respect to each other. This analysis can also be used to determine if in a smaller region, an optimized parameter can lead to more reliable results. To evaluate the agreement, we performed fittings over different ranges around the Γ -point, from 2% up to 20% of the FBZ, obtaining a large number of $\mathbf{k} \cdot \mathbf{p}$ parameter sets.

6. Optimal parameter set

In order to evaluate the assertiveness of our parameters, we employed the root mean square deviation (RMSD) to compare the *reference* and *parametrized* band structures using the appropriate definition of the RMSD to our problem

$$\text{RMSD} = \sqrt{\frac{1}{N} \sum_d \sum_{\mathbf{k}_d} \sum_n [\epsilon_n^p(\mathbf{k}_d) - \epsilon_n^r(\mathbf{k}_d)]^2}, \quad (14)$$

where the summations run over the directions in which the FBZ was sampled, d , the points of the reciprocal space calculated in each direction, \mathbf{k}_d , and the bands taken into account, n . N_d , $N_{\mathbf{k}}$ and N_n are the total values of each one of these variables. The super-index p (r) in the energy bands denotes the *parametrized* (*reference*) band structure. Notice that the normalization condition (with $N = N_d \times N_{\mathbf{k}} \times N_n$) allows us to compare sets with different numbers of points. The smaller the value of the RMSD, the better our Hamiltonian and parameters fit the DFT-HSE+SOC band structure.

The search for the optimal parameter set is performed as follows: (i) we determine the parameter sets for different fitting percentages of the FBZ; (ii) for each of these parameter sets, we calculate the RMSD for different FBZ percentages; (iii) the optimal parameter set presents the minimum RMSD value for a given FBZ percentage. We considered 16 different percentage values in the range from 2% to 20%, that were used to define either the parameter sets and the analyzed region.

In figure 3(a) we show the RMSD density map, with y -axis representing the fitting percentage of the parameter sets and the x -axis, the FBZ percentage used in the RMSD determination. The lowest RMSD values for each range are represented by the black dashed line. These parameter sets represent the best parameters that describe each range. We found that all parameter sets reproduce the band structure in the region below 6% with an average deviation of around 2 meV. If the parameter set is in the fitting range between 6% and 14%, the region of optimal agreement is extended to approximately 12% of the FBZ with just a slight increase of the RMSD value. If one considers a higher deviation, e.g. 10 meV, this region would be extended to around 15%. Animations of the optimal $\mathbf{k} \cdot \mathbf{p}$ band structure changes with the fitting region limit can be found in the supplemental materials.

Figure 3(b) shows the RMSD for the optimal parameters sets. We can see an increase of the average deviation by the increase of the FBZ range. This would be expected since the $8 \times 8 \mathbf{k} \cdot \mathbf{p}$ Hamiltonian is valid in a region around Γ -point. The results presented here show that the average deviation for the 20% range is still below 20 meV, reasonable for most of the optical simulations and for ranges below 14% the average deviation is only 4 meV.

The maximum deviation from the DFT-HSE calculation for each range in the 3 different directions, $\Gamma - X$, $\Gamma - K$ and $\Gamma - L$, is shown in figures 3(c)–(e), respectively. Although CB and SO present large deviations at 20% of the FBZ (approx. 100 meV along $\Gamma - K$ for CB and SO and also along $\Gamma - L$ for CB), for all other sampled curves, the bands present up to this percentage a deviation much smaller (around 50 meV for CB and LH at $\Gamma - X$ and smaller than 25 meV for all others). The large values of the deviation for CB and SO, indicate that they are mainly responsible for the steep increase of the RMSD around 15%, i.e., all other curves have a very small deviation up to this percentage.

A general overview of the parameter sets with and without the optimization approach is presented in figure 4 for different FBZ regions. The dashed lines represent the raw data, i.e., the parameter sets obtained directly from the fitting of the specific range while the solid lines are used for the optimal parameters for the same range. One can clearly distinguish two different regions: (i) below 7%, we can see a fast decay of the values for the interband interaction parameter, P , (on top) and a fast increase for the effective masses (on bottom); and (ii) above 7%, the parameters are almost stable with a very slight linear variation.

Analyzing the band structure behavior, it is easy to notice that using a range that takes into account the nonparabolicity around 8% is essential to determine a stable set of parameters. In light of figure 3(b) however, one can state that, even with

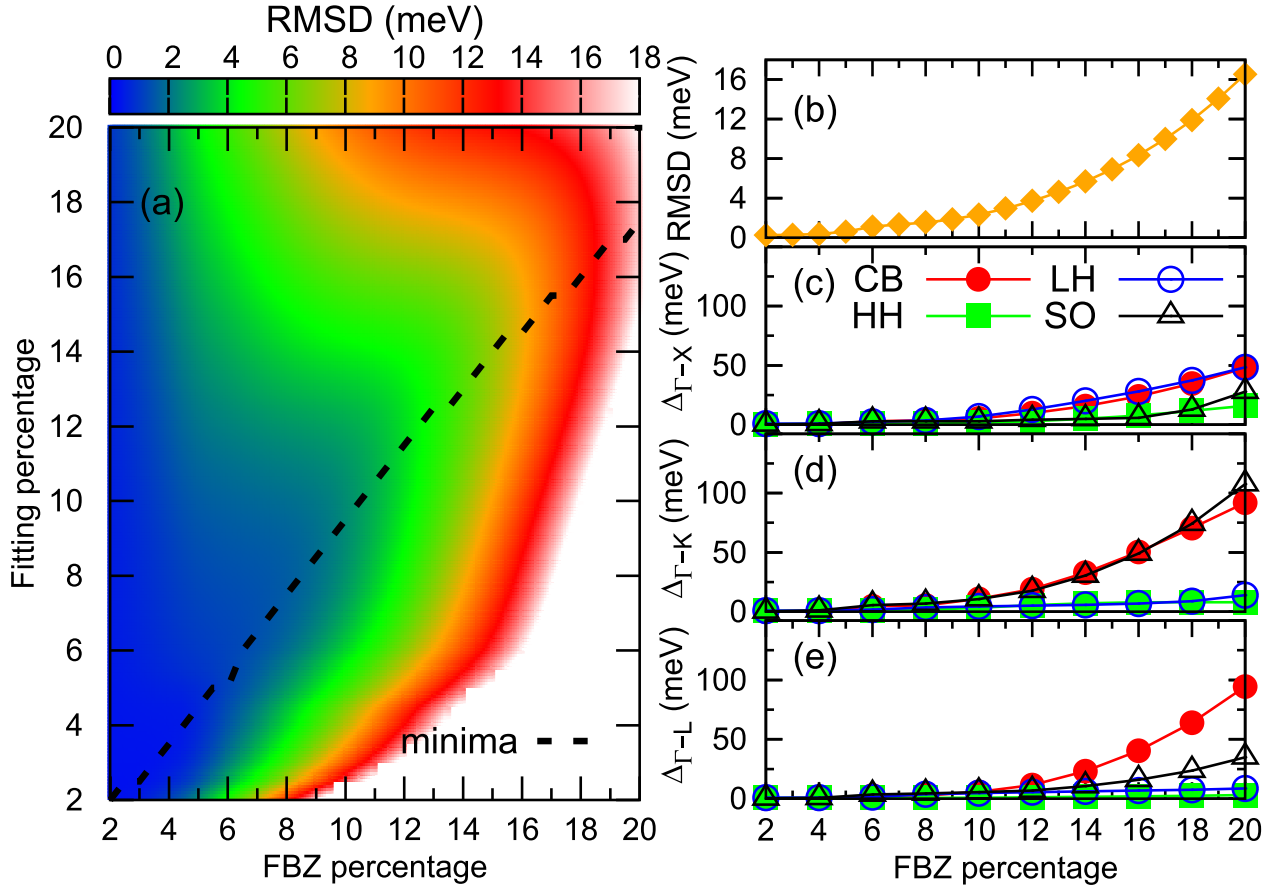


Figure 3. (a) Root mean square deviation (RMSD) density map showing the agreement of the different adjusted parameter sets against the range around the Γ -point they are sampled. The optimal parameter sets are indicated by the dashed line. (b) RMSD of the optimal set of parameters for each enclosing region. (c)–(e) show the maximum deviation for each optimal parameter set for the three directions used in the fitting process.

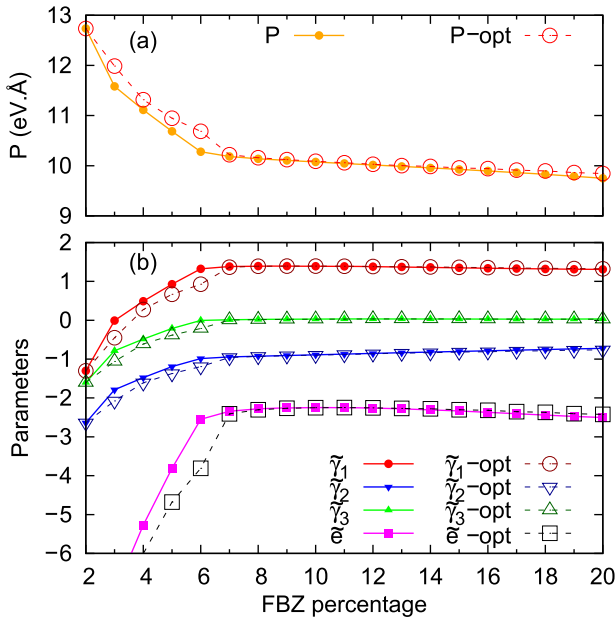


Figure 4. Comparison between optimal and nonoptimal parameter sets. (a) P parameter in eV Å units and (b) $\tilde{\gamma}_1$, $\tilde{\gamma}_2$, $\tilde{\gamma}_3$ and \tilde{e} .

the stability of the parameter values, an optimal set must be chosen to enhance the accuracy of the fitting. This can be seen on figure 5, where we present the agreement of *parametrized* and *reference* band structures for the optimal (solid lines) and nonoptimal (dashed lines) parameter sets for the range of 20%. The optimal parameters for 20% were obtained for the fitting using the range of 17.5% and read as: $\tilde{\gamma}_1 = 1.28$, $\tilde{\gamma}_2 = -0.73$, $\tilde{\gamma}_3 = 0.03$ and $\tilde{e} = -2.34$ and $P = 9.85$ eV Å. Since the behavior of the bands in the different directions is very similar, we chose to present only the $\Gamma - L$ direction. The supplemental materials provide other directions expressions. The differences are more striking in CB and split-off bands, where the choice of the parameters can reduce the total deviation to approximately two thirds for a specific point, i.e. from 25–15 meV on CB and from 15–10 meV on SO. To see a complete table with optimal parameters for the full range of enclosing regions, please refer to the supplemental materials.

7. Comparison with literature parameters

The literature presents in general a unique set of parameters for any material. As we suggest optimal parameters for

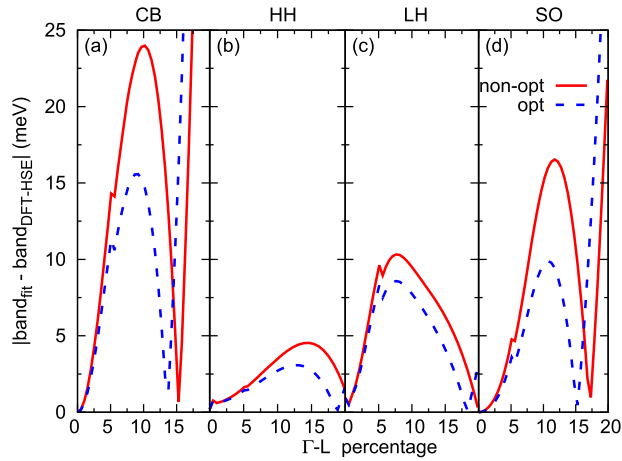


Figure 5. Difference between the DFT-HSE and $\mathbf{k} \cdot \mathbf{p}$ band structures calculated with optimal (solid lines) and nonoptimal (dashed lines) parameter sets along $\Gamma - L$ direction for: (a) CB; (b) HH; (c) LH; and (d) SO bands. The optimal parameters set shows better agreement with the DFT-HSE band structure. Other directions show similar behaviors.

specific ranges of the FBZ, in our comparison we chose 7 different parameter sets from the literature [33, 36, 54–56, 58, 73], see table in appendix. Using these sets, we calculated the average value for each parameter and its standard deviation. In figure 6 we plot the optimal parameters together with shadowed regions showing the intervals of the standard deviation around the average values of the parameters. Our results show good agreement with the literature data in general, since the values obtained for ranges larger than 7% are stable and lie always inside the standard deviation interval around the average of the values selected from the literature.

The behavior presented for regions smaller than 7% may be understood by a simple analysis the band structure and the role of E_p in the secular equation. E_p can be adimensionalized by defining a new parameter that reads as $\tilde{\gamma}_p = E_p/E_g$, showing that, even if P appears in first order perturbation terms, $\tilde{\gamma}_p$ acts as an effective mass parameter. According to this new definition, we have now five different effective mass parameters and four bands to do the fitting. As up to 7%, the bands show a clear parabolic behavior, the fitting of the parameters become undetermined. Around this percentage all the bands start mixing and nonparabolic behavior may be seen. Just above this region, a new parabolic behavior emerges and all the bands change their curvatures accordingly. Including the two parabolic regions in the fitting, e.g., fitting from Γ to 12%, provides the necessary relations to distinguish among the different parameters influence on the effective masses, giving parameters that agree with the literature parameters as can be seen in figure 6. An evaluation of the method can be done by analyzing the exceptional agreement with literature parameters. The curvatures obtained by our fitting reproduce the most reliable data from literature. Moreover, this indicates that the choice of hybrid DFT-HSE combined methods reproduce

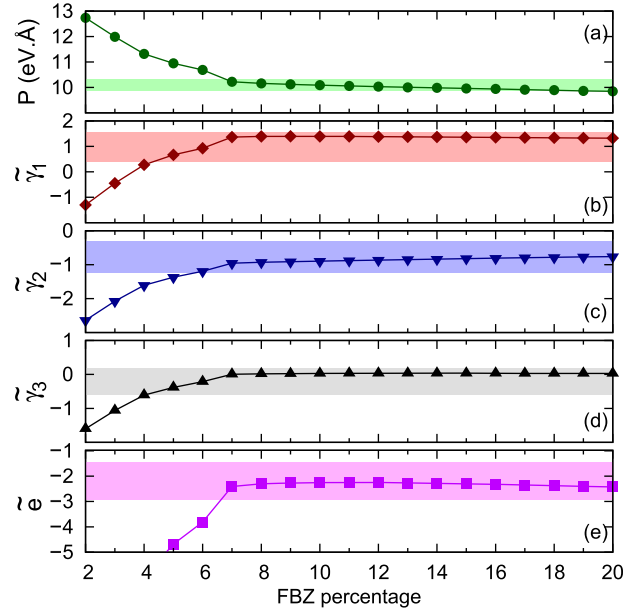


Figure 6. Comparison of the optimal parameters with the literature. The optimal parameters are shown in the curves and the shadowed regions present the intervals of the standard deviation around the average values of the parameters, determined from 7 traditional papers. (a) P parameter in $\text{eV} \cdot \text{\AA}$, and (b) $\tilde{\gamma}_1$, (c) $\tilde{\gamma}_2$, (d) $\tilde{\gamma}_3$ and (e) \tilde{e} .

accurately the properties of the actual electronic properties of the material, validating our choice.

Finally, joining the information of the agreement of the model with literature parameters together with the deviation from the DFT-HSE calculation described in section 6, we have a tool to assess some insights about the accuracy of the effective mass approximation. The lack of agreement of the fitting after 15%, specially for the CB and SO bands, suggests that this specific approximation starts to lose its validity at this region. However, even in this region, our calculations indicate an average deviation of less than 15 meV, indicating that, with proper parameters, the determination of properties depending on band structures inside this range of the FBZ are reliable.

8. Conclusions

We developed and implemented a general method to extract multiband $\mathbf{k} \cdot \mathbf{p}$ parameters using the secular equation of the Hamiltonian. Our approach considers the simultaneous fitting of multiple directions of the FBZ of preexistent band structure and, combined with the RMSD analysis, provides a tool to evaluate the global deviation between the fitted and the original data in a systematic way. Within this approach, an optimal set of parameters may be proposed for each specific region of the FBZ.

In order to test our approach, we fitted the conventional 8×8 zinc blende Hamiltonian to GaAs band structure obtained by a state-of-the-art hybrid DFT-HSE+SOC

Table A1. $\mathbf{k} \cdot \mathbf{p}$ parameters obtained in this work (using 20% of the FBZ) and from selected references showing well established $\mathbf{k} \cdot \mathbf{p}$ parameter sets. P is given in eV Å.

	This work fit (20%)	Literature						
		[33]	[36]	[58]	[73]	[54]	[55]	[56]
$\tilde{\gamma}_1$	1.28	0.66	0.36	2.02	0.60	0.98	0.47	1.21
$\tilde{\gamma}_2$	-0.73	-1.10	-1.08	-0.41	-1.17	-0.61	-1.24	-0.10
$\tilde{\gamma}_3$	0.03	0.23	-0.45	0.46	-0.37	-0.61	-0.48	-0.07
$\tilde{\epsilon}$	-2.34	-2.87	-3.28	-0.94	-2.18	-2.62	-2.76	-1.77
P	9.85	10.47	10.25	9.89	10.27	10.37	10.48	10.18

calculation. The use of hybrid potentials provided a way of guaranteeing that the electronic properties of the systems are directly associated with their experimental values, addressing the most important issues when using DFT calculations to determine effective parameters.

Our fitted band structures present good agreement with the DFT values when using up to 20% of FBZ. Particularly, below 15% we showed an average deviation of less than 10 meV. Above this range, we found that the deviation rapidly increases due to the lack of additional coupling terms in the Hamiltonian. Besides the good agreement on regions below 7%, our analysis show that the parameters are not stable in this range. The stability present above 7% and the small deviation below 15% define the range that can be used to obtain parameter sets that accurately describe the band structure up to 20% of the FBZ. Finally, the comparison with experimental and theoretical available data show that the optimal parameter sets lie inside the range of the most reliable parameters from the literature.

Concluding, our approach provides a method of finding parameters for a general $\mathbf{k} \cdot \mathbf{p}$ model allowing its use for any phase or crystalline structure. As a consequence it can be used to extract parameters of new $\mathbf{k} \cdot \mathbf{p}$ Hamiltonians, opening a large range of opportunities to study new physical phenomena.

Acknowledgments

The authors acknowledge financial support from the Brazilian agencies CNPq (grant #246549/2012-2), FAPESP (grants #2011/19333-4, #2012/05618-0 and #2013/23393-8) and CAPES (PVE grant #88881.068174/2014-01).

Appendix. Parameters table for comparison with the literature

In section 7 we compared the optimal parameters for a region comprising up to 20% with the literature. In table A1 we present the literature data used to calculate the average and standard deviation of the parameters.

References

- [1] Bernevig B A, Hughes T L and Zhang S C 2006 *Science* **314** 1757–61
- [2] Baum Y, Böttcher J, Brüne C, Thienel C, Molenkamp L W, Stern A and Hankiewicz E M 2014 *Phys. Rev. B* **89** 245136
- [3] Miao M S, Yan Q, Van de Walle C G, Lou W K, Li L L and Chang K 2012 *Phys. Rev. Lett.* **109** 186803
- [4] Alicea J 2012 *Rep. Prog. Phys.* **75** 076501
- [5] Mourik V, Zuo K, Frolov S M, Plissard S R, Bakkers E P A M and Kouwenhoven L P 2012 *Science* **336** 1003–7
- [6] Stanescu T D and Tewari S 2013 *J. Phys.: Condens. Matter* **25** 233201
- [7] Reuther J, Alicea J and Yacoby A 2013 *Phys. Rev. X* **3** 031011
- [8] Faria Junior P E and Sipahi G M 2012 *J. Appl. Phys.* **112** 103716
- [9] Faria Junior P E, Campos T and Sipahi G M 2014 *J. Appl. Phys.* **116** 193501
- [10] Jungwirth T, Wunderlich J, Novák V, Olejník K, Gallagher B L, Campion R P, Edmonds K W, Rushforth A W, Ferguson A J and Němec P 2014 *Rev. Mod. Phys.* **86** 855–96
- [11] Lazić P, Sipahi G M, Kawakami R K and Žutić I 2014 *Phys. Rev. B* **90** 085429
- [12] Kane E O 1957 *J. Phys. Chem. Solids* **1** 249–61
- [13] Walukiewicz W, Ager J W, Yu K M, Liliental-Weber Z, Wu J, Li S X, Jones R E and Denlinger J D 2006 *J. Phys. D* **39** R83–99
- [14] Jones R O 2015 *Rev. Mod. Phys.* **87** 897–923
- [15] Hohenberg P and Kohn W 1964 *Phys. Rev.* **136** B864–71
- [16] Kohn W and Sham L J 1965 *Phys. Rev.* **140** A1133–8
- [17] Kane E 1966 *Semiconductors and Semimetals* ed R Willardson and A C Beer vol 1 (Amsterdam: Elsevier) pp 75–100
- [18] Sipahi G M, Enderlein R, Scolfaro L M R, Leite J R, da Silva E C F and Levine A 1998 *Phys. Rev. B* **57** 9168–78
- [19] Slater J C and Koster G F 1954 *Phys. Rev.* **94** 1498–524
- [20] Harrison W 1989 *Dover Books on Physics* (New York: Dover)
- [21] Goringe C M, Bowler D R and Hernandez E 1997 *Rep. Prog. Phys.* **60** 1447
- [22] Enderlein R and Horing J M N 1997 *Fundamentals Of Semiconductor Physics And Devices* (Singapore: World Scientific) (doi:10.1142/9789812384690)
- [23] Willatzen M and Lew Yan Voon L C 2009 *The k.p Method* (Berlin: Springer) (doi:10.1007/978-3-540-92872-0)
- [24] Enderlein R, Sipahi G M, Scolfaro L M R and Leite J R 1998 *Phys. Status Solidi b* **206** 623–33
- [25] Chuang S L and Chang C S 1996 *Phys. Rev. B* **54** 2491–504
- [26] Mears A and Stradling R 1971 *J. Phys. C: Solid State Phys.* **4** L22
- [27] Herlach F 1974 *J. Phys. C: Solid State Phys.* **7** L308

- [28] Becker W M, Ramdas A K and Fan H Y 1961 *J. Appl. Phys.* **32** 2094–102
- [29] Spitzer W G and Fan H Y 1957 *Phys. Rev.* **106** 882–90
- [30] Cardona M 1961 *Phys. Rev.* **121** 752–8
- [31] Dugdale D J, Brand S and Abram R A 2000 *Phys. Rev. B* **61** 12933–8
- [32] Ramos L E, Teles L K, Scolfaro L M R, Castineira J L P, Rosa A L and Leite J R 2001 *Phys. Rev. B* **63** 165210
- [33] Vurgaftman I, Meyer J R and Ram-Mohan L R 2001 *J. Appl. Phys.* **89** 5815
- [34] Boujdaria K, Ridene S and Fishman G 2001 *Phys. Rev. B* **63** 235302
- [35] Vurgaftman I and Meyer J R 2003 *J. Appl. Phys.* **94** 3675
- [36] Shokhovets S, Ambacher O and Gobsch G 2007 *Phys. Rev. B* **76** 125203
- [37] Luttinger J M and Kohn W 1955 *Phys. Rev.* **97** 869–83
- [38] Sirenko Y M, Jeon J B, Kim K W, Littlejohn M A and Strosio M A 1996 *Phys. Rev. B* **53** 1997–2009
- [39] Jancu J M, Scholz R, de Andrada e Silva E and La Rocca G 2005 *Phys. Rev. B* **72** 193201
- [40] Winkler R 2003 *Springer Tracts in Modern Physics* vol 191 (Berlin: Springer)
- [41] Radhia S B, Ridene S, Boujdaria K, Bouchriha H and Fishman G 2002 *J. Appl. Phys.* **92** 4422
- [42] Ben Radhia S, Boujdaria K, Ridene S, Bouchriha H and Fishman G 2003 *J. Appl. Phys.* **94** 5726
- [43] Saïdi I, Ben Radhia S and Boujdaria K 2008 *J. Appl. Phys.* **104** 023706
- [44] Sadi I, Ben Radhia S and Boujdaria K 2010 *J. Appl. Phys.* **107** 043701
- [45] Heyd J, Scuseria G E and Ernzerhof M 2003 *J. Chem. Phys.* **118** 8207–15
- [46] Heyd J and Scuseria G E 2004 *J. Chem. Phys.* **121** 1187–92
- [47] Perdew J P, Ernzerhof M and Burke K 1996 *J. Chem. Phys.* **105** 9982–5
- [48] Moses P G, Miao M, Yan Q and Van de Walle C G 2011 *J. Chem. Phys.* **134** 084703
- [49] Blöchl P E 1994 *Phys. Rev. B* **50** 17953–79
- [50] Kresse G and Joubert D 1999 *Phys. Rev. B* **59** 1758–75
- [51] Kresse G and Hafner J 1993 *Phys. Rev. B* **48** 13115–8
- [52] Kresse G and Furthmüller J 1996 *Phys. Rev. B* **54** 11169–86
- [53] Wyckoff R W G 1963 *Crystal Structures* vol 1 (Wiley) ISBN: 9780470968604
- [54] Vrehen Q 1968 *J. Phys. Chem. Solids* **29** 129–41
- [55] Molenkamp L W, Eppenga R, t' Hooft G W, Dawson P, Foxon C T and Moore K J 1988 *Phys. Rev. B* **38** 4314–7
- [56] Neumann C, Nöthe A and Lipari N O 1988 *Phys. Rev. B* **37** 922–32
- [57] Binggeli N and Baldereschi A 1991 *Phys. Rev. B* **43** 14734(R)
- [58] Lawaetz P 1971 *Phys. Rev. B* **4** 3460–7
- [59] Kim K, Lambrecht W R L, Segall B and van Schilfgaarde M 1997 *Phys. Rev. B* **56** 7363–75
- [60] Yeo Y C, Chong T C and Li M F 1998 *J. Appl. Phys.* **83** 1429
- [61] Rezaei B, Asgari A and Kalafi M 2006 *Physica B* **371** 107–11
- [62] Kim Y S, Marsman M, Kresse G, Tran F and Blaha P 2010 *Phys. Rev. B* **82** 205212
- [63] Cheiwchanchnangij T and Lambrecht W R L 2011 *Phys. Rev. B* **84** 035203
- [64] Suzuki M, Uenoyama T and Yanase A 1995 *Phys. Rev. B* **52** 8132–9
- [65] Pugh S K, Dugdale D J, Brand S and Abram R A 1999 *Semicond. Sci. Technol.* **14** 23–31
- [66] Ren G B, Liu Y M and Blood P 1999 *Appl. Phys. Lett.* **74** 1117
- [67] Fritsch D, Schmidt H and Grundmann M 2003 *Phys. Rev. B* **67** 235205
- [68] Rinke P, Winkelkemper M, Qteish A, Bimberg D, Neugebauer J and Scheffler M 2008 *Phys. Rev. B* **77** 075202
- [69] Purnya A and Lambrecht W R L 2012 *Phys. Rev. B* **85** 195147
- [70] Cardona M and HPollak F 1966 *Phys. Rev.* **142** 530
- [71] <http://reference.wolfram.com/applications/eda/FittingDataToNonlinearModels.html> (accessed: 21 August 2015)
- [72] Adams L, Nazareth J, Society A M, Statistics I M and Mathematics S 1996 *Proc. Applied Mathematics Series* (Society for Industrial and Applied Mathematics)
- [73] Ostromek T E 1996 *Phys. Rev. B* **54** 14467



A comprehensive study of g -factors, elastic, structural and electronic properties of III-V semiconductors using hybrid-density functional theory

Carlos M. O. Bastos,¹ Fernando P. Sabino,¹ Guilherme M. Sipahi,¹
and Juarez L. F. Da Silva^{2,a)}

¹São Carlos Institute of Physics, University of São Paulo, PO Box 369, 13560-970 São Carlos, SP, Brazil

²São Carlos Institute of Chemistry, University of São Paulo, PO Box 780, 13560-970 São Carlos, SP, Brazil

(Received 5 December 2017; accepted 18 January 2018; published online 9 February 2018)

Despite the large number of theoretical III-V semiconductor studies reported every year, our atomistic understanding is still limited. The limitations of the theoretical approaches to yield accurate structural and electronic properties on an equal footing, is due to the unphysical self-interaction problem that mainly affects the band gap and spin-orbit splitting (SOC) in semiconductors and, in particular, III-V systems with similar magnitude of the band gap and SOC. In this work, we report a consistent study of the structural and electronic properties of the III-V semiconductors by using the screening hybrid-density functional theory framework, by fitting the α parameters for 12 different III-V compounds, namely, AlN, AlP, AlAs, AlSb, GaN, GaP, GaAs, GaSb, InN, InP, InAs, and InSb, to minimize the deviation between the theoretical and experimental values of the band gap and SOC. Structural relaxation effects were also included. Except for AlP, whose $\alpha=0.127$, we obtained α values that ranged from 0.209 to 0.343, which deviate by less than 0.1 from the universal value of 0.25. Our results for the lattice parameter and elastic constants indicate that the fitting of α does not affect those structural parameters when compared with the HSE06 functional, where $\alpha=0.25$. Our analysis of the band structure based on the $\mathbf{k}\cdot\mathbf{p}$ method shows that the effective masses are in agreement with the experimental values, which can be attributed to the simultaneous fitting of the band gap and SOC. Also, we estimate the values of g -factors, extracted directly from the band structure, which are close to experimental results, which indicate that the obtained band structure produced a realistic set of $\mathbf{k}\cdot\mathbf{p}$ parameters. *Published by AIP Publishing.*

<https://doi.org/10.1063/1.5018325>

I. INTRODUCTION

Semiconductors have been playing a key role in the development of new technologies since the 1950s, e.g., light-emitting diodes and lasers,^{1–3} infrared detectors,⁴ solar cells,⁵ and, more recently, spin-lasers.⁶ These developments have been possible due to the large number of fundamental studies that used theoretical or experimental techniques, along the decades,^{7,8} which have contributed to the present understanding of the semiconductors electronic band-structure properties, punctual and extended defects, and structural control.^{8,9} Beyond that, new fields have emerged along the years, such as topological insulators¹⁰ and Majorana fermions in nanowires,^{11,12} which are expected to contribute to future technological applications.

Among a wide range of semiconductor materials,^{7–9,13} the III-V AB semiconductors, where $A = \text{Al, Ga, In}$, and where $B = \text{N, P, As, Sb}$ (i.e., 12 compounds), occupy an important place due to their role in several technological developments.^{1,2,4–6} Although there is an impressive number of papers published every year based on experimental and/or first-principles calculations,^{3,14–20} our atomistic understanding is still limited, in particular, due to the limitations in theoretical approaches to describe structural and electronic properties on an equal footing. For example, first-principles

calculations based on density functional theory (DFT), with local or semilocal exchange-correlation energy functionals, have the unphysical self-interaction problem,^{21–23} which mainly affects the band gap and spin-orbit splitting (SOC) in semiconductors,^{22,24} and, in particular, for a few III-V AB semiconductors, where the SOC can have a similar magnitude as the band gap, e.g., GaSb, InP, InAs, and InSb.^{9,25}

Along the years, the self-interaction problem has motivated the widespread use of approximations or alternative descriptions of the electronic states, such as the GW^{26,27} or the nonlocal hybrid density functionals, e.g., PBE0,^{28,29} HSE06,^{30–32} and B3LYP.³³ In principle, both GW and hybrid-DFT can yield an improved description of the band structure compared with local or semilocal functionals; however, GW was designed to address electronic properties but not the structural properties.^{26,27} In contrast with GW, hybrid-DFT can describe both structural and electronic properties on an equal footing; however, the electronic properties, e.g., the band gap, depend strongly on the magnitude of the nonlocal Fock exchange, α , that replaces part of the semilocal exchange term. Although a universal value for α was suggested, i.e., 25% in PBE0,^{28,30} it is not as universal as expected.³⁴

Because the band increases almost linearly by increasing the magnitude of the nonlocal Fock exchange,³⁵ several studies proposed a fitting of the α parameter to improve the description of the band gap.^{34–36} However, those studies

^{a)}Author to whom correspondence should be addressed: juarez_dasilva@iqsc.usp.br

used, in most cases, atomic structures optimized with the local or semilocal functionals,^{37–39} i.e., the differences in the structural parameters, are neglected. This is a good approximation, but it might fail in cases in which the fine details of the electronic structure strongly depend on the lattice parameters, e.g., III-V systems with large SOC.

In this work, we propose to perform a consistent study of the structural and electronic properties of the III-V semiconductors by using the screening hybrid-DFT framework, where the α parameters for the different compounds are fitted by the minimization of the deviation between the theoretical and experimental values for the band gap and SOC. We also used optimized lattice parameters based on screening hybrid-DFT, i.e., small differences in the lattice constant were taken into account for the electronic parameters. Based on this framework, we calculated the equilibrium lattice constant, elastic constants, bulk modulus, band structures, effective masses, etc. Furthermore, we used the $\mathbf{k} \cdot \mathbf{p}$ method to perform a deep analysis of the band structures, from which it was possible to extract the $\mathbf{k} \cdot \mathbf{p}$ parameters and the electronic g -factors.

Except for AIP, we obtained α parameters, which ranged from 0.209 to 0.343, i.e., close to the universal value of 0.25. For AIP, the calculated α value is 0.127. Based on several analyses, we found, with few exceptions, that the α values correlate well with the atomic radius of the cationic species, and, hence, α values for different semiconductors could be extrapolated from this finding without additional calculations. Our results for the lattice and elastic constants indicate that the fitting of the α does not affect those structural parameters when compared with the HSE06 functional, where $\alpha = 0.25$.

Our analysis of the band structure based on the $\mathbf{k} \cdot \mathbf{p}$ method shows that the effective masses are in agreement with the experimental values,^{9,40} i.e., the fitting of α at the Γ point improved the description of the band curvatures. We also determined the g -factors directly from the effective band structures and found values that are close to the experimental results.^{9,25} Finally, with having both g -factors and effective masses in good agreement with the experimental results indicates that we determined realistic sets of $\mathbf{k} \cdot \mathbf{p}$ parameters.

II. THEORETICAL APPROACH AND COMPUTATIONAL DETAILS

A. Density functional theory

It has been known for decades that DFT^{41,42} within local (local density approximation—LDA)⁴³ or semilocal (generalized gradient approximation—GGA)^{44,45} exchange-correlation energy functionals is unable to yield a correct description of the fundamental band gap even for the most simple systems,^{22,24} which has mainly been attributed to the unphysical self-interaction problem.^{21–23} This limitation has motivated the widespread use of approximations or alternative descriptions of the electronic valence states, such as the GW^{26,27} or nonlocal hybrid functional, e.g., PBE0,^{29,46} HSE06,^{30–32} and B3LYP.³³ In principle, both the GW and nonlocal hybrid functionals can yield an improved

description of the band structure compared with LDA or GGA. However, in contrast with the GW framework, the nonlocal hybrid functional can also provide a reliable description of the structural and energetics properties,^{39,47–49} which is a plus compared with GW.

In this work, we use the DFT framework within the GGA formulation proposed by Perdew, Burk, and Ernzerhof⁴⁵ (PBE) and the hybrid functional proposed by Heyd, Scuzeria, and Ernzerhof^{30–32} (HSE), in which the magnitude of the nonlocal Fock exchange replaces part of the PBE exchange. As will be described below, we fit the magnitude of the nonlocal Fock exchange based on the experimental results of the fundamental band gap and the spin-orbit (SO) splitting, while using the same screening parameter derived for the HSE06 functional.^{32,50}

To describe the electronic states we used the scalar-relativistic approximation^{51,52} in which relativistic corrections are considered for the core-states, whereas the SOC is not considered for the valence states, and hence, the spin-orbit splitting for the III-V semiconductors cannot be described. For example, for InSb, the SOC splitting at the Γ -point and valence band maximum (VBM) has a similar magnitude as the fundamental band gap,^{24,53} and, hence, it plays a crucial role for the characterization of the band structure parameters, e.g., effective mass, g -factor. Thus, to improve the description of the band structure properties, we used the addition of the SOC for the valence states via the second-variational approach.⁵¹

To solve the Kohn–Sham equations, we used the projected augmented wave (PAW) method,⁵⁴ as implemented in the Vienna *ab initio* simulation package (VASP, version 5.4.1)^{55,56} by using the PAW projectors provided with the package.⁵⁷ To describe the electronic states, the Kohn–Sham orbitals are expanded in plane waves by using a finite cutoff energy, which depends on the calculated properties. This is necessary because several properties, e.g., stress tensor and elastic constants, converge slowly as the number of plane waves increases.

From a large number of PBE and HSE convergence tests, we demonstrated that well-converged total energies, band structures, and densities of states can be obtained by using a cutoff energy that is 1.125 times the recommended maximum cutoff energy (ENMAX_{max}). Stress tensor and elastic constants calculations, however, require at least $1.50 \times \text{ENMAX}_{\text{max}}$. A further increase in the cutoff energy can slightly improve the results, and, for the particular case of the PBE calculations, we increased the multiplication factor from 1.50 to 2.0 (stress tensor) and to 2.5 (elastic constants) in aiming to provide reference data that can be used for further comparisons. For example, for AlN, we used 473 eV for total energy and band structure, 631 eV (HSE) and 841 eV (PBE) for stress tensor, and 631 eV (HSE) and 1052 eV (PBE) for the elastic constants calculations. For the Brillouin zone integration, we used a Monkhorst–Pack \mathbf{k} -mesh of $10 \times 10 \times 10$, whereas the same \mathbf{k} -point density was used for the remaining III-V semiconductors. All these parameters are provided in the [supplementary material](#).

To obtain the equilibrium volume, we minimized the stress tensor, which was performed by several consecutive

optimizations of the equilibrium volume to ensure that the optimized equilibrium volume is consistent with the initial setup of the basis vector sizes. To calculate the elastic properties, we considered the combination of two schemes, namely, (i) rigid lattice parameters obtained from the stress-tensor optimization⁵⁸ and (ii) ionic volume relaxation from the inversion of the ionic Hessian matrix and internal stress tensor,⁵⁹ as implemented in VASP. For those calculations, we used atomic steps of 0.010 Å, which are slightly smaller than the recommended value by VASP, e.g., 0.15 Å.

B. Hybrid HSE functional: Fitting of the α value

The hybrid PBE0 functional is composed of the PBE correlation energy, and a fraction of 25% of the PBE exchange is replaced by the nonlocal Fock exchange of the Hartree–Fock (HF) method, i.e., $E_{XC}^{PBE0} = E_c^{PBE} + \alpha E_x^{HF} + (1 - \alpha)E_x^{PBE}$, where $\alpha = 0.25$.^{29,46} The hybrid HSE functional^{30–32} is derived from PBE0 by using a screening function to split the semilocal PBE exchange and nonlocal Fock term into two parts, namely, short- (SR) and long-range (LR) exchange contributions, in which the nonlocal Fock LR contribution cancels with part of the PBE LR exchange. Thus, the hybrid HSE functional is given by the following equation:

$$E_{XC}^{HSE} = E_c^{PBE} + E_x^{PBE,LR}(\omega) + \alpha E_x^{HF,SR}(\omega) + (1 - \alpha)E_x^{PBE,SR}(\omega), \quad (1)$$

where the new parameter, ω , measures the intensity of the screening and, hence, the extension of the nonlocal Fock interactions. For example, if ω is null, then the SR contribution is equivalent to the full Fock operator and the LR contribution will become zero, whereas for $\omega \rightarrow \infty$, the range of SR terms decrease, which asymptotically recovered the PBE functional. As defined in the PBE0 functional, the parameter α controls the amount of PBE exchange replaced by the nonlocal Fock exchange, and, hence, in principle, it can range from 0 to 1. For the hybrid HSE06 functional, $\alpha = 0.25$ was obtained from the adiabatic perturbation theory and $\omega = 0.206 \text{ \AA}^{-1}$ was fitted using a large number of systems, respectively.^{32,50}

Although, the hybrid HSE06 functional yields better results than the LDA and GGA functionals, HSE06 does not yield the experimental band gaps in most of the cases,^{24,60,61} and, hence, improved results can be obtained by fitting the ω or α parameters. Recently, Viñes *et al.*³⁴ indicated that a large number of combinations of ω and α values can yield the band gap of oxides; however, it is important to mention that the fitting of ω can drastically affect the small contribution of the LR nonlocal Fock terms, which has the potential to decrease the stability of the electron density convergence. In contrast with ω , the fitting of α mainly affects the SR nonlocal Fock contribution, which plays a crucial role in the physical properties.^{62–65}

Therefore, to improve the description of the experimental fundamental band gap, E_{gap} , and the spin-orbit (SO) splitting energies, Δ_{so} , we fixed the ω parameter to the same value used in HSE06 and fitted the α parameter to reproduce

the experimental E_{gap} and Δ_{so} results. The fitting was performed by using the linear dependence of E_{gap} and Δ_{so} as a function of α , which is well known in the literature.^{66–68} Due to the nearly perfect linear dependence, the angular coefficient (slope) can be calculated by using two points, namely, by using the E_{gap} or $E_{\Delta_{\text{so}}}$ values calculated with the PBE ($\alpha = 0$) and HSE06 ($\alpha = 0.25$) functionals. Thus, the angular coefficient for the fitting of the band gap is given by the following relation:

$$m_{\text{gap}} = \frac{E_{\text{gap}}^{\text{HSE06}} - E_{\text{gap}}^{\text{PBE}}}{0.25}, \quad (2)$$

while $m_{\Delta_{\text{so}}}$ is obtained by replacing the band gap energies by the spin-orbit splittings. Thus, the α value that yields the experimental band gap, $E_{\text{gap}}^{\text{exp}}$, or the experimental spin-orbit splitting, $E_{\Delta_{\text{so}}}^{\text{exp}}$, can be obtained from the following equation:

$$\alpha_{\text{gap}} = \frac{E_{\text{gap}}^{\text{exp}} - E_{\text{gap}}^{\text{PBE}}}{m_{\text{gap}}}. \quad (3)$$

Consequently, from this scheme, we obtained two values for α , namely, an optimized value for α_{gap} ($\alpha_{\Delta_{\text{so}}}$) that yields the experimental band gap (spin-orbit splitting). To obtain a unique α for each III-V system, we performed a minimization of the standard deviation between the experimental and the extrapolated $E_{\text{gap}}^{\text{exp}}$ and $E_{\Delta_{\text{so}}}^{\text{exp}}$ parameters obtained from the slope. Further technical details are reported in the [supplementary material](#). Thus, from now on, the fitted hybrid HSE functional is noted as HSE $_{\alpha}$, where α is different for each semiconductor. Finally, to compare our results with the literature and among different functionals, we adopted, as a measure, the normalized-root-mean-square deviation (NRMSD).⁶⁹

III. RESULTS

A. Magnitude of the non-local Fock exchange

Except for AIP, the optimal α values that minimize the relative errors for the fundamental band gap and SOC splitting are in between 0.209 and 0.343, i.e., close to the universal value of 0.25.²⁸ For AIP, the value is 0.127. Therefore, we conclude that a unique α value is unable to yield the fundamental band gap and SOC splitting for a wide range of compounds as well as further physical properties, which have also been reported in a previous study.⁶⁶ Although the value of α has been obtained from a solid theoretical framework, to our knowledge only one study has tried to obtain a correlation between the magnitude of α and a particular physical property,³⁴ which can help in several applications. Thus, with the aim to identify the most important physical parameters that play major roles in the magnitude of α , we performed several analyses (also in the [supplementary material](#)). Among all analyses, we found a good correlation between the magnitude of α versus the cationic radius,⁷⁰ which is shown in Fig. 1. Our results indicate that the value of the optimized α decreases almost linearly as a function of the atomic cationic radius, except for the cases of AlN and AIP.

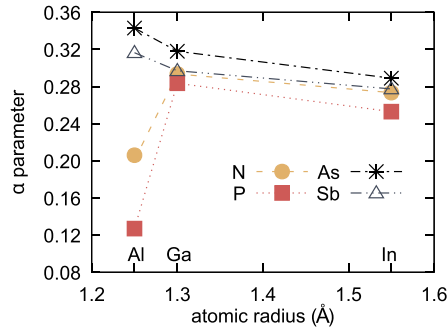


FIG. 1. Optimal magnitude of the nonlocal Fock exchange, α , in the hybrid HSE $_{\alpha}$ functional obtained from the fitting of the fundamental band gap and the spin-orbit coupling versus the cation atomic radii obtained from Ref. 70. The atomic radii are given in Å and α is dimensionless.

B. Equilibrium lattice parameter

The most stable crystalline phase of the III-V semiconductors is the zinc-blende structure,⁷¹ which has a face-centered cubic (fcc) lattice and $F\bar{4}3m$ space group. The exceptions for this rule are the III-nitrides (AlN, GaN, InN), which prefer to crystallize in the hexagonal wurtzite structure, which belongs to the $P6_3mc$ space group;⁷² however, through the use of experimental techniques such as molecular beam epitaxy, they can also be grown as a zinc-blende structure.^{7,72} Thus, to rationalize our understanding, all the III-V semiconductors were studied in the zinc-blende structure, which contains two fourfold atoms with tetrahedral local symmetry. The equilibrium lattice parameter, a_0 , was calculated by using several approximations, namely, PBE, PBE+SOC, HSE06, and HSE $_{\alpha}$, and the results are summarized in Table I, along with the experimental results.

In agreement with previous DFT-PBE calculations,^{38,60,75} we obtained equilibrium PBE lattice constants that

TABLE I. Equilibrium lattice parameters a_0 (in Å) for all the III-V semiconductors, calculated with the PBE, PBE with spin-orbit coupling for the valence states (PBE+SOC), HSE06, and HSE $_{\alpha}$ functionals. For the hybrid HSE $_{\alpha}$ functional, the adjusted α parameter is indicated within parentheses. The NRMSD indicates the normalized percentage deviation between theoretical and experimental parameters for the full series.

	PBE	PBE+SOC	HSE06	HSE $_{\alpha}$ (α)	Exp.
AlN	4.399	4.399	4.361	4.367 (0.219)	4.38 ^a
AlP	5.505	5.505	5.471	5.487 (0.127)	5.46 ^b
AlAs	5.731	5.731	5.678	5.660 (0.343)	5.661 ^b
AlSb	6.213	6.215	6.160	6.146 (0.318)	6.135 ^b
GaN	4.545	4.545	4.492	4.483 (0.293)	4.52 ^a
GaP	5.499	5.499	5.456	5.449 (0.283)	5.45 ^b
GaAs	5.742	5.738	5.669	5.652 (0.318)	5.653 ^b
GaSb	6.203	6.203	6.124	6.124 (0.297)	6.095 ^b
InN	5.042	5.039	4.976	4.956 (0.274)	4.97 ^c
InP	5.946	5.942	5.886	5.885 (0.253)	5.868 ^b
InAs	6.174	6.172	6.090	6.078 (0.289)	6.058 ^b
InSb	6.619	6.618	6.526	6.549 (0.277)	6.479 ^b
NRMSD	1.49	1.47	0.40	0.49	...

^aFrom Ref. 73.

^bFrom Ref. 9.

^cFrom Ref. 74.

overestimate experimental results, with the largest deviation smaller than 2.2% for InSb. The addition of the SOC for the valence states reduces the lattice constant only to the third decimal place, and, hence, the improvement over the PBE compared with the experimental results is almost negligible and can be evaluated by the NRMSD, shown in Table I. For example, the NRMSD is 1.49% for PBE and 1.47% for PBE+SOC. Therefore, the SOC does not affect the equilibrium lattice constants, in contrast with the electronic properties, where it plays an essential role (see below).

To reduce the computational cost, which increases substantially for HSE06+SOC, the HSE06 and HSE $_{\alpha}$ equilibrium lattice constants were calculated by using stress tensor without the addition of the SOC for the valence states. The HSE06 and HSE $_{\alpha}$ functionals yield a_0 parameters closer to the experimental results and, hence, with smaller relative errors compared with the PBE results. These small errors were expected because we provided an improved description of the exchange energy by the nonlocal Fock term. The differences between the HSE06 and HSE $_{\alpha}$ results are very small, i.e., the NRMSD changes from 0.4% (HSE06) to 0.49% (HSE $_{\alpha}$). This is an important result because it shows that the lattice parameters were only slightly affected by the improvement of the description of the fundamental band gap and spin-orbit splitting at the Γ -point. The HSE06 results are in excellent agreement with previous hybrid HSE06 results,⁶¹ e.g., indium compounds have differences smaller than 0.3%, 0.4%, and 0.5% for InP, InAs, and InSb, respectively.

The lattice parameter has a slight linear dependence with the atomic radius of the material compound elements (occupation of the electronic shells), i.e., if the anionic atom size increases, then the lattice parameter also increases, as shown in Fig. 2. This effect occurs due to the electrostatic repulsion between atoms, i.e., the bond length depends on the atom size by changing the lattice parameter. Because Al and Ga have similar atomic radii, with 1.25 Å and 1.30 Å, respectively,⁷⁰ the lattice parameters for the Al-V compounds are closer to the Ga-V values, as shown in Fig. 2. The In has a greater atomic radius, 1.55 Å,⁷⁰ which results in a larger lattice parameter for the In-V compounds. To

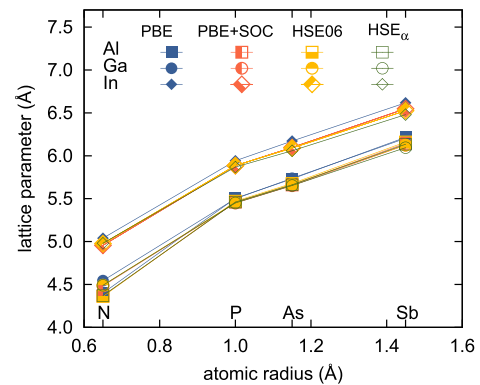


FIG. 2. Lattice parameters versus the atomic radius of the anion species. The lattice parameters were obtained by using the following exchange-correlation functionals: PBE, PBE+SOC, HSE06, HSE $_{\alpha}$. The atomic radii were extracted from Ref. 70.

TABLE II. Elastic constants calculated with PBE and α -optimized HSE (HSE $_{\alpha}$), functionals. The bulk moduli, B_0 , were obtained from the elastic constants results, namely, $B_0 = (C_{11} + 2C_{12})/3$, and are compared with the experimental values obtained from elastic constants (Exp. $^{C_{ij}}$) and direct measures (Exp. B_0). All constants are given in GPa.

	C_{11}			C_{12}			C_{44}			B_0			
	PBE	HSE $_{\alpha}$	Exp.	PBE	HSE $_{\alpha}$	Exp.	PBE	HSE $_{\alpha}$	Exp.	PBE	HSE $_{\alpha}$	Exp. $^{C_{ij}}$	Exp. B_0
AlN	283.1	308.1	...	149.8	161.6	...	179.2	197.2	...	194.2	210.5
AlP	125.8	133.6	141 ^a	61.3	65.1	62 ^a	60.8	64.1	70 ^a	82.8	87.9	88.3	...
AlAs	103.9	122.1	122 ^a	49.1	58.5	57 ^a	51.1	59.0	60 ^a	67.4	79.7	78.7	74 ^b
AlSb	77.0	93.7	88 ^a	35.8	43.2	40 ^a	36.8	47.5	43 ^a	49.5	60.0	56.0	55.1 ^c
GaN	253.3	290.0	...	125.2	149.0	...	146.4	173.9	...	167.9	196.0
GaP	124.6	150.0	140 ^a	56.0	64.3	62 ^a	65.2	78.4	70 ^a	78.9	92.9	88.0	...
GaAs	98.1	122.0	119 ^a	42.1	49.4	53 ^a	50.8	65.3	60 ^a	60.8	73.6	75.0	...
GaSb	74.6	90.1	88 ^a	32.0	35.7	40 ^a	35.9	49.0	43 ^a	46.2	53.8	56.0	...
InN	159.3	188.7	...	102.0	125.8	...	78.9	93.3	...	121.1	146.8
InP	87.4	105.9	101 ^d	45.9	56.4	56 ^d	41.9	49.3	46 ^d	59.7	72.9	71.0	...
InAs	70.9	91.5	83 ^a	37.8	48.8	45 ^a	33.1	42.4	40 ^a	48.8	62.7	57.6	58 ^e
InSb	55.3	74.1	69 ^a	29.1	34.8	37 ^a	25.4	39.0	31 ^a	37.8	47.9	47.7	...
NRMSD (%)	14.3	4.9	...	15.0	5.1	...	13.8	9.2	...	14.4 _f	3.7 _f

^aUltrasound Ref. 77.

^bX-ray diffraction data from Ref. 9.

^cEnergy dispersive X-ray from Ref. 9.

^dUltrasonic-wave transit times Ref. 77.

^eUltrasound from Ref. 9.

^fComparison with Exp. $^{C_{ij}}$.

investigate the linearity break shown for the III-N compounds, we evaluated the effective Bader charge, as shown in the Table VI in Appendix B. The III-N compounds have a large charge transfer, which indicates that the break in the linearity behavior is due to the high ionicity combined with the smaller atomic radius of the N when compared with the other cations of the III-A column of the Periodic Table. This hypothesis is also supported by the fact that the III-N compounds showed the highest elastic constants values in the series, as discussed in Sec. III C, and the larger observed bond strengths.⁷⁶

C. Elastic constants

The cubic zinc-blende crystal structure has the symmetry defined by the space group $F\bar{4}3m$, which is associated to the point group T_d .⁷ The symmetry analysis shows that it possess only three non-equivalent elastic constants: C_{11} , C_{12} , and C_{44} . C_{11} represents the modulus for the axial compression, i.e., the stress in one direction induces a strain in the same direction. In contrast, C_{12} represents the stress that induces a strain in the perpendicular directions, and C_{44} , the shear modulus, represents the strain across the faces induced by the stress in a direction parallel to it. PBE, HSE $_{\alpha}$, and the experimental results of C_{11} , C_{12} , and C_{44} are shown in Table II. We also present the bulk modulus, B_0 , which was calculated from the expression $B_0 = (C_{11} + 2C_{12})/3$.

Unrelated to the exchange and correlation functionals, the elastic constants in all directions decrease as the ionic radius increases. For the PBE functional, e.g., C_{11} decreases from 283.1 in AlN to 77 in InSb. The ionic bond character is responsible for the increase on the hardness of the material, and, as shown in the Table VI in Appendix B, the ionicity

(related to the Bader charge) decreases as the anion radius decreases. Therefore, it is expected that the elastic constant decreases as the lattice parameter (associated with the cation and anion radii) of the crystal structure increases. In fact, analysis of our results indicates a slight linear dependence with the lattice parameter, as shown in Fig. 3, where the dashed line shows a linear fitting by using all the materials, nitrides excluded. This behavior was reported in the literature^{25,78} and was traditionally used to estimate the elastic constants^{79,80} by the extrapolation of the data.

In contrast with the lattice parameter overestimation by HSE functionals, the PBE functional underestimates the elastic constants in all the directions, which is consistent with the literature.⁸¹ However, the HSE $_{\alpha}$ results show better

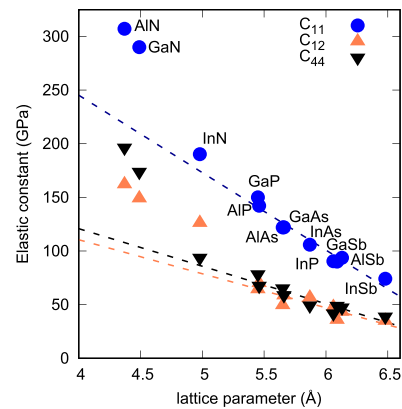


FIG. 3. Dependence of elastic constants on the equilibrium lattice parameter. Elastic constants and lattice parameters have been obtained by using HSE $_{\alpha}$ functional.

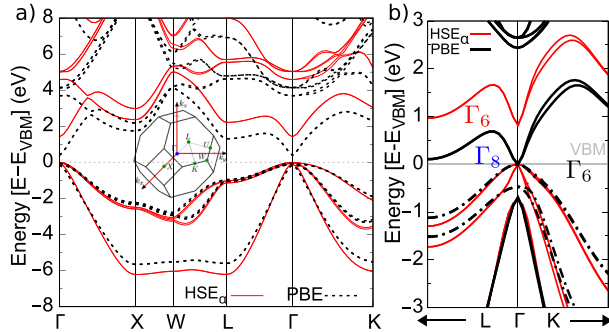


FIG. 4. InP and GaSb band structures evaluated with PBE (dashed line) and HSE $_{\alpha}$ (solid line), including spin-orbit coupling. (a) band structure for InP. The first Brillouin zone of zinc-blende phase is shown. (b) GaSb band structure close to Γ point: PBE presents a negative band gap, and the HSE $_{\alpha}$ shows a positive band gap. The band symmetries are indicated.

agreement with the experimental results, which present NRMSDs of 4.9% and 5.1% for C_{11} and C_{12} , respectively. The inclusion of nonlocal effects in the Fock exchange in HSE $_{\alpha}$ indicates an increasing of the bond hardness, which increases the elastic constants when compared with the PBE functional. For C_{44} , our results, when compared with the experimental data, show deviations for the HSE $_{\alpha}$ functional similar to the PBE ones when presenting NRMSDs of 13.8% and 9.2%, respectively. Similar C_{44} values were found by Caro *et al.*⁸² by using the HSE06 for nitrides. Nonetheless, PBE underestimates the experimental values of C_{11} and C_{12} , whereas HSE $_{\alpha}$ overestimates them. Because the bulk modulus, B_0 , in a cubic system has dependence only in the C_{11} and C_{12} elastic constant directions, the PBE functional also underestimates the B_0 values, whereas the HSE $_{\alpha}$ functional yields better results. This can be observed by the NRMSD, which is 3.7% and 14.4% for HSE $_{\alpha}$ and PBE, respectively.

TABLE III. Band gap, $E_{\text{gap}} = \Gamma_6^c - \Gamma_8^v$, and spin-orbit splitting, $\Delta_{\text{so}} = \Gamma_8^v - \Gamma_7^v$, energies by using the different functionals: PBE, PBE+SOC, HSE06, HSE06+SOC, and HSE $_{\alpha}$ +SOC. The contribution of nonlocal exchange in the HSE, α , adjusted to obtain the experimental values of gap energy and spin-orbit splitting is also shown. The energies are given in eV.

	α	PBE		PBE+SOC		HSE06	HSE06+SOC		HSE $_{\alpha}$ +SOC		Literature	
		E_{gap}	E_{gap}	Δ_{so}	E_{gap}	E_{gap}	Δ_{so}	E_{gap}	Δ_{so}	E_{gap}	Δ_{so}	
AlN	0.219	4.003	3.997	0.019	5.609	5.601	0.021	5.383	0.022	5.40 ^a	0.019 ^a	
AIP	0.127	3.090	3.070	0.059	4.164	4.153	0.064	3.611	0.061	3.62 ^b	0.06 ^c	
AlAs	0.343	1.757	1.662	0.290	2.819	2.732	0.316	3.157	0.324	3.13 ^b	0.3 ^b	
AlSb	0.318	1.314	1.105	0.652	2.286	2.111	0.691	2.397	0.700	2.38 ^b	0.673 ^b	
GaN	0.293	1.564	1.560	0.012	3.043	3.042	0.021	3.312	0.022	3.30 ^d	0.017 ^a	
GaP	0.283	1.603	1.576	0.082	2.748	2.739	0.092	2.915	0.093	2.895 ^b	0.08 ^a	
GaAs	0.318	0.166	0.072	0.325	1.297	1.210	0.358	1.471	0.365	1.519 ^b	0.341 ^b	
GaSb	0.297	-0.259	-0.477	0.694	0.782	0.614	0.743	0.819	0.751	0.82 ^b	0.756 ^b	
InN	0.274	-0.504	-0.497	0.002	0.507	0.530	0.016	0.674	0.017	0.61 ^e	0.005 ^a	
InP	0.253	0.468	0.452	0.095	1.402	1.408	0.111	1.422	0.111	1.42 ^b	0.108 ^b	
InAs	0.289	-0.525	-0.626	0.335	0.372	0.301	0.373	0.373	0.385	0.418 ^b	0.38 ^b	
InSb	0.277	-0.558	-0.782	0.716	0.335	0.136	0.778	0.232	0.783	0.235 ^b	0.81 ^b	
NRMSD (%)		55.7	59.1	12.0	9.1	10.9	4.8	1.3	5.4			

^aTheory from Ref. 40.

^bExp. from Ref. 9.

^cTheory GW from Ref. 83.

^dExp. from Ref. 84.

^eExp. from Ref. 85.

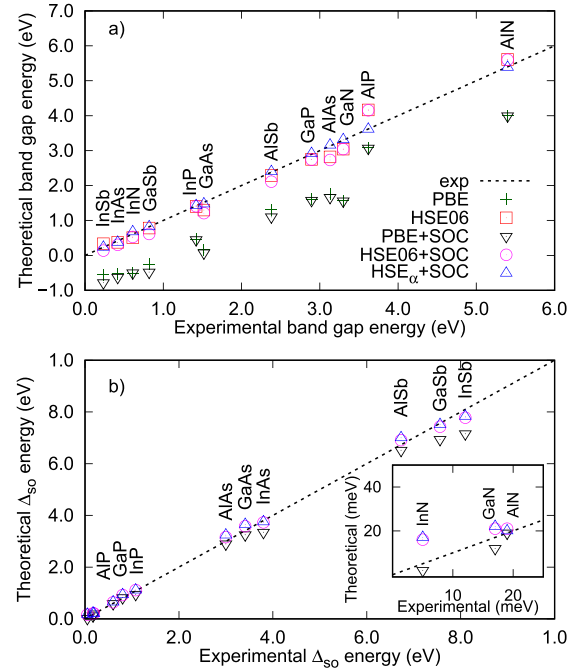


FIG. 5. Energies of the 12 compounds determined with the different functionals with and without the inclusion of the spin-orbit coupling: (a) band gaps (b) spin-orbit splittings. In both figures, the dashed lines show the literature values.

D. Band structures

As discussed previously,^{22,24} the PBE functional strongly underestimates the band gap energy. In the specific case of the small band gap III-V materials, its application results in null band gaps or even in the inversion of the ordering of Γ_6 and Γ_8 states, as shown in Fig. 4(b). This

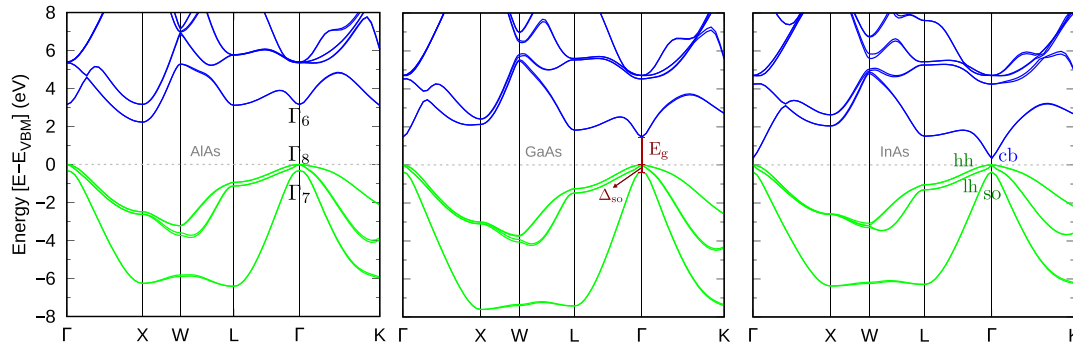


FIG. 6. Band structures obtained by using HSE $_{\alpha}$ +SOC along high symmetry lines for AlAs, GaAs, and InAs. The blue lines indicate conduction bands, whereas the green lines indicate the valence bands. The band structures for the other III-V materials are shown in the [supplementary materials](#).

result is completely inconsistent with the experimental data.^{9,40} To get rid of this problem, we used the HSE06 and HSE $_{\alpha}$ exchange and correlation functions. The differences in the results when using the different functionals may be clarified by analyzing the results, as shown in Fig. 4. The HSE06 and HSE $_{\alpha}$ gaps are closer to the experimental values than PBE predictions, e.g., InP shows an increase in the value of 68% from PBE to HSE $_{\alpha}$. An even more dramatic example is the wrong prediction of negative band gaps for InSb, GaSb, InAs, and InN made by using the PBE functional. HSE06 or HSE $_{\alpha}$ functionals show the correct trend.

Although both HSE06 or HSE $_{\alpha}$ functionals predict the correct trend, the tuning of α provides a much better agreement for the band gap value, when changing the deviations from the experimental results from 0.8% (InP) up to 42.1% (InSb) when using HSE06 to 0.3% (AlN) and 10.5% (InN) with HSE $_{\alpha}$. The accuracy in the description of Δ_{so} is also improved when using the hybrid functionals instead of PBE, as shown in Table III. The band structures for all the other materials are presented in the [supplementary material](#).

Regardless of the gap adjustment, i.e., by using the HSE06 calculations, one can notice a monotonic relation between the anionic radius and the band gap energies; e.g., in Al compounds, we observe that $E_{gap}^{AlN} > E_{gap}^{AlP} > E_{gap}^{AlAs} > E_{gap}^{AlSb}$.

This trend is also valid for the As compounds, as shown in Fig. 6. It fails, however, for the In compounds, in which the calculated InN band gap is smaller than the trend indicates as shown in Fig. 5. Carrier and Wei⁸⁶ indicated, when this same rule was violated for wurtzite compounds, that this was due to the high electronegativity of N and the smaller band gap deformation potentials. In our understanding, the same explanation should be applied to the zinc-blende case (Fig. 6).

E. $\mathbf{k} \cdot \mathbf{p}$ parameters

Despite the fact that band gaps and Δ_{so} are close to the experimental values, there is no guarantee that the calculated band structures are in agreement with the experimental results. To perform this analysis, we calculated the effective masses by using the $\mathbf{k} \cdot \mathbf{p}$ approach. In the $\mathbf{k} \cdot \mathbf{p}$ method, the interactions that involve electrons and nuclei are described through an effective potential with the same periodicity of the lattice, which allows the utilization of the Bloch's theorem. To find an effective Hamiltonian, we used the perturbative technique proposed by Löwdin,⁸⁷ where the basis set is divided in two classes: A and B. States within class A are the states of interest and are described exactly, whereas states from class B are taken into account perturbatively through

TABLE IV. Kane and Luttinger-Kohn parameters obtained through the fitting of the Kane $\mathbf{k} \cdot \mathbf{p}$ Hamiltonian in the band structure obtained by using HSE $_{\alpha}$ +SOC close to the Γ point. A range of Luttinger-Kohn parameters found in the compilation of the literature in Refs. 40, 53, and 94 is given for comparison. The $\tilde{\gamma}_s$, γ_s , \tilde{e} , and e values are in $\hbar^2/2m_0$ units, whereas E_p values are in eV.

	Kane					Luttinger-Kohn				Range in literature for Luttinger-Kohn parameters				
	$\tilde{\gamma}_1$	$\tilde{\gamma}_2$	$\tilde{\gamma}_3$	\tilde{e}	E_p	γ_1	γ_2	γ_3	e	γ_1	γ_2	γ_3	e	E_p
AlN	0.36	-0.20	0.06	-0.10	18.8	1.52	0.38	0.64	3.38	1.92	0.47	0.85	3.03-4.0	27.1
AlP	0.81	-0.48	0.09	-1.01	22.1	2.85	0.54	1.11	5.07	3.35-3.47	0.06-0.71	1.15-1.19	4.55	17.7
AlAs	0.95	-0.61	0.06	-1.26	27.2	3.79	0.92	1.50	6.99	3.25-4.04	0.65-0.9	1.21-1.38	6.67	21.1
AlSb	0.89	-1.05	-0.11	-3.66	27.9	5.02	1.15	1.95	7.88	4.15-5.18	1.01-1.19	1.71-1.81	3.03-8.33	18.7
GaN	0.68	-0.28	0.08	-0.27	16.4	2.39	0.60	0.94	4.87	2.67-3.07	0.75-0.86	1.1-1.16	6.67	25
GaP	1.38	-0.62	0.16	-1.67	25.2	4.20	0.87	1.58	6.68	4.05-4.2	0.49-0.98	1.25-1.95	7.69-10.81	31.4
GaAs	1.37	-0.81	0.10	-2.02	25.9	7.10	2.15	2.99	14.05	6.8-7.8	2.02-2.50	1.0-2.43	14.93-15.43	25.9-27.6
GaSb	1.74	-1.15	0.15	-3.23	24.8	11.78	3.87	5.19	22.04	11.08-13.4	4.03-4.7	5.26-5.74	24.27-25.64	23.7-25.1
InN	0.65	-0.25	0.05	-0.16	11.1	6.13	2.49	2.79	16.15	3.72	1.26	1.63	8.33-14.29	17.2-21.1
InP	1.23	-0.54	0.14	-1.18	18.3	5.33	1.58	2.20	10.86	4.95-6.28	0.94-2.08	1.62-2.08	12.38-14.71	18.1-19.6
InAs	1.29	-0.77	0.10	-1.38	18.9	18.20	7.69	8.55	40.75	19.67-20.5	8.30-8.50	9.10-9.17	37.74-45.66	21.5-21.9
InSb	1.68	-1.04	0.12	-2.09	20.4	31.05	13.65	14.80	63.37	34.5-37.1	14.5-16.5	15.7-17.7	68.49-84.75	23.1-23.5

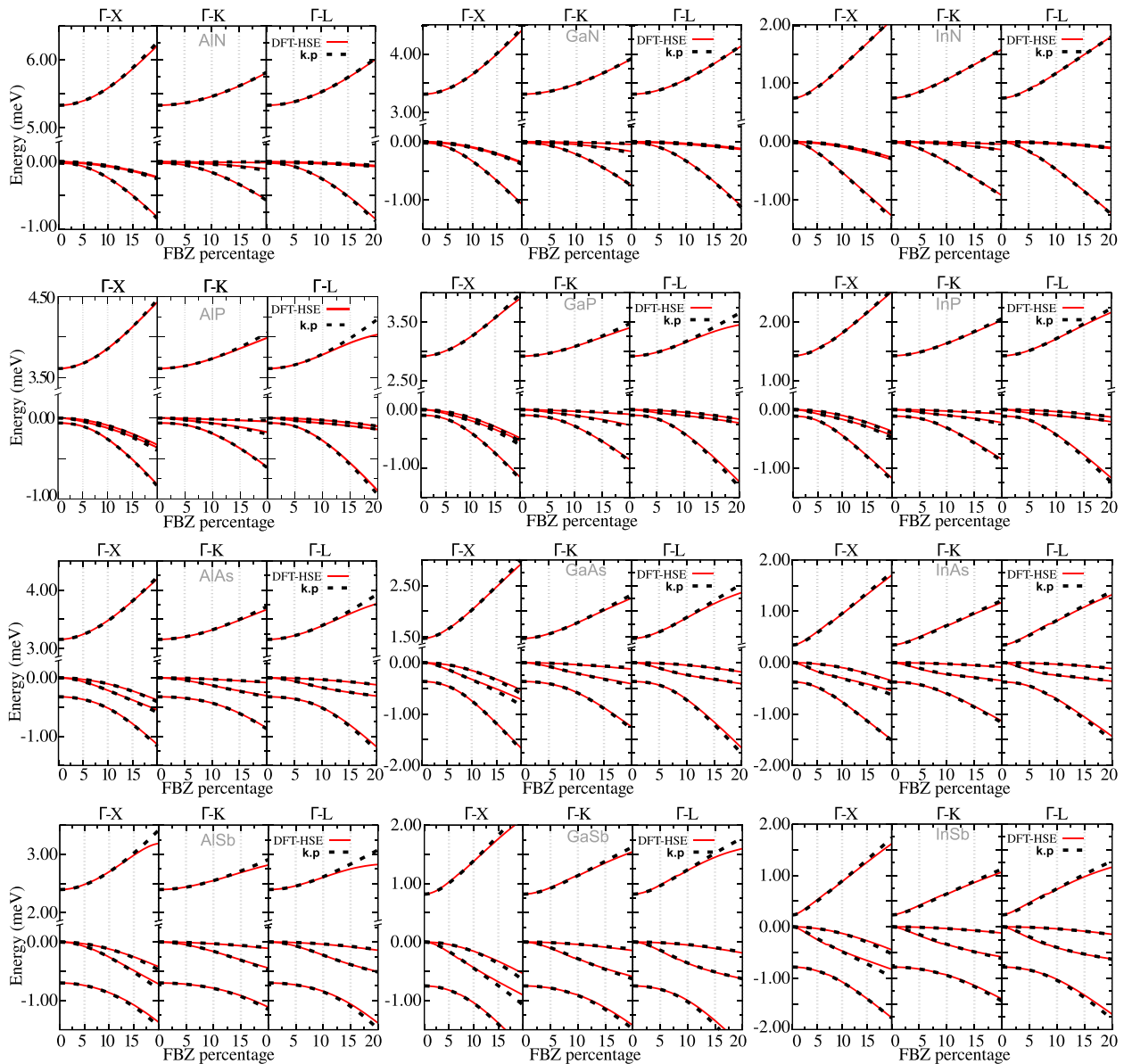


FIG. 7. HSE₂ and $\mathbf{k} \cdot \mathbf{p}$ band structure comparisons. The optimal parameters were obtained from fitting by using 10% of the FBZ. Three high symmetry directions are shown: Γ -X, Γ -K, and Γ -L.

the interactions with the states of class A. Class A states are chosen according to the energy range at the point of the first Brillouin zone (FBZ), with the goal of defining the effective Hamiltonian.

In this work, we used the 6×6 zinc-blende effective $\mathbf{k} \cdot \mathbf{p}$ Hamiltonians proposed by Luttinger and Kohn⁸⁸ (LK6) and extended by Kane⁸⁹ to an 8×8 model. In the LK6 model, in the vicinity of the Γ point, class A is composed of the three topmost valence bands (VB), i.e., heavy hole (HH), light hole (LH), and spin-orbit split-off hole (SO), and the matrix elements are determined by using the perturbation theory up to the second order. In the Kane model, the same bands and perturbative order were used, but class A also includes the first conduction band (CB). The use the symmetry properties of zinc-blende crystals and some algebraic

manipulation^{8,90} shows that the Kane Hamiltonian depend on 5 different effective mass parameters $\tilde{\gamma}_1$, $\tilde{\gamma}_2$, $\tilde{\gamma}_3$, \tilde{e} , and P , plus the gap and Δ_{so} , whereas the LK6 depends only on 3 parameters, γ_1 , γ_2 , and γ_3 , plus the Δ_{so} .⁹¹ Because the $\mathbf{k} \cdot \mathbf{p}$ method is semi-empirical, all effective mass parameters are obtained, with little algebraic manipulations, from the direct measurements of the effective masses of the carriers in the materials, except for the P parameter.

Distinct from the other effective mass parameters, P cannot be obtained by direct measures but must be extracted from the interband (CB-VB) interaction energy E_P . An accurate measure of E_P is hard to obtain due to the inherent difficulties associated with the decoupling of the CB-VB interaction to the interaction of them with the remote bands. E_P values have been estimated indirectly by experimental

techniques such as electron-spin-resonance, through inter-band matrix elements^{92,93} and from measures of the g -factors, which have little influence from the remote bands and yield more accurate values.⁴⁰ Due to the difficulties involved in measuring the g -factor in III-V semiconductors, the traditional procedure is to obtain the P parameter from the effective mass parameters by using the $6 \times 6 \mathbf{k} \cdot \mathbf{p}$ Hamiltonian. When the P is determined, the 8×8 parameters can be evaluated by using the relations shown in [Appendix A](#).

We chose, in this work, an alternative method to determine the effective mass and P parameters from band structures evaluated by DFT calculations. We fitted the HSE _{α} band structure by using the secular equation of the 8×8 Hamiltonian proposed in Ref. 36, by simultaneously determining all the parameters. All the points have the same weight and the same distance for all the materials. By using different percentages of the FBZ around the Γ point, we determined different parameter sets, and the choice of the final set of parameters was done by root mean square deviation (RMSD) analysis³⁶ by using the euclidean distance between the band structures from HSE _{α} and the effective Hamiltonian $\mathbf{k} \cdot \mathbf{p}$ with the adjusted parameters. Technical details about the fitting are available in the [supplementary material](#).

As the difference between $\mathbf{k} \cdot \mathbf{p}$ and HSE _{α} increases considerably for large FBZ percentages, we recommend the values from the fitting for 10%, as shown in Table IV. This choice is a compromise between describing a reasonable percentage of the band and obtaining a small deviation of HSE _{α} band structure. A general feature of the band structures is the non-parabolicity in the region between 6 and 8% of the FBZ, better seen on CB and SO bands, as shown in Fig. 7. Another non-parabolicity also arises near 15%, and depending on the magnitude of this second non-parabolicity in a specific direction, the deviations of the values become more or less important at 20% of the FBZ.

In Table IV, we show the values for Kane ($\tilde{\gamma}_1, \tilde{\gamma}_2, \tilde{\gamma}_3, \tilde{e}$, and E_P), and Luttinger-Kohn ($\gamma_1, \gamma_2, \gamma_3$, and e) parameters, determined with the data by using the range of up to 10% of the FBZ (and in any up to a range of 2% to 20% in the [supplementary materials](#)). The ranges of the values observed in the literature are also given for comparison. Due to the small number of results founded in the literature, we included both experimental and theoretical works, which indicate the maximum and minimum values extracted from traditional sources, such as Madelung *et al.*,⁵³ Vurgaftman *et al.*,⁴⁰ Vurgaftman and Meyer,⁹⁴ and Winkler.⁹⁵ Our results are in agreement with the literature, i.e., the obtained effective mass parameters are inside the range of the most accepted values. In addition, the highest deviation comes from the nitrides. Because the most stable phase for the III-nitrides is wurtzite and not zinc-blende, the scarce experimental data prevents a more controlled comparison.

On the Kane models, the P parameter, or its related energy E_P , is essential. This parameter represents the influence of the conduction band on the masses of the valence states and, consequently, the influence of the valence band on the conduction states. Our results for the E_P parameter differ from those in the literature. The main reason for this difference is a divergence on the interpretation of the influence of

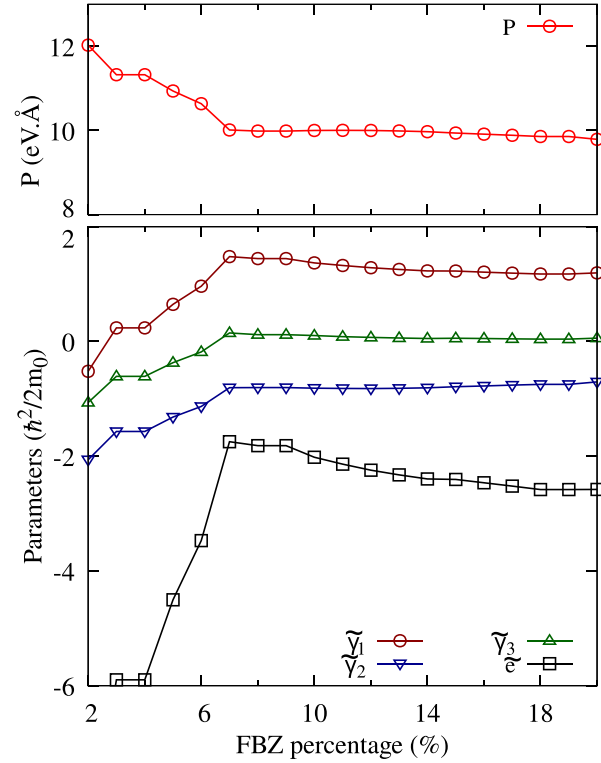


FIG. 8. GaAs dependence of P and Kane parameters with FBZ region used in the fitting process.

the remote bands on the experimental measurements of the electron spin resonance as pointed out by Shantharama *et al.*⁹⁶ and Adams *et al.*⁹⁷ In their article they compare, e.g., Chadi *et al.*,⁹³ the value for GaAs of $E_P = 29 \text{ eV}$, with their estimation based on an analysis of a $14 \times 14 \mathbf{k} \cdot \mathbf{p}$ Hamiltonian of $E_P = 25 \pm 0.5 \text{ eV}$. The reason for the divergence is attributed to an overestimation of the influence of the remote bands. Our suggested value for this parameter is $E_P = 25.9 \text{ eV}$. Because E_P is directly related to the Kane parameter P , its fitting is essential.

As we previously showed,³⁶ to correctly assign a value to P , it is necessary to include the first non-parabolicity in the range used for the fitting. If only the values below it are included, then there is a fast variation of the values of P , depending on the range used. However, the fittings done with ranges, including the non-parabolicity, show a stabilization of the value. As an example, in Fig. 8, we present a curve of the fitted parameter for GaAs, which shows the fast variation for ranges very close to the Γ -point and the stabilized values for ranges above 8%. The stabilization of our values indicates that our method improves the evaluation of the P parameter, which provides a way to distinguish the interactions of near and distant bands in the effective mass tensor. In the [supplementary materials](#), we provide the stabilization curves for the P as well as the effective mass parameters for all the materials.

F. Effective mass and g -factors

To verify the accuracy of our calculations, we compared the experimental effective masses with the ones obtained

TABLE V. Effective masses for light and the heavy holes along three directions ([100], [110], and [111]), isotropic masses from conduction band electrons and spin-orbit splitting holes, and electron g -factors, obtained around the Γ point, from the Luttinger-Kohn parameters. The ranges of values that comprise the values found in the literature (experimental and theoretical results) are also shown for comparison.

		[100]		[110]		[111]		m_{so}^*	m_c^*	g_c^*
		m_{HH}^*	m_{LH}^*	m_{HH}^*	m_{LH}^*	m_{HH}^*	m_{LH}^*			
AlN	This work	1.320	0.437	4.123	0.357	2.858	0.371	0.659	0.296	1.99
	Literature								0.330 ^a	
AlP	This work	0.563	0.255	1.599	0.197	1.176	0.206	0.355	0.197	1.93
	Literature	0.513 ^b	0.211 ^b			1.372 ^b	0.145 ^b	0.30 ^a		
AlAs	This work	0.503	0.177	0.955	0.152	1.253	0.146	0.282	0.143	1.46
	Literature	0.409 ^c	0.153 ^c			1.022 ^c	0.109 ^c	0.28 ^a	0.15 ^c	
AlSb	This work	0.359	0.136	0.682	0.115	0.890	0.111	0.240	0.127	0.20
	Literature	0.336 ^c	0.123 ^c			0.872 ^c	0.091 ^c		0.14 ^a	
GaN	This work	0.841	0.279	1.542	0.243	1.991	0.234	0.421	0.205	1.98
	Literature									1.95 ^d
GaP	This work	0.405	0.168	0.754	0.141	0.966	0.136	0.243	0.150	1.82
	Literature					0.670 ^c	0.170 ^c	0.465 ^c	0.13 ^a	
GaAs	This work	0.357	0.088	0.672	0.079	0.898	0.076	0.169	0.071	-0.34
	Literature	0.34 ^b	0.094 ^b			0.75 ^b	0.082 ^b		0.0662 ^b	-0.44 ^f
GaSb	This work	0.247	0.051	0.500	0.046	0.710	0.045	0.144	0.045	-7.66
	Literature	0.29 ^c		0.36 ^c		0.40 ^c		0.12 ^a	0.039 ^b	-9.1 ^c
InN	This work	0.874	0.090	1.851	0.085	1.460	0.086	0.167	0.062	1.73
	Literature									
InP	This work	0.460	0.118	0.828	0.106	1.073	0.103	0.199	0.092	1.38
	Literature							0.121 ^b	0.0808 ^b	1.48 ^b
InAs	This work	0.354	0.030	0.911	0.028	0.661	0.029	0.104	0.025	-15.18
	Literature	0.35 ^b				0.85 ^b		0.14 ^a	0.0265 ^b	-15.3 ^b
InSb	This work	0.266	0.017	0.498	0.017	0.692	0.016	0.119	0.016	-43.30
	Literature	0.32 ^c		0.42 ^c		0.44 ^c		0.11 ^a	0.013 ^b	-51.31 ^b

^aTheory from Ref. 40.

^bExp. from Ref. 9.

^cExp. from Ref. 77.

^dExp. from Ref. 85.

^eTheory from Ref. 77.

^fExp. from Ref. 99.

from our effective mass parameters (see relations in Appendix A). By using the electronic g -factors, which are directly related to the spin splitting of the carrier bands, we compared the measured values in the literature with our own values estimated from the $\mathbf{k} \cdot p$ parameters by using the Roth's formula⁹⁸

$$g_c^* = 2 - \frac{2E_p \Delta_{so}}{3E_{gap}(E_{gap} + \Delta_{so})}, \quad (4)$$

and the values for E_p , E_{gap} , and Δ_{so} . This equation includes only the interaction between VB and CB, whereas the interactions between the other bands are neglected.

Table V shows the effective masses and g -factors obtained by the $\mathbf{k} \cdot p$ parameters calculation. SO and CB electronic effective masses are considered to be isotropic, and HH and LH were evaluated along three different directions of the FBZ: [111], [110], and [100]. The CB g -factors were estimated by using Eq. (4). Tabulated values, extracted from Refs. 40, 53, 77, and 94, are presented for comparison. The supplementary material provides tables for all calculated parameter sets.

Because we can distinguish the effects of the interactions from inner and outer bands, our g -factors show

excellent agreement with the literature values except those materials with large spin-orbit coupling, such as antimonides and indium compounds. In these materials, we found large deviations from the reference values of HH and LH effective masses along the [110] and [111] directions. The lack of k dependence on the spin-orbit coupling on the $\mathbf{k} \cdot p$ Hamiltonian used in our description may be responsible for such deviation. However, even for these materials, the LH and HH g -factors along the [100] direction present good agreement with the experimental values because the specific symmetry of the zinc-blende systems prevent the splitting of the bands along that specific direction. Finally, CB and SO bands also present good agreement with the experimental values because the spin split for them is small.

IV. SUMMARY AND CONCLUSION

We reported an extensive *ab initio* study of electronic and structural properties of the III-V semiconductors (12 systems) based on DFT within the PBE, PBE+SOC, HSE06, HSE $_{\alpha}$, and HSE $_{\alpha}$ +SOC functionals. For the hybrid HSE $_{\alpha}$

functional, we fitted the magnitude of the nonlocal Fock exchange that replaces part of the PBE exchange based on the experimental results for the fundamental band gap and spin-orbit splitting energies. Except for the AIP compound, whose α is 0.127, our α parameters are in between 0.209 and 0.343, deviating less than 0.1 from the universal value of 0.25 estimated by Perdew *et al.*²⁸

Although the electronic properties were improved by the fitting, our results and analysis clearly indicate that HSE $_{\alpha}$ does not yield a significant improvement of the structural properties when compared with HSE06. In fact, it is an excellent result because it shows that it is possible to improve the electronic properties without affecting the structural parameters by using fitted HSE $_{\alpha}$ functionals. This conclusion is valid at least for small changes in α near to the 0.25 value. Furthermore, based on several analysis, we found a correlation between the values of α with the cationic radius, namely, the optimized α value decreases almost linearly as a function of the atomic cationic radius, except for the case of AlN. Therefore, our findings, combined with previous results obtained by Viñes *et al.*,³⁴ indicate that it is possible to correlate the values of the α with the physical properties, and, hence, it opens new possibilities in the study of much more complex materials.

We found that the HSE $_{\alpha}$ overestimates the elastic constants, whereas PBE underestimates them. However, the magnitude of the relative error is smaller when using the HSE $_{\alpha}$ functional. We see from our results that the elastic constants decrease as the ionic radius increase, and, hence, the elastic constants decrease by increasing the lattice parameter of the crystal structures. This behavior was reported in the literature^{25,78} and was traditionally used to estimate the elastic constants^{79,80} by the extrapolation of the data.

To provide a deeper understanding of the band structure curvatures, we used the DFT band structures to determine accurate $\mathbf{k} \cdot \mathbf{p}$ parameters and, from them, obtained the effective masses and the g -factors beyond the parabolic model. For the antimonides and indium compounds in specific directions, we observed large deviations of the g -factors from the experimental results, which indicate that the $8 \times 8 \mathbf{k} \cdot \mathbf{p}$ Hamiltonian may still not be adequate for describing systems with small band gap or large spin-orbit splittings. The k -dependent spin-orbit term, responsible for the spin-orbit splitting outside of the Γ point, is neglected in our model, which results in the deviations observed. Finally, we tabulated the effective masses and $\mathbf{k} \cdot \mathbf{p}$ parameters by presenting a full set of III-V parameters that may be used in realistic simulations of systems with higher complexity, such as nanowires and quantum dots or devices based on these compounds.

SUPPLEMENTARY MATERIAL

See [supplementary material](#) for additional data: computational parameters used for every system, analyses of the α parameter versus different physical properties, band structures, and $\mathbf{k} \cdot \mathbf{p}$ parameters for different percentages of the BZ for all the systems.

ACKNOWLEDGMENTS

The authors thank D. J. As for the help with experimental data on nitride systems. The authors acknowledge financial support from the Brazilian agencies CAPES, PVE Grant No. 88881.068174/2014-01 (G. M. Sipahi), São Paulo research foundation, Grant No. 2013/21045-2 (J. L. F. Da Silva), national council for scientific and technological development, 301190/2015-1 (J. L. F. Da Silva), and the coordination for improvement of higher level education (C. M. O. Bastos and F. P. Sabino). The authors also thank the infrastructure provided to our computer cluster by the department of information technology, campus São Carlos.

APPENDIX A: EFFECTIVE BADER CHARGE

TABLE VI. Effective Bader charge evaluated by using the PBE functional for III-V semiconductors. All units are in C.

	N	P	As	Sb
Al	2.37	2.06	1.92	1.63
Ga	1.52	0.84	0.68	0.34
In	1.40	0.88	0.74	0.47

APPENDIX B: LUTTINGER-KOHN PARAMETERS AND EFFECTIVE MASS RELATIONS

Because class A and B states differ among the 6×6 and 8×8 models, the definitions of the effective mass parameters differ from one model to the other.^{8,90} The relation between both model parameters, for zinc-blende structures, is given by the following expressions:

$$\begin{aligned} \gamma_1 &= \tilde{\gamma}_1 + \frac{E_p}{3E_{\text{gap}}}, & \gamma_2 &= \tilde{\gamma}_2 + \frac{E_p}{6E_{\text{gap}}}, \\ \gamma_3 &= \tilde{\gamma}_3 + \frac{E_p}{6E_{\text{gap}}}, & e &= \tilde{e} + \frac{\left(E_{\text{gap}} + \frac{2}{3}\Delta_{\text{so}}\right)E_p}{E_{\text{gap}}(E_{\text{gap}} + \Delta_{\text{so}})}, \\ E_p &= \frac{2m_0}{\hbar^2} P^2. \end{aligned}$$

The effective masses may be determined from the parameters by using the following relations:

$$\begin{aligned} m_{\text{lh}[100]} &= (\gamma_1 + 2\gamma_2)^{-1}, & m_{\text{lh}[110]} &= (\gamma_1 + 2\gamma_3)^{-1}, \\ m_{\text{hh}[100]} &= (\gamma_1 - 2\gamma_2)^{-1}, & m_{\text{hh}[110]} &= (\gamma_1 - 2\gamma_3)^{-1}, \\ m_e &= e^{-1}, & m_{\text{lh}[111]} &= (\gamma_1 + \sqrt{\gamma_2^2 + 3\gamma_3^2})^{-1}, \\ m_{\text{hh}[111]} &= (\gamma_1 - \sqrt{\gamma_2^2 + 3\gamma_3^2})^{-1}, \\ m_{\text{so}} &= \left(\gamma_1 - \frac{1}{3} \frac{\Delta_{\text{so}} E_p}{E_{\text{gap}}(E_{\text{gap}} + \Delta_{\text{so}})}\right)^{-1}. \end{aligned}$$

¹E. F. Schubert, *Light-Emitting Diodes* (Cambridge University Press, 2006).

²S. Nakamura, *Rev. Mod. Phys.* **87**, 1139 (2015).

- ³Y. Sun, K. Zhou, Q. Sun, J. Liu, M. Feng, Z. Li, Y. Zhou, L. Zhang, D. Li, S. Zhang, M. Ikeda, S. Liu, and H. Yang, *Nat. Photonics* **10**, 595 (2016).
- ⁴A. Rogalski, *Infrared Detectors* (CRC Press, 2010).
- ⁵J. Nelson, *The Physics of Solar Cells* (ICP, 2003).
- ⁶D. Basu, D. Saha, C. C. Wu, M. Holub, Z. Mi, and P. Bhattacharya, *Appl. Phys. Lett.* **92**, 091119 (2008).
- ⁷P. Y. Yu and M. Cardona, *Fundamentals of Semiconductors*, 2nd ed. (Springer-Verlag, Berlin, 1999).
- ⁸R. Enderlein, *Fundamentals of Semiconductor Physics and Devices* (World Scientific, 1997).
- ⁹O. Madelung, *Semiconductors: Data Handbook* (Springer, Berlin/Heidelberg, 2004).
- ¹⁰M. Z. Hasan and C. L. Kane, *Rev. Mod. Phys.* **82**, 3045 (2010).
- ¹¹T. D. Stanesco, R. M. Lutchyn, and S. D. Sarma, *Phys. Rev. B* **84**, 144522 (2011).
- ¹²V. Mourik, K. Zuo, S. M. Frolov, S. R. Plissard, E. P. A. M. Bakkers, and L. P. Kouwenhoven, *Science* **336**, 1003 (2012).
- ¹³*Liquid Crystalline Semiconductors*, edited by R. J. Bushby, S. M. Kelly, and M. O'Neill (Springer, Netherlands, 2013).
- ¹⁴M. Gmitra and J. Fabian, *Phys. Rev. B* **94**, 165202 (2016).
- ¹⁵M. A. T. Sandoval, E. A. de Andrada e Silva, A. F. da Silva, and G. C. La Rocca, *Semicond. Sci. Technol.* **31**, 115008 (2016).
- ¹⁶S. J. Polly, C. G. Bailey, A. J. Grede, D. V. Forbes, and S. M. Hubbard, *J. Cryst. Growth* **454**, 64 (2016).
- ¹⁷M. S. Seghilani, M. Myara, M. Sellahi, L. Legratiet, I. Sagnes, G. Beaudoin, P. Lalanne, and A. Garnache, *Sci. Rep.* **6**, 38156 (2016).
- ¹⁸P. E. Faria Junior, T. Campos, C. M. O. Bastos, M. Gmitra, J. Fabian, and G. M. Sipahi, *Phys. Rev. B* **93**, 235204 (2016).
- ¹⁹C.-Z. Zhao, T. Wei, X.-D. Sun, S.-S. Wang, and K.-Q. Lu, *Physica B* **494**, 71 (2016).
- ²⁰M. O. Nestoklon, R. Benchamekh, and P. Voisin, *J. Phys.: Condens. Matter* **28**, 305801 (2016).
- ²¹J. P. Perdew and A. Zunger, *Phys. Rev. B* **23**, 5048 (1981).
- ²²J. P. Perdew and M. Levy, *Phys. Rev. Lett.* **51**, 1884 (1983).
- ²³R. O. Jones and O. Gunnarsson, *Rev. Mod. Phys.* **61**, 689 (1989).
- ²⁴Y.-S. Kim, M. Marsman, G. Kresse, F. Tran, and P. Blaha, *Phys. Rev. B* **82**, 205212 (2010).
- ²⁵S. Adachi, *Physical Properties of III-V Semiconductor Compounds* (Wiley-Blackwell, 1992).
- ²⁶L. Hedin, *Phys. Rev.* **139**, A796 (1965).
- ²⁷F. Aryasetiawan and O. Gunnarsson, *Rep. Prog. Phys.* **61**, 237 (1998).
- ²⁸J. P. Perdew, M. Ernzerhof, and K. Burke, *J. Chem. Phys.* **105**, 9982 (1996).
- ²⁹C. Adamo and V. Barone, *J. Chem. Phys.* **110**, 6158 (1999).
- ³⁰J. Heyd, G. E. Scuseria, and M. Ernzerhof, *J. Chem. Phys.* **118**, 8207 (2003).
- ³¹J. Heyd and G. E. Scuseria, *J. Chem. Phys.* **121**, 1187 (2004).
- ³²J. Heyd, G. E. Scuseria, and M. Ernzerhof, *J. Chem. Phys.* **124**, 219906 (2006).
- ³³A. D. Becke, *J. Chem. Phys.* **98**, 5648 (1993).
- ³⁴F. Viñes, O. Lamiel-García, K. C. Ko, J. Y. Lee, and F. Illas, *J. Comput. Chem.* **38**, 781 (2017).
- ³⁵P. G. Moses, M. Miao, Q. Yan, and C. G. Van de Walle, *J. Chem. Phys.* **134**, 084703 (2011).
- ³⁶C. M. O. Bastos, F. P. Sabino, P. E. F. Junior, T. Campos, J. L. F. Da Silva, and G. M. Sipahi, *Semicond. Sci. Technol.* **31**, 105002 (2016).
- ³⁷L. E. Ramos, L. K. Teles, L. M. R. Scolfaro, J. L. P. Castineira, A. L. Rosa, and J. R. Leite, *Phys. Rev. B* **63**, 165210 (2001).
- ³⁸A. Dal Corso, *Phys. Rev. B* **86**, 085135 (2012).
- ³⁹J. Paier, M. Marsman, K. Hummer, G. Kresse, I. C. Gerber, and J. G. Ángyán, *J. Chem. Phys.* **124**, 154709 (2006).
- ⁴⁰I. Vurgaftman, J. R. Meyer, and L. R. Ram-Mohan, *J. Appl. Phys.* **89**, 5815 (2001).
- ⁴¹P. Hohenberg and W. Kohn, *Phys. Rev.* **136**, B864 (1964).
- ⁴²W. Kohn and L. J. Sham, *Phys. Rev.* **140**, A1133 (1965).
- ⁴³J. P. Perdew and Y. Wang, *Phys. Rev. B* **45**, 13244 (1992).
- ⁴⁴J. P. Perdew, J. A. Chevary, S. H. Vosko, K. A. Jackson, M. R. Pederson, D. J. Singh, and C. Fiolhais, *Phys. Rev. B* **46**, 6671 (1992).
- ⁴⁵J. P. Perdew, K. Burke, and M. Ernzerhof, *Phys. Rev. Lett.* **77**, 3865 (1996).
- ⁴⁶M. Ernzerhof and G. E. Scuseria, *J. Chem. Phys.* **110**, 5029 (1999).
- ⁴⁷J. L. F. Da Silva, M. V. Ganduglia-Pirovano, J. Sauer, V. Bayer, and G. Kresse, *Phys. Rev. B* **75**, 045121 (2007).
- ⁴⁸M. V. Ganduglia-Pirovano, J. L. F. Da Silva, and J. Sauer, *Phys. Rev. Lett.* **102**, 026101 (2009).
- ⁴⁹Y. Hinuma, A. Grüneis, G. Kresse, and F. Oba, *Phys. Rev. B* **90**, 155405 (2014).
- ⁵⁰A. V. Krukau, O. A. Vydrov, A. F. Izmaylov, and G. E. Scuseria, *J. Chem. Phys.* **125**, 224106 (2006).
- ⁵¹D. D. Koelling and B. N. Harmon, *J. Phys. C: Solid State Phys.* **10**, 3107 (1977).
- ⁵²T. Takeda, *Z. Phys. B* **32**, 43 (1978).
- ⁵³*Semiconductors: Physics of Group IV Elements and III-V Compounds*, Landolt-Börnstein, New Series, Group III Vol. 17, edited by O. Madelung, M. Schultz, and H. Weiss (Springer-Verlag, Berlin, 1982).
- ⁵⁴P. E. Blöchl, *Phys. Rev. B* **50**, 17953 (1994).
- ⁵⁵G. Kresse and J. Hafner, *Phys. Rev. B* **48**, 13115 (1993).
- ⁵⁶G. Kresse and J. Furthmüller, *Phys. Rev. B* **54**, 11169 (1996).
- ⁵⁷G. Kresse and D. Joubert, *Phys. Rev. B* **59**, 1758 (1999).
- ⁵⁸Y. L. Page and P. Saxe, *Phys. Rev. B* **65**, 104104 (2002).
- ⁵⁹X. Wu, D. Vanderbilt, and D. R. Hamann, *Phys. Rev. B* **72**, 035105 (2005).
- ⁶⁰J. Heyd, J. E. Peralta, G. E. Scuseria, and R. L. Martin, *J. Chem. Phys.* **123**, 174101 (2005).
- ⁶¹Y.-S. Kim, K. Hummer, and G. Kresse, *Phys. Rev. B* **80**, 035203 (2009).
- ⁶²J. P. Perdew, W. Yang, K. Burke, Z. Yang, E. K. U. Gross, M. Scheffler, G. E. Scuseria, T. M. Henderson, I. Y. Zhang, A. Ruzsinszky, H. Peng, J. Sun, E. Trushin, and A. Görling, *Proc. Natl. Acad. Sci. U. S. A.* **114**, 2801 (2017).
- ⁶³V. Atalla, I. Y. Zhang, O. T. Hofmann, X. Ren, P. Rinke, and M. Scheffler, *Phys. Rev. B* **94**, 035140 (2016).
- ⁶⁴N. Sai, P. F. Barbara, and K. Leung, *Phys. Rev. Lett.* **106**, 226403 (2011).
- ⁶⁵W. Yang, A. J. Cohen, and P. Mori-Sánchez, *J. Chem. Phys.* **136**, 204111 (2012).
- ⁶⁶A. Walsh, J. L. F. Da Silva, and S.-H. Wei, *Phys. Rev. Lett.* **100**, 256401 (2008).
- ⁶⁷H.-P. Komsa and A. Pasquarello, *Phys. Rev. B* **84**, 075207 (2011).
- ⁶⁸D. Colleoni and A. Pasquarello, *J. Phys.: Condens. Matter* **28**, 495801 (2016).
- ⁶⁹R. Todeschini, V. Consonni, R. Mannhold, H. Kubinyi, and G. Folkers, *Molecular Descriptors for Chemoinformatics* (Wiley VCH Verlag GmbH, 2009), Vol. 41.
- ⁷⁰J. C. Slater, *J. Chem. Phys.* **41**, 3199 (1964).
- ⁷¹C. Kittel, *Introduction to Solid State Physics*, 8th ed. (John Wiley & Sons, Inc., New York, 2004).
- ⁷²H. Morkoç, *Handbook of Nitride Semiconductors and Devices, Materials Properties, Physics and Growth* (John Wiley & Sons, 2009), Vol. 1.
- ⁷³S. J. Pearton, *GaN and Related Materials II (Optoelectronic Properties of Semiconductors and Superlattice)* (CRC Press, 2000), Vol. 2.
- ⁷⁴*New Data and Updates for IV-IV, III-V, II-VI and I-VII Compounds, Their Mixed Crystals and Diluted Magnetic Semiconductors*, edited by U. Rössler (Springer, Berlin/Heidelberg, 2011).
- ⁷⁵N. N. Anua, R. Ahmed, A. Shaari, M. A. Saeed, B. U. Haq, and S. Goumri-Said, *Semicond. Sci. Technol.* **28**, 105015 (2013).
- ⁷⁶*Introduction to Nitride Semiconductor Blue Lasers and Light Emitting Diodes*, edited by S. Nakamura and S. F. Chichibu (CRC Press, 2000).
- ⁷⁷*Springer Handbook of Condensed Matter and Materials Data*, edited by W. Martienssen and H. Warlimont (Springer Nature, 2005).
- ⁷⁸R. W. Keyes, *J. Appl. Phys.* **33**, 3371 (1962).
- ⁷⁹*Semiconductors and Semimetals: Transport Phenomena*, edited by R. K. Willardson and A. C. Beer (Academic Press Inc., 1975), Vol. 10.
- ⁸⁰S. Adachi, *J. Appl. Phys.* **58**, R1 (1985).
- ⁸¹M. Łopuszyński and J. A. Majewski, *Phys. Rev. B* **76**, 045202 (2007).
- ⁸²M. A. Caro, S. Schulz, and E. P. O'Reilly, *Phys. Rev. B* **86**, 014117 (2012).
- ⁸³A. N. Chantis, M. van Schilfgaarde, and T. Kotani, *Phys. Rev. Lett.* **96**, 086405 (2006).
- ⁸⁴B. Monemar, *Phys. Rev. B* **10**, 676 (1974).
- ⁸⁵J. H. Buß, T. Schupp, D. J. As, D. Hägele, and J. Rudolph, *J. Appl. Phys.* **118**, 225701 (2015).
- ⁸⁶P. Carrier and S.-H. Wei, *J. Appl. Phys.* **97**, 033707 (2005).
- ⁸⁷P.-O. Löwdin, *J. Chem. Phys.* **19**, 1396 (1951).
- ⁸⁸J. M. Luttinger and W. Kohn, *Phys. Rev.* **97**, 869 (1955).
- ⁸⁹E. O. Kane, *Semiconductors and Semimetals* (Elsevier BV, 1966), pp. 75–100.
- ⁹⁰M. W. Lok and C. Lew Yan Voon, *The k.p Method* (Springer-Verlag GmbH, 2009).

⁹¹We denoted the 6×6 parameters, the so called Luttinger-Kohn parameters without tilde. In opposition, the 8×8 ones are referred as Kane parameters.

⁹²C. Weisbuch and C. Hermann, *Phys. Rev. B* **15**, 816 (1977).

⁹³D. J. Chadi, A. H. Clark, and R. D. Burnham, *Phys. Rev. B* **13**, 4466 (1976).

⁹⁴I. Vurgaftman and J. R. Meyer, *J. Appl. Phys.* **94**, 3675 (2003).

⁹⁵R. Winkler, *Spin-Orbit Coupling Effects in Two-Dimensional Electron and Hole Systems* (Springer-Verlag, Berlin, 2003).

⁹⁶L. G. Shantharama, A. R. Adams, C. N. Ahmad, and R. J. Nicholas, *J. Phys. C: Solid State Phys.* **17**, 4429 (1984).

⁹⁷A. R. Adams, L. G. Shantharama, R. J. Nicholas, and C. K. Sarkar, *Physica B* **139–140**, 401 (1986).

⁹⁸L. M. Roth, B. Lax, and S. Zwerdling, *Phys. Rev.* **114**, 90 (1959).

⁹⁹M. Oestreich and W. W. Rühle, *Phys. Rev. Lett.* **74**, 2315 (1995).

***Ab initio* investigation of structural stability and exfoliation energies in transition metal dichalcogenides based on Ti-, V-, and Mo-group elements**

Carlos M. O. Bastos,¹ Rafael Besse,¹ Juarez L. F. Da Silva,² and Guilherme M. Sipahi^{1,*}

¹São Carlos Institute of Physics, University of São Paulo, P.O. Box 369, 13560-970 São Carlos, SP, Brazil

²São Carlos Institute of Chemistry, University of São Paulo, P.O. Box 780, 13560-970 São Carlos, SP, Brazil



(Received 5 October 2018; revised manuscript received 30 January 2019; published 10 April 2019)

In this work, we report an *ab initio* investigation based on density functional theory of the structural, energetic, and electronic properties of 2D layered chalcogenides compounds based in the combination of the transition-metals (Ti, Zr, Hf, V, Nb, Ta, Cr, Mo, W) and chalcogenides (S, Se, Te) in three polymorphic phases: trigonal prismatic (2H), octahedral (1T), and distorted octahedral (1T_d). We determined the most stable phases for each compound, verifying the existence of the 1T_d phase for a small number of the compounds and we have also identified the magnetic compounds. In addition, with the determination of the exfoliation energies, we indicated the potential candidates to form one layer material and we have also found a relation between the exfoliation energy and the effective Bader charge in the metal, suggesting that when the materials present small exfoliation energies, it is due to the Coulomb repulsion between the chalcogen planes. Finally, we analyzed the electronic properties, identifying the semiconductor, semimetal, and metal materials and predicting the band gap of the semiconductors. In our results, the dependence of the band gap on the *d*-orbital is explicit. In conclusion, we have investigated the properties of stable and metastable phases for a large set of TMD materials, and our findings may be auxiliary in the synthesis of metastable phases and in the development of new TMDs applications.

DOI: [10.1103/PhysRevMaterials.3.044002](https://doi.org/10.1103/PhysRevMaterials.3.044002)

I. INTRODUCTION

Layered materials have been known for 50 years [1] and are applied in areas as diverse as dry lubricants [2], batteries [3], catalysts [4], among others. Recently, layered transition-metal dichalcogenides (TMDs), materials with chemical formula MQ_2 , with M being a transition-metal and Q a chalcogen (S, Se, and Te), have attracted wide technological interest due to their capacity of being isolated into one layer, like graphene does [5,6], and the wide spectrum of the electronic properties they present, being metals, semimetals, semiconductors, and insulators [7]. Recently, there were reported TMDs presenting exotic electronic properties, such as having topological insulator states [8], being a Weyl semimetal [9], and displaying charge density waves [7]. The wide spectrum of properties presented by TMDs is enabled by their large number of chemical compositions combining M and Q and the existence of several polymorphic phases [5,7,10].

In TMDs, layers composed of covalently bound M and Q planes are bound to each other by van der Waals interactions, and distinct coordination environments of the metal atoms within each layer generate structural polymorphism in these materials. Among these polymorphic phases, we highlight the most stable ones for a wide variety of materials [10,11]: (i) trigonal prismatic (2H), (ii) octahedral (1T), and (iii) distorted octahedral (1T_d). The lowest energy polymorph for a TMD depends mainly on the atomic radii and on the filling of the metal *d*-orbitals [11], e.g., Ti group metals (Ti, Zr, and Hf) favor 1T as the lowest energy phase [12]. However, the Peierls distortion mechanism is crucial for the energetic favoring

of the 1T_d phase in some compounds, since it breaks the degeneracy of electronic states, reducing the energy [12,13].

The coexistence among different phases is linked to parameters such as temperature or pressure [14,15], and for the same material two different polymorphic phases may drastically change properties, e.g., MoS₂ in 2H and 1T phase is a semiconductor and a metal, respectively [16,17]. The synthesis of many polymorphic phases has been possible with the advance of experimental techniques [18–21], allowed to obtain polymorphic phases which are not at the lowest energies. However, few studies were done in these metastable phases and a comprehensive characterization of TMD compounds and polymorphs is important to explore their properties and identify stability factors.

A key factor for the renewed interest in layered TMDs is the production of two-dimensional (2D) materials from the mechanical or chemical exfoliation of the layers [22]. The easiness to exfoliate the materials comes from the weak binding between layers, which depends on the van der Waals interactions, much weaker than the in-plane covalent bonding. However, some materials are more difficult to exfoliate than others due to stronger interlayer binding and, as suggested by Monet *et al.* [23], the exfoliation energy can be used to determine how easy it is to exfoliate the layers from the crystal. Previous studies report exfoliation energies only for TMDs at the lowest energy phases and studies involving another polymorphic phases are not common. Therefore, a thorough evaluation of the exfoliation energy in different TMD compounds and polymorphs is called for as an effective way to guide the production of two-dimensional materials.

To obtain a comprehensive description of the properties of layered TMDs, we performed a first-principles investigation of the stability, exfoliation energy, and electronic properties

*Corresponding author: sipahi@ifsc.usp.br

of TMDs formed by Ti-, V-, and Cr-group transition metals and S, Se, and Te, in three different polymorphic phases: 2H, 1T, 1T'. The elastic constants of the materials were calculated, which provide means to evaluate their stability, and the magnetic order was also considered. Based on the exfoliation energies and on the analysis of charge transfer between metals and chalcogens, we identified trends correlating the intralayer charge transfer with the magnitude of interlayer binding. Last, we classified all the studied TMDs compositions and polymorphic phases according to their electronic properties.

II. THEORETICAL APPROACH AND COMPUTATIONAL DETAILS

Our first-principles calculations are based on the density functional theory (DFT) formalism [24,25] within the semilocal exchange and correlation functional proposed by Perdew–Burke–Ernzerhof (PBE) [26]. The Kohn–Sham equations were solved using the PAW method [27] as implemented in the Vienna *ab initio* simulation package (VASP), version 5.4.1 [28,29]. We focus on layered dichalcogenides, and it is well known from the literature that the PBE functional underestimates long-range interactions such as the London dispersion [30]. To minimize this problem, we employed the semiempirical DFT-D3 method proposed by Grimme *et al.* [31], which has been shown to provide structural properties for MoS₂ in good agreement with experimental results [32].

It has been well known that (semi-)local functionals fail to accurately predict band gap energies [33–38], and hence, to minimize this problem, the electronic properties, such as density of states (DOS) and band structures, were computed using the hybrid functional proposed by Heyd–Scuseria–Ernzerhof [39,40] (HSE06), which contains the PBE correlation and separates the exchange term in long- and short-range terms by a screening function with the parameter $\omega = 0.206 \text{ \AA}^{-1}$. The short-range term is composed of 25% of exact exchange and 75% of PBE exchange, while the long-range term is composed only by PBE exchange. We included also the relativistic effects of spin-orbit-coupling (SOC) for the valence states through the second-variational approach [41].

Spin-orbit coupling (SOC) effects were included for the valence states through the second-variational approach [41]. As showed in our previous work [38], the SOC have small impact in the structural properties, hence, for volume equilibrium, relative energy stability, exfoliation energy, and elastic constants calculations, the SOC was neglected. For electronic properties, such as band structures and DOS, SOC corrections were considered only in combination with the PBE functional, due to the high computational cost of the combined HSE06-SOC calculations.

Structural optimizations were performed with PBE+D3 through the minimization of the stress tensor and of the forces on every atom. We used, for the plane-waves basis set, cutoff energy of $2 \times$ the maximum energy recommended by VASP (ENMAX parameter from POTCAR file, as described in Table I of the Supplemental Material [42]) to determine the equilibrium lattice parameters. Using the optimized structures, the elastic constants were computed using (i) contributions from strain-stress relations for distortions in the lattice with rigid ions and (ii) ionic relaxation contributions, determined from

the inversion of ionic Hessian matrix [43,44]. To achieve the convergence condition for the elastic constant we increased the cutoff energy to $2.5 \times \text{ENMAX}$. The cutoff energy employed to compute the electronic properties, i.e., DOS, band structure, and Bader charge, as well as to obtain cohesive energy and exfoliation energy, was $1.125 \times \text{ENMAX}$.

For the integration in the first Brillouin zone, we employed a Monkhorst–Pack scheme [45] using a \mathbf{k} -mesh of $11 \times 11 \times 2$ for 2H-MoS₂, and meshes with same \mathbf{k} -point density for the remaining structures, to obtain the equilibrium structure parameters. However, the \mathbf{k} -mesh was increased in all systems, e.g., to $22 \times 22 \times 5$ for 2H-MoS₂, to compute the electronic properties. Due to the limitations of parallel calculations of elastic constants in VASP, we employed a Γ -centered \mathbf{k} -mesh with fixed grid of $16 \times 16 \times 4$, $12 \times 12 \times 6$, and $10 \times 18 \times 5$ for 2H, 1T, and 1T_d structures, respectively, for all chemical compositions. More details about the computational approach are provided in the Supplemental Material [42].

III. CRYSTAL STRUCTURES: MQ₂

Our study concentrates on the most commonly observed TMD structural phases, 2H, 1T, and 1T_d [7]. In Fig. 1, we present the schematics of the polytypes crystal structures, with Figs. 1(a)–1(c) showing the top and lateral views and Fig. 1(d) indicating an example of supercell employed to access the magnetic ordering. The 2H structure, shown in Fig. 1(a), is composed of a hexagonal lattice, with 2 formula units (f.u.) per unit cell, whose atoms planes are in the AbA BaB stacking sequence (capital and lower case letters for chalcogen and metal atoms planes, respectively), belonging to the $P6_3/mmc$ space group [10]. The 1T structure, shown in Fig. 1(b), is composed of a hexagonal lattice with 1 f.u. per unit cell, with AbC AbC stacking sequence, belonging to the $P\bar{3}m1$ space group [10]. Each layer of the 1T_d structure, shown in Fig. 1(c), can be generated from a 1T monolayer by reconstructions in a 2×1 orthorhombic cell, originating dimerized lines of metal atoms, a distortion which has been shown to be driven by a Peierls transition mechanism [13]. The 1T_d structure is composed of an orthorhombic lattice with 4 f.u. in the unit cell, belonging to the $Pnm2_1$ space group. The bonding geometry symmetries correspond to D_{6h} , D_{3d} , and C_{2v} point groups for 2H, 1T, and 1T_d, respectively.

We address materials composed by Ti-, V-, and Mo-group metals, with not fully occupied *d*-orbitals, thus some of the TMDs can exhibit nonzero magnetic moment, as has been experimentally observed in VS₂ and VSe₂ with ferromagnetic ordering in low temperatures [10,46]. To address the intrinsic magnetism in bulk TMDs, we employed supercells containing eight f.u., allowing to model antiferromagnetic configurations, as exemplified in Fig. 1(d). For nonmagnetic and ferromagnetic orderings, the unit cell was employed, since it can represent such configurations. To increase the reliability of our results, we built four antiferromagnetic initial configurations with supercells, plus the ferromagnetic one, and equilibrium volumes were obtained for every initial configuration, from which the lowest energy structure was subsequently selected. Tables with the energy comparison for the five initial configurations can be found in the Supplemental Material [42].

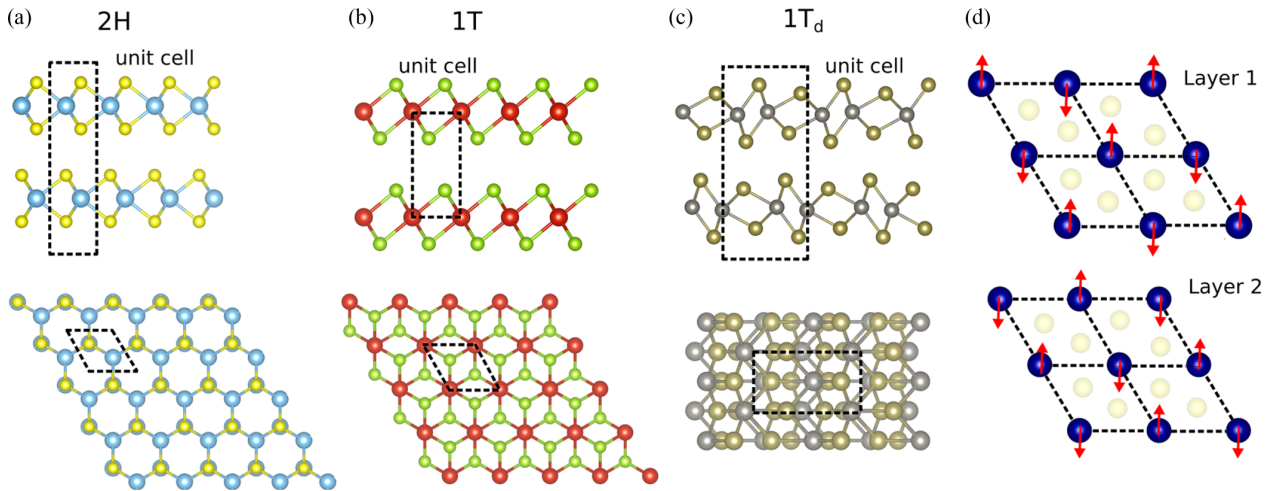


FIG. 1. Lateral and top view of the TMDs crystal structures of polytypes (a) trigonal prismatic (2H), (b) octahedral (1T), and (c) distorted octahedral ($1T_d$). The unit cells are represented in dashed lines. (d) Example of the supercell used to obtain the magnetic ordering, where the red arrows represent the initial magnetic moments in transition metal atoms.

IV. RESULTS

A. Relative energy stability

We obtained the equilibrium geometric configurations for all compounds and analyzed the relative stability between the phases (2H, 1T, $1T_d$) by comparison of the total energy, Fig. 2. For Ti group compounds, V group selenides and tellurides, and CrTe_2 , the $1T_d$ phase does not present a local minimum structure in the potential surface, i.e., even if the structural relaxation starts from the $1T_d$ structure, it yields the structural configuration of the 1T phase. Therefore, these compounds are not stable in the $1T_d$ phase and these structures were not further considered in our calculations.

Figure 2 shows the relative total energies obtained for the three polymorphic phases using 2H phase as the reference. For all the Ti group compounds (Ti, Zr, and Hf combined with S, Se, and Te) the lowest energy phase is 1T, as expected [5], while for the V and Cr groups compounds there is an alternation of the lowest energy phase. The V group compounds

have a small energy difference between the phases, which is manifested with the synthesis of 2H and 1T phases among these materials [7], and 2H is the most stable for compounds with S and Se whereas $1T_d$ is the most stable for compounds with Te. Compounds with V are experimentally observed in the 2H phase, in contrast with our results, however it has been shown that due to the small energy difference between the phases, temperature effects might change the lowest energy phase, in agreement with the synthesis of $1T\text{-VS}_2$ at room temperature [47].

In Cr group, 2H predominates as the lowest energy phase (MoQ_2 , WS_2 , WSe_2), as expected [5]. The exceptions are CrSe_2 (1T), CrTe_2 (1T), and WTe_2 ($1T_d$), which were all experimentally observed crystal structures [7,48,49]. Finally, the room temperature crystal structures of NbTe_2 and TaTe_2 , which are formed of a monoclinic lattice [50], are not considered in our calculations. However, among the structures considered, the $1T_d$ phase, that has the same intra-layer structural configuration of distorted octahedral coordination

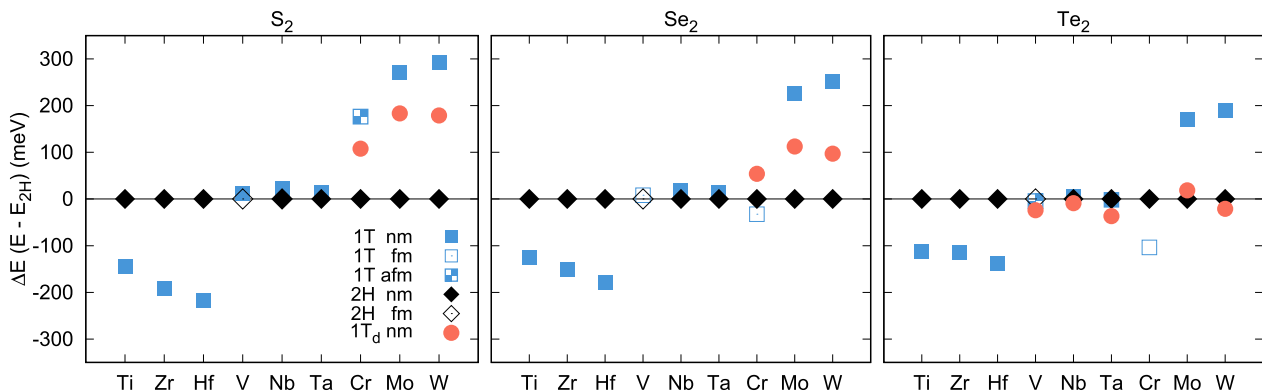


FIG. 2. Relative total energy between 1T, $1T_d$, and 2H phases for MS_2 , MSe_2 , and MTe_2 , where M is the metal indicated in the x axis. 2H phase is used as reference, so the vertical axis presents the values for $(E_{(1T,1T_d,2H)} - E_{2H})$. The magnetic ordering is indicated by the symbols in the key: nonmagnetic (nm), ferromagnetic (fm), and antiferromagnetic (afm).

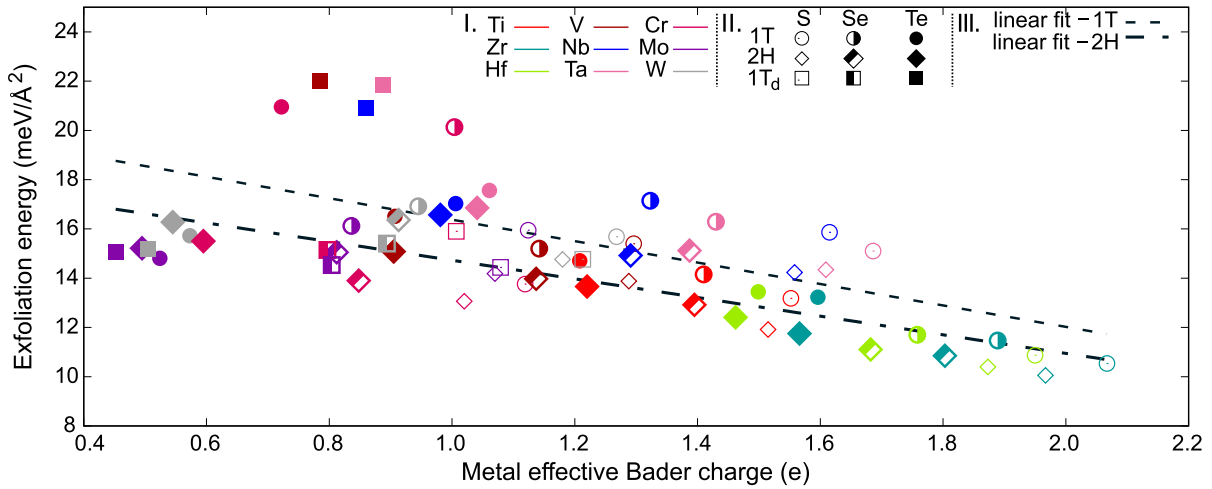


FIG. 3. Exfoliation energy as function of the metal effective Bader charge. Compounds can be identified by the combination of the color in Legend I with the symbol in Legend II. Legend III presents the key for the linear fitting of phases 1T and 2H.

of metal atoms, was obtained as the lowest energy one for these compounds.

Therefore, our results are in line with the general rule of the strong influence of the filling of metal d orbitals on the lowest energy phase of each compound [5,12], as can be seen in the preference of 1T phase for Ti group compounds, and mostly 2H phase for TMDs of V and Cr groups. However, other effects are important to determine the energetic favored phase, like magnetism. From our results, only the V group and Cr compounds favor a magnetic ordering, depending on the phase: VS_2 , VSe_2 , VTe_2 , and NbS_2 in 2H phase are ferromagnetic, as well as VSe_2 and TaTe_2 in 1T phase, while CrS_2 and VTe_2 in 1T phase are antiferromagnetic. This information is also presented in Fig. 2. A recent theoretical work [23] reported that the 1T monolayers of V dichalcogenides are ferromagnetic, and 1T- CrSe_2 monolayer is reported as antiferromagnetic.

The antiferromagnetic ordering was also obtained by experimental measurements in bulk 1T- CrSe_2 [48], although we obtained lower energy for the ferromagnetic ordering. The energy difference between the two orderings in our calculations, however, is of only 4 meV, i.e., the phases are approximately degenerate and stable. Furthermore, this difference is so small that, the use of a different vdW correction may change the result, also considering that variations on the c lattice parameter were shown to modify the energetic preference between the two orderings [48]. The relative energies for all magnetic configurations are presented in the Supplemental Material [42].

B. Exfoliation energy

To investigate the strength of interlayer binding in TMDs and determine how easily they can be exfoliated, we calculated the exfoliation energy. As the polymorphic structures have different unit cells, we calculate exfoliation energies per monolayer area in the unit cell. In Fig. 3, the exfoliation energy is shown as a function of metal effective Bader charge [51,52], i.e., an estimate of the charge transfer from metal to chalcogen atoms. Several works, using different

levels of vdW corrections [23,53–56], propose a classification of the materials that are easily or potentially exfoliable based on the exfoliation energy. We adopt the classification in which materials with exfoliation energy of 15 to 20 $\text{meV}/\text{\AA}^2$ are considered easily exfoliable, while materials with energies above these values up to 130 $\text{meV}/\text{\AA}^2$ are considered potentially exfoliable.

In our results, almost all the studied compounds have exfoliation energies in the range of 10 to 17 $\text{meV}/\text{\AA}^2$ and can be classified as easily exfoliable, as shown in Fig. 3. The exceptions are: (i) CrSe_2 and CrTe_2 in the 1T phase, with 20 and 21 $\text{meV}/\text{\AA}^2$, respectively; (ii) VTe_2 , TaTe_2 , and NbTe_2 in the $1T_d$ phase, with 22, 22, and 21 $\text{meV}/\text{\AA}^2$, respectively.

An analysis of Fig. 3 shows that the exfoliation energy decreases linearly with the increase of the metal effective Bader charge, presenting a clear trend. This relation arises because with the increase of the charge on metal atoms, and consequently with the increase of the magnitude of the charge on the chalcogen plane, the effective Coulomb repulsion among the layers also increases, resulting in larger interlayer distances and smaller exfoliation energies. There is a small difference between polymorphic phases, as indicated by the separate linear fittings in Fig. 3, which may be related to the atom ordering in the chalcogen plane. As generally 1T phase has higher in-plane lattice parameters when compared with 2H, less charge is accumulated in the chalcogen plane in 1T than in 2H. As a result, the distance between planes is smaller and the exfoliation energy is larger. Nevertheless, this difference is small, as shown for 2H and 1T ZrS_2 in Fig. 3. When the charge transfer is lower, Coulomb repulsion plays a smaller role, leading the exfoliation energies to be more dependent on other effects, e.g., van der Waals interaction, causing larger deviations from the linear trend, as with the cases of stronger ($>20 \text{ meV}/\text{\AA}^2$) interlayer binding. Thus, the linear correlation is not clear for $1T_d$, which may be due to the nonuniformities in the chalcogen plane caused by the distortions typical of this phase. All values of exfoliation energy and Bader charge are available in Supplemental Material [42].

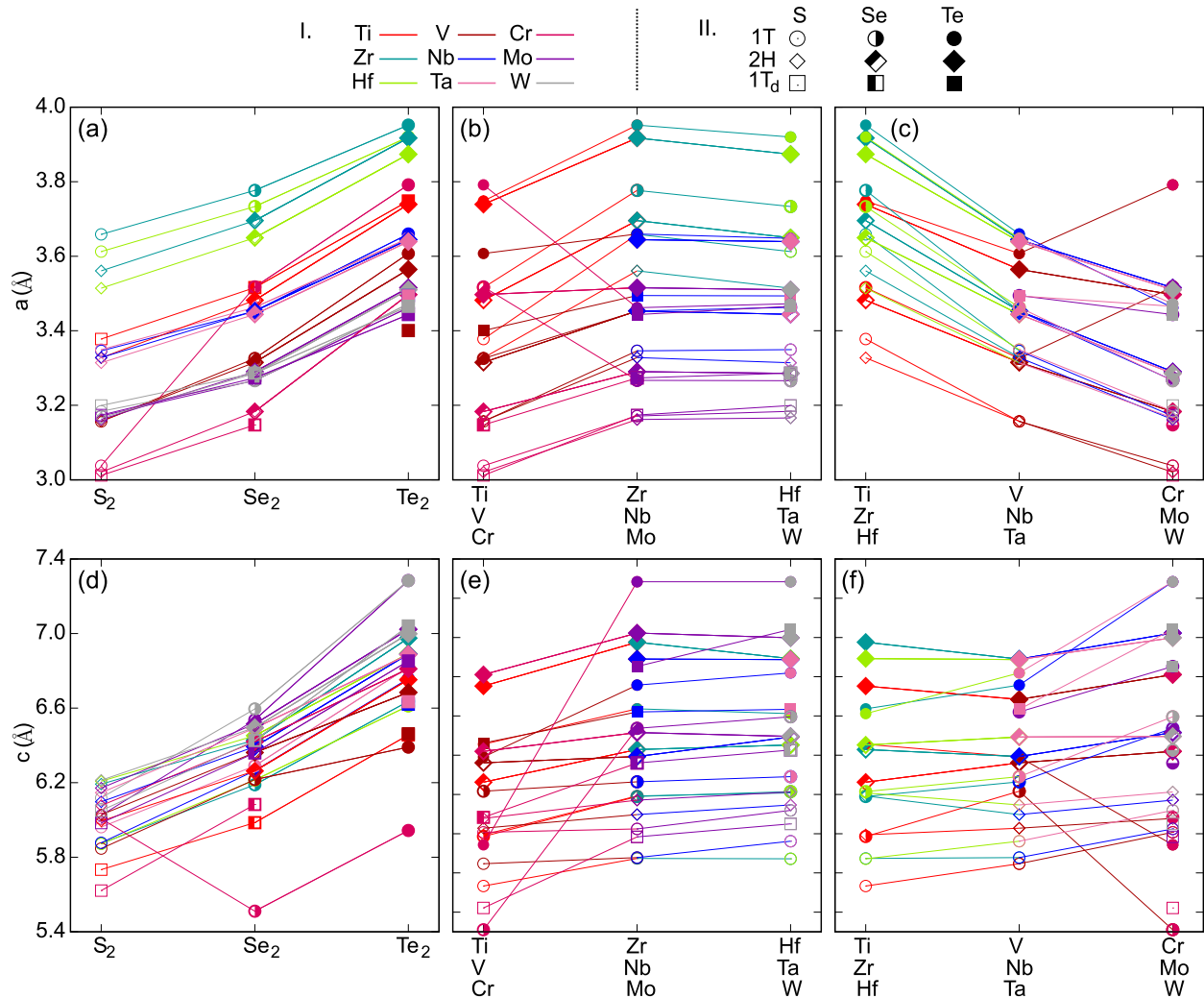


FIG. 4. Lattice parameters of the 2H, 1T, and 1T_d TMDs. Compounds are identified by the combination of the color, in Legend I, with the symbols, in Legend II. The out-of-plane lattice parameter is normalized by the number of layers in the unit cell. In (a) and (d) the dependence on the chalcogen species is shown, (b) and (e) present the dependence on the transition metal period, and (c) and (f) show the dependence on the metal group. All numerical values are presented in the Supplemental Material [42].

C. Equilibrium volume

In Fig. 4, we show in-plane, a , and perpendicular, c , lattice parameters. Due to the different number of layers in the unit cells between the polymorphs, in order to compare all the materials, we used the value of the out-of-plane lattice parameter divided by the number of layers to obtain c . As expected, the lattice parameters increase monotonically with the chalcogen atomic radius (covalent radius reference values are 1.04 Å, 1.14 Å, and 1.32 Å for S, Se, Te, respectively [57]), as shown in Figs. 4(a) and 4(d). The exceptions are the 1T Cr compounds that present an abnormal increase of c from CrSe₂ to CrS₂.

The effect of varying transition-metal period, with fixed metal group and chalcogen species, on the lattice parameters is represented in Figs. 4(b) and 4(e). Compounds with transition-metal belonging to period 4 (Ti, V, and Cr) have the smallest parameters, while compounds with transition metals belonging to periods 5 (Zr, Nb, and Mo) and 6 (Hf, Ta, and W)

have similar lattice parameters. This is also in agreement with the trend of atomic radii of the transition metals, which are the smallest for transition metals belonging to period 4 and have closer values for transition metals from periods 5 and 6, for example 1.28 Å, 1.40 Å and 1.41 Å for Cr, Mo, and W, respectively [57].

The atomic radii of transition metals (e.g., 1.46 Å, 1.35 Å and 1.28 Å for Ti, V, and Cr, respectively [57]) also determine the decrease of the parameter a with the increase of the column number of the transition metal group, for a fixed period and a chalcogen species, as shown in Fig. 4(c). There is no clearly defined trend for the c parameter. Compared with the experimental data for the already synthesized TMDs, as showed in the Table I, the calculated lattice parameters present mean absolute percentage errors (MAPE) lower than 1% for in-plane lattice parameters (a and b) and lower than 2% for the perpendicular lattice parameter (c), indicating that PBE-D3 predicts reasonable values for vdW effects in TMDs.

TABLE I. Lattice parameters obtained from DFT, compared to their experimental values. Materials that are unstable in the phase $1T_d$ are indicated. The experimental values were extracted from Ref. [10]. All values are presented in Å.

Phase			a_0	b_0	c_0	Phase			a_0	b_0	c_0	Phase			a_0	b_0	c_0
TiS ₂	2H	DFT	3.33	3.33	11.99	TiSe ₂	2H	DFT	3.48	3.48	12.51	TiTe ₂	2H	DFT	3.73	3.73	13.50
	1T		3.38	3.38	5.73		1T		3.51	3.51	5.98		1T		3.74	3.74	6.45
	$1T_d$		Unstable				$1T_d$		Unstable				$1T_d$		Unstable		
ZrS ₂	1T	Exp.	3.41	3.41	5.70	ZrSe ₂	1T	Exp.	3.53	3.53	6.00	ZrTe ₂	1T	Exp.	3.76	3.76	6.52
	2H	DFT	3.56	3.56	12.38		2H	DFT	3.69	3.69	12.85		2H	DFT	3.91	3.91	13.95
	1T		3.65	3.65	5.87		1T		3.77	3.77	6.18		1T		3.95	3.95	6.63
HfS ₂	$1T_d$		Unstable			HfSe ₂	$1T_d$		Unstable			HfTe ₂	$1T_d$		Unstable		
	1T	Exp.	3.66	3.66	5.81		1T	Exp.	3.77	3.77	6.13		1T	Exp.	3.95	3.95	6.63
	2H	DFT	3.51	3.51	12.41		2H	DFT	3.64	3.64	12.90		2H	DFT	3.87	3.87	13.78
VS ₂	1T		3.61	3.61	5.87	VSe ₂	1T		3.73	3.73	6.21	VTe ₂	1T		3.91	3.91	6.61
	$1T_d$		Unstable				$1T_d$		Unstable				$1T_d$		Unstable		
	2H	Exp.	3.37	3.37	11.78		2H	Exp.	3.44	3.44	12.38		2H	Exp.			
NbS ₂	1T		3.95	3.95	6.65	NbSe ₂	1T		3.74	3.74	6.14	NbTe ₂	1T		3.95	3.95	6.65
	2H	DFT	3.15	3.15	12.05		2H	DFT	3.31	3.31	12.72		2H	DFT	3.56	3.56	13.36
	1T		3.15	3.15	5.84		1T		3.32	3.32	6.21		1T		3.60	3.60	6.39
TaS ₂	$1T_d$		Unstable			TaSe ₂	$1T_d$		Unstable			TaTe ₂	$1T_d$		Unstable		
	1T	Exp.					1T	Exp.	3.34	3.34	6.12		1T	Exp.			
	2H	DFT	3.33	3.33	12.18		2H	DFT	3.45	3.45	12.78		2H	DFT	3.64	3.64	13.76
CrS ₂	1T		3.34	3.34	5.87	CrSe ₂	1T		3.45	3.45	6.26	CrTe ₂	1T		3.65	3.65	6.76
	$1T_d$		Unstable				$1T_d$		Unstable				$1T_d$		Unstable		
	2H	Exp.	3.31	3.31	11.88		2H	Exp.	3.44	3.44	12.55		2H	Exp.			
MoS ₂	1T		3.53	3.53	6.08	MoSe ₂	1T		3.53	3.53	6.29	MoTe ₂	1T		3.40	6.42	6.46
	2H	DFT	3.16	3.16	12.34		2H	DFT	3.44	3.44	12.98		2H	DFT	3.56	3.56	13.36
	1T		3.17	3.17	6.02		1T		3.46	3.46	6.29		1T		3.60	3.60	6.39
WS ₂	$1T_d$		Unstable			WSe ₂	$1T_d$		Unstable			WTe ₂	$1T_d$		Unstable		
	2H	Exp.	3.15	3.15	12.29		2H	Exp.	3.43	3.43	12.72		2H	Exp.			
	1T	DFT	3.02	3.02	12.15		1T	DFT	3.18	3.18	12.83		1T	DFT	3.49	3.49	13.62
TaS ₂	1T		3.31	3.31	5.96	TaSe ₂	1T		3.46	3.46	6.29	TaTe ₂	1T		3.64	3.64	6.81
	$1T_d$		Unstable				$1T_d$		Unstable				$1T_d$		Unstable		
	2H	Exp.	3.31	3.31	12.10		2H	Exp.	3.43	3.43	12.72		2H	Exp.			
CrS ₂	1T		3.36	3.36	5.90	CrSe ₂	1T		3.47	3.47	6.27	CrTe ₂	1T		3.79	3.79	5.94
	2H	DFT	3.02	3.02	12.15		2H	DFT	3.18	3.18	12.83		2H	DFT	3.49	3.49	13.62
	$1T_d$		3.01	5.53	5.62		$1T_d$		3.14	5.75	6.08		$1T_d$		Unstable		
MoS ₂	2H	DFT	3.16	3.16	12.34	MoSe ₂	2H	DFT	3.29	3.29	13.03	MoTe ₂	2H	DFT	3.51	3.51	14.04
	1T		3.17	3.17	6.02		1T		3.26	3.26	6.53		1T		3.46	3.46	7.28
	$1T_d$		3.17	5.71	5.98		$1T_d$		3.27	5.94	6.35		$1T_d$		3.44	6.37	6.85
WS ₂	2H	Exp.	3.15	3.15	12.29	WSe ₂	2H	Exp.	3.29	3.29	12.90	WTe ₂	2H	Exp.	3.51	3.51	13.97
	1T	DFT	3.16	3.16	12.42		2H	DFT	3.28	3.28	12.99		2H	DFT	3.50	3.50	13.99
	1T		3.18	3.18	6.11		1T		3.26	3.26	6.59		1T		3.37	3.37	5.73
WS ₂	$1T_d$		3.19	5.70	6.05	WSe ₂	$1T_d$		3.28	5.92	6.42	WTe ₂	$1T_d$		3.46	6.27	7.04
	2H	Exp.	3.17	3.17	12.36		2H	Exp.	3.28	3.28	12.95		2H	Exp.	3.477	6.25	7.01

D. Elastic constants

As we consider some compositions and polymorphic phases not yet synthesized, the structural stability of the materials was addressed by the Born elastic stability criteria [58], and hence, we analyzed the stability of the TMDs through the evaluation of the elastic constants and verification of the Born elastic stability criteria as discussed by Mouhat and Coudert [59]. Due to their symmetry, the crystals of 1T, 2H, and $1T_d$ phases present 6, 5, and 9 nonzero and independent elastic constants, respectively, which must satisfy the necessary and sufficient conditions for stability discussed below.

For the 1T phase ($P\bar{3}m1$ space group), with elastic constants C_{11} , C_{12} , C_{13} , C_{14} , C_{33} , and C_{44} [and $C_{66} = (C_{11} - C_{12})/2$], the conditions are

$$\begin{aligned} C_{11} &> |C_{12}|, & C_{44} &> 0, \\ C_{13}^2 &< \frac{1}{2}C_{33}(C_{11} + C_{12}), \\ C_{14}^2 &< \frac{1}{2}C_{44}(C_{11} - C_{12}). \end{aligned} \quad (1)$$

For the crystal of 2H phase ($P6_3/mmc$ space group), that has the elastic constants C_{11} , C_{12} , C_{13} , C_{33} , C_{44} [with $C_{66} = (C_{11} - C_{12})/2$], the conditions are

$$C_{11} > |C_{12}|, \quad C_{13}^2 < \frac{1}{2}C_{33}(C_{11} + C_{12}), \quad C_{44} > 0. \quad (2)$$

Finally, the elastic constants of the $1T_d$ phase crystal ($Pnm2_1$ space group), C_{11} , C_{12} , C_{13} , C_{22} , C_{23} , C_{33} , C_{44} , C_{55} , and C_{66} , must satisfy the following conditions:

$$\begin{aligned} [C_{11}C_{22}C_{33} + 2C_{12}C_{13}C_{23} - C_{11}C_{23}^2 \\ - C_{22}C_{13}^2 - C_{33}C_{12}^2] &> 0, \\ C_{11}C_{12} &> C_{12}^2, \quad C_{11} > 0, \quad C_{44} > 0, \\ C_{55} &> 0, \quad C_{66} > 0. \end{aligned} \quad (3)$$

All the elastic constants values are shown in the Supplemental Material [42], while the diagonal elastic constants are shown in Fig. 5. We found that all conditions for the elastic

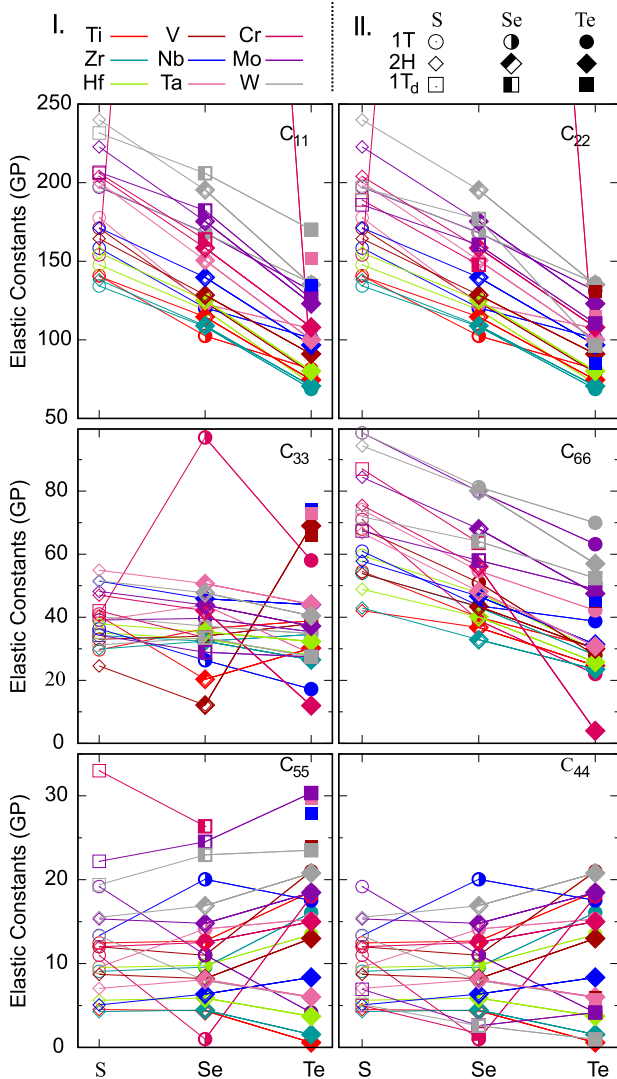


FIG. 5. Diagonal elements of the elastic matrix of the 1T, 2H, and 1T_d TMD bulks.

stability are satisfied, and hence, those configurations are local minimum structures. Our results are in agreement with previous calculations [60] and experimental results [7,61]. For the elastic constants C_{11} and C_{22} , which are not related to the out of plane direction (z), the magnitude decreases with the chalcogen radius and have higher values when compared with the other elastic constants, as shown in Fig. 5. This occurs because in plane binding, that is dominated by covalent bonds, is weaker for larger chalcogen radius, and is stronger than the out of plane van der Waals interactions. Therefore, the other elastic constants, which are related to the z direction, have a smaller magnitude, and present deviant trends for the chalcogen radius, due to the role of the van der Waals interactions in the interlayer interactions.

E. Band structure and density of states

To characterize the materials according to their electronic properties, we calculated the band structure and the density of states of the 64 stable TMDs with the hybrid functional HSE06. The results for 2H-phase selenides of the 3d-metals are shown in Fig. 6, and the results for the other systems are in the Supplemental Material [42]. From the analysis of the results, the materials were classified as metals, semi-metals or semiconductors, as indicated in Fig. 7. Among all the studied TMDs, 22 were identified as semiconductors, with band gaps ranging from 0.20 to 1.75 eV.

In the literature, works that estimate the band gaps for TMDs in the bulk phase mainly use the crystal structures acquired from crystallographic databases [62,63] presenting band gap values that differ from our results. The difference of values is due to the use of the PBE functional, that is known to underestimate the band gap [33,38,64]. In Table II, we present the values of PBE, PBE+SOC, HSE06 and experimental band gaps for the TMD semiconductor materials. The comparison of PBE and PBE+SOC shows that the inclusion of SOC modify the gap values usually from less than one to a few decades of meV, exception made for ZrSe₂-1T, HfSe₂-1T, and WTe₂-2H where this difference is about 150 meV. However, the PBE functional usually underestimates the gap in the order of several hundreds of meVs. Despite the absence of the

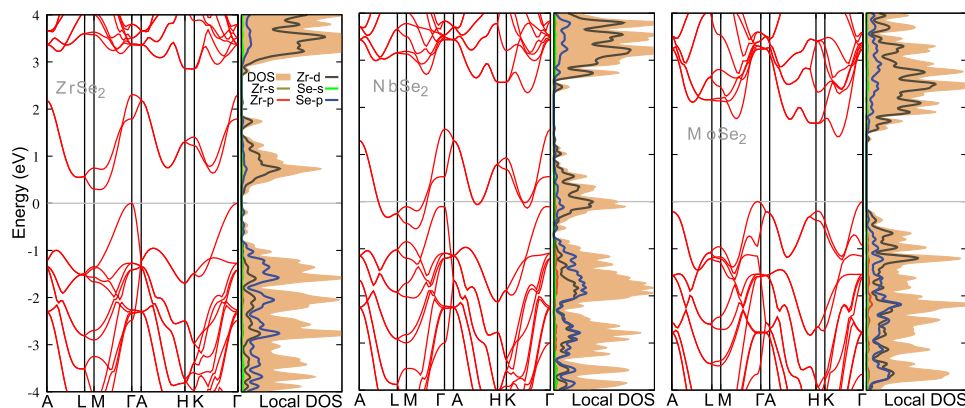


FIG. 6. 2H-phase DFT-HSE06 band structures and densities of states of ZrSe₂ (left), NbSe₂ (center), and MoSe₂ (right). Vertical lines indicate high-symmetry points in the first Brillouin zone. At the right panels, shadowed curves indicate the density of states (DOS) while the solid lines indicate the local density of states in s -, p -, and d -orbitals of each atomic species.

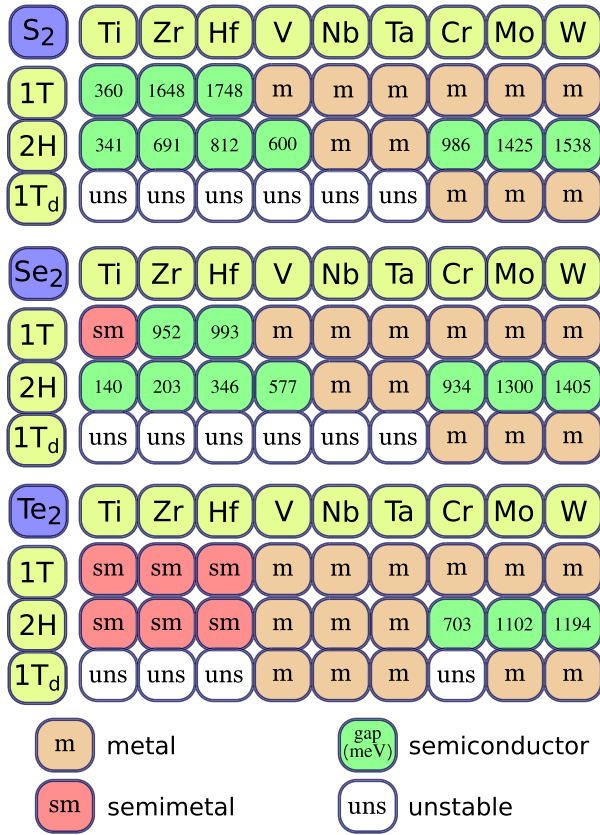


FIG. 7. Classification of stable material phases according to their electronic band gap: metal (m), semimetal (sm), or semiconductor. In semiconductors, predicted gap energy values are shown in meV units. Unstable phases are indicated by (uns).

SOC corrections on the HSE06 calculations this functional shows more realistic band gaps when compared with the experimentally measured values, preventing the high computational costs associated to the combined use of HSE06 and SOC.

For each phase and considering compositions with the same chalcogen, the transition metal d electron count determines the electronic character of the material. For example, in 2H-MSe₂ compounds, as shown in Fig. 6, with the progressive filling of the d band from Zr to Nb to Mo ZrSe₂ is a semiconductor, while NbSe₂ is a metal, and the band is fully occupied in MoSe₂, recovering the semiconductor character. Therefore, if the d -orbitals are completely occupied or empty, then the TMDs have semiconducting behavior, while if the d -orbitals have the partial occupation, then the TMDs have conducting behavior. These results are in agreement with other reports in the literature [11,12]. Because the crystal symmetry, i.e., the polymorphic phase, strongly affects the energy of the d bands, the same compound can have different electronic properties depending on the polymorphic phase. For example, MoS₂ is metallic in the 1T phase, but is a semiconductor in the 2H phase [16,17].

TABLE II. PBE, PBE with spin-orbit coupling (PBE+SOC), HSE06 and experimental band gaps for TMD semiconductor materials. All energies are given in meV.

Material	Phase	PBE	PBE+SOC	HSE06	Exp.
TiS ₂	1T	0	15	360	
ZrS ₂	1T	848	850	1648	
ZrSe ₂	1T	260	109	952	
HfS ₂	1T	988	974	1748	
HfSe ₂	1T	378	203	993	
TiS ₂	2H	0	0	341	
TiSe ₂	2H	0	0	140	
ZrS ₂	2H	0	0	691	
ZrSe ₂	2H	0	0	203	
HfS ₂	2H	159	172	812	
HfSe ₂	2H	0	0	346	
VS ₂	2H	0	0	600	
VSe ₂	2H	0	0	577	
CrS ₂	2H	604	600	986	
CrSe ₂	2H	600	589	934	
CrTe ₂	2H	327	313	703	
MoS ₂	2H	918	912	1425	1230 ^b
MoSe ₂	2H	870	860	1300	1090 ^b
MoTe ₂	2H	739	720	1102	880 ^a
WS ₂	2H	1040	990	1538	1350 ^b
WSe ₂	2H	959	882	1405	1200 ^b
WTe ₂	2H	757	603	1194	

^aScanning tunneling spectroscopy and ionic-liquid gated transistors at room temperature [65].

^bPhotocurrent spectra at room temperature [66].

Band gaps vary with the composition in a similar way for the three studied phases. The increase in chalcogen atomic number narrows the band gap, because the energy of Q - p derived states, which compose the valence band maximum, is increased. For semiconductors with the same phase and chalcogen, the band gap increases with the transition metal atomic number, e.g., $\text{TiQ}_2^{\text{gap}} < \text{ZrQ}_2^{\text{gap}} < \text{HfQ}_2^{\text{gap}}$ in phase 1T, as shown in Fig. 7. This trend occurs due to the localization of the d orbitals, since their energy difference from the Fermi energy increases, i.e., looking for compounds with the same phase, the d -orbitals in TiS₂ have energies closer to Fermi energy than those in ZrS₂.

V. CONCLUSION

We investigated 27 TMD bulk compounds obtained by the combination of nine transition-metals (Ti, Zr, Hf, V, Nb, Ta, Cr, Mo, and W) with three chalcogens (S, Se, and Te) in three polymorphic phases, namely, 1T, 2H, and 1T_d. We obtained the equilibrium geometry configuration and the lowest energy phase for each material, which are in good agreement with experimental data for the already synthesized compositions. The magnetic ordering was also addressed, and some of the materials with transition-metal from the V group and compounds with Cr showed ferromagnetic or antiferromagnetic behavior. The effects of chemical composition on the equilibrium lattice parameters mostly follow the expected trends based on the atomic radius.

To investigate the stability of the crystal structures, we obtained the elastic constants and employed the Born elastic stability criteria, which was satisfied for all the systems. The exfoliation energy of all stable materials was calculated, indicating that the majority of the studied TMDs have weak interlayer binding and therefore are predicted as easy to exfoliate in order to obtain their two-dimensional form. We found that the increase of the charge transfer within each layer decreases the magnitude of the exfoliation energy, due to the Coulomb repulsion between chalcogen planes. The electronic band structure and density of states were calculated, which allowed classifying the materials like metal, semimetal or semiconductor, according to their band gap. We demonstrated that the occupation of metal d band determines the electronic character of the material. This study provides a comprehensible understanding of the properties of layered TMDs in different polymorphic phases, including material

not yet synthesized, and therefore can contribute to further development of layered and two-dimensional materials based on TMDs.

ACKNOWLEDGMENTS

The authors gratefully acknowledge support from FAPESP (São Paulo Research Foundation, Grant No. 2017/11631-2), Shell and the strategic importance of the support given by ANP (Brazil's National Oil, Natural Gas and Biofuels Agency) through the R&D levy regulation. R.B. acknowledges financial support (Ph.D. fellowship) from FAPESP, Grant No. 2017/09077-7. This study was financed in part by the Coordenação de Aperfeiçoamento de Pessoal de Nível Superior-Brasil (CAPES)-Finance Code 001. G.M.S. acknowledges CAPES-CsF (Grant No. 88881.068174/2014-01) and CNPq (Grants No. 304289/2015-9 and No. 308806/2018-2).

- [1] J. Wilson and A. Yoffe, *Adv. Phys.* **18**, 193 (1969).
- [2] F. J. Clauss, *Solid Lubricants and Self-Lubricating Solids* (Elsevier, Amsterdam, 1972).
- [3] M. S. Whittingham, *Chem. Rev.* **104**, 4271 (2004).
- [4] R. Lv, J. A. Robinson, R. E. Schaak, D. Sun, Y. Sun, T. E. Mallouk, and M. Terrones, *Acc. Chem. Res.* **48**, 56 (2014).
- [5] M. Chhowalla, H. S. Shin, G. Eda, L.-J. Li, K. P. Loh, and H. Zhang, *Nat. Chem.* **5**, 263 (2013).
- [6] A. K. Geim and K. S. Novoselov, *Nat. Mater.* **6**, 183 (2007).
- [7] A. V. Kolobov and J. Tominaga, *Two-Dimensional Transition-Metal Dichalcogenides* (Springer International Publishing, Berlin, 2016).
- [8] L. Peng, Y. Yuan, G. Li, X. Yang, J.-J. Xian, C.-J. Yi, Y.-G. Shi, and Y.-S. Fu, *Nat. Commun.* **8**, 65 (2017).
- [9] K. Deng, G. Wan, P. Deng, K. Zhang, S. Ding, E. Wang, M. Yan, H. Huang, H. Zhang, Z. Xu, J. Denlinger, A. Fedorov, H. Yang, W. Duan, H. Yao, Y. Wu, S. Fan, H. Zhang, X. Chen, and S. Zhou, *Nat. Phys.* **12**, 1105 (2016).
- [10] F. Hulliger and F. Lévy, *Structural Chemistry of Layer-Type Phases*, 1st ed., Physics and Chemistry of Materials with Layered Structures 5 (Springer, Netherlands, 1977).
- [11] D. Voiry, A. Mohite, and M. Chhowalla, *Chem. Soc. Rev.* **44**, 2702 (2015).
- [12] H. Yang, S. W. Kim, M. Chhowalla, and Y. H. Lee, *Nat. Phys.* **13**, 931 (2017).
- [13] R. Besse, N. A. M. S. Caturello, C. M. O. Bastos, D. Guedes-Sobrinho, M. P. Lima, G. M. Sipahi, and J. L. F. D. Silva, *J. Phys. Chem. C* **122**, 20483 (2018).
- [14] D. H. Keum, S. Cho, J. H. Kim, D.-H. Choe, H.-J. Sung, M. Kan, H. Kang, J.-Y. Hwang, S. W. Kim, H. Yang, K. J. Chang, and Y. H. Lee, *Nat. Phys.* **11**, 482 (2015).
- [15] S. Cho, S. Kim, J. H. Kim, J. Zhao, J. Seok, D. H. Keum, J. Baik, D.-H. Choe, K. J. Chang, K. Suenaga, S. W. Kim, Y. H. Lee, and H. Yang, *Science* **349**, 625 (2015).
- [16] F. Wypych and R. Schöllhorn, *J. Chem. Soc., Chem. Commun.* **0**, 1386 (1992).
- [17] Q. Tang and D. en Jiang, *Chem. Mater.* **27**, 3743 (2015).
- [18] S. L. Wong, H. Liu, and D. Chi, *Prog. Cryst. Growth Charact. Mater.* **62**, 9 (2016).
- [19] H. C. Diaz, Y. Ma, R. Chaghi, and M. Batzill, *Appl. Phys. Lett.* **108**, 191606 (2016).
- [20] T. A. J. Loh, D. H. C. Chua, and A. T. S. Wee, *Sci. Rep.* **5**, 18116 (2015).
- [21] L. K. Tan, B. Liu, J. H. Teng, S. Guo, H. Y. Low, and K. P. Loh, *Nanoscale* **6**, 10584 (2014).
- [22] K. S. Novoselov, D. Jiang, F. Schedin, T. J. Booth, V. V. Khotkevich, S. V. Morozov, and A. K. Geim, *Proc. Natl. Acad. Sci. USA* **102**, 10451 (2005).
- [23] N. Mounet, M. Gibertini, P. Schwaller, D. Campi, A. Merkys, A. Marrazzo, T. Sohier, I. E. Castelli, A. Cepellotti, G. Pizzi, and N. Marzari, *Nat. Nanotechnol.* **13**, 246 (2018).
- [24] P. Hohenberg and W. Kohn, *Phys. Rev.* **136**, B864 (1964).
- [25] W. Kohn and L. J. Sham, *Phys. Rev.* **140**, A1133 (1965).
- [26] J. P. Perdew, K. Burke, and M. Ernzerhof, *Phys. Rev. Lett.* **77**, 3865 (1996).
- [27] P. E. Blöchl, *Phys. Rev. B* **50**, 17953 (1994).
- [28] G. Kresse and J. Hafner, *Phys. Rev. B* **48**, 13115 (1993).
- [29] G. Kresse and J. Furthmüller, *Phys. Rev. B* **54**, 11169 (1996).
- [30] T. Tsuneda, *Density Functional Theory in Quantum Chemistry* (Springer Nature, Berlin, 2014).
- [31] S. Grimme, J. Antony, S. Ehrlich, and H. Krieg, *J. Chem. Phys.* **132**, 154104 (2010).
- [32] H. Peelaers and C. G. V. de Walle, *J. Phys.: Condens. Matter* **26**, 305502 (2014).
- [33] J. P. Perdew and A. Zunger, *Phys. Rev. B* **23**, 5048 (1981).
- [34] R. G. Parr and Y. Weitao, *Density-Functional Theory of Atoms and Molecules (International Series of Monographs on Chemistry)* (Oxford University Press, Oxford, 1994).
- [35] P. Mori-Sánchez, A. J. Cohen, and W. Yang, *Phys. Rev. Lett.* **100**, 146401 (2008).
- [36] Y.-S. Kim, K. Hummer, and G. Kresse, *Phys. Rev. B* **80**, 035203 (2009).
- [37] E. Engel and R. M. Dreizler, *Density Functional Theory* (Springer, Berlin/Heidelberg, 2011).
- [38] C. M. O. Bastos, F. P. Sabino, G. M. Sipahi, and J. L. F. D. Silva, *J. Appl. Phys.* **123**, 065702 (2018).
- [39] J. Heyd, G. E. Scuseria, and M. Ernzerhof, *J. Chem. Phys.* **118**, 8207 (2003).

- [40] J. Heyd, G. E. Scuseria, and M. Ernzerhof, *J. Chem. Phys.* **124**, 219906 (2006).
- [41] D. D. Koelling and B. N. Harmon, *J. Phys. C: Solid State Phys.* **10**, 3107 (1977).
- [42] See Supplemental Material at <http://link.aps.org/supplemental/10.1103/PhysRevMaterials.3.044002> for computational details, convergence tests, initial magnetic configurations, relative energies, elastic constants, exfoliation energies, band structures, and density of states of the materials described in this article.
- [43] Y. LePage and P. Saxe, *Phys. Rev. B* **65**, 104104 (2002).
- [44] X. Wu, D. Vanderbilt, and D. R. Hamann, *Phys. Rev. B* **72**, 035105 (2005).
- [45] H. J. Monkhorst and J. D. Pack, *Phys. Rev. B* **13**, 5188 (1976).
- [46] D. Gao, Q. Xue, X. Mao, W. Wang, Q. Xu, and D. Xue, *J. Mater. Chem. C* **1**, 5909 (2013).
- [47] H. Zhang, L.-M. Liu, and W.-M. Lau, *J. Mater. Chem. A* **1**, 10821 (2013).
- [48] D. C. Freitas, M. Núñez, P. Strobel, A. Sulpice, R. Weht, A. A. Aligia, and M. Núñez-Regueiro, *Phys. Rev. B* **87**, 014420 (2013).
- [49] D. C. Freitas, R. Weht, A. Sulpice, G. Remenyi, P. Strobel, F. Gay, J. Marcus, and M. Núñez-Regueiro, *J. Phys.: Condens. Matter* **27**, 176002 (2015).
- [50] B. E. Brown, *Acta Crystallogr.* **20**, 264 (1966).
- [51] R. F. W. Bader, *Atoms in Molecules: A Quantum Theory*, International Ser. of Monogr. on Chem (Clarendon Press, Oxford, 1994).
- [52] W. Tang, E. Sanville, and G. Henkelman, *J. Phys.: Condens. Matter* **21**, 084204 (2009).
- [53] T. Björkman, A. Gulans, A. V. Krasheninnikov, and R. M. Nieminen, *Phys. Rev. Lett.* **108**, 235502 (2012).
- [54] T. Björkman, A. Gulans, A. V. Krasheninnikov, and R. M. Nieminen, *J. Phys.: Condens. Matter* **24**, 424218 (2012).
- [55] K. Choudhary, I. Kalish, R. Beams, and F. Tavazza, *Sci. Rep.* **7**, 5179 (2017).
- [56] M. Ashton, J. Paul, S. B. Sinnott, and R. G. Hennig, *Phys. Rev. Lett.* **118**, 106101 (2017).
- [57] C. Kittel, *Introduction to Solid State Physics*, 7th ed. (John Wiley & Sons, New York, 1996).
- [58] M. Born and K. Huang, *Dynamical Theory of Crystal Lattices (Oxford Classic Texts in the Physical Sciences)* (Clarendon Press, Oxford, 1998).
- [59] F. Mouhat and F.-X. Coudert, *Phys. Rev. B* **90**, 224104 (2014).
- [60] H. Peelaers and C. G. V. de Walle, *J. Phys. Chem. C* **118**, 12073 (2014).
- [61] J. Feldman, *J. Phys. Chem. Solids* **37**, 1141 (1976).
- [62] S. Lebègue, T. Björkman, M. Klintonberg, R. M. Nieminen, and O. Eriksson, *Phys. Rev. X* **3**, 031002 (2013).
- [63] Y. Zhu, X. Kong, T. D. Rhone, and H. Guo, *Phys. Rev. Mater.* **2**, 081001 (2018).
- [64] C. M. O. Bastos, F. P. Sabino, P. E. F. Junior, T. Campos, J. L. F. D. Silva, and G. M. Sipahi, *Semicond. Sci. Technol.* **31**, 105002 (2016).
- [65] I. G. Lezama, A. Ubaldini, M. Longobardi, E. Giannini, C. Renner, A. B. Kuzmenko, and A. F. Morpurgo, *2D Mater.* **1**, 021002 (2014).
- [66] K. K. Kam and B. A. Parkinson, *J. Phys. Chem.* **86**, 463 (1982).

4 CONCLUSIONS AND PERSPECTIVES

Each paper showed a specific conclusion of each subproject of this PhD project. Here, we make a brief review and general conclusion of the project.

We have defined a framework that combines two main methods in the electronic calculation: DFT and $\mathbf{k}\cdot\mathbf{p}$ methods. In order to obtain a realistic band structure, we modified the internal parameters values of the hybrid functional HSE, using a fitting procedure of the functional parameter, that we called (HSE_α). We have also shown that, the adjusted functional does not play an important role for the structural parameters (lattice parameters and elastic properties) leading to results in good agreement with the experimental values, but very similar to the ones obtained with another version of the functional (HSE06). Its role in the description of the electronic properties (like the band gap and spin-orbital splitting) is fundamental, however, and enhances the accuracy of the description of E_{gap} and Δ_{so} when compared with previous papers.^{55,56} With a realistic band structure evaluate from hybrid-DFT, we applied a fitting method developed in this project to determine the accurate $\mathbf{k}\cdot\mathbf{p}$ parameters, obtaining from them effective masses and the g-factors beyond the parabolic model. For the antimonides and Indium compounds, we observed, in specific directions, large deviations of the g-factors from the experimental results indicating that the 8×8 $\mathbf{k}\cdot\mathbf{p}$ Hamiltonian may still not be adequate for describing systems with small band gap and/or large spin-orbit splittings.

We also applied this same framework to a new class of materials, TMDs. We investigated the magnetic order, structural and electronic properties for 81 of such materials in order to identify new semiconductor materials. We studied the relative stability of them, determining the more stable phases, lattice parameters, elastic constants, and the electronic band structure. Using the latter, we classified the TMDs as semiconductors, semimetals and metals. We also identified an important trend between exfoliation energy* and Bader charge, i.e., the charge transfer between metal and chalcogen. We showed that, for some TMDs, the effect of the Coulomb repulsion between layers can have the same importance as the Van der Waals correction. Due to requirements of the development of a new $\mathbf{k}\cdot\mathbf{p}$ Hamiltonian for TMDs, we have not extracted the $\mathbf{k}\cdot\mathbf{p}$ parameters. However, an extensively work was presented in this subproject, that, since a $\mathbf{k}\cdot\mathbf{p}$ Hamiltonian is defined for TMDs would allow to obtain the $\mathbf{k}\cdot\mathbf{p}$ parameters.

Therefore, we showed that the framework combining the hybrid-DFT calculations and the $\mathbf{k}\cdot\mathbf{p}$ method is a powerful tool to improve the agreement between experimental and theoretical results. Also, using this framework, as $\mathbf{k}\cdot\mathbf{p}$ method calculations presents similar result as as the much costlier Hybrid-DFT calculations, one could reduce the computational

* Energy required to isolate an one layer

cost of determining the properties of larger systems involving a wide number of atoms, as nanowires and quantum dots, by using the DFT obtained parameters in $\mathbf{k}\cdot\mathbf{p}$ Hamiltonians. Moreover, the framework can be used in the proposal of new $\mathbf{k}\cdot\mathbf{p}$ Hamiltonians, showing a consistent performance to obtain the $\mathbf{k}\cdot\mathbf{p}$ parameters.

Finally, the framework can be used to review $\mathbf{k}\cdot\mathbf{p}$ Hamiltonians present in the literature or Hamiltonians which include amore physical effects, e.g., the 14 bands $\mathbf{k}\cdot\mathbf{p}$ Hamiltonian for III-V semiconductor, that correctly describes degeneracy break in the band structure out of the Γ point. The same framework can be used to study the inclusion of these new effects, analyzing the stability of the $\mathbf{k}\cdot\mathbf{p}$ parameters and non-parabolic regions, among others. Therefore, the new fitting method, framework and computational tools proposed and developed in this PhD project will help to increase our understanding of the semiconductor physics and will be auxiliary in the development of new semiconductor devices.

REFERENCES

- 1 RIDEOUT, V. A review of the theory, technology and applications of metal-semiconductor rectifiers. **Thin Solid Films**, Elsevier BV, v. 48, n. 3, p. 261–291, 1978.
- 2 MORRISON, P. **A history of the world semi-conductor industry**. London: The Institution of Engineering and Technology, 1989.
- 3 ENDERLEIN, R. **Fundamentals of semiconductor physics and devices**. Singapore: World Scientific, 1997.
- 4 ROGALSKI, A. **Infrared detectors**, 2nd. ed. New York: CRC Press, 2010.
- 5 SCHUBERT, E. F. **Light emitting diodes**. 2nd. ed. Cambridge: Cambridge University Press, 2006.
- 6 NAKAMURA, S. Nobel lecture: Background story of the invention of efficient blue ingan light emitting diodes. **Review Modern Physics**, American Physical Society, v. 87, p. 1139–1151, out. 2015.
- 7 ESSIG, S.; STEINER, M. A.; ALLEBE, C.; GEISZ, J. F.; PAVIET-SALOMON, B.; WARD, S.; DESCOEUDRES, A.; LASALVIA, V.; BARRAUD, L.; BADEL, N.; FAES, A.; LEVRAT, J.; DESPEISSE, M.; BALLIF, C.; STRADINS, P.; YOUNG, D. L. Realization of GaInP/si dual-junction solar cells with 29.8% 1-sun efficiency. **IEEE Journal of Photovoltaics**, Institute of Electrical and Electronics Engineers (IEEE), v. 6, n. 4, p. 1012–1019, jul. 2016.
- 8 WONG, J.; JARIWALA, D.; TAGLIABUE, G.; TAT, K.; DAVOYAN, A. R.; SHERROTT, M. C.; ATWATER, H. A. High photovoltaic quantum efficiency in ultrathin van der waals heterostructures. **ACS Nano**, American Chemical Society (ACS), v. 11, n. 7, p. 7230–7240, jun. 2017.
- 9 ZUTIC, I.; FABIAN, J.; SARMA, S. D. Spintronics: fundamentals and applications. **Review Modern Physics**., American Physical Society, v. 76, p. 323–410, abr. 2004.
- 10 CHUANG, P.; HO, S.-C.; SMITH, L. W.; SFIGAKIS, F.; PEPPER, M.; CHEN, C.-H.; FAN, J.-C.; GRIFFITHS, J. P.; FARRER, I.; BEERE, H. E.; JONES, G. A. C.; RITCHIE, D. A.; CHEN, T.-M. All-electric all-semiconductor spin field-effect transistors. **Nature Nanotechnology**, Springer Science and Business Media LLC, v. 10, n. 1, p. 35–39, dez. 2014.
- 11 KITTEL, C. **Introduction to solid state physics**. 8th. ed. New York: Wiley, 2004.
- 12 ASHCROFT, N. W.; MERMIN, N. M. **Solid state physics**. [S.l.]: Holt-Saunders International Editions, 1976.
- 13 YU, P. Y.; CARDONA, M. **Fundamentals of semiconductors**. 2nd. ed. Berlin: Spinger-Verlag, 1999.

- 14 HULLIGER, F.; LÉVY, F. **Structural chemistry of layer-type phases**. Netherlands: Springer, 1977. (Physics and Chemistry of Materials with Layered Structures 5).
- 15 RAHMANPOUR, P.; SALID, S.; HOVD, M. Run-to-run control of the czochralski process. **Computers & Chemical Engineering**, Elsevier BV, v. 104, p. 353–365, set. 2017.
- 16 JONES, A. C.; HITCHMAN, M. L. (Ed.). Overview of chemical vapour deposition. In: _____ **Chemical vapour deposition**. Cambridge: Royal Society of Chemistry, 2009. cap. 1, p. 1–36.
- 17 ORTON, J.; FOXON, T. **Molecular beam epitaxy**. Oxford: Oxford University Press, 2015.
- 18 LEMITI, M. **Crystal growth of Si for solar cells**. Berlin: Springer Verlag, 2009.
- 19 MOURIK, V.; ZUO, K.; FROLOV, S. M.; PLISSARD, S. R.; BAKKERS, E. P. A. M.; KOUWENHOVEN, L. P. Signatures of majorana fermions in hybrid superconductor-semiconductor nanowire devices. **Science**, American Association for the Advancement of Science (AAAS), v. 336, n. 6084, p. 1003–1007, abr. 2012.
- 20 HASAN, M. Z.; KANE, C. L. Colloquium: Topological insulators. **Review Modern Physics**, American Physical Society (APS), v. 82, n. 4, p. 3045–3067, nov. 2010.
- 21 ZHANG, D.; LOU, W.; MIAO, M.; ZHANG, S. C.; CHANG, K. Interface-induced topological insulator transition in GaAs / Ge / GaAs quantum wells. **Physical Review Letter**, American Physical Society (APS), v. 111, n. 15, p. 156402, out. 2013.
- 22 SUN, Q.; DAI, Y.; NIU, C.; MA, Y.; WEI, W.; YU, L.; HUANG, B. Lateral topological crystalline insulator heterostructure. **2D Materials**, IOP Publishing, v. 4, n. 2, p. 025038, fev. 2017.
- 23 PERDEW, J. P.; ERNZERHOF, M.; BURKE, K. Rationale for mixing exact exchange with density functional approximations. **The Journal of Chemical Physics**, AIP Publishing, v. 105, n. 22, p. 9982–9985, 1996.
- 24 ADAMO, C.; BARONE, V. Toward reliable density functional methods without adjustable parameters: The PBE0 model. **Journal of Chemical Physics**, v. 110, p. 6158, 1999.
- 25 HEYD, J.; SCUSERIA, G. E.; ERNZERHOF, M. Hybrid functionals based on a screened coulomb potential. **The Journal of Chemical Physics**, AIP Publishing, v. 118, n. 18, p. 8207–8215, 2003.
- 26 _____. Erratum: “Hybrid functionals based on a screened coulomb potential” [J. Chem. Phys. 118, 8207 (2003)]. **The Journal of Chemical Physics**, AIP Publishing, v. 124, n. 21, p. 219906, 2006.
- 27 BECKE, A. D. Density-functional thermochemistry. III. the role of exact exchange. **The Journal of Chemical Physics**, AIP Publishing, v. 98, n. 7, p. 5648–5652, 1993.

-
- 28 BASTOS, C. M. O.; SABINO, F. P.; JUNIOR, P. E. F.; CAMPOS, T.; SILVA, J. L. F. D.; SIPAHI, G. M. Stability and accuracy control of $k \cdot p$ parameters. **Semiconductor Science and Technology**, IOP Publishing, v. 31, n. 10, p. 105002, Sept. 2016.
- 29 GEIM, A. K.; GRIGORIEVA, I. V. Van der Waals heterostructures. **Nature**, Nature Publishing Group, v. 499, n. 7459, p. 419–425, jul. 2013.
- 30 GEIM, A. K.; NOVOSELOV, K. S. The rise of graphene. **Nature Materials**, Springer Science and Business Media LLC, v. 6, n. 3, p. 183–191, mar. 2007.
- 31 JARIWALA, D.; SANGWAN, V. K.; LAUHON, L. J.; MARKS, T. J.; HERSAM, M. C. Emerging device applications for semiconducting two-dimensional transition metal dichalcogenides. **ACS Nano**, American Chemical Society (ACS), v. 8, n. 2, p. 1102–1120, jan. 2014.
- 32 KOLOBOV, A. V.; TOMINAGA, J. **Two-dimensional transition-metal dichalcogenides**. Switzerland: Springer International Publishing, 2016.
- 33 CHOI, W.; CHOUDHARY, N.; HAN, G. H.; PARK, J.; AKINWANDE, D.; LEE, Y. H. Recent development of two-dimensional transition metal dichalcogenides and their applications. **Materials Today**, Elsevier BV, v. 20, n. 3, p. 116–130, abr. 2017.
- 34 ZHOU, J.; QIN, J.; ZHANG, X.; SHI, C.; LIU, E.; LI, J.; ZHAO, N.; HE, C. 2d space-confined synthesis of few-layer MoS₂ anchored on carbon nanosheet for lithium-ion battery anode. **ACS Nano**, American Chemical Society (ACS), v. 9, n. 4, p. 3837–3848, mar. 2015.
- 35 DONARELLI, M.; PREZIOSO, S.; PERROZZI, F.; BISTI, F.; NARDONE, M.; GIANCATERINI, L.; CANTALINI, C.; OTTAVIANO, L. Response to NO₂ and other gases of resistive chemically exfoliated MoS₂-based gas sensors. **Sensors and Actuators B**, Elsevier BV, v. 207, p. 602–613, fev. 2015.
- 36 LEE, C.-H.; LEE, G.-H.; ZANDE, A. M. van der; CHEN, W.; LI, Y.; HAN, M.; CUI, X.; AREFE, G.; NUCKOLLS, C.; HEINZ, T. F.; GUO, J.; HONE, J.; KIM, P. Atomically thin p–n junctions with van der waals heterointerfaces. **Nature Nanotechnology**, Springer Science and Business Media LLC, v. 9, n. 9, p. 676–681, ago. 2014.
- 37 NARAYANAN, T. N.; VUSA, C. S. R.; ALWARAPPAN, S. Selective and efficient electrochemical biosensing of ultrathin molybdenum disulfide sheets. **Nanotechnology**, IOP Publishing, v. 25, n. 33, p. 335702, jul. 2014.
- 38 CHENG, R.; JIANG, S.; CHEN, Y.; LIU, Y.; WEISS, N.; CHENG, H.-C.; WU, H.; HUANG, Y.; DUAN, X. Few-layer molybdenum disulfide transistors and circuits for high-speed flexible electronics. **Nature Communications**, Springer Science and Business Media LLC, v. 5, n. 1, out. 2014.
- 39 LIM, H.; YOON, S. I.; KIM, G.; JANG, A.-R.; SHIN, H. S. Stacking of two-dimensional materials in lateral and vertical directions. **Chemistry of Materials**, American Chemical Society (ACS), v. 26, n. 17, p. 4891–4903, set. 2014.
- 40 ENGEL, E.; DREIZLER, R. M. **Density functional theory**. Berlin: Springer Verlag, 2011.

- 41 DRESSELHAUS, M. S. **Group theory**: application to the physics of condensed matter. Berlin: Springer, 2008.
- 42 HOHENBERG, P.; KOHN, W. Inhomogeneous Electron Gas. **Physical Review**, American Physical Society (APS), v. 136, n. 3B, p. B864–B871, nov. 1964.
- 43 KOHN, W.; SHAM, L. J. Self-consistent equations including exchange and correlation effects. **Physical Review**, American Physical Society (APS), v. 140, n. 4A, p. A1133–A1138, nov. 1965.
- 44 PERDEW, J. P.; WANG, Y. Accurate and simple analytic representation of the electron-gas correlation energy. **Physical Review B**, American Physical Society (APS), v. 45, n. 23, p. 13244–13249, jun. 1992.
- 45 PERDEW, J. P.; BURKE, K.; ERNZERHOF, M. Generalized gradient approximation made simple. **Physical Review Letter**, American Physical Society (APS), v. 77, n. 18, p. 3865–3868, out. 1996.
- 46 PERDEW, J. P.; ZUNGER, A. Self-interaction correction to density-functional approximations for many-electron systems. **Physical Review B**, American Physical Society (APS), v. 23, n. 10, p. 5048–5079, maio 1981.
- 47 HEYD, J.; SCUSERIA, G. E. Efficient hybrid density functional calculations in solids: Assessment of the Heyd-Scuseria-Ernzerhof screened coulomb hybrid functional. **The Journal of Chemical Physics**, AIP Publishing, v. 121, n. 3, p. 1187–1192, jul. 2004.
- 48 KRUKAU, A. V.; VYDROV, O. A.; IZMAYLOV, A. F.; SCUSERIA, G. E. Influence of the exchange screening parameter on the performance of screened hybrid functionals. **The Journal of Chemical Physics**, AIP Publishing, v. 125, n. 22, p. 224106, dez. 2006.
- 49 KRESSE, G.; HAFNER, J. Ab initio molecular dynamics for open-shell transition metals. **Physical Review B**, American Physical Society, v. 48, p. 13115–13118, nov. 1993.
- 50 KRESSE, G.; FURTHMÜLLER, J. Efficient iterative schemes for ab initio total-energy calculations using a plane-wave basis set. **Physical Review B**, American Physical Society, v. 54, p. 11169–11186, out. 1996.
- 51 BLÖCHL, P. E. Projector augmented-wave method. **Physical Review B**, American Physical Society, v. 50, p. 17953–17979, dez. 1994.
- 52 HAFNER, J. Ab-initio simulations of materials using VASP: density-functional theory and beyond. **Journal of Computational Chemistry**, Wiley, v. 29, n. 13, p. 2044–2078, out. 2008.
- 53 OLIPHANT, T. E. **A guide to NumPy**. [S.l.]: Trelgol Publishing USA, 2006. v. 1.
- 54 NEWVILLE, M.; STENSITZKI, T.; ALLEN, D. B.; INGARGIOLA, A. **LMFIT: non-linear least-square minimization and curve-fitting for python**. 2014. Available at: <<https://zenodo.org/record/11813#.XbBHBuhKiM8>>. Accessed on: Oct.21, 2019.

- 55 KIM, Y.-S.; HUMMER, K.; KRESSE, G. Accurate band structures and effective masses for InP, InAs, and InSb using hybrid functionals. **Physical Review B**, v. 80, n. 3, p. 035203, jul. 2009.
- 56 KIM, Y.-S.; MARSMAN, M.; KRESSE, G.; TRAN, F.; BLAHA, P. Towards efficient band structure and effective mass calculations for III-v direct band-gap semiconductors. **Physical Review B**, American Physical Society (APS), v. 82, n. 20, p. 205212, nov. 2010.

Appendix

APPENDIX A – COLLABORATION PUBLISHED PAPERS

Realistic multiband $k \cdot p$ approach from *ab initio* and spin-orbit coupling effects of InAs and InP in wurtzite phase

Paulo E. Faria Junior,^{1,*} Tiago Campos,^{1,2} Carlos M. O. Bastos,¹ Martin Gmitra,² Jaroslav Fabian,² and Guilherme M. Sipahi^{1,3}

¹São Carlos Institute of Physics, University of São Paulo, 13566-590 São Carlos, São Paulo, Brazil

²Institute for Theoretical Physics, University of Regensburg, 93040 Regensburg, Germany

³Department of Physics, State University of New York at Buffalo, Buffalo, New York 14260, USA

(Received 20 April 2016; published 30 June 2016)

Semiconductor nanowires based on non-nitride III-V compounds can be synthesized under certain growth conditions to favor the appearance of the wurtzite crystal phase. Despite reports in the literature of *ab initio* band structures for these wurtzite compounds, we still lack effective multiband models and parameter sets that can be simply used to investigate physical properties of such systems, for instance, under quantum confinement effects. In order to address this deficiency, in this study we calculate the *ab initio* band structure of bulk InAs and InP in the wurtzite phase and develop an $8 \times 8 k \cdot p$ Hamiltonian to describe the energy bands around the Γ point. We show that our $k \cdot p$ model is robust and can be fitted to describe the important features of the *ab initio* band structure. The correct description of the spin-splitting effects that arise due to the lack of inversion symmetry in wurtzite crystals is obtained with the k -dependent spin-orbit term in the Hamiltonian, often neglected in the literature. All the energy bands display a Rashba-like spin texture for the in-plane spin expectation value. We also provide the density of states and the carrier density as functions of the Fermi energy. Alternatively, we show an analytical description of the conduction band, valid close to the Γ point. The same fitting procedure is applied to the 6×6 valence band Hamiltonian. However, we find that the most reliable approach is the $8 \times 8 k \cdot p$ Hamiltonian for both compounds. The $k \cdot p$ Hamiltonians and parameter sets that we develop in this paper provide a reliable theoretical framework that can be easily applied to investigate electronic, transport, optical, and spin properties of InAs- and InP-based nanostructures.

DOI: [10.1103/PhysRevB.93.235204](https://doi.org/10.1103/PhysRevB.93.235204)

I. INTRODUCTION

In the past decade, the development of low-dimensional III-V semiconductor nanostructures has witnessed great advances [1]. For instance, one interesting feature that was observed in the synthesis of III-V nanowires is the appearance of the wurtzite (WZ) crystal phase, instead of the usual zinc-blende (ZB) [2]. This created new possibilities of III-V compounds with WZ structure besides the well-established nitride-based materials. Moreover, controlling the growth conditions, e.g., temperature and III/V ratio, it is possible to achieve not only single crystal phase nanowires [3,4] but also to mix ZB and WZ regions with sharp interfaces in the same nanostructure, which is known as polytypism [5–7]. It has been demonstrated that mixed phases greatly affect the physical properties, for example, of the light polarization [8–10], electron transport [11,12], and photoconductivity [13].

Among these new III-V compounds with WZ structure, InAs and InP are particularly important. InAs WZ has a large spin-orbit coupling (SOC) which favors the study of spin-related phenomena, for instance, spin field effect transistors [14], and the search for the elusive Majorana fermions [15]. Also, InAs WZ shows remarkable piezoelectric and piezoresistive properties [16] that, combined with the InAs narrow band gap, can operate in the near-infrared regime. On the other hand, InP is a promising candidate for photovoltaic applications [17] and for enhancing the efficiency of solar cells [18]. In fact, a silicon-integrated nanolaser

of InP nanowire has already been demonstrated at room temperature with a wide wavelength range due to the WZ/ZB polytypism [19]. Furthermore, it is also possible to combine InAs and InP WZ compounds in axial [20] and radial [21] heterostructures, which opens the path for novel opportunities in band gap engineering.

Theoretical studies based on WZ III-V compounds including InAs and InP were reported using different *ab initio* approaches. The main focus of these studies was the determination of the lattice parameters, band gaps, and SOC energy splittings in the valence band [22–27]. Of these references, De and Pryor [23] provide useful information that can be used in effective models, such as the effective masses and the spin-splitting parameters. The issue of using these parameters is that they are only valid in the immediate vicinity of the Γ point [$\sim 2\%$ of the first Brillouin zone (FBZ)], limiting the range of physical phenomena that can be investigated. In order to achieve a better description farther away from the Γ point, a multiband effective model is desirable. Although $k \cdot p$ models and parameters are well established for WZ III-nitride compounds [28,29], there are only a few reports in the literature for non-nitrides, such as InP [10,30] and GaAs [31].

In this study, we develop a robust $8 \times 8 k \cdot p$ Hamiltonian to describe the *ab initio* band structure calculated by WIEN2k [32] of InAs and InP in the WZ phase. We show that our fitted parameters reproduce the *ab initio* band structure, capturing the important anticrossings and spin-splitting features up to 1.0 nm^{-1} ($\sim 10\%$ of the FBZ in the $k_x k_y$ plane and $\sim 22\%$ in the k_z direction). At Γ point, each band is twofold degenerate and for the valence band we found that the band ordering, from top to bottom, is HH (heavy hole), CH

*fariajunior.pe@gmail.com

(crystal field split-off hole), and LH (light hole) for InAs and HH, LH, and CH for InP. This ordering is due to an interplay of SOC energy splittings and the crystal field energy splitting. The intricate behavior of spin splittings, arising from the bulk inversion asymmetry (BIA) of the WZ structure, is correctly described by the k -dependent SOC term, often neglected in the literature. Calculating the spin expectation value for the Bloch states, we find a Rashba-like spin texture [33] with either clockwise (CW) or counterclockwise (CCW) orientation. All these spin-dependent features extracted from our $k \cdot p$ Hamiltonian and parameter sets were systematically checked to agree with *ab initio* calculations. Furthermore, based on our effective 8×8 Hamiltonian, we calculated the density of states (DOS) and predict the carrier density as a function of the Fermi energy. We also provide an analytical description of the conduction band valid close to the Γ point and a compact description of the valence band (6×6 Hamiltonian). But, we would like to emphasize that the best description of InAs and InP WZ is obtained using the total 8×8 Hamiltonian. In summary, the main goal of our paper is to provide a realistic $k \cdot p$ description that can be used to study charge and spin transport, optics, as well as (superconducting) proximity effects in semiconductor heterostructures, e.g., quantum wells and wires. Such heterostructures cannot be investigated by first principles due to their mesoscopic sizes, and the $k \cdot p$ technique (using the prescription $k \rightarrow -i\nabla$) is currently perhaps the best choice for obtaining physically relevant quantities for them.

This paper is organized as follows: In Sec. II we present the *ab initio* band structure of InAs and InP WZ. The multiband $k \cdot p$ model and its considerations are discussed in Sec. III. In Sec. IV, we describe our main results: (i) the fitting approach, (ii) the comparison between the *ab initio* and $k \cdot p$ for band structure and the spin splittings, (iii) the spin expectation value for all energy bands, and (iv) the DOS extracted from the 8×8 Hamiltonian. The analytical description of the conduction band (CB) close to the Γ point is presented in Sec. V, and the compact form of the valence Hamiltonian, along with its parameters, is shown in Sec. VI. Finally, in Sec. VII we present our conclusions and possible direct applications of our effective multiband model.

II. AB INITIO BAND STRUCTURE

The *ab initio* electronic structure for InAs and InP in the WZ phase was calculated within the density functional theory (DFT) framework [34], using the full potential linearized augmented plane wave method implemented by the WIEN2k code [32]. To account for local and semilocal functional deficiencies to correctly describe band gaps in semiconductors, we used an efficient and accurate alternative for electronic structure calculations based on the modified Becke-Johnson (mBJ) exchange potential [35] with LDA (local density approximation) correlation [36]. It has been shown that the semilocal mBJ exchange potential provides prediction of band gaps of the same order [37–39] as hybrid functionals [40] and the GW method [41–43]. In addition, the semilocal approach to the exchange-correlation functional is barely expensive when compared to the LDA [44] or the generalized gradient approximation [45]. The SOC is included within

the second variational step [46]. Regarding the technical details of our calculations, we expanded the wave functions in atomic spheres for orbital quantum numbers up to 10; the plane wave cutoff multiplied with the smallest atomic radii equals 10 and the irreducible Brillouin zone was sampled with 600 k points. Further details on *ab initio* calculations of III-V semiconductors, either with ZB or WZ structure, using the mBJ potential can be found in Ref. [47].

The particular order of cation (In) and anions (As, P) within the unit cell determines spin orientation [49]. We consider the following primitive basis vectors for corresponding hexagonal Bravais lattice, $\vec{a}_1 = a(\sqrt{3}, -1, 0)/2$, $\vec{a}_2 = a(0, 1, 0)$, and $\vec{a}_3 = c(0, 0, 1)$, where a and c are the WZ lattice parameters. Using the three basis vectors \vec{a}_i ($i = 1, 2, 3$) we define the following four atomic positions that form the WZ structure: $(2/3, 1/3, u)$ and $(1/3, 2/3, 1/2 + u)$, with $u = 0$ for anion and $u = 3/8$ for cation. We note that in general there might be $u = 3/8 + \epsilon$ with a small dimensionless cell-internal structural parameter ϵ describing a deviation from ideal tetrahedrons as one observes for SiC polytypes [50]. In our calculations we considered $\epsilon = 0$ since it is a rather small valued parameter [25, 51]. For the lattice parameters we considered $a = 4.2742 \text{ \AA}$ and $c = 7.025 \text{ \AA}$ [52] for InAs and $a = 4.1148 \text{ \AA}$ and $c = 6.7515 \text{ \AA}$ [53] for InP.

We show the band structures obtained with WIEN2k in Fig. 1(a) for InAs and Fig. 1(b) for InP. Both compounds show a direct band gap at the Γ point with values of $E_g = 0.467 \text{ eV}$ for InAs and $E_g = 1.494 \text{ eV}$ for InP. Due to the hexagonal

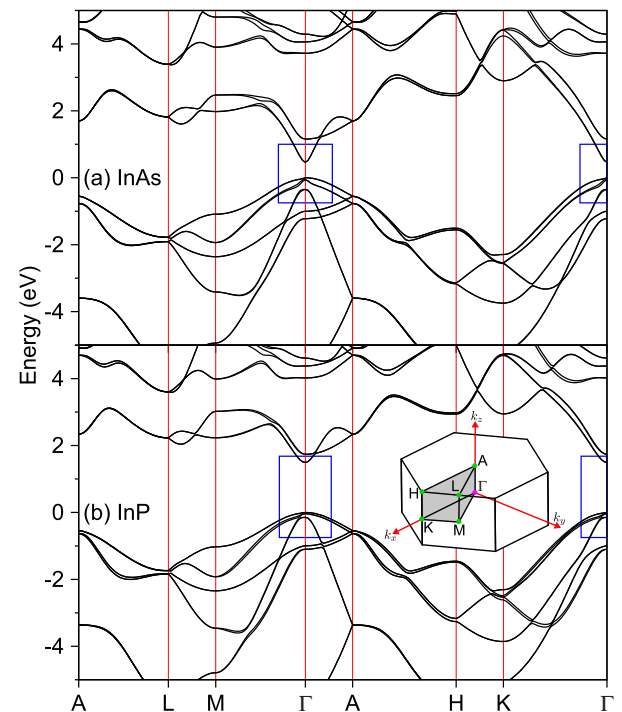


FIG. 1. *Ab initio* band structure along high-symmetry lines for (a) InAs and (b) InP in WZ phase. The inset shows the FBZ of WZ structure indicating the high-symmetry points. The rectangles highlight the region of interest around the Γ point.

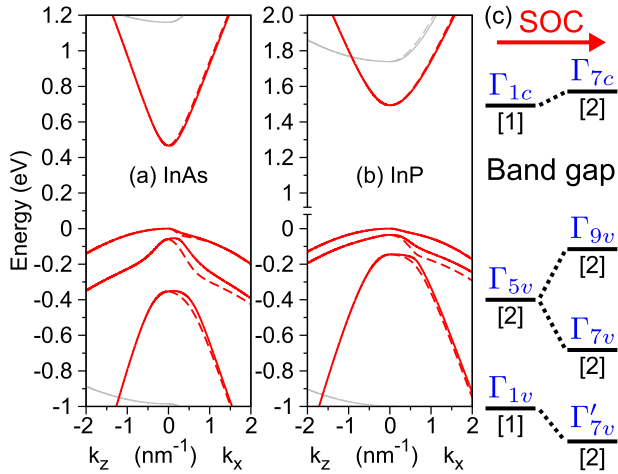


FIG. 2. Band structure for WZ (a) InAs and (b) InP around Γ point for k_z (Γ -A) and k_x (Γ -K) directions. The solid lines indicate the outer branch and the dashed lines indicate the inner branch of the spin-split bands. The thin (gray) lines indicate the energy bands outside our range of interest. (c) Change in the irreducible representations of energy bands at Γ point under SOC. The subscripts v and c added to the irreducible representations indicate valence and conduction bands, respectively, and the prime distinguishes between the two possibilities of Γ_7 . The numbers in square brackets are the degeneracy of the bands. Our notation for the irreducible representations follows Ref. [48].

symmetry of WZ, the Γ point, as well as the symmetry line connecting Γ -A (hexagonal axis), belongs to the C_{6v} symmetry group [54], which has only two-dimensional double-group representations. From this follows that the states along the hexagonal axis are spin degenerate [54,55]. Irreducible representations of other points in the FBZ compatible with spin are singly degenerate. Hence, except for accidental or time-reversal degeneracies at Γ and A points, spin splittings must occur for all bands.

In Figs. 2(a), for InAs, and 2(b), for InP, we display the rectangular regions of Fig. 1, i.e., a zoom of the band structure around the Γ point. At this energy range, the anticrossing and spin-splitting features of the band structures are evident. Because of large SOC in InAs, the valence band energy levels are farther apart than InP bands and additional curvatures are present along the k_z direction. For InP the top two valence bands along k_z show similar curvatures and no anticrossing is visible. The effect of SOC in the energy bands at the Γ point is shown schematically in Fig. 2(c). Without SOC, the irreducible representations belong to the simple group, while with SOC, they are referred to as the double group. This distinction is important for $k \cdot p$ perturbative approaches.

We present a comparison between our *ab initio* calculations and other theoretical papers in the literature in Table I. Besides the lattice constants a and c we compare the values of the internal parameter u , the energy gap E_g , and the energy difference between the top valence band Γ_{9v} and the other bands Γ_{7v} and Γ'_{7v} [following the notation of Fig. 2(c)]. These energy differences are defined as $\Delta E_{97} = E(\Gamma_{9v}) - E(\Gamma_{7v})$ and $\Delta E'_{97} = E(\Gamma_{9v}) - E(\Gamma'_{7v})$. It is very common to compare the crystal field splitting energy, Δ_1 , and the SOC energy,

TABLE I. Comparison of theoretical data for InAs and InP in WZ phase. The lattice constants a and c are given in \AA , and u is dimensionless. The band gap, E_g , and the valence band energy differences, ΔE_{97} and $\Delta E'_{97}$, are given in eV.

		a	c	u	E_g	ΔE_{97}	$\Delta E'_{97}$
InAs	This study	4.2742	7.0250	0.37500	0.4670	0.0592	0.3527
	Ref. [23]	4.1505	6.7777	0.37500	0.4810	0.1050	0.4690
	Ref. [25]*	4.2570	6.9894	0.37447	0.4810	0.0573	0.3937
	Ref. [27]	4.2564	7.0046	0.37400	0.4610	0.0700	0.3640
	Ref. [47]	4.2742	7.0250	0.37422	0.4610	0.0660	0.3600
InP	This study	4.1148	6.7515	0.37500	1.4940	0.0354	0.1450
	Ref. [23]	4.2839	6.9955	0.37500	1.4740	0.0630	0.3480
	Ref. [24]	4.1500	6.9120	0.37100	1.4936	0.0450	0.2430
	Ref. [25] ^a	4.1148	6.7515	0.37458	1.5760	0.0321	0.1339

^aThe values of a , c , and u are from Ref. [53].

Δ_{SO} ; however, these parameters are usually obtained under the quasicubic approximation and do not provide a direct comparison with experiments such as ΔE_{97} and $\Delta E'_{97}$. We can see that all the values obtained by our calculations are within the range of reported data in previous papers. We also compare experimental measurements of the energy gap with our calculated values, shown in Table II. We focused on experimental data obtained by photoluminescence measurements at low temperature of large-diameter nanowires, so that lateral quantum confinement is negligible. For both InAs (despite the reduced set of available data) and InP compounds, our calculated values of the energy gaps are consistent with the experiments. Furthermore, photoluminescence excitation measurements can probe the Γ_{7v} and Γ'_{7v} valence bands and allow us to check our calculated values for ΔE_{97} and $\Delta E'_{97}$ energies. To the best of our knowledge, such experiments are only available for InP. Typical values found for ΔE_{97} and $\Delta E'_{97}$ in InP WZ are 0.044 eV and 0.187 eV in Ref. [9], 0.043 eV and 0.179 eV in Ref. [56], and 0.044 eV and 0.182 eV in Ref. [57]. Our calculated values for InP of $\Delta E_{97} = 0.0354$ eV and

TABLE II. Comparison between theoretical and experimental values of the energy gap. We indicate the temperature of the photoluminescence measurements in parentheses.

	E_g (eV) This study	E_g (eV) Experiment
InAs	0.467	0.520 (7 K) ^a , 0.500 (20 K) ^b 0.458 (5 K) ^c
InP	1.494	1.492 (10 K) ^d , 1.494 (10 K) ^e
		1.490 (20 K) ^f , 1.491 (4 K) ^g
		1.493 (4 K) ^h , 1.488 (6 K) ⁱ

^aReference [60]

^bReference [61]

^cReference [62]

^dReference [57]

^eReference [56]

^fReference [63]

^gReference [3]

^hReference [64]

ⁱReference [9].

$\Delta E'_{g7} = 0.145$ eV (from Table I) are also in good agreement with these experimental trends. For completeness, we provide in Appendix A the calculated values of effective masses around the Γ point.

III. $k \cdot p$ FORMULATION

One alternative approach to *ab initio* band structure calculations is the $k \cdot p$ method. In the $k \cdot p$ approach, the many-body interactions of electrons with nuclei and other electrons are described by an effective potential which has the same periodicity as the Bravais lattice of the crystal [58]. Such periodic property of the potential allows us to use Bloch's theorem for the total wave function. The single-particle Hamiltonian for the periodic part of the Bloch function, $u_{n,\vec{k}}(\vec{r})$, can be written as

$$\mathbf{H} = \underbrace{\frac{p^2}{2m_0} + V(\vec{r})}_{\mathbf{H}_0} + \underbrace{\frac{\hbar}{4m_0^2c^2}[\vec{\nabla}V(\vec{r}) \times \vec{p}] \cdot \vec{\sigma}}_{\mathbf{H}_{SO}} + \underbrace{\frac{\hbar^2k^2}{2m_0}}_{\mathbf{H}_{k2}} + \underbrace{\frac{\hbar}{m_0}\vec{k} \cdot \vec{p}}_{\mathbf{H}_{kp}} + \underbrace{\frac{\hbar^2}{4m_0^2c^2}[\vec{\nabla}V(\vec{r}) \times \vec{k}] \cdot \vec{\sigma}}_{\mathbf{H}_{kSO}}, \quad (1)$$

in which the different terms in the Hamiltonian are identified for convenience.

We can solve the above equation perturbatively expanding the functions $u_{n,\vec{k}}(\vec{r})$ around a specific reciprocal space point for which we know the solutions for the Hamiltonian. Since WZ InAs and InP have a direct band gap at the Γ point, this is the chosen expansion point. The perturbative technique we use in this paper is Löwdin's formalism [59]. In this approach, the functions at the Γ point, i.e., the basis set to expand $u_{n,\vec{k}}(\vec{r})$, are divided into classes A and B. The energy bands we are interested in describing comprise the class A while the other energy bands belong to class B. The contribution of states in class B appear in second or higher orders of perturbation. The matrix elements we consider can arise from first- or second-order perturbation, reading as

$$H_{f,\alpha\alpha'}^{(1)} = \langle \alpha | \mathbf{H}_f | \alpha' \rangle \quad (2)$$

and

$$H_{fg,\alpha\alpha'}^{(2)} = \sum_{\beta}^B \frac{\langle \alpha | \mathbf{H}_f | \beta \rangle \langle \beta | \mathbf{H}_g | \alpha' \rangle}{E_{\alpha\alpha'} - E_{\beta}}, \quad (3)$$

where \mathbf{H}_f and \mathbf{H}_g can be any of the terms of Eq. (1), except \mathbf{H}_0 .

Since the unperturbed term, \mathbf{H}_0 , in Eq. (1) does not contain SOC effects explicitly, we consider the simple group description of the energy bands, the most usual approach in the literature [65]. Under such approximation, the states in class A belong to the irreducible representations shown on the left side of Fig. 2(c), a 4-dimensional Hilbert space, combined with the spin-1/2 angular momentum, a 2-dimensional Hilbert space. Therefore, the 8-dimensional basis set for the $k \cdot p$

Hamiltonian in Dirac notation [66] is given by

$$\begin{aligned} |c_1\rangle &= -\frac{|\Gamma_{5v}^x + i\Gamma_{5v}^y\rangle\uparrow}{\sqrt{2}}, & |c_5\rangle &= -\frac{|\Gamma_{5v}^x + i\Gamma_{5v}^y\rangle\downarrow}{\sqrt{2}}, \\ |c_2\rangle &= \frac{|\Gamma_{5v}^x - i\Gamma_{5v}^y\rangle\uparrow}{\sqrt{2}}, & |c_6\rangle &= |\Gamma_{1v}\downarrow\rangle, \\ |c_3\rangle &= |\Gamma_{1v}\uparrow\rangle, & |c_7\rangle &= i|\Gamma_{1c}\uparrow\rangle, \\ |c_4\rangle &= \frac{|\Gamma_{5v}^x - i\Gamma_{5v}^y\rangle\downarrow}{\sqrt{2}}, & |c_8\rangle &= i|\Gamma_{1c}\downarrow\rangle, \end{aligned} \quad (4)$$

with 1–6 representing the valence band states and 7–8 the conduction band states. Since Γ_{5v} is two dimensional, we identified its basis states by $|\Gamma_{5v}^x\rangle \sim x$ and $|\Gamma_{5v}^y\rangle \sim y$. The single arrows (\uparrow, \downarrow) represent the projection of spin up and spin down, eigenvalues of the σ_z Pauli matrix. The states in class B have simple group symmetries $\Gamma_1, \Gamma_3, \Gamma_5$, and Γ_6 , which is the only necessary information to calculate second-order contributions.

To describe the interaction among the energy bands, we consider all terms of Eq. (1) in first-order perturbation and only the term \mathbf{H}_{kp} in second order. Therefore, the total matrix Hamiltonian in the basis set (4) comprises the following terms:

$$H = H_0 + H_{SO}^{(1)} + H_{kp}^{(1)} + H_{kSO}^{(1)} + H_{kp}^{(2)}, \quad (5)$$

with the explicit form of each matrix and the definition of the parameters given in Appendix B.

In Fig. 3 we show schematically the interactions for each term in the total Hamiltonian (5). The Fig. 3(a) represents the unperturbed Hamiltonian without SOC, where states $|c_{1(4)}\rangle$ and $|c_{2(5)}\rangle$ are degenerate for spin up (down). The only terms that couple different spin projections arise from $H_{SO}^{(1)}$ or $H_{kSO}^{(1)}$, Figs. 3(b) and 3(d), respectively. Usually $H_{kSO}^{(1)}$ is neglected in WZ Hamiltonians [28,29,31,67–70]. However, the explicit interactions for nonzero k values are crucial to correctly describe the spin-splitting properties. We included $H_{kSO}^{(1)}$ following the approach of Dresselhaus for ZB [71]. Moreover, the coupling of $H_{SO}^{(1)}$ to other terms provides additional contributions to the spin splitting of energy bands. Besides spin-splitting properties, we want a good description of the band structure curvatures. Such effects can be modeled by linear and quadratic terms of the $H_{kp}^{(1)}$ and $H_{kp}^{(2)}$, Figs. 3(c) and 3(e), respectively. The only term that allows a k -dependent self-interaction of states is $H_{kp}^{(2)}$ which gives the effective mass contribution to our model.

Although the $k \cdot p$ method provides the functional form of the Hamiltonian, the parameters that describe different materials cannot be found by group theory arguments only. In order to calculate the matrix elements we would need the functions at the expansion point and also the periodic potential $V(\vec{r})$. Alternatively, we can directly fit the $k \cdot p$ Hamiltonian to the *ab initio* band structure to extract the parameters [29,31,67,69,72].

IV. NUMERICAL FITTING OF THE 8×8 $k \cdot p$ HAMILTONIAN

We start our fitting approach by calculating the k -independent parameters of the Hamiltonian, i.e., the energy

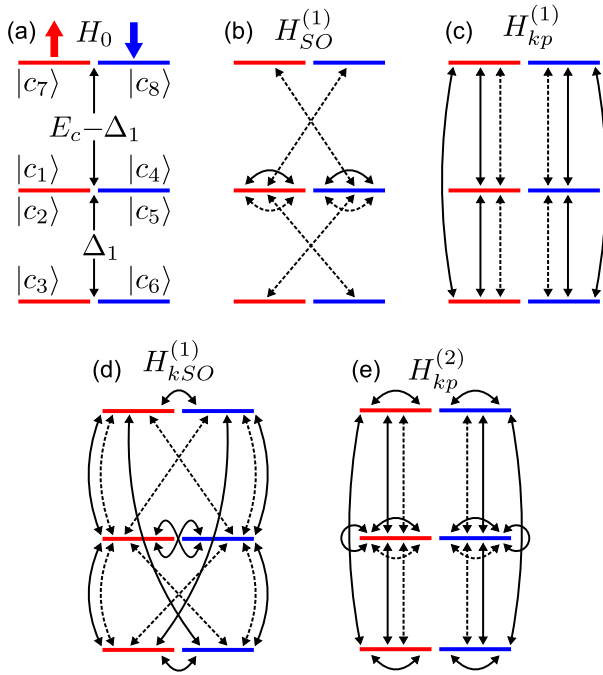


FIG. 3. Possible interactions of the Hamiltonian terms (a) H_0 , (b) $H_{SO}^{(1)}$, (c) $H_{kp}^{(1)}$, (d) $H_{kSO}^{(1)}$, and (e) $H_{kp}^{(2)}$. The arrows on top of panel (a) indicate spin-up and spin-down projections of the basis states. Since $|c_{1(4)}\rangle$ and $|c_{2(5)}\rangle$ are degenerate, we indicate the interactions arising from $|c_{1(4)}\rangle$ with solid lines and the interactions arising from $|c_{2(5)}\rangle$ with dashed lines. For the other states without degeneracy we used solid lines. In panel (a) we show the energy splittings without SOC, formally defined in Appendix B.

splittings. The values for crystal field splitting, Δ_1 , and the conduction band energy, E_c , can be obtained from the *ab initio* calculation without SOC, which is in fact the assumption of the $k \cdot p$ perturbative theory [H_0 term; see Fig. 3(a)]. This approach is very useful because it simplifies the calculation of the SOC energy splittings inside the valence band, Δ_2 (coupling same spins) and Δ_3 (coupling different spins), and the SOC between conduction and valence bands, Δ_4 . Please refer to Appendix B for the formal definition of these splitting energies. By setting the values of Δ_1 and E_c , it is possible to have $\Delta_2 \neq \Delta_3$ and neglect the cubic approximation [28]. If the values of Δ_1 and E_c were not found without SOC, we would have to determine 5 variables having only 3 linear independent combinations of the energy bands with SOC. This approach would provide a range of possible values and further analysis would be necessary. Starting with Δ_1 and E_c values without SOC, we obtained four different solution sets for the SOC splitting energies since Δ_3 and Δ_4 are off-diagonal terms in the Hamiltonian and can assume positive or negative values with the same magnitude. At the Γ point any of these solution sets give the same eigenvalues; therefore we set Δ_3 to be positive [23–25,27] and investigated the effect of positive and negative values of Δ_4 .

Before starting the fitting of the k -dependent parameters, it is important to define the fitting region we are interested in, which is connected to the limits of our $k \cdot p$ model. Basically,

in order to describe as precisely as possible the 8 bands we are interested in, we should stay in a region away from the influence of remote bands, roughly $k \sim 1.5 \text{ nm}^{-1}$; see Figs. 2(a) and 2(b). We also want to have a nice description of the anticrossings in the band structure around $k \sim 0.5 \text{ nm}^{-1}$. Furthermore, in the $k \cdot p$ Hamiltonian k_x and k_y directions are equivalent, but this is not the case for the *ab initio* band structure. Around $k \sim 1.0 \text{ nm}^{-1}$, the *ab initio* band structures along the Γ -K and Γ -M directions are different, especially the spin splitting, which is another feature to be described. Therefore, it is reasonable to set the goal of our fitting at $k = 1.0 \text{ nm}^{-1}$ to find the best parameter set that describes the *ab initio* band structure around the Γ point for all 8 bands.

To increase the accuracy of our parameter sets, we fitted, simultaneously, the energy bands in multiple directions of the FBZ (Γ -K, Γ -M, Γ -A, Γ -H, and Γ -L). The fitting algorithm was developed using the LMFIT [73] package of Python assuming several minimization methods available. We noticed that the minimization methods behave differently and usually provide different parameter sets. After an initial fit, we chose the best parameter set and used it as input for a new fit using all minimization methods again. To find the best fit, the band structures and spin splittings are compared by their residue [74] up to $k = 1.0 \text{ nm}^{-1}$ for all directions. The best parameter sets for InAs and InP found by our fitting approach are presented in Table III.

TABLE III. Parameter sets of the 8×8 Hamiltonian for InAs and InP WZ. The energy splittings are given in eV, linear parameters in eV \AA , and second-order parameters in units of $\hbar^2/2m_0$.

Parameter	InAs	InP
Energy splittings		
Δ_1	0.1003	0.0945
Δ_2	0.1023	0.0279
Δ_3	0.1041	0.0314
Δ_4	0.0388	0.0411
E_c	0.6649	1.6142
Linear parameters		
A_7	-0.4904	-0.1539
P_1	8.3860	7.6349
P_2	6.8987	5.5651
α_1	-0.0189	0.2466
α_2	-0.2892	-0.2223
α_3	-0.5117	-0.2394
β_1	-0.0695	-0.0481
β_2	-0.2171	-0.1386
γ_1	0.5306	0.2485
Second order parameters		
A_1	1.5726	-1.0419
A_2	-1.6521	-0.9645
A_3	-2.6301	-0.0694
A_4	0.5126	-1.2760
A_5	0.1172	-1.1024
A_6	1.3103	-0.5677
e_1	-3.2005	-0.5732
e_2	0.6363	2.4084
B_1	-2.3925	-7.7892
B_2	2.3155	4.3981
B_3	-1.7231	9.1120

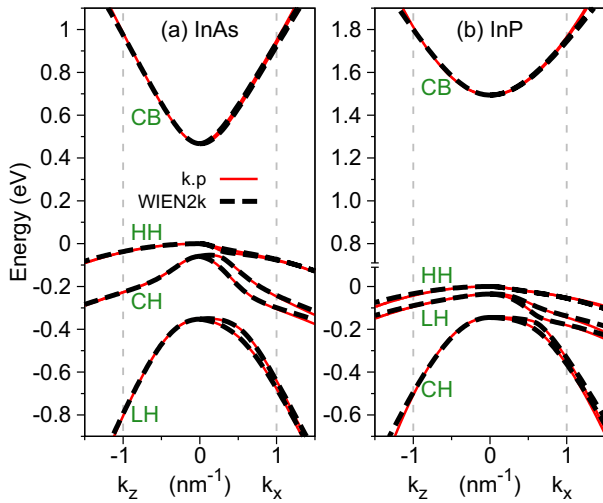


FIG. 4. Comparison of band structures calculated from the fitted $k \cdot p$ model (solid lines) and the *ab initio* WIEN2k (dashed lines) for (a) InAs and (b) InP. The vertical dashed lines at 1.0 nm^{-1} indicate the borders of the fitting range.

In Fig. 4, we present the comparison between the fitted and WIEN2k *ab initio* band structures along k_z and k_x for InAs and InP. All the important features around the Γ point, i.e., anticrossings and spin splittings, are captured by our model. We notice a good agreement up to $k = 1.0 \text{ nm}^{-1}$ with small deviations above it, indicating that we are reaching the region where the influence of remote energy bands becomes important. We labeled the valence bands according to the composition of states at the Γ point. Following Chuang and Chang's notation [75], HH is purely composed of $|c_{1(4)}\rangle$ states, LH has more contribution from $|c_{2(5)}\rangle$ than $|c_{3(6)}\rangle$ states, and CH has more contribution from $|c_{3(6)}\rangle$ than $|c_{2(5)}\rangle$ states. Since this analysis is usually performed without the Δ_4 parameter, we also calculated Δ_2 and Δ_3 considering $\Delta_4 = 0$ and we found that the same labeling holds (these values are shown in Sec. VI). Furthermore, we also compared the $k \cdot p$ composition with the projection to atomic orbitals of the *ab initio* wave functions and the same trends can be noticed. The labeling order of CH-LH in InAs is due to the values of SOC splitting energies, which are slightly larger than the crystal field splitting. For InP, the crystal field splitting is dominant leading to LH-CH ordering. Although this labeling of the valence band can be confusing, it is very useful to extract optical trends from the band-edge transitions. For instance, if we take into account optical transitions arising from the top two valence bands, we can expect InP light polarization to be more in-plane due to LH contribution than InAs due to CH contribution. Finally, for the conduction band of both InAs and InP we simply label it CB, short notation for conduction band; CB is mainly composed of $|c_{7(8)}\rangle$ states.

Let us take a closer look at the spin-splitting properties obtained from the $k \cdot p$ model and the *ab initio*. We show the comparison between the two methods in Fig. 5 for InAs and InP along the k_x direction. Similarly to the band structure, we have a good agreement up to $k = 1.0 \text{ nm}^{-1}$ with deviations above this region. The intricate behaviors, i.e., the appearance of maxima and crossings between HH spin-split bands, are also

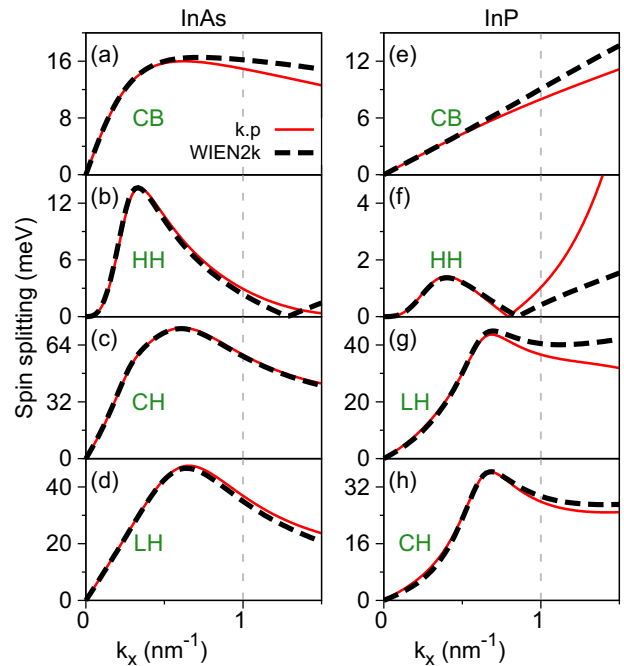


FIG. 5. Comparison of the spin splittings along k_x for the energy bands (a) CB, (b) HH, (c) CH, and (d) LH of InAs and (e) CB, (f) HH, (g) LH, and (h) CH of InP. The line schemes follow Fig. 4.

described by our model. All these spin-splitting characteristics have only one physical origin, the BIA of the WZ structure. The strength of SOC is greater in InAs than InP, visible at the peak values and positions. From the largest to the smallest values of the spin splitting, we have CH (LH), LH (CH), CB, and HH for InAs (InP). Furthermore, a linear behavior is maintained for InP CB throughout the fitting region. For InAs, this linear behavior is attained only in a small region close to the Γ point. In Appendix C, we present the band structure and spin splittings for the other FBZ directions used in the fitting.

Another feature we investigated is the spin orientation, i.e., the spin expectation value, $\langle \vec{\sigma} \rangle$, for the different energy bands, presented in Fig. 6 for the $k_x k_y$ plane ($k_z = 0$). We chose the constant-energy contours to be $E_n(k_x = 0.5 \text{ nm}^{-1}, k_y = 0, k_z = 0)$ of the outer branch, i.e., $E_{CB} \sim 630.0 \text{ meV}$, $E_{HH} \sim -37.2 \text{ meV}$, $E_{CH} \sim -123.0 \text{ meV}$, $E_{LH} \sim -391.8 \text{ meV}$ for InAs and $E_{CB} \sim 1563.5 \text{ meV}$, $E_{HH} \sim -21.9 \text{ meV}$, $E_{LH} \sim -75.0 \text{ meV}$, $E_{CH} \sim -156.7 \text{ meV}$ for InP. We found that all the investigated energy bands show a Rashba-like spin texture. For InAs, the bands CB, HH, and CH have the same spin texture, i.e., CW (CCW) orientation for the inner (outer) branch, while LH has the CCW (CW) orientation for the inner (outer) branch. In other words, the top two valence bands have the same spin texture while the third valence band has the opposite. For InP, the same spin texture holds, even though the labeling of CH and LH is reversed. The spin textures calculated with the $k \cdot p$ model were also checked with the *ab initio* calculations.

Performing the fitting approach with the negative sign of Δ_4 we obtained the same behavior of the band structure and the spin splittings, but with a reversed orientation in the spin texture, i.e., CW orientation becomes CCW and vice versa for

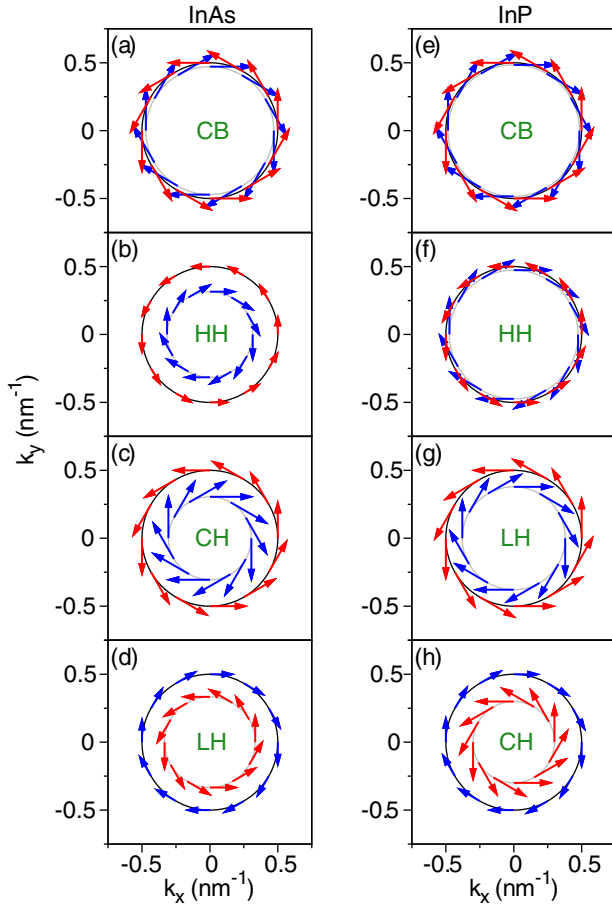


FIG. 6. Spin texture in the $k_x k_y$ plane ($k_z = 0$) for the energy bands (a) CB, (b) HH, (c) CH, and (d) LH of InAs and (e) CB, (f) HH, (g) LH, and (h) CH of InP. The blue arrows indicate clockwise orientation while the red arrows indicate counterclockwise orientation. The amplitudes of all arrows are multiplied by 0.3 to fit the figure. The constant-energy contours are also drawn in the figure in black for the outer branches and in gray for the inner branches.

all bands. Specifically, we found that starting with negative value of Δ_4 , the signs of parameters A_7 , α_1 , α_2 , α_3 , γ_1 , B_1 , B_2 , and B_3 are changed, but not their amplitude. This change in the spin texture is a feature expected from *ab initio* regarding the cation and anion positions within the crystal unit cell [49] and it is reflected in our $k \cdot p$ model and parameters. Therefore, in order to provide reliable parameter sets for $k \cdot p$ Hamiltonians, not only the band structure and the spin splittings should be checked but also the spin orientation. We would like to emphasize that all these features were systematically checked in this study.

A. Density of states and carrier density

Relying on the effective 8×8 $k \cdot p$ Hamiltonian, it is straightforward to calculate a smooth DOS using a fine 3-dimensional (3D) mesh of k points ($300 \times 300 \times 300$) without much computational effort. In Fig. 7(a) we show the DOS for the conduction band of InAs and InP. For comparison, we also

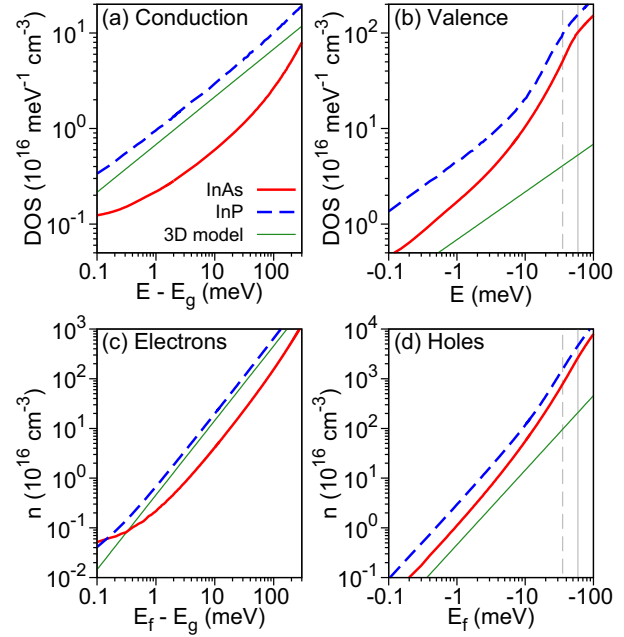


FIG. 7. Calculated DOS for (a) conduction band and (b) valence band of InAs, InP, and the 3D parabolic band model using an effective mass of $m^* = 0.1$. Carrier density, n , as a function of Fermi energy, E_f , for (c) electrons and (d) holes obtained by the integration of the DOS in panels (a) and (b), respectively. The dashed vertical lines in panels (b) and (d) indicate the LH energy at Γ point for InP while the solid vertical lines indicate the CH energy energy at Γ point for InAs.

show the DOS for the 3D parabolic band model [$\text{DOS}(E) \propto \sqrt{E}$], which is just a straight line in the log-log scale. Due to the complex behavior of the InAs and InP conduction bands, we clearly see deviations from the linear behavior, especially for InAs. For the DOS of the valence band, presented in Fig. 7(b), the deviations from the parabolic model are much more visible, showing explicitly the need of a multiband approach. When the valence band energy approaches the CH (LH) region of InAs (InP), the DOS changes its curvature. Moreover, the valence band DOS is approximately one order of magnitude larger than the DOS of the conduction band, a behavior attributed to the small curvatures of the valence bands, i.e., large effective masses for holes (in a single band picture). Integrating the DOS we obtain the carrier density as a function of the Fermi energy, presented in Figs. 7(c) and 7(d) for electrons and holes, respectively. Typically, InP supports larger values of the carrier density than InAs. For instance, for 100 meV above the energy gap $\sim 1.6 \times 10^{18} \text{ cm}^{-3}$ for InAs and $\sim 6.5 \times 10^{18} \text{ cm}^{-3}$. In the Supplemental Material [76] we provide a curve fitting of the carrier density curves that can be directly applied to predict the carrier concentration or the Fermi energy without the explicit DOS calculation using the 8×8 $k \cdot p$ Hamiltonian.

V. ANALYTICAL DESCRIPTION FOR CONDUCTION BAND

Since the conduction band has a predominant contribution of $|c_{7(8)}\rangle$ states, it is useful to provide an analytical description that holds for small regions close to the Γ point that can

be easily used in spin dynamics studies. We apply Löwdin's approach again, but now dividing the basis states A [Eq. (4)] of the full matrix into two new classes A' ($|c_{7,8}\rangle$) and B' ($|c_{1,\dots,6}\rangle$). Using only the terms we already calculated in the full Hamiltonian as contribution to the effective Hamiltonian, this Löwdin approach is usually referred to as folding down [59,68]. The effective Hamiltonian for the first-order folding down, keeping terms up to k^3 , can be written as

$$H_{CB} = M(\vec{k})\mathcal{I}_2 + \vec{\Omega}(\vec{k}) \cdot \vec{\sigma}, \quad (6)$$

in which \mathcal{I}_2 is a 2×2 identity matrix and M is the effective mass term given by

$$M = E_g + m_z k_z^2 + m_{xy}(k_x^2 + k_y^2), \quad (7)$$

with the coefficients m_z and m_{xy} given by

$$\begin{aligned} m_z &= e_1 + \frac{P_1^2}{E_c} + \frac{2\beta_1^2}{E_c - \Delta_1 + \Delta_2} + \frac{2\Delta_4^2(A_1 + A_3)}{(E_c - \Delta_1 + \Delta_2)^2}, \\ m_{xy} &= e_2 + \frac{1}{2} \frac{(P_2 + \beta_1)^2}{E_c - \Delta_1 + \Delta_2} + \frac{1}{2} \frac{(P_2 - \beta_1)^2}{E_c - \Delta_1 - \Delta_2} \\ &\quad + \frac{\beta_2^2}{E_c} + \frac{2\Delta_4^2(A_2 + A_4)}{(E_c - \Delta_1 + \Delta_2)^2}. \end{aligned} \quad (8)$$

The SOC field $\vec{\Omega}(\vec{k})$ is written as

$$\vec{\Omega}(\vec{k}) = [\alpha + \gamma_z k_z^2 + \gamma_{xy}(k_x^2 + k_y^2)] \begin{bmatrix} k_y \\ -k_x \\ 0 \end{bmatrix}, \quad (9)$$

with linear and cubic coefficients given by

$$\begin{aligned} \alpha &= -\gamma_1 + \frac{2\Delta_4(P_2 + \beta_1)}{E_c - \Delta_1 + \Delta_2}, \\ \gamma_z &= 2\sqrt{2}\beta_1 B_3 - \frac{2\beta_2 B_1}{E_c} + \frac{2\Delta_4(P_2 + \beta_1)(A_1 + A_3)}{(E_c - \Delta_1 + \Delta_2)^2}, \\ \gamma_{xy} &= -\frac{2\beta_2 B_2}{E_c} + \frac{2\Delta_4(P_2 + \beta_1)(A_2 + A_4)}{(E_c - \Delta_1 + \Delta_2)^2}. \end{aligned} \quad (10)$$

This analytical approach for the conduction band provides a reasonable description up to 0.2 nm^{-1} for InAs and 0.6 nm^{-1} for InP, which is roughly 100 meV above the energy gap in both cases. The numerical values of m_z , m_{xy} , α , γ_z , and γ_{xy} can be obtained by replacing the parameters with values presented in Table III. Setting the k -dependent SOC parameters γ_1 and β_1 to zero, we recover the analytical linear splitting found in Ref. [68]. Our approach has the advantage of also providing the analytical description of the cubic terms. For additional corrections to the cubic term, it is possible to include higher order terms in the folding-down approach. The comparison to *ab initio* data using the analytical expressions presented in this section can be found in the Supplemental Material [76].

VI. COMPACT DESCRIPTION FOR VALENCE BAND

Because of the coupling from the crystal field and SOC energies, the best simplified description for the valence band is simply neglecting the coupling with the conduction band, thus leading to a 6×6 matrix. It is possible to write this 6×6 Hamiltonian in a compact form using direct products of 3×3 (orbital) and 2×2 (spin) matrices [28,72]. In the basis

set $\{|c_1\rangle, |c_3\rangle, |c_2\rangle, |c_5\rangle, |c_6\rangle, |c_4\rangle\}$, the compact form of valence band is written as

$$\begin{aligned} H_{VB} &= \Delta_1 J_z^2 \mathcal{I}_2 + \Delta_2 J_z \sigma_z + \sqrt{2}\Delta_3 (J_+ \sigma_- + J_- \sigma_+) \\ &\quad + (A_1 \mathcal{I}_3 + A_3 J_z^2) k_z^2 \mathcal{I}_2 + (A_2 \mathcal{I}_3 + A_4 J_z^2) (k_x^2 + k_y^2) \mathcal{I}_2 \\ &\quad - A_5 (J_+^2 k_-^2 + J_-^2 k_+^2) \mathcal{I}_2 \\ &\quad - 2A_6 k_z (\{J_z J_+\} k_- + \{J_z, J_-\} k_+) \mathcal{I}_2 \\ &\quad + iA_7 (J_+ k_- - J_- k_+) \mathcal{I}_2 \\ &\quad + i\sqrt{2}\alpha_1 [\{J_z J_-\} (\sigma_z k_+ - 2\sigma_- k_z) \\ &\quad - \{J_z J_+\} (\sigma_z k_- - 2\sigma_+ k_z)] \\ &\quad + i[(\alpha_3 - \alpha_2) J_z^2 - \alpha_3 \mathcal{I}_3] (\sigma_+ k_- - \sigma_- k_+) \end{aligned} \quad (11)$$

with $\{J_a J_b\} = \frac{1}{2}(J_a J_b + J_b J_a)$, $J_\pm = \frac{1}{\sqrt{2}}(J_x \pm J_y)$, $\sigma_\pm = \frac{1}{2}(\sigma_x \pm \sigma_y)$, and $k_\pm = k_x \pm ik_y$. The definitions of J_x, J_y , and J_z matrices can be found in Appendix A [Eq. (A3)] of Ref. [28]. The matrix \mathcal{I}_n is an n -dimensional identity. The product of 3×3 matrices (A) with 2×2 matrices (a) is defined here as

$$Aa = \begin{bmatrix} a_{11}A & a_{12}A \\ a_{22}A & a_{22}A \end{bmatrix}. \quad (12)$$

To obtain the best parameter sets that describe the *ab initio* band structure, we performed the same fitting approach as described in Sec. IV. We found that, in order to attain the monotonic behavior of the bands, some features of the band structure or the spin splittings are not matched as precisely as the results using the 8×8 Hamiltonian. For instance, the band structures and the spin splittings for InP look reasonable; however, the spin orientation for LH and CH shows opposite trends. For InAs, the spin texture follows the correct behavior; however, the band structure and the spin splittings show the *ab initio* features shifted to higher k values. We show the fitting results for the 6×6 description and the comparison to *ab initio* in the Supplemental Material [76]. The best parameter sets are displayed in Table IV. We would like to emphasize that the

TABLE IV. Parameter sets of the 6×6 valence band Hamiltonian for InAs and InP WZ. The units follow Table III.

Parameter	InAs	InP
Energy splittings		
Δ_1	0.1003	0.0945
Δ_2	0.1038	0.0286
Δ_3	0.1037	0.0310
Linear parameters		
A_7	-0.5565	-0.0917
α_1	-0.0237	0.3309
α_2	-0.0758	-0.0702
α_3	-0.0967	-0.0521
Second order parameters		
A_1	-17.2689	-10.5414
A_2	-1.2047	-1.4542
A_3	16.6637	9.4589
A_4	-7.6202	-3.2741
A_5	-5.9281	3.9468
A_6	-7.3872	-0.2759

most reliable approach is to use the 8×8 Hamiltonian with parameter sets we provide in Sec. IV.

VII. CONCLUSIONS

In this paper, we have calculated the band structure of InAs and InP in the WZ phase using the WIEN2k *ab initio* code. Both compounds have a direct band gap at the Γ point with the SOC effects clearly larger for InAs than InP. Our calculations are consistent with theoretical and experimental reported values in the literature. In order to describe the band structure around the FBZ center, we developed a multiband $8 \times 8 k \cdot p$ model for the first conduction band and the top three valence bands, including spin. The fitted parameters we obtained for the $k \cdot p$ Hamiltonian recover the important features of the *ab initio* band structure with good agreement up to 1.0 nm^{-1} for multiple directions in the FBZ. Due to the stronger SOC of InAs compared to its crystal field splitting, the labeling of LH and CH energy bands at the Γ point is reversed from InP. Regarding the spin-splitting properties, we included the k -dependent SOC term in the Hamiltonian, which is usually neglected in the literature. This term, combined with the other indirect couplings in the Hamiltonian, allowed the description of the spin-splitting properties farther away from the vicinity of the Γ point. Our model captured all the important features including the description of maxima values and also the crossing between the spin-split bands (clearly seen in the HH band of InP, for instance). All these intricate behaviors of spin splitting have a unique physical origin, the BIA of the WZ structure. Furthermore, we calculated the in-plane spin orientation, i.e., the spin expectation value, of the energy bands and found that they all have a Rashba-like spin texture, either CW or CCW. This spin orientation was also compared to *ab initio* data to correctly identify the signs of the parameters in the Hamiltonian. Using our multiband $k \cdot p$ Hamiltonian, we obtained the DOS for conduction and valence bands and calculated the carrier density as a function of the Fermi energy. In addition to the 8×8 Hamiltonian, we present analytical expressions for the effective masses and the SOC field of conduction band which holds in the vicinities of the Γ point. For completeness, we also fitted the $6 \times 6 k \cdot p$ model for the valence band to the *ab initio* data. We emphasize that the best effective description that matches our *ab initio* calculations is the full $8 \times 8 k \cdot p$ Hamiltonian.

In conclusion, we provided in this study robust $k \cdot p$ models and parameter sets that can be straightforwardly applied to investigate novel effects in InAs- and InP-based nanostructures. For instance, polytypic systems of mixed WZ and ZB have already been demonstrated experimentally for both InAs and InP with great growth control of the different phases [2] and there are also theoretical models to treat such systems [10,30,77]. Furthermore, InAs nanowires are also a platform for studies in Majorana fermions [15]. One of the key ingredients for such realization is the presence of a robust SOC to split the energy bands, a feature already included in our model. Finally, it is straightforward to include strain effects by using the well-established WZ strain Hamiltonian [28,30] combined with the elastic constants and deformation potentials for InAs and InP in the WZ phase already reported in the literature [26,78–80].

ACKNOWLEDGMENTS

The authors acknowledge financial support from CAPES PVE (Grant No. 88881.068174/2014-01), CNPq (Grants No. 149904/2013-4, No. 88887.110814/2015-00, and No. 304289/2015-9), DFG SFB 689, and FAPESP (Grant No. 2012/05618-0). P.E.F.J. thanks A. Polimeni for suggesting the calculation of effective masses.

APPENDIX A: EFFECTIVE MASSES

Very close to the Γ point we can estimate the effective masses by fitting a parabolic dispersion to the *ab initio* data. In Table V, we show the values of effective masses along the k_z and k_x directions for the highlighted energy bands of Figs. 2(a) and 2(b). For the k_x direction, we calculated the effective masses assuming the average value of the spin-splitting bands, i.e., $(E_o + E_i)/2$ with the subindex o (i) indicating the outer (inner) branch.

APPENDIX B: HAMILTONIAN TERMS AND PARAMETERS

In this Appendix, we present the matrix forms of all terms in Eq. (5) and the definition of parameters using the simple group formalism.

Matrix representation of H_0 :

$$H_0 = \text{diag}[\Delta_1, \Delta_1, 0, \Delta_1, \Delta_1, 0, E_c, E_c], \quad (\text{B1})$$

with the definitions $\langle \Gamma_{5v}^x | H_0 | \Gamma_{5v}^x \rangle = \langle \Gamma_{5v}^y | H_0 | \Gamma_{5v}^y \rangle = \Delta_1$, $\langle \Gamma_{1v} | H_0 | \Gamma_{1v} \rangle = 0$, and $\langle \Gamma_{1c} | H_0 | \Gamma_{1c} \rangle = E_c$.

The zero energy is defined without SOC for states $|c_3\rangle$ and $|c_6\rangle$. The parameter Δ_1 is the crystal field splitting energy, which arises due to the WZ anisotropy between the xy plane and z direction, and the conduction band energy is denoted by the parameter E_c . It is possible to make the connection with the energy gap including SOC coupling by writing $E_c = E_g + \Delta_c$, for instance. It is also convenient to consider a diagonal energy offset to set the top valence band at zero energy.

TABLE V. Effective masses for InAs and InP along k_z (m_{\parallel}^*) and k_x (m_{\perp}^*) for the highlighted bands of Figs. 2(a) and 2(b). The effective masses were obtained by fitting a parabola up to 2% of the FBZ along the specified directions.

	InAs		InP	
	m_{\parallel}^*	m_{\perp}^*	m_{\parallel}^*	m_{\perp}^*
Γ_{7c}	0.0370	0.0416	0.0947	0.1183
Γ_{9v}	-0.9738	-0.0795	-1.0646	-0.2091
Γ_{7v}	-0.0551	-0.1046	-0.3064	-0.1988
Γ'_{7v}	-0.0863	-0.1838	-0.1016	-0.4887

Matrix representation of $H_{SO}^{(1)}$:

$$H_{SO}^{(1)} = \begin{bmatrix} \Delta_2 & 0 & 0 & 0 & 0 & 0 & 0 & 0 \\ 0 & -\Delta_2 & 0 & 0 & 0 & \sqrt{2}\Delta_3 & 0 & i\sqrt{2}\Delta_4 \\ 0 & 0 & 0 & 0 & \sqrt{2}\Delta_3 & 0 & 0 & 0 \\ 0 & 0 & 0 & \Delta_2 & 0 & 0 & 0 & 0 \\ 0 & 0 & \sqrt{2}\Delta_3 & 0 & -\Delta_2 & 0 & i\sqrt{2}\Delta_4 & 0 \\ 0 & \sqrt{2}\Delta_3 & 0 & 0 & 0 & 0 & 0 & 0 \\ 0 & 0 & 0 & 0 & -i\sqrt{2}\Delta_4 & 0 & 0 & 0 \\ 0 & -i\sqrt{2}\Delta_4 & 0 & 0 & 0 & 0 & 0 & 0 \end{bmatrix}, \quad (\text{B2})$$

with the definitions

$$\begin{aligned} \Delta_2 &= \frac{i\hbar}{4m_0^2c^2} \langle \Gamma_{5v}^x | \frac{\partial V}{\partial x} p_y - \frac{\partial V}{\partial y} p_x | \Gamma_{5v}^y \rangle, \\ \Delta_3 &= \frac{i\hbar}{4m_0^2c^2} \langle \Gamma_{5v}^y | \frac{\partial V}{\partial y} p_z - \frac{\partial V}{\partial z} p_y | \Gamma_{1v} \rangle = \frac{i\hbar}{4m_0^2c^2} \langle \Gamma_{1v} | \frac{\partial V}{\partial z} p_x - \frac{\partial V}{\partial x} p_z | \Gamma_{5v}^x \rangle, \\ \Delta_4 &= \frac{i\hbar}{4m_0^2c^2} \langle \Gamma_{5v}^y | \frac{\partial V}{\partial y} p_z - \frac{\partial V}{\partial z} p_y | \Gamma_{1c} \rangle = \frac{i\hbar}{4m_0^2c^2} \langle \Gamma_{1c} | \frac{\partial V}{\partial z} p_x - \frac{\partial V}{\partial x} p_z | \Gamma_{5v}^x \rangle. \end{aligned} \quad (\text{B3})$$

Matrix representation of $H_{kp}^{(1)}$:

$$H_{kp}^{(1)} = \begin{bmatrix} 0 & 0 & iA_7k_- & 0 & 0 & 0 & -\frac{1}{\sqrt{2}}P_2k_- & 0 \\ 0 & 0 & -iA_7k_+ & 0 & 0 & 0 & \frac{1}{\sqrt{2}}P_2k_+ & 0 \\ -iA_7k_+ & iA_7k_- & 0 & 0 & 0 & 0 & P_1k_z & 0 \\ 0 & 0 & 0 & 0 & 0 & -iA_7k_+ & 0 & \frac{1}{\sqrt{2}}P_2k_+ \\ 0 & 0 & 0 & 0 & 0 & iA_7k_- & 0 & -\frac{1}{\sqrt{2}}P_2k_- \\ 0 & 0 & 0 & iA_7k_- & -iA_7k_+ & 0 & 0 & P_1k_z \\ -\frac{1}{\sqrt{2}}P_2k_+ & \frac{1}{\sqrt{2}}P_2k_- & P_1k_z & 0 & 0 & 0 & 0 & 0 \\ 0 & 0 & 0 & \frac{1}{\sqrt{2}}P_2k_- & -\frac{1}{\sqrt{2}}P_2k_+ & P_1k_z & 0 & 0 \end{bmatrix}, \quad (\text{B4})$$

with the definitions

$$\begin{aligned} A_7 &= \frac{i}{\sqrt{2}} \frac{\hbar}{m_0} \langle \Gamma_{5v}^x | p_x | \Gamma_{1v} \rangle = \frac{i}{\sqrt{2}} \frac{\hbar}{m_0} \langle \Gamma_{5v}^y | p_y | \Gamma_{1v} \rangle, \\ P_2 &= i \frac{\hbar}{m_0} \langle \Gamma_{5v}^x | p_x | \Gamma_{1c} \rangle = i \frac{\hbar}{m_0} \langle \Gamma_{5v}^y | p_y | \Gamma_{1c} \rangle, \\ P_1 &= i \frac{\hbar}{m_0} \langle \Gamma_{1v} | p_z | \Gamma_{1c} \rangle, \\ k_{\pm} &= k_x \pm ik_y. \end{aligned} \quad (\text{B5})$$

Matrix representation of $H_{kSO}^{(1)}$:

$$H_{kSO}^{(1)} = \begin{bmatrix} 0 & 0 & -\frac{i}{\sqrt{2}}\alpha_1k_- & 0 & -i\alpha_2k_- & 0 & \frac{1}{\sqrt{2}}\beta_1k_- & 0 \\ 0 & 0 & -\frac{i}{\sqrt{2}}\alpha_1k_+ & -i\alpha_2k_- & 0 & i\sqrt{2}\alpha_1k_z & \frac{1}{\sqrt{2}}\beta_1k_+ & -\sqrt{2}\beta_1k_z \\ \frac{i}{\sqrt{2}}\alpha_1k_+ & \frac{i}{\sqrt{2}}\alpha_1k_- & 0 & 0 & -i\sqrt{2}\alpha_1k_z & -i\alpha_3k_- & 0 & \beta_2k_- \\ 0 & i\alpha_2k_+ & 0 & 0 & 0 & \frac{i}{\sqrt{2}}\alpha_1k_+ & 0 & -\frac{1}{\sqrt{2}}\beta_1k_+ \\ i\alpha_2k_+ & 0 & i\sqrt{2}\alpha_1k_z & 0 & 0 & \frac{i}{\sqrt{2}}\alpha_1k_- & -\sqrt{2}\beta_1k_z & -\frac{1}{\sqrt{2}}\beta_1k_- \\ 0 & -i\sqrt{2}\alpha_1k_z & i\alpha_3k_+ & -\frac{i}{\sqrt{2}}\alpha_1k_- & -\frac{i}{\sqrt{2}}\alpha_1k_+ & 0 & -\beta_2k_+ & 0 \\ \frac{1}{\sqrt{2}}\beta_1k_+ & \frac{1}{\sqrt{2}}\beta_1k_- & 0 & 0 & -\sqrt{2}\beta_1k_z & -\beta_2k_- & 0 & -i\gamma_1k_- \\ 0 & -\sqrt{2}\beta_1k_z & \beta_2k_+ & -\frac{1}{\sqrt{2}}\beta_1k_- & -\frac{1}{\sqrt{2}}\beta_1k_+ & 0 & i\gamma_1k_+ & 0 \end{bmatrix}, \quad (\text{B6})$$

with the definitions

$$\begin{aligned}
\alpha_1 &= \frac{\hbar^2}{4m_0^2c^2} \langle \Gamma_{5v}^x | \frac{\partial V}{\partial x} | \Gamma_{1v} \rangle = \frac{\hbar^2}{4m_0^2c^2} \langle \Gamma_{5v}^y | \frac{\partial V}{\partial y} | \Gamma_{1v} \rangle, \\
\alpha_2 &= \frac{\hbar^2}{4m_0^2c^2} \langle \Gamma_{5v}^x | \frac{\partial V}{\partial z} | \Gamma_{5v}^x \rangle = \frac{\hbar^2}{4m_0^2c^2} \langle \Gamma_{5v}^y | \frac{\partial V}{\partial z} | \Gamma_{5v}^y \rangle, \\
\alpha_3 &= \frac{\hbar^2}{4m_0^2c^2} \langle \Gamma_{1v} | \frac{\partial V}{\partial z} | \Gamma_{1v} \rangle, \\
\beta_1 &= \frac{\hbar^2}{4m_0^2c^2} \langle \Gamma_{5v}^x | \frac{\partial V}{\partial x} | \Gamma_{1c} \rangle = \frac{\hbar^2}{4m_0^2c^2} \langle \Gamma_{5v}^y | \frac{\partial V}{\partial y} | \Gamma_{1c} \rangle, \\
\beta_2 &= \frac{\hbar^2}{4m_0^2c^2} \langle \Gamma_{1v} | \frac{\partial V}{\partial z} | \Gamma_{1c} \rangle, \\
\gamma_1 &= \frac{\hbar^2}{4m_0^2c^2} \langle \Gamma_{1c} | \frac{\partial V}{\partial z} | \Gamma_{1c} \rangle.
\end{aligned} \tag{B7}$$

Matrix representation of $H_{kp}^{(2)}$:

$$H_{kp}^{(2)} = \begin{bmatrix} \lambda + \theta & -K^* & -H^* & 0 & 0 & 0 & T^* & 0 \\ -K & \lambda + \theta & H & 0 & 0 & 0 & T & 0 \\ -H & H^* & \lambda & 0 & 0 & 0 & U & 0 \\ 0 & 0 & 0 & \lambda + \theta & -K & H & 0 & T \\ 0 & 0 & 0 & -K^* & \lambda + \theta & -H^* & 0 & T^* \\ 0 & 0 & 0 & H^* & -H & \lambda & 0 & U \\ T & T^* & U^* & 0 & 0 & 0 & V & 0 \\ 0 & 0 & 0 & T^* & T & U^* & 0 & V \end{bmatrix}, \tag{B8}$$

with elements given by

$$\begin{aligned}
\lambda &= A_1 k_z^2 + A_2 (k_x^2 + k_y^2), \\
\theta &= A_3 k_z^2 + A_4 (k_x^2 + k_y^2), \\
K &= A_5 k_+^2, \\
H &= A_6 k_+ k_z, \\
T &= i B_3 k_+ k_z, \\
U &= i [B_1 k_z^2 + B_2 (k_x^2 + k_y^2)], \\
V &= e_1 k_z^2 + e_2 (k_x^2 + k_y^2),
\end{aligned} \tag{B9}$$

and all the parameters in units of $\hbar^2/2m_0$.

The term $\mathbf{H}_{\mathbf{k}2}$ is already included in the diagonal terms of $H_{kp}^{(2)}$. Strictly speaking, the matrix representation $H_{kp}^{(2)}$ is defined as

$$H_{kp,\alpha\alpha'}^{(2)} = \mathbf{H}_{\mathbf{k}2} \delta_{\alpha\alpha'} + \sum_{\beta} \frac{\langle \alpha | \mathbf{H}_{\mathbf{k}p} | \beta \rangle \langle \beta | \mathbf{H}_{\mathbf{k}p} | \alpha' \rangle}{E_{\alpha\alpha'} - E_{\beta}}. \tag{B10}$$

The second-order $k \cdot p$ parameters A_1 to A_6 are defined the same way as in Ref. [28], while e_1 , e_2 , B_1 , B_2 , and B_3 are given by

$$e_1 = 1 + \frac{2}{m_0} \sum_{\beta} \frac{| \langle \Gamma_{1c} | p_z | \beta \rangle |^2}{E_{1c} - E_{\beta}},$$

$$\begin{aligned}
e_2 &= 1 + \frac{2}{m_0} \sum_{\beta} \frac{B[\Gamma_5]}{E_{1c} - E_{\beta}} \frac{| \langle \Gamma_{1c} | p_x | \beta \rangle |^2}{E_{1c} - E_{\beta}} \\
&= 1 + \frac{2}{m_0} \sum_{\beta} \frac{B[\Gamma_5]}{E_{1c} - E_{\beta}} \frac{| \langle \Gamma_{1c} | p_y | \beta \rangle |^2}{E_{1c} - E_{\beta}}, \\
B_1 &= \frac{2}{m_0} \sum_{\beta} \frac{B[\Gamma_1]}{E_{1v1c} - E_{\beta}} \langle \Gamma_{1v} | p_z | \beta \rangle \langle \beta | p_z | \Gamma_{1c} \rangle, \\
B_2 &= \frac{2}{m_0} \sum_{\beta} \frac{B[\Gamma_5]}{E_{1v1c} - E_{\beta}} \langle \Gamma_{1v} | p_x | \beta \rangle \langle \beta | p_x | \Gamma_{1c} \rangle \\
&= \frac{2}{m_0} \sum_{\beta} \frac{B[\Gamma_5]}{E_{1v1c} - E_{\beta}} \langle \Gamma_{1v} | p_y | \beta \rangle \langle \beta | p_y | \Gamma_{1c} \rangle, \\
B_3 &= \frac{\sqrt{2}}{m_0} \left(\sum_{\beta} \frac{B[\Gamma_1]}{E_{5v1c} - E_{\beta}} \langle \Gamma_{5v}^x | p_x | \beta \rangle \langle \beta | p_z | \Gamma_{1c} \rangle \right. \\
&\quad \left. + \sum_{\beta} \frac{B[\Gamma_5]}{E_{5v1c} - E_{\beta}} \langle \Gamma_{5v}^x | p_z | \beta \rangle \langle \beta | p_x | \Gamma_{1c} \rangle \right) \\
&= \frac{\sqrt{2}}{m_0} \left(\sum_{\beta} \frac{B[\Gamma_1]}{E_{5v1c} - E_{\beta}} \langle \Gamma_{5v}^y | p_y | \beta \rangle \langle \beta | p_z | \Gamma_{1c} \rangle \right. \\
&\quad \left. + \sum_{\beta} \frac{B[\Gamma_5]}{E_{5v1c} - E_{\beta}} \langle \Gamma_{5v}^y | p_z | \beta \rangle \langle \beta | p_y | \Gamma_{1c} \rangle \right),
\end{aligned} \tag{B11}$$

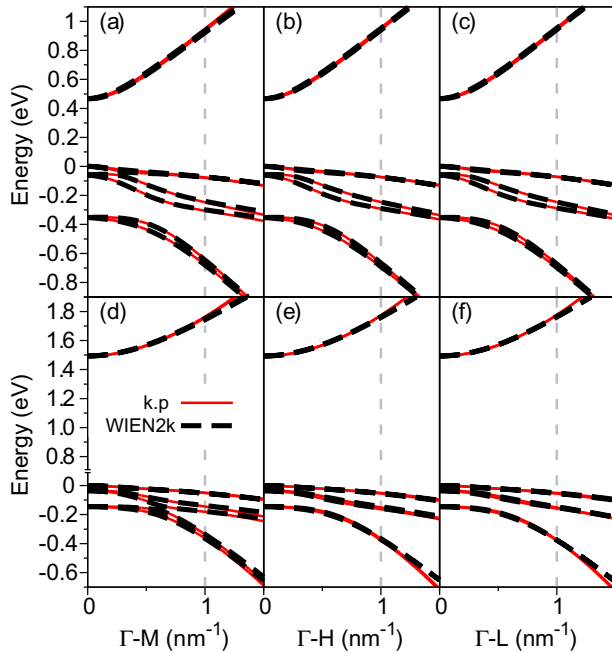


FIG. 8. Comparison of band structures for (a) Γ -M, (b) Γ -H, and (c) Γ -L directions of InAs and (d) Γ -M, (e) Γ -H, and (f) Γ -L directions of InP. The line schemes follow Fig. 4.

with nonzero contributions represented by the irreducible representations in the brackets above the summation.

APPENDIX C: FITTING IN OTHER DIRECTIONS

The comparison between the fitted and WIEN2k *ab initio* band structures is displayed in Fig. 8 for the Γ -M, Γ -H, and Γ -L directions. For the Γ -M direction, we have the same behavior discussed for Γ -K. However, the $k \cdot p$ band structures in the Γ -H and Γ -L directions have closer values to *ab initio*. This better agreement arises from the second-order parameters A_6 and B_3 which only couple the $k_x k_y$ plane to k_z , providing additional corrections to the band structures.

In Fig. 9 and Fig. 10, we show the comparison of spin splittings along the Γ -M, Γ -H, and Γ -L directions for InAs and InP, respectively. For the Γ -H and Γ -L directions, the spin splittings are usually smaller compared to Γ -K and Γ -M. This difference, however, depends on the material and the energy band. For instance, CH and LH values for InAs in Γ -H and Γ -L are approximately half the value in the Γ -K and Γ -M directions while LH and CH values for InP are approximately one-fourth of the values. Because of these larger differences for InP, the spin splittings for CH bands along Γ -H and Γ -L show a small deviation compared to *ab initio* [Figs. 10(h) and 10(l)]. However, the crossings for HH bands [Figs. 10(f) and 10(j)] are precisely reproduced. Comparing all directions, we verify that our $k \cdot p$ model and parameter sets reproduce with great agreement the *ab initio* band structure and spin splittings along all the considered directions of the FBZ.

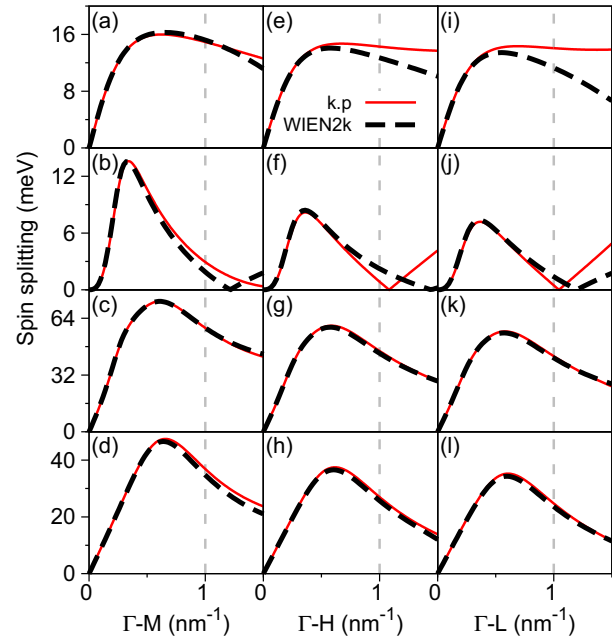


FIG. 9. Comparison of the InAs spin splittings for (a), (e), (i) CB; (b), (f), (j) HH; (c), (g), (k) LH; and (d), (h), (l) LH along Γ -M, Γ -H, and Γ -L directions. The line schemes follow Fig. 4.

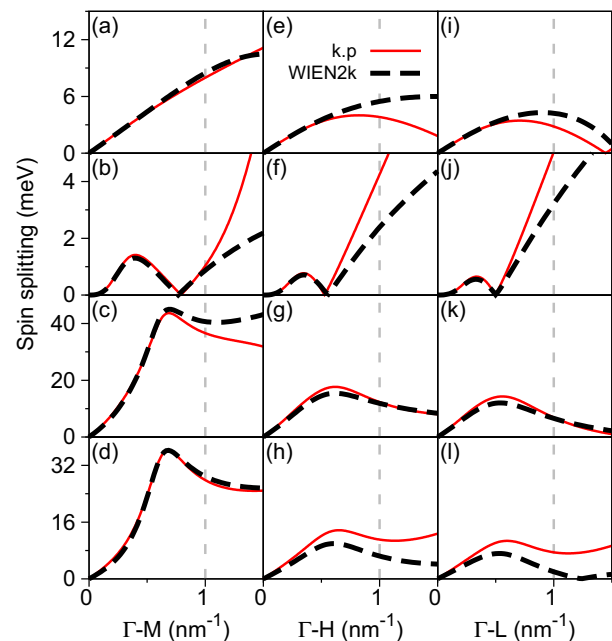


FIG. 10. Comparison of the InP spin splittings for (a), (e), (i) CB; (b), (f), (j) HH; (c), (g), (k) LH; and (d), (h), (l) CH along Γ -M, Γ -H, and Γ -L directions. The line schemes follow Fig. 4.

- [1] Y. Li, F. Qian, J. Xiang, and C. M. Lieber, *Mater. Today* **9**, 18 (2006).
- [2] P. Caroff, K. A. Dick, J. Johansson, M. E. Messing, K. Deppert, and L. Samuelson, *Nat. Nanotechnol.* **4**, 50 (2009).
- [3] T. T. T. Vu, T. Zehender, M. A. Verheijen, S. R. Plissard, G. W. G. Immink, J. E. M. Haverkort, and E. P. A. M. Bakkers, *Nanotechnology* **24**, 115705 (2013).
- [4] D. Pan, M. Fu, X. Yu, X. Wang, L. Zhu, S. Nie, S. Wang, Q. Chen, P. Xiong, S. von Molnár, and J. Zhao, *Nano Lett.* **14**, 1214 (2014).
- [5] K. A. Dick, C. Thelander, L. Samuelson, and P. Caroff, *Nano Lett.* **10**, 3494 (2010).
- [6] J. Bolinsson, P. Caroff, B. Mandl, and K. A. Dick, *Nanotechnology* **22**, 265606 (2011).
- [7] S. Lehmann, J. Wallentin, D. Jacobsson, K. Deppert, and K. A. Dick, *Nano Lett.* **13**, 4099 (2013).
- [8] T. Ba Hoang, A. F. Moses, L. Ahtapodov, H. Zhou, D. L. Dheeraj, A. T. J. van Helvoort, B.-O. Fimland, and H. Weman, *Nano Lett.* **10**, 2927 (2010).
- [9] E. G. Gadret, G. O. Dias, L. C. O. Dacal, M. M. de Lima, C. V. R. S. Ruffo, F. Iikawa, M. J. S. P. Brasil, T. Chiaramonte, M. A. Cotta, L. H. G. Tizei, D. Ugarte, and A. Cantarero, *Phys. Rev. B* **82**, 125327 (2010).
- [10] P. E. Faria Junior, T. Campos, and G. M. Sipahi, *J. Appl. Phys.* **116**, 193501 (2014).
- [11] C. Thelander, P. Caroff, S. Plissard, A. Dey, and K. Dick, *Nano Lett.* **11**, 2424 (2011).
- [12] A. Konar, J. Mathew, K. Nayak, M. Bajaj, R. K. Pandey, S. Dhara, K. V. R. M. Murali, and M. M. Deshmukh, *Nano Lett.* **15**, 1684 (2015).
- [13] J. Li, X. Yan, F. Sun, X. Zhang, and X. Ren, *Appl. Phys. Lett.* **107**, 263103 (2015).
- [14] P. Chuang, S.-C. Ho, L. W. Smith, F. Sfigakis, M. Pepper, C.-H. Chen, J.-C. Fan, J. P. Griffiths, I. Farrer, H. E. Beere, G. A. C. Jones, D. A. Ritchie, and T.-M. Chen, *Nat. Nanotechnol.* **10**, 35 (2014).
- [15] A. Das, Y. Ronen, Y. Most, Y. Oreg, M. Heiblum, and H. Shtrikman, *Nat. Phys.* **8**, 887 (2012).
- [16] X. Li, X. Wei, T. Xu, D. Pan, J. Zhao, and Q. Chen, *Adv. Mater.* **27**, 2852 (2015).
- [17] H. J. Joyce, C. J. Docherty, Q. Gao, H. H. Tan, C. Jagadish, J. Lloyd-Hughes, L. M. Herz, and M. B. Johnston, *Nanotechnology* **24**, 214006 (2013).
- [18] Y. Cui, J. Wang, S. R. Plissard, A. Cavalli, T. T. T. Vu, R. P. J. van Veldhoven, L. Gao, M. Trainor, M. A. Verheijen, J. E. M. Haverkort, and E. P. A. M. Bakkers, *Nano Lett.* **13**, 4113 (2013).
- [19] Z. Wang, B. Tian, M. Paladugu, M. Pantouvaki, N. Le Thomas, C. Merckling, W. Guo, J. Dekoster, J. V. Campenhout, P. Absil, and D. V. Thourhout, *Nano Lett.* **13**, 5063 (2013).
- [20] S. F. Svensson, S. Jeppesen, C. Thelander, L. Samuelson, H. Linke, and K. A. Dick, *Nanotechnology* **24**, 345601 (2013).
- [21] D. Lindgren, K. Kawaguchi, M. Heurlin, M. T. Borgström, M.-E. Pistol, L. Samuelson, and A. Gustafsson, *Nanotechnology* **24**, 225203 (2013).
- [22] Z. Zanolli, F. Fuchs, J. Furthmüller, U. von Barth, and F. Bechstedt, *Phys. Rev. B* **75**, 245121 (2007).
- [23] A. De and C. E. Pryor, *Phys. Rev. B* **81**, 155210 (2010).
- [24] L. C. O. Dacal and A. Cantarero, *Solid State Commun.* **151**, 781 (2011).
- [25] A. Belabbes, C. Panse, J. Furthmüller, and F. Bechstedt, *Phys. Rev. B* **86**, 075208 (2012).
- [26] C. Hajlaoui, L. Pedesseau, F. Raouafi, F. Ben CheikhLarbi, J. Even, and J.-M. Jancu, *J. Phys. D: Appl. Phys.* **46**, 505106 (2013).
- [27] L. C. O. Dacal and A. Cantarero, *Mater. Res. Express* **1**, 015702 (2014).
- [28] S. L. Chuang and C. S. Chang, *Phys. Rev. B* **54**, 2491 (1996).
- [29] P. Rinke, M. Winkelkemper, A. Qteish, D. Bimberg, J. Neugebauer, and M. Scheffler, *Phys. Rev. B* **77**, 075202 (2008).
- [30] P. E. Faria Junior and G. M. Sipahi, *J. Appl. Phys.* **112**, 103716 (2012).
- [31] T. Cheiwchanchamnangij and W. R. Lambrecht, *Phys. Rev. B* **84**, 035203 (2011).
- [32] P. Blaha, K. Schwarz, G. K. H. Madsen, D. Kvasnicka, and J. Luitz, *WIEN2k, An Augmented Plane Wave + Local Orbitals Program for Calculating Crystal Properties* (Vienna University of Technology, Vienna, 2013).
- [33] I. Žutić, J. Fabian, and S. Das Sarma, *Rev. Mod. Phys.* **76**, 323 (2004).
- [34] J. Hohenberg and W. Kohn, *Phys. Rev.* **136**, B864 (1964).
- [35] A. D. Becke and E. R. Johnson, *J. Chem. Phys.* **124**, 221101 (2006).
- [36] F. Tran and P. Blaha, *Phys. Rev. Lett.* **102**, 226401 (2009).
- [37] Y.-S. Kim, M. Marsman, G. Kresse, F. Tran, and P. Blaha, *Phys. Rev. B* **82**, 205212 (2010).
- [38] D. Koller, F. Tran, and P. Blaha, *Phys. Rev. B* **83**, 195134 (2011).
- [39] D. Koller, F. Tran, and P. Blaha, *Phys. Rev. B* **85**, 155109 (2012).
- [40] Y.-S. Kim, K. Hummer, and G. Kresse, *Phys. Rev. B* **80**, 035203 (2009).
- [41] A. N. Chantis, M. van Schilfgaarde, and T. Kotani, *Phys. Rev. Lett.* **96**, 086405 (2006).
- [42] J.-W. Luo, G. Bester, and A. Zunger, *Phys. Rev. Lett.* **102**, 056405 (2009).
- [43] A. N. Chantis, N. E. Christensen, A. Svane, and M. Cardona, *Phys. Rev. B* **81**, 205205 (2010).
- [44] J. P. Perdew and A. Zunger, *Phys. Rev. B* **23**, 5048 (1981).
- [45] J. P. Perdew, K. Burke, and M. Ernzerhof, *Phys. Rev. Lett.* **77**, 3865 (1996).
- [46] D. J. Singh and L. Nordstrom, *Planewaves, Pseudopotentials, and the LAPW Method* (Springer, Berlin, 2006).
- [47] M. Gmitra and J. Fabian, [arXiv:1606.00588](https://arxiv.org/abs/1606.00588).
- [48] M. S. Dresselhaus, G. Dresselhaus, and A. Jorio, *Group Theory: Application to the Physics of Condensed Matter*, 1st ed. (Springer, Berlin, 2008). From Table D.11, replace $\Delta_{1...6}$ with $\Gamma_{1...6}$ and use the factor $T_{\Delta} = 1$.
- [49] M. Cardona, N. E. Christensen, and G. Fasol, *Phys. Rev. B* **38**, 1806 (1988).
- [50] P. Käckell, B. Wenzien, and F. Bechstedt, *Phys. Rev. B* **50**, 17037 (1994).
- [51] M. I. McMahon and R. J. Nelves, *Phys. Rev. Lett.* **95**, 215505 (2005).
- [52] D. Kriegner, C. Panse, B. Mandl, K. A. Dick, M. Keplinger, J. M. Persson, P. Caroff, D. Ercolani, L. Sorba, F. Bechstedt, J. Stangl, and G. Bauer, *Nano Lett.* **11**, 1483 (2011).
- [53] C. Panse, D. Kriegner, and F. Bechstedt, *Phys. Rev. B* **84**, 075217 (2011).
- [54] R. C. Casella, *Phys. Rev.* **114**, 1514 (1959).
- [55] J. J. Hopfield, *J. Appl. Phys.* **32**, 2277 (1961).

- [56] M. De Luca, A. Zilli, A. Fonseca, S. Mokkalapati, A. Miriametro, H. Tan, L. Smith, C. Jagadish, M. Capizzi, and A. Polimeni, *Nano Lett.* **15**, 998 (2015).
- [57] A. Zilli, M. De Luca, D. Tedeschi, A. Fonseca, A. Miriametro, H. Tan, C. Jagadish, M. Capizzi, and A. Polimeni, *ACS Nano* **9**, 4277 (2015).
- [58] R. Enderlein and N. J. Horing, *Fundamentals of Semiconductor Physics and Devices*, 1st ed. (World Scientific Publishing, Singapore, 1997).
- [59] P. O. Löwdin, *J. Chem. Phys.* **19**, 1396 (1951).
- [60] J. Bao, D. C. Bell, F. Capasso, N. Erdman, D. Wei, L. Fröberg, T. Mårtensson, and L. Samuelson, *Adv. Mater.* **21**, 3654 (2009).
- [61] G. Koblmüller, S. Hertenberger, K. Vizbaras, M. Bichler, F. Bao, J.-P. Zhang, and G. Abstreiter, *Nanotechnology* **21**, 365602 (2010).
- [62] M. Möller, M. M. de Lima Jr., A. Cantarero, T. Chiamonte, M. A. Cotta, and F. Iikawa, *Nanotechnology* **23**, 375704 (2012).
- [63] A. Mishra, L. V. Titova, T. B. Hoang, H. E. Jackson, L. M. Smith, J. M. Yarrison-Rice, Y. Kim, H. J. Joyce, Q. Gao, H. H. Tan, and C. Jagadish, *Appl. Phys. Lett.* **91**, 263104 (2007).
- [64] G. L. Tuin, M. T. Borgström, J. Trägårdh, M. Ek, L. R. Wallenberg, L. Samuelson, and M.-E. Pistol, *Nano Res.* **4**, 159 (2011).
- [65] As far as we are concerned, the only paper in the literature that provides a double-group description of the $k \cdot p$ model (for cubic crystals) is W. J. Elder, R. M. Ward, and J. Zhang, *Phys. Rev. B* **83**, 165210 (2011).
- [66] Explicitly, $u_{n,\Gamma}(\vec{r}) = \langle \vec{r} | c_n \rangle$, with $n = 1, \dots, 8$ running over the energy bands at the Γ point we are describing.
- [67] R. Beresford, *J. Appl. Phys.* **95**, 6216 (2004).
- [68] J. Y. Fu and M. W. Wu, *J. Appl. Phys.* **104**, 093712 (2008).
- [69] A. Marnetto, M. Penna, and M. Goano, *J. Appl. Phys.* **108**, 033701 (2010).
- [70] M. S. Miao, Q. Yan, C. G. Van de Walle, W. K. Lou, L. L. Li, and K. Chang, *Phys. Rev. Lett.* **109**, 186803 (2012).
- [71] G. Dresselhaus, *Phys. Rev.* **100**, 580 (1955).
- [72] A. Punya and W. R. L. Lambrecht, *Phys. Rev. B* **85**, 195147 (2012).
- [73] M. Newville, T. Stensitzki, D. B. Allen, and A. Ingargiola, LMFIT: Non-linear least-square minimization and curve-fitting for Python (2014), doi:10.5281/zenodo.11813.
- [74] The residue calculated for a specific direction in the FBZ is given by $r = \frac{1}{N} \sum_{n,\vec{k}} [f_n(\vec{k}) - t_n(\vec{k})]^2$, in which n runs over the 8 energy bands or 4 spin splitting curves, \vec{k} runs over the k points, $f_n(\vec{k})$ is the fitted data, $t_n(\vec{k})$ is the *ab initio* data, and N is a normalization constant which includes the number of k points used multiplied by the size of n . The total residue is the sum of the residues in all directions.
- [75] S. L. Chuang and C. S. Chang, *Appl. Phys. Lett.* **68**, 1657 (1996).
- [76] See Supplemental Material at <http://link.aps.org/supplemental/10.1103/PhysRevB.93.235204> for the curve fitting of the carrier density, the comparison between *ab initio* and the analytical approach for conduction band and the fitting of the 6×6 Hamiltonian approach for valence band.
- [77] J. I. Climente, C. Segarra, F. Rajadell, and J. Planelles, *J. Appl. Phys.* **119**, 125705 (2016).
- [78] M. W. Larsson, J. B. Wagner, M. Wallin, P. Håkansson, L. E. Fröberg, L. Samuelson, and L. R. Wallenberg, *Nanotechnology* **18**, 015504 (2007).
- [79] F. Boxberg, N. Søndergaard, and H. Q. Xu, *Adv. Mater.* **24**, 4692 (2012).
- [80] C. Hajlaoui, L. Pedesseau, F. Raouafi, F. Ben Cheikh Larbi, J. Even, and J.-M. Jancu, *J. Exp. Theor. Phys.* **121**, 246 (2015).

Size-Induced Phase Evolution of MoSe₂ Nanoflakes Revealed by Density Functional Theory

Rafael Besse,[†] Naidel A. M. S. Caturello,[‡] Carlos M. O. Bastos,[†] Diego Guedes-Sobrinho,^{§,‡} Matheus P. Lima,^{||} Guilherme M. Sipahi,[†] and Juarez L. F. Da Silva^{*,‡,||}

[†]São Carlos Institute of Physics, University of São Paulo, P.O. Box 369, 13560-970 São Carlos, São Paulo, Brazil

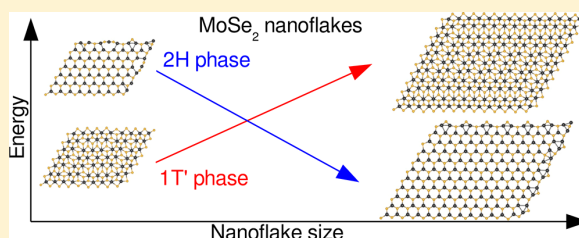
[‡]São Carlos Institute of Chemistry, University of São Paulo, P.O. Box 780, 13560-970 São Carlos, São Paulo, Brazil

[§]Department of Physics, Technological Institute of Aeronautics, 12228-900 São José dos Campos, São Paulo, Brazil

^{||}Department of Physics, Federal University of São Carlos, 13565-905 São Carlos, São Paulo, Brazil

Supporting Information

ABSTRACT: The control of the relative stability between trigonal prismatic and octahedral structures in transition-metal dichalcogenides (TMDs) is an important step toward technological applications of 2D TMDs materials, where the electronic properties have a strong dependence on the structural phase and size effects. We report a density functional theory investigation of the size effect on the relative phase stability of stoichiometric (MoSe₂)_n nanoflakes with parallelogram shape for $n = 15, 63, 108, 130, 154, 192$. We found that the octahedral phase adopts a distorted configuration, which is driven by the Peierls transition mechanism, and, as expected, the Mo-terminated edges of the trigonal prismatic nanoflakes exhibit a strong reconstruction. Furthermore, for the smallest nanoflakes, the octahedral phase has the lowest energy, but with increasing the nanoflake size, the trigonal prismatic phase becomes the most stable. From our results and analyses, this transition is shown to be mainly caused by a difference in edge formation energy of the two structural configurations. Although the physical trends have been obtained for MoSe₂ nanoflakes, we expect that similar trends might be observed in different 2D TMDs.



1. INTRODUCTION

Recently, the research on 2D materials has been greatly expanded, motivated by the novel properties they exhibit in contrast with conventional bulk materials.^{1,2} For example, layered transition-metal dichalcogenides (TMDs),^{3,4} MQ₂ (M = transition metals, Q = S, Se, Te), have particularly attracted great attention, driven by several promising applications, such as nanoscale transistors,⁵ optoelectronics,⁶ electrocatalysis,⁷ energy storage,⁸ and so on. In contrast with traditional semiconductors, the physical and chemical properties of TMDs can be tuned by a wide range of approaches, namely, (i) a large number of M and Q combinations,^{3,4} which includes also the extension for ternary or quaternary systems,^{9,10} (ii) control of the number of monolayers (van der Waals heterostructures)¹¹ and size of the nanoflakes,¹² and (iii) exploration of different atomic configurations within the monolayers (polymorphism),¹³ which can give rise to the appearance of metallic or semiconductor behavior^{14,15} or even topological states.¹³ Although several of those effects have been deeply investigated in the last years, many problems still remain open, such as the mechanisms that drive structural transitions in 2D-TMD nanoflakes.

The crystal structures of 2D-TMDs (Figure 1) are composed of MQ₂ layers bound by van der Waals (vdW)

interactions, where each monolayer consists of a triangular lattice of M atoms sandwiched between two triangular lattices of Q atoms.³ Structural polymorphism in the monolayers arises from an intralayer variety of coordination environments, which are generated by the location of the Q atoms around M , that is, trigonal prismatic and octahedral.^{3,13} Distinct interlayer stacking patterns of each monolayer polymorph originate different structural phases of bulk TMDs, of which the most commonly observed are named 2H,³ with trigonal prismatic coordinated M , and 1T,³ where M atoms are octahedrally coordinated. Another structural phase, 1T',¹³ is generated from the 1T structure by reconstructions in a 2×1 orthorhombic lattice, with dimerization of the M atom rows,^{4,13} as depicted in Figure 1. This phase deserves considerable attention due to the possibility to obtain quantum spin Hall phases.¹⁶ The 1T' structure has been observed in group 6 TMDs and is the ground-state structure of WTe₂.^{4,13}

The d-electron count of M is relevant to determine which of the structural phases is adopted by a TMD because of the differences between electronic structures induced by the

Received: April 6, 2018

Revised: August 4, 2018

Published: August 14, 2018

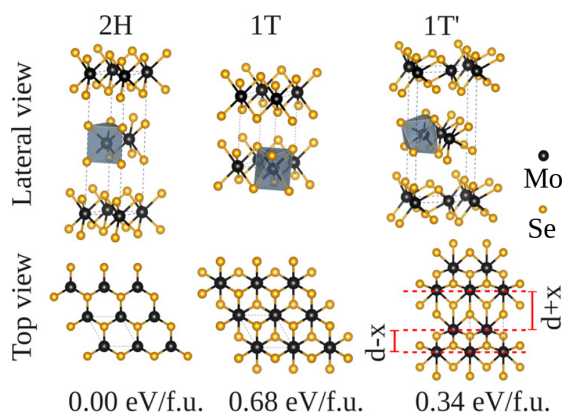


Figure 1. Crystal MoSe_2 structures in the 2H, 1T, and 1T' phases and relative total energy per formula unit ($\Delta E_i = E_{\text{tot}}^i - E_{\text{tot}}^{2\text{H}}$). Top views of each layer are shown in the bottom row, where the Peierls distortion dimerization pattern is indicated in the 1T' structure.

coordination environment and the symmetry of each structure.^{3,13,17} For example, the group 4 TMDs (TiS_2 , ZrS_2 , ZrSe_2) adopt the 1T phase, whereas the group 6 TMDs (MoS_2 , MoSe_2 , WS_2 , WSe_2) are mostly observed in the 2H phase.^{3,4} Recently, the understanding based on the occupation of electronic states has been applied to describe the phase transition in group 6 TMDs from trigonal prismatic to octahedral structure due to (i) electron transfer by the insertion of Li atoms,^{18,19} (ii) substitutional doping with electron donors and electron beam irradiation,²⁰ and (iii) electron transfer induced by the exposure to chemical vapor of organic electron donors.¹⁵ Furthermore, other strategies to control phase stability in TMDs have been suggested, for example, temperature control along the chemical vapor deposition (CVD) growing process¹⁴ and strain.²¹

Although several mechanisms have been identified to modify the relative stability among 2D-TMDs, most of those investigations considered large monolayers. Thus the importance of size effects on the structural polymorphism of 2D-TMDs should be deeply investigated. For example, it has been recently suggested that in TMD ribbons, reducing the width may affect the relative phase stability.²² However, this theoretical investigation considered infinite ribbons, and additionally, no trend of the relation between size and relative phase stability was clearly demonstrated. Therefore, it is necessary to improve the understanding of size reduction effects on the relative phase stability of 2D-TMDs and their correlation with the nanoflake electronic properties.

To contribute to the solution of this problem, we performed a density functional theory (DFT) investigation employing trigonal prismatic and octahedral $(\text{MoSe}_2)_n$ nanoflakes with parallelogram shape, ranging from $n = 15$ to 192 formula units (f.u.). We found that the size of the nanoflake plays a crucial role in the relative energetic stability between the structural phases in MoSe_2 . For nanoflakes composed of a number of formula units up to 150, the 1T' derived structure is the lowest energy conformation. On the contrary, the 2H derived structure is the ground-state structure for nanoflakes composed of more than 150 f.u. In the 2H nanoflakes, there are considerable reconstructions close to their edges. The size-induced 2H-1T' phase transition occurs mainly due to the higher edge energy of the 2H nanoflakes in comparison with

1T'. Nanoflakes of both structural phases are shown to have no band gap, which for the 2H phase is due to the electronic states from the edge atoms.

2. THEORETICAL APPROACH AND COMPUTATIONAL DETAILS

Our spin-polarized DFT simulations were based on the generalized gradient approximation (GGA), as developed by Perdew–Burke–Ernzerhof (PBE),²³ for the exchange–correlation functional. Furthermore, we employed the vdW D3 correction proposed by Grimme et al.²⁴ to improve the description of vdW interlayer interactions.²⁵ Our calculations were performed using the projector augmented wave (PAW) method,^{26,27} as implemented in the Vienna ab initio simulation package (VASP).^{28,29}

A total energy convergence criterion of 1×10^{-6} eV was used for the self-consistent solution of the Kohn–Sham (KS) equations. The KS orbitals were expanded in a plane-wave basis set with a cutoff energy of 390 eV, except for stress tensor calculations, for bulks and monolayers, in which a larger cutoff energy of 520 eV was employed due to the slower convergence of the stress tensor with the number of plane waves. For the Brillouin zone integration, an $11 \times 11 \times 2$ k-points mesh was employed for the 2H crystal structure. The k-point density was kept in all bulk and monolayer calculations but was doubled for band structure and density of states (DOS) calculations, while only the Γ point was used for nanoflake calculations. Because periodic boundary conditions were applied, to avoid spurious interactions between periodic images, the nanoflakes were placed in large supercells to ensure a distance of 15 Å from its periodic images. For the monolayer calculations, vacuum thicknesses of 15 Å were set between periodic images of the monolayers. Equilibrium structure geometries were determined by the minimization of the stress tensor and forces on atoms to <0.025 eV Å⁻¹.

3. RESULTS AND DISCUSSION

3.1. Relative Phase Stability of Bulk and Monolayer MoSe_2 . We compared the energetic stability of MoSe_2 considering the bulk 2H, 1T, and 1T' structures, as shown in Figure 1. The bulk 2H phase has the lowest energy, which is 0.34 eV/f.u. (PBE+D3) lower than bulk 1T' and 0.68 eV/f.u. (PBE+D3) lower than the bulk 1T phase. For the monolayers, the same trend is observed, that is, 2H monolayer has lower energy than 1T' and 1T monolayers by 0.33 eV/f.u. (PBE+D3) and 0.70 eV/f.u. (PBE+D3), respectively, which are in agreement with previous results.²¹ Monolayer relative energies calculated without the vdW D3 correction differ from PBE+D3 results by <13 meV/f.u. Thus we conclude that the vdW interactions do not affect the relative stability among the monolayer structures, and hence it is expected that the intramonolayer interactions are dominated by ionic and covalent bonding. Therefore, calculations for nanoflakes were safely performed without the vdW D3 correction.

3.2. Peierls Distortion. The lower energy of the 1T' phase compared with 1T can be explained by the Peierls distortion mechanism.^{16,30} This is clearly demonstrated by the band structures shown in Figure 2. It is worth noting in the 1T band structure the degeneracies at the Y high-symmetry point, which is the edge of the reduced Brillouin zone. Structural distortions typical of the Peierls mechanism, with dimerization of Mo atom rows throughout the structure, Figure 1, will break these

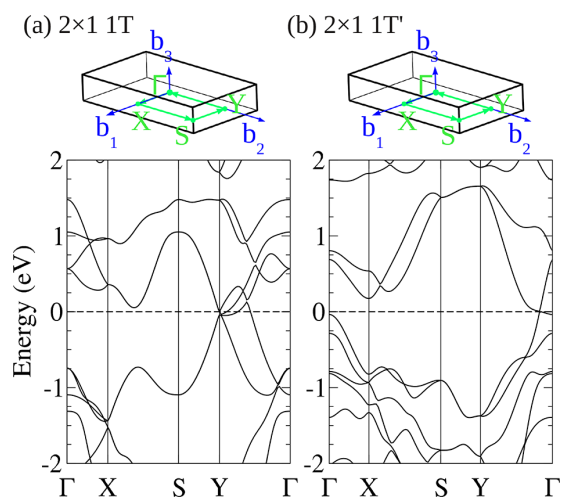


Figure 2. Brillouin zone paths and DFT-PBE band structures of MoSe_2 monolayers. (a) 2×1 1T orthorhombic cell and (b) 2×1 1T' orthorhombic cell. The Fermi level is set to zero energy.

degeneracies, resulting in energy gain. This can be seen in panel b, which presents the band structure for the 1T' monolayer with orthorhombic unit cell, which evolves from the orthorhombic 1T lattice by simple atomic relaxations (see Figure S1, Supporting Information). Comparing the band structures of the 1T and 1T' monolayers, it is clearly observed that the structural modifications that originate 1T' open a band gap of ~ 3 eV in the Y point, lowering the energy of occupied electronic bands. This reduction in the electronic energy contribution turns the distorted 1T' structure more energetically favorable than 1T. This effect can also be seen from the electronic DOS because the peak in the DOS located at the Fermi level in 1T disappears due to the distortion to 1T' (Figure S3, Supporting Information).

To study the effect of Peierls distortion on the geometric relaxation of MoSe_2 monolayers, 1T monolayer was relaxed using different cells, namely, hexagonal 1×1 , hexagonal 2×2 , hexagonal 3×3 , and orthorhombic 2×1 . As indicated in Figure 3a, we found that only the 1×1 model preserved the 1T configuration, while the others adopted a distorted

configuration, as observed for MoS_2 monolayers.¹⁸ Therefore, without the lattice constraints, the 1T structure is distorted upon geometric optimization as well as the nanoflakes constructed as 1T monolayer fragments, which directly evolve to 1T' nanoflakes (Figure 3b), so that there is no need to further consider nanoflakes in the 1T' structure. No structural distortions were observed when 2H monolayers were relaxed. The relaxation process is demonstrated for nanoflakes with 108 f.u. in Figure 3b, and similar nanoflakes with the number of formula units ranging from 15 to 192 were also considered and present the same characteristics of the relaxation process (Figures S4 and S5, Supporting Information). Substrate coupling may affect monolayer relative phase stability, for example, through charge transfer³¹ or induced strain; however, these effects particularly depend on the type of substrate and monolayer. Therefore, to obtain a general picture of the size-induced trend in the relative phase stability of 2D-TMDs, gas-phase nanoflakes were assumed in our calculations.

3.3. Size Effect on the Phase Stability of MoSe_2 Nanoflakes. The energy differences between the relaxed 2H and 1T' nanoflakes are shown as a function of the size in Figure 4a. The results indicate that the nanoflake size has an important role in the relative stability of the 2H and 1T' phases and reveal the existence of a size-induced 2H-1T' phase transition. Contrary to the preferential phase for the monolayer and bulk, the 1T' is the most energetically stable for the small-sized nanoflakes, and 2H becomes the most stable phase for nanoflakes with $n > 150$. We fitted the relative energy of relaxed nanoflakes with the function $\Delta E_{2\text{H}-1\text{T}'} = (-0.32 + ae^{-bn})$ (eV/f.u.), where -0.32 eV/f.u. is the 2H-1T' monolayer energy difference (see Figure S6, Supporting Information), which shows that relative energies within a 10% difference from the monolayer value are obtained with $n > 420$ f.u. For the nanoflakes with frozen structural configurations (2H and 1T monolayer fragments) (Figure 4b), 1T is the lowest energy structure only for the smallest nanoflake, thus indicating a minor role of the Peierls distortions in the relative energy trend and size-induced phase transition in the nanoflakes. The influence of size on the energetic properties of the nanoflakes is associated with the relevance of edge effects on total energy, which decreases as the nanoflakes grow. Therefore, the difference in edge energy between the two phases has an

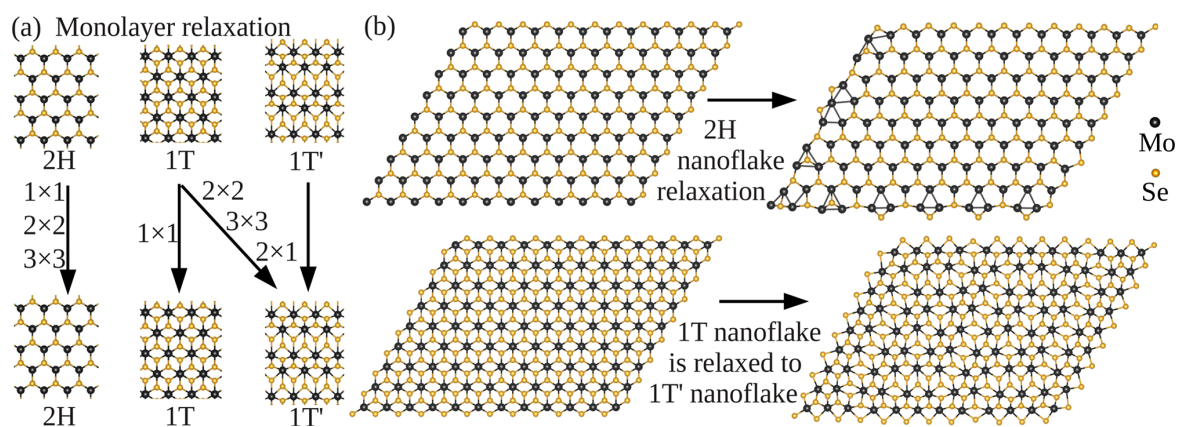


Figure 3. (a) Effect of relaxation on 2H, 1T and 1T' monolayers with different cells. (b) Atomic structural configurations of $(\text{MoSe}_2)_n$ nanoflakes with $n = 108$ for the initial structures (2H and 1T monolayer fragments) and relaxed structures.

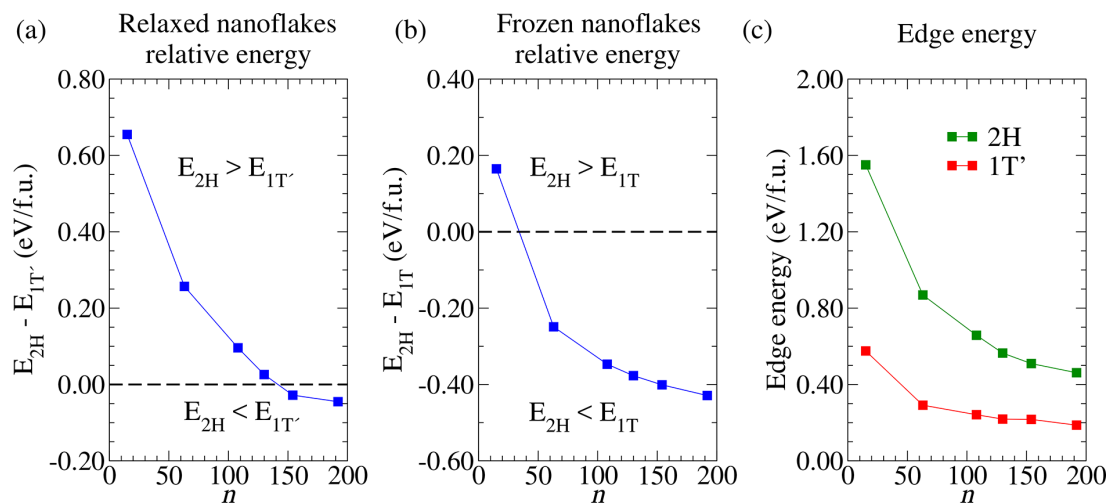


Figure 4. (a) Energy difference per f.u. between relaxed 2H and 1T' (MoSe₂)_n nanoflakes as a function of n . (b) Energy difference per f.u. between frozen 2H and 1T (MoSe₂)_n nanoflakes as a function of n . (c) Edge energy of the relaxed 2H and 1T' (MoSe₂)_n nanoflakes, calculated as described in the text.

important role in the relation between size and relative phase stability.

3.4. Role of Edge Energy and Structural Reconstructions. An estimate for the edge energy E_{edge} can be obtained by comparing the total energy of the nanoflakes with the monolayers, $E_{\text{edge}} = E_{\text{nanoflake}}^n - E_{\text{monolayer}}$, where $E_{\text{nanoflake}}^n$ is the total energy per f.u. of the relaxed nanoflake with n f.u. and $E_{\text{monolayer}}$ is the total energy per f.u. of the monolayer, in which 2H nanoflakes were compared with the 2H monolayer and 1T' nanoflakes were compared with the 1T' monolayer. In Figure 4c, it is shown that 2H nanoflakes have higher E_{edge} than 1T', and the difference decreases as nanoflake sizes increase, which is in line with the discussion made above for the edge energy role in the 2H-1T' phase transition.

Considering the unrelaxed nanoflake structures (Figure 3b), it is possible to note the characteristics of their edges. The nanoflakes derived from the 2H monolayer present two kinds of edges, (i) Mo-terminated and (ii) Se-terminated edges, whereas the 1T nanoflakes present only Se-terminated edges. After the minimization of the atomic forces in 2H nanoflakes, the Se-terminated edges were only minorly reconstructed, with small rearrangements of bond lengths, which also occurs in 1T' nanoflake edges. On the contrary, significant reconstructions occur in Mo-terminated edges of 2H nanoflakes: The Mo atoms tend to be displaced to the interior of the structure, and some of the neighboring Se atoms are moved outward. A similar pattern of reconstruction has been recently reported for the M-terminated zigzag edges of MQ₂ nanoribbons and is described as a mechanism of self-passivation of the metal atoms.^{32,33}

A small difference is observed between the relative energy trend of the relaxed nanoflakes (Figure 4a) and of the frozen nanoflakes (Figure 4b). In the case of the frozen nanoflakes, a change in the energetically favored phase occurs with smaller n when compared with the case of relaxed nanoflakes. Therefore, the structural reconstructions at the core region of the nanoflakes have a smaller importance to define the size effects on the relative energy. In 2H nanoflakes, energy changes due to relaxation (Figure S7, Supporting Information) come practically entirely from reconstructions of the edges, whereas

in 1T' this energy decrease is larger than in 2H (Figure S7, Supporting Information) and can be divided into two contributions, namely, edge relaxations and the Peierls distortions in the core.

3.5. Electronic Properties of (MoSe₂)_n Nanoflakes. The trigonal prismatic to octahedral phase transition in Mo dichalcogenides causes a change from semiconducting to metallic behavior.^{14,15} Therefore, to study the effect of the 2H-1T' phase transition on the electronic structure of the nanoflakes, the electronic DOS was examined and is shown for representative nanoflakes and also for 2H and 1T' monolayers in Figure 5 (DOS for the remaining nanoflakes are shown in Figure S8, Supporting Information). To represent the DOS, the contributions from edge atoms are separated from the remaining (core) atoms. This separation exposes a relevant feature of the 2H nanoflakes. Contrary to the 2H monolayer, the 2H nanoflakes have zero band gap, which is mainly due to the existence of edge Mo d and edge Se p states in the energy range of the 2H monolayer band gap. Contribution from core atoms is less relevant in this region, and its features are very similar to the 2H monolayer. In the 1T' nanoflakes, no relevant distinction exists between core and edge atom DOS, and they display the general features of the 1T' monolayer, with no band gap.

4. CONCLUSIONS

We conclude from our DFT investigation that nanoflake size plays a crucial role in the determination of relative phase stability of TMDs. Our results clearly demonstrate the change of energetic preference from octahedral to trigonal prismatic phase as MoSe₂ nanoflake size increases due to the higher edge energy of the trigonal prismatic structure. It was observed that nanoflakes in the trigonal prismatic phase have significant edge reconstructions, whereas nanoflakes and monolayers in the octahedral phase have a preference for a distorted structural configuration, driven by the mechanism of Peierls transition. The 2H-1T' phase transition generates modifications in the electronic structure of the MoSe₂ nanoflakes. Although both nanoflake structural phases have no band gap, in the trigonal prismatic structures this is caused by the electronic states from

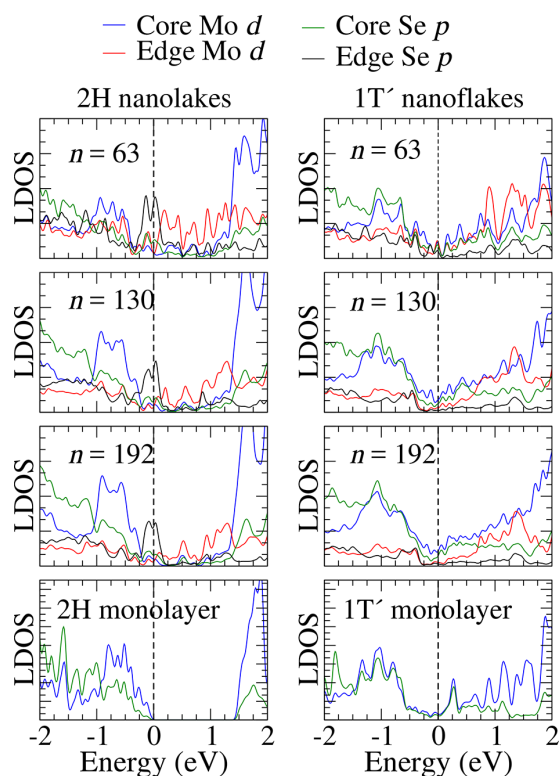


Figure 5. Local electronic density of states of the 2H and 1T' (MoSe_2)_n nanoflakes, $n = 63, 130,$ and $192,$ in which the contributions from edge and core atoms are distinguished. In the bottom panels, the DOS per unit cell of the 2H and 1T' monolayers are shown. The top of the valence band is set to zero energy.

atoms close the edges. The demonstrated size-induced phase transition in MoSe_2 nanoflakes points to an important path to investigate the mechanisms of structural phase transformations in TMDs and other 2D materials.

■ ASSOCIATED CONTENT

📄 Supporting Information

The Supporting Information is available free of charge on the ACS Publications website at DOI: 10.1021/acs.jpcc.8b03254.

Representation of orthorhombic supercell for 1T monolayer, density of states of 1T and 1T' monolayers, representation of the structural configurations of nanoflakes, fitting of the relative energy of relaxed nanoflakes, energy difference between the initial and reconstructed nanoflakes, electronic density of states of the nanoflakes, and geometric coordinates of the nanoflakes before and after relaxation. (PDF)

■ AUTHOR INFORMATION

Corresponding Author

*E-mail: juarez_dasilva@iqsc.usp.br.

ORCID

Rafael Besse: 0000-0002-1387-1273

Naidel A. M. S. Caturello: 0000-0002-0147-9514

Carlos M. O. Bastos: 0000-0002-9988-5202

Diego Guedes-Sobrinho: 0000-0002-3313-2822

Matheus P. Lima: 0000-0001-5389-7649

Guilherme M. Sipahi: 0000-0001-5563-9619

Juarez L. F. Da Silva: 0000-0003-0645-8760

Notes

The authors declare no competing financial interest.

■ ACKNOWLEDGMENTS

We acknowledge financial support from National Council for Scientific and Technological Development (CNPq, Brazil), Coordination for the Improvement of Higher Education Personnel (CAPES, Brazil), and São Paulo Research Foundation (FAPESP), Grant No. 2017/11631-2. R.B. acknowledges financial support (Ph.D. fellowship) from FAPESP, Grant No. 2017/09077-7. D.G.-S. acknowledges financial support (Ph.D. fellowship) from FAPESP, Grant No. 2013/15112-9. G.M.S. acknowledges financial support from CAPES CSF-PVE Grant No. 88881.068174/2014-01 and CNPq, Research Fellowship Grant No. 304289/2015-9. We acknowledge the National Laboratory for Scientific Computing (LNCC/MCTI, Brazil) for providing HPC resources of the SDumont supercomputer, which have contributed to the research results reported within this paper (<http://sdumont.lncc.br>). We acknowledge the infrastructure provided to our computer cluster by the Department of Information Technology – Campus São Carlos.

■ REFERENCES

- (1) Bhimanapati, G. R.; Lin, Z.; Meunier, V.; Jung, Y.; Cha, J.; Das, S.; Xiao, D.; Son, Y.; Strano, M. S.; Cooper, V. R.; et al. Recent Advances in Two-Dimensional Materials Beyond Graphene. *ACS Nano* **2015**, *9*, 11509–11539.
- (2) Novoselov, K. S.; Mishchenko, A.; Carvalho, A.; Castro Neto, A. H. 2D Materials and van der Waals Heterostructures. *Science* **2016**, *353*, aac9439.
- (3) Chhowalla, M.; Shin, H. S.; Eda, G.; Li, L.-J.; Loh, K. P.; Zhang, H. The Chemistry of Two-Dimensional Layered Transition Metal Dichalcogenide Nanosheets. *Nat. Chem.* **2013**, *5*, 263–275.
- (4) Manzeli, S.; Ovchinnikov, D.; Pasquier, D.; Yazyev, O. V.; Kis, A. 2D Transition Metal Dichalcogenides. *Nat. Rev. Mater.* **2017**, *2*, 17033.
- (5) Desai, S. B.; Madhupathy, S. R.; Sachid, A. B.; Llinas, J. P.; Wang, Q.; Ahn, G. H.; Pitner, G.; Kim, M. J.; Bokor, J.; Hu, C.; et al. MoS_2 Transistors with 1-Nanometer Gate Lengths. *Science* **2016**, *354*, 99–102.
- (6) Wang, Q. H.; Kalantar-Zadeh, K.; Kis, A.; Coleman, J. N.; Strano, M. S. Electronics and Optoelectronics of Two-Dimensional Transition Metal Dichalcogenides. *Nat. Nanotechnol.* **2012**, *7*, 699–712.
- (7) Tao, H.; Gao, Y.; Talreja, N.; Guo, F.; Texter, J.; Yan, C.; Sun, Z. Two-Dimensional Nanosheets for Electrocatalysis in Energy Generation and Conversion. *J. Mater. Chem. A* **2017**, *5*, 7257–7284.
- (8) Kang, W.; Wang, Y.; Xu, J. Recent Progress in Layered Metal Dichalcogenide Nanostructures as Electrodes for High-Performance Sodium-Ion Batteries. *J. Mater. Chem. A* **2017**, *5*, 7667–7690.
- (9) Du, K.-Z.; Wang, X.-Z.; Liu, Y.; Hu, P.; Utama, M. I. B.; Gan, C. K.; Xiong, Q.; Kloc, C. Weak Van der Waals Stacking, Wide-Range Band Gap, and Raman Study on Ultrathin Layers of Metal Phosphorus Trichalcogenides. *ACS Nano* **2016**, *10*, 1738–1743.
- (10) Besse, R.; Sabino, F. P.; Da Silva, J. L. F. Electronic Structure of Layered Quaternary Chalcogenide Materials for Band-gap Engineering: The Example of $\text{Cs}_2\text{M}^{\text{II}}\text{M}_3^{\text{IV}}\text{Q}_8$. *Phys. Rev. B: Condens. Matter Mater. Phys.* **2016**, *93*, 165205.
- (11) Geim, A. K.; Grigorieva, I. V. Van der Waals Heterostructures. *Nature* **2013**, *499*, 419–425.

- (12) Wei, G.; Czaplewski, D. A.; Lenferink, E. J.; Stanev, T. K.; Jung, I. W.; Stern, N. P. Size-Tunable Lateral Confinement in Monolayer Semiconductors. *Sci. Rep.* **2017**, *7*, 3324.
- (13) Yang, H.; Kim, S. W.; Chhowalla, M.; Lee, Y. H. Structural and Quantum-State Phase Transition in van der Waals Layered Materials. *Nat. Phys.* **2017**, *13*, 931–937.
- (14) Empante, T. A.; Zhou, Y.; Klee, V.; Nguyen, A. E.; Lu, I.-H.; Valentin, M. D.; Naghibi Alvilari, S. A.; Preciado, E.; Berges, A. J.; Merida, C. S.; et al. Chemical Vapor Deposition Growth of Few-Layer MoTe₂ in the 2H, 1T', and 1T Phases: Tunable Properties of MoTe₂ Films. *ACS Nano* **2017**, *11*, 900–905.
- (15) Friedman, A. L.; Hanbicki, A. T.; Perkins, F. K.; Jernigan, G. G.; Culbertson, J. C.; Campbell, P. M. Evidence for Chemical Vapor Induced 2H to 1T Phase Transition in MoX₂ (X = Se, S) Transition Metal Dichalcogenide Films. *Sci. Rep.* **2017**, *7*, 3836.
- (16) Qian, X.; Liu, J.; Fu, L.; Li, J. Quantum Spin Hall Effect in Two-Dimensional Transition Metal Dichalcogenides. *Science* **2014**, *346*, 1344–1347.
- (17) Kertesz, M.; Hoffmann, R. Octahedral vs. Trigonal-Prismatic Coordination and Clustering in Transition-Metal Dichalcogenides. *J. Am. Chem. Soc.* **1984**, *106*, 3453–3460.
- (18) Kan, M.; Wang, J.-Y.; Li, X.-W.; Zhang, S.-H.; Li, Y.-W.; Kawazoe, Y.; Sun, Q.; Jena, P. Structures and Phase Transition of a MoS₂ Monolayer. *J. Phys. Chem. C* **2014**, *118*, 1515–1522.
- (19) Wang, L.; Xu, Z.; Wang, W.; Bai, X. Atomic Mechanism of Dynamic Electrochemical Lithiation Processes of MoS₂ Nanosheets. *J. Am. Chem. Soc.* **2014**, *136*, 6693–6697.
- (20) Lin, Y.-C.; Dumcenco, D. O.; Huang, Y.-S.; Suenaga, K. Atomic Mechanism of the Semiconducting-to-Metallic Phase Transition in Single-Layered MoS₂. *Nat. Nanotechnol.* **2014**, *9*, 391–396.
- (21) Duerloo, K.-A. N.; Li, Y.; Reed, E. J. Structural Phase Transitions in Two-Dimensional Mo- and W- Dichalcogenide Monolayers. *Nat. Commun.* **2014**, *5*, 4214.
- (22) Zhou, S.; Han, J.; Sun, J.; Srolovitz, D. J. MoS₂ Edges and Heterophase Interfaces: Energy, Structure and Phase Engineering. *2D Mater.* **2017**, *4*, 025080.
- (23) Perdew, J. P.; Burke, K.; Ernzerhof, M. Generalized Gradient Approximation Made Simple. *Phys. Rev. Lett.* **1996**, *77*, 3865–3868.
- (24) Grimme, S.; Antony, J.; Ehrlich, S.; Krieg, H. A Consistent and Accurate *Ab Initio* Parametrization of Density Functional Dispersion Correction (DFT-D) for the 94 Elements H-Pu. *J. Chem. Phys.* **2010**, *132*, 154104.
- (25) Peelaers, H.; Van de Walle, C. G. First-Principles Study of van der Waals Interactions in MoS₂ and MoO₃. *J. Phys.: Condens. Matter* **2014**, *26*, 305502.
- (26) Blöchl, P. E. Projector Augmented-Wave Method. *Phys. Rev. B: Condens. Matter Mater. Phys.* **1994**, *50*, 17953–17979.
- (27) Kresse, G.; Joubert, D. From Ultrasoft Pseudopotentials to the Projector Augmented-Wave Method. *Phys. Rev. B: Condens. Matter Mater. Phys.* **1999**, *59*, 1758–1775.
- (28) Kresse, G.; Hafner, J. *Ab-Initio* Molecular Dynamics for Open-Shell Transition Metals. *Phys. Rev. B: Condens. Matter Mater. Phys.* **1993**, *48*, 13115–13118.
- (29) Kresse, G.; Furthmüller, J. Efficient Iterative Schemes for *Ab-Initio* Total-Energy Calculations Using a Plane-Wave Basis Set. *Phys. Rev. B: Condens. Matter Mater. Phys.* **1996**, *54*, 11169–11186.
- (30) Keum, D. H.; Cho, S.; Kim, J. H.; Choe, D.-H.; Sung, H.-J.; Kan, M.; Kang, H.; Hwang, J.-Y.; Kim, S. W.; Yang, H.; et al. Bandgap Opening in Few-Layered Monoclinic MoTe₂. *Nat. Phys.* **2015**, *11*, 482–486.
- (31) Ouyang, B.; Ou, P.; Wang, Y.; Mi, Z.; Song, J. Phase Engineering of MoS₂ Through GaN/AlN Substrate Coupling and Electron Doping. *Phys. Chem. Chem. Phys.* **2016**, *18*, 33351–33356.
- (32) Cui, P.; Choi, J.-H.; Chen, W.; Zeng, J.; Shih, C.-K.; Li, Z.; Zhang, Z. Contrasting Structural Reconstructions, Electronic Properties, and Magnetic Orderings Along Different Edges of Zigzag Transition Metal Dichalcogenide Nanoribbons. *Nano Lett.* **2017**, *17*, 1097–1101.
- (33) Chen, Y.; Cui, P.; Ren, X.; Zhang, C.; Jin, C.; Zhang, Z.; Shih, C.-K. Fabrication of MoSe₂ Nanoribbons via an Unusual Morphological Phase Transition. *Nat. Commun.* **2017**, *8*, 15135.

APPENDIX B – SUPPORTING INFORMATION

Supplementary Data to Stability and accuracy control of $\mathbf{k}\cdot\mathbf{p}$ parameters

Carlos M. O. Bastos,¹ Fernando P. Sabino,¹ Paulo E. Faria Junior,^{1,2}
Tiago Campos,¹ Juarez L. F. Da Silva,³ and Guilherme M. Sipahi^{1,2}

¹*São Carlos Institute of Physics, University of São Paulo,
PO Box 369, 13560-970, São Carlos, SP, Brazil.*

²*Department of Physics, State University of New York at Buffalo, 14260, Buffalo, New York, USA*

³*São Carlos Institute of Chemistry, University of São Paulo,
PO Box 780, 13560-970, São Carlos, SP, Brazil.*

I. THE $\mathbf{k}\cdot\mathbf{p}$ METHOD

The quantum-mechanical treatment of the many body problem composed by electrons and nuclei in solid state materials is a complex task, in particular, due to the electron-electron interactions. Along the years, several approaches have been proposed to address this problem, which include the solution of the Schroedinger equation using trial wave functions at different levels of approximations such as the Hartree-Fock method combined with Møller-Plesset perturbation theory or methods based on DFT [1, 2]. Although accurate, these methods are computationally demanding. The limit of thousand-atoms on one system using state-of-the-art computational resources precludes their use on mesoscopic and even in nanoscopic systems, e.g., a 100 Å wide zinc blende GaAs nanowire would demand at least 950 atoms for the correct description of one atomic layer. Plenty of interesting problems reside beyond this hard wall barrier. Alternatively, the use of the crystal symmetry to extract the main features of the electronic structure leads to another class of approaches that overcome the computational resources barrier, known generally as effective mass methods. In such methods, the many-body problem can be simplified by using an approximation in which an effective single electron moves in the field generated by the screened electron-nuclei and electron-electron systems. When many bands are included in this description the method is known as the $\mathbf{k}\cdot\mathbf{p}$ method, and have been used since the 50's [3–5] to predict electronic and optical properties of semiconductors.

Below, we will summarize the key features of the $\mathbf{k}\cdot\mathbf{p}$ method as it is described in several references elsewhere [3, 6, 7]. The one-electron Hamiltonian including relativistic SOC effects can be written as follows,

$$H = \frac{p^2}{2m_0} + V(\mathbf{r}) + \frac{\hbar}{4m_0^2c^2} [\nabla V(\mathbf{r}) \times \mathbf{p}] \cdot \boldsymbol{\sigma}, \quad (1)$$

where the first term is the kinetic energy of the electrons, the second term is the effective potential experienced by the electrons and the last term is the SOC contribution. The linear momentum operator is given by $\mathbf{p} = -i\hbar\nabla$, m_0 is the electron mass, c is the velocity of light, \hbar is the Planck constant divided by 2π and $\boldsymbol{\sigma}$ is a vector containing the Pauli matrices. Due to the translational symmetry of ideal crystalline systems, the effective potential is a periodic function, and hence, the wave function solution must satisfy the Bloch's theorem, i.e.,

$$\Psi_{n,\mathbf{k}}(\mathbf{r}) = e^{i\mathbf{k}\cdot\mathbf{r}} u_{n,\mathbf{k}}(\mathbf{r}), \quad (2)$$

where $\Psi(\mathbf{r})$ is the total wave function (known as the Bloch function), \mathbf{k} is a wave vector usually restricted to the FBZ, $u_{n,\mathbf{k}}(\mathbf{r})$ is a function with the same period as the crystal, and n indicates the energy band index. A simple algebraic manipulation shows that

$$\mathbf{p}\Psi_{n,\mathbf{k}}(\mathbf{r}) = e^{i\mathbf{k}\cdot\mathbf{r}} (\hbar\mathbf{k} + \mathbf{p}) u_{n,\mathbf{k}}(\mathbf{r}), \quad (3)$$

and by applying this transformation on the wave functions (2), the Hamiltonian (1), from now on identified as H_{kp} , may be simplified to act only on the periodic functions, $u_{n,\mathbf{k}}(\mathbf{r})$, i.e.,

$$H_{kp} u_{n,\mathbf{k}}(\mathbf{r}) = E_n(\mathbf{k}) u_{n,\mathbf{k}}(\mathbf{r}), \quad (4)$$

where,

$$\begin{aligned} H_{kp} = & \frac{p^2}{2m_0} + V(\mathbf{r}) + \frac{\hbar^2 k^2}{2m_0} + \frac{\hbar}{m_0} \mathbf{k} \cdot \mathbf{p} \\ & + \frac{\hbar}{4m_0^2c^2} [\nabla V(\mathbf{r}) \times \mathbf{p}] \cdot \boldsymbol{\sigma} + \frac{\hbar^2}{4m_0^2c^2} \mathbf{k} \cdot [\boldsymbol{\sigma} \times \nabla V(\mathbf{r})]. \end{aligned} \quad (5)$$

Equation (5) is the $\mathbf{k}\cdot\mathbf{p}$ Hamiltonian with SOC. This is an exact Hamiltonian that describes the motion of an electron in a periodic crystal. Despite been exact, there is no analytical solution for equation (4) and, at least, three approximations should be made in order to solve it to a certain degree.

The first approximation is to assume that we know the solutions for a particular point in reciprocal space, usually defined as k_0 . Then, we can expand Hamiltonian (5) around such point, and separate it into two different terms: one containing only non-vanishing terms at the expansion point

$$H_0 = \frac{p^2}{2m_0} + V(\mathbf{r}) + \frac{\hbar^2 k_0^2}{2m_0} + \frac{\hbar}{m_0} \mathbf{k}_0 \cdot \mathbf{p} + \frac{\hbar^2}{4m_0^2 c^2} \mathbf{k}_0 \cdot [\boldsymbol{\sigma} \times \nabla V(\mathbf{r})], \quad (6)$$

and the other containing the other terms

$$H_P = \frac{\hbar^2}{2m_0} (k^2 - k_0^2) + \frac{\hbar}{m_0} (\mathbf{k} - \mathbf{k}_0) \cdot \mathbf{p} + \frac{\hbar}{4m_0^2 c^2} [\nabla V(\mathbf{r}) \times \mathbf{p}] \cdot \boldsymbol{\sigma} + \frac{\hbar^2}{4m_0^2 c^2} (\mathbf{k} - \mathbf{k}_0) \cdot [\boldsymbol{\sigma} \times \nabla V(\mathbf{r})]. \quad (7)$$

Rewriting equation (4), we get

$$H_{kp} u_{n,\mathbf{k}}(\mathbf{r}) = (H_0 + H_P) u_{n,\mathbf{k}}(\mathbf{r}) = E_n(\mathbf{k}) u_{n,\mathbf{k}}(\mathbf{r}). \quad (8)$$

The second approximation is to define a basis set for equation (8). In principle a complete basis set would be all orbitals on each atom of the basis of the crystal structure, i. e., any state from any atom of the crystal unit cell. Although this basis set is complete, it does not help on solving the problem, it is too big. An educated guess would be to use a truncated basis set that describe the most important features of the host crystal. Group theory is used to determine the symmetry of the states.

The third approximation is to use perturbation theory in order to define the matrix elements of equation (8). A perturbative approach, proposed by Löwdin [8] in the early 50's is used to solve this problem. In this formalism, the states are separated into two classes, A and B. The states in class A will be chosen in order to address the energy bands of interest and consequently, will be the basis set of the Hamiltonian matrix. Class B will comprise the remaining bands of the system. Even if the remote bands are outside the energy range we are interested in, their interaction with states in class A can provide important additional terms to the Hamiltonian. Using Dirac notation, from now on, a total state of the system can be written as

$$|n\mathbf{k}\rangle = \sum_{\alpha}^A c_{\alpha n}(\mathbf{k}) |\alpha\rangle + \sum_{\beta}^B c_{\beta n}(\mathbf{k}) |\beta\rangle, \quad (9)$$

where $|\alpha\rangle$ and $|\beta\rangle$ are the states in class A and B, respectively. For clarity, we have $u_{n,\mathbf{k}}(\mathbf{r}) = \langle n\mathbf{k}|\mathbf{r}\rangle$, $u_{\alpha,\mathbf{k}_0}(\mathbf{r}) = \langle \alpha|\mathbf{r}\rangle$ and $u_{\beta,\mathbf{k}_0}(\mathbf{r}) = \langle \beta|\mathbf{r}\rangle$. The symmetry provided in the previous step is used in this one to reduce the work by indicating the terms that are forbidden by symmetry.

Therefore, the matrix elements of equation (8) are given by

$$\begin{aligned} \langle \alpha | H_0 + H_P | \alpha' \rangle &= E_{\alpha}(\mathbf{k} - \mathbf{k}_0) \delta_{\alpha\alpha'} + \langle \alpha | \frac{\hbar}{m_0} (\mathbf{k} - \mathbf{k}_0) \cdot \mathbf{p} | \alpha' \rangle \\ &+ \langle \alpha | \frac{\hbar}{4m_0^2 c^2} [\nabla V(\mathbf{r}) \times \mathbf{p}] \cdot \boldsymbol{\sigma} | \alpha' \rangle \\ &+ \sum_{\beta} \frac{\langle \alpha | \frac{\hbar}{m_0} (\mathbf{k} - \mathbf{k}_0) \cdot \mathbf{p} | \beta \rangle \langle \beta | \frac{\hbar}{m_0} (\mathbf{k} - \mathbf{k}_0) \cdot \mathbf{p} | \alpha' \rangle}{E_{\alpha} - E_{\beta}}, \end{aligned} \quad (10)$$

with

$$E_{\alpha}(\mathbf{k} - \mathbf{k}_0) = E_{\alpha}(\mathbf{k}_0) + \frac{\hbar^2}{2m_0} (k^2 - k_0^2), \quad (11)$$

where $E_{\alpha}(\mathbf{k}_0)$ is given by

$$H_0 u_{\alpha,\mathbf{k}_0}(\mathbf{r}) = E_{\alpha}(\mathbf{k}_0) u_{\alpha,\mathbf{k}_0}(\mathbf{r}). \quad (12)$$

The evaluation of the matrix elements in equation (10) is indeed a very complicated task. Looking carefully into this expression, one can see that the dipole moments (proportional to the matrix elements $\langle \alpha | \frac{\hbar}{m_0} (\mathbf{k} - \mathbf{k}_0) \cdot \mathbf{p} | \beta \rangle$) of all the transitions among the different states in the description are needed, as well as the transition energies associated with them (E_α and E_β). An alternative approach to look for all these data and performing all these sums, would be determining their functional form using group theory arguments [3, 5, 9], replacing their analytical definitions by a parametrization.

Our material of choice is the zinc blende GaAs that has a direct band gap with the maximum valence band (VBM) and the minimum conduction band (CBM) at the Γ -point. Thus, to investigate electronic properties such as optical transitions and transport, the choice of the Γ -point ($\mathbf{k}_0 = \mathbf{0}$) for the unperturbed Hamiltonian is straightforward. We considered as class A the following electronic states, the topmost six states in the valence band (VB) (usually referred to as p -like states) and the first two states at the conduction band (CB) (usually referred to as s -like states), as described below:

$$\begin{aligned}
|\text{HH } \uparrow\rangle &= \frac{1}{\sqrt{2}} |(X + iY) \uparrow\rangle & |\text{HH } \downarrow\rangle &= \frac{i}{\sqrt{2}} |(X - iY) \downarrow\rangle \\
|\text{LH } \uparrow\rangle &= \frac{i}{\sqrt{6}} |(X + iY) \downarrow - 2Z \uparrow\rangle & |\text{LH } \downarrow\rangle &= \frac{1}{\sqrt{6}} |(X - iY) \uparrow + 2Z \downarrow\rangle, \\
|\text{SO } \uparrow\rangle &= \frac{1}{\sqrt{3}} |(X + iY) \downarrow + Z \uparrow\rangle & |\text{SO } \downarrow\rangle &= \frac{i}{\sqrt{3}} |-(X - iY) \uparrow + Z \downarrow\rangle \\
|\text{CB } \uparrow\rangle &= |S \uparrow\rangle & |\text{CB } \downarrow\rangle &= |S \downarrow\rangle
\end{aligned} \tag{13}$$

where HH, LH and SO are the heavy hole, light hole and split-off hole valence band states, respectively, and CB is the conduction band state. \uparrow and \downarrow represent a pseudo-spin variable used to distinguish the degenerate solutions at Γ -point.

In the zinc blende symmetry group, T_d , the Bloch functions at Γ -point have the following symmetries [9, 10]: $|X\rangle \sim x$, $|Y\rangle \sim y$, $|Z\rangle \sim z$ and $|S\rangle \sim x^2 + y^2 + z^2$. The symbol \sim means that the state on the left (e. g., $|X\rangle$) transforms as the function on the right (e. g., x -coordinate) under the symmetry operations of the T_d group. The linear combinations of $|X\rangle$, $|Y\rangle$, $|Z\rangle$ and $|S\rangle$ given in the basis set (13) diagonalizes the SOC interaction at $\mathbf{k} = (0, 0, 0)$ [6, 11]. The matrix representation of (10) in the basis set (13) is

$$\begin{pmatrix}
Q & S & R & 0 & i\frac{S}{\sqrt{2}} & -i\sqrt{2}R & -iP_- & 0 \\
S^\dagger & T & 0 & R & i\frac{(T-Q)}{\sqrt{2}} & i\sqrt{\frac{2}{3}}S & \sqrt{\frac{2}{3}}P_z & -\frac{1}{\sqrt{3}}P_- \\
R^\dagger & 0 & T & -S & -i\sqrt{\frac{3}{2}}S^\dagger & i\frac{(T-Q)}{\sqrt{2}} & -\frac{i}{\sqrt{3}}P_+ & -i\sqrt{\frac{2}{3}}P_z \\
0 & R^\dagger & -S^\dagger & Q & -i\sqrt{2}R^\dagger & -i\frac{S^\dagger}{\sqrt{2}} & 0 & -P_+ \\
-i\frac{S^\dagger}{\sqrt{2}} & -i\frac{(T-Q)^\dagger}{\sqrt{2}} & i\sqrt{\frac{3}{2}}S & i\sqrt{2}R & \frac{Q+T}{2} + \Delta_{so} & 0 & -\frac{i}{\sqrt{3}}P_z & -i\sqrt{\frac{2}{3}}P_- \\
i\sqrt{2}R^\dagger & -i\sqrt{\frac{3}{2}}S^\dagger & -i\frac{(T-Q)^\dagger}{\sqrt{2}} & i\frac{S}{\sqrt{2}} & 0 & \frac{Q+T}{2} + \Delta_{so} & \sqrt{\frac{2}{3}}P_+ & -\frac{1}{\sqrt{3}}P_z \\
-iP_- & \sqrt{\frac{2}{3}}P_z & \frac{i}{\sqrt{3}}P_- & 0 & \frac{i}{\sqrt{3}}P_z & \sqrt{\frac{2}{3}}P_- & E_c & 0 \\
0 & -\frac{1}{\sqrt{3}}P_+ & i\sqrt{\frac{2}{3}}P_z & -P_- & i\sqrt{\frac{2}{3}}P_+ & -\frac{1}{\sqrt{3}}P_z & 0 & E_c
\end{pmatrix} \tag{14}$$

where the terms are given by

$$\begin{aligned}
Q &= -\frac{\hbar^2}{2m_0} [(\tilde{\gamma}_1 + \tilde{\gamma}_2)(k_x^2 + k_y^2) - (\tilde{\gamma}_1 - 2\tilde{\gamma}_2)k_z^2] & R &= -\frac{\hbar^2}{2m_0}\sqrt{3} [\tilde{\gamma}_2(k_x^2 - k_y^2) + 2i\tilde{\gamma}_3k_xk_y] \\
E_c &= E_g + \frac{\hbar^2}{2m_0}\tilde{\epsilon}k^2 & P_z &= P k_z \\
T &= -\frac{\hbar^2}{2m_0} [(\tilde{\gamma}_1 - \tilde{\gamma}_2)(k_x^2 + k_y^2) + (\tilde{\gamma}_1 + 2\tilde{\gamma}_2)k_z^2] & S &= i\frac{\hbar^2}{2m_0} [2\sqrt{3}\tilde{\gamma}_3k_z(k_x - ik_y)] \\
P_\pm &= \frac{1}{\sqrt{2}}P(k_x \pm ik_y) & k^2 &= k_x^2 + k_y^2 + k_z^2
\end{aligned} \tag{15}$$

II. ANALYTICAL FUNCTIONS FOR THE Γ - K AND Γ - L DIRECTIONS

In the main article, we presented the general procedure to determine analytical functions and their numerical counterparts. In this appendix we show the functions for all directions used in this work.

For the Γ - X direction:

$$\begin{aligned}
c_{HH}^A(k_{\Gamma X}, \{p\}) &= -(\tilde{\gamma}_1 - 2\tilde{\gamma}_2) \frac{\hbar^2 k_{\Gamma X}^2}{2m_0} \\
c_0^A(k_{\Gamma X}, \{p\}) &= \Delta_{SO} - E_g + [2(\tilde{\gamma}_1 + \tilde{\gamma}_2) - \tilde{e}] \frac{\hbar^2 k_{\Gamma X}^2}{2m_0} \\
c_1^A(k_{\Gamma X}, \{p\}) &= -\Delta_{SO} E_g - \left[\Delta_{SO} (\tilde{e} - \tilde{\gamma}_1 - 2\tilde{\gamma}_2) + 2E_g (\tilde{\gamma}_1 + \tilde{\gamma}_2) + \frac{2m_0}{\hbar^2} P^2 \right] \frac{\hbar^2 k_{\Gamma X}^2}{2m_0} \\
&\quad + [-2\tilde{e}(\tilde{\gamma}_1 + \tilde{\gamma}_2) + \tilde{\gamma}_1^2 + 2\tilde{\gamma}_1\tilde{\gamma}_2 - 8\tilde{\gamma}_2^2] \left(\frac{\hbar^2 k_{\Gamma X}^2}{2m_0} \right)^2 \\
c_2^A(k_{\Gamma X}, \{p\}) &= - \left[\Delta_{SO} E_g (\tilde{\gamma}_1 + 2\tilde{\gamma}_2) + \frac{2}{3} \Delta_{SO} \frac{2m_0}{\hbar^2} P^2 \right] \frac{\hbar^2 k_{\Gamma X}^2}{2m_0} \\
&\quad - \left[\Delta_{SO} \tilde{e} (\tilde{\gamma}_1 + 2\tilde{\gamma}_2) + E_g (\tilde{\gamma}_1 + 4\tilde{\gamma}_2) (\tilde{\gamma}_1 - 2\tilde{\gamma}_2) + \frac{2m_0}{\hbar^2} P^2 (\tilde{\gamma}_1 - 2\tilde{\gamma}_2) \right] \left(\frac{\hbar^2 k_{\Gamma X}^2}{2m_0} \right)^2 \\
&\quad - \tilde{e} (\tilde{\gamma}_1 + 4\tilde{\gamma}_2) (\tilde{\gamma}_1 - 2\tilde{\gamma}_2) \left(\frac{\hbar^2 k_{\Gamma X}^2}{2m_0} \right)^3
\end{aligned} \tag{16}$$

where $k_{\Gamma X}$ indicates a point along the $\Gamma - X$ direction. Please notice that in these expressions the Kane parameter P appear always as part of its energetic counterpart $E_P = 2m_0 P^2 / \hbar^2$.

For the Γ - K direction we have

$$\begin{aligned}
c_0^A(k_{\Gamma K}, \{p\}) &= \Delta_{SO} - E_g - (\tilde{e} - 3\tilde{\gamma}_1) \frac{\hbar^2 k_{\Gamma K}^2}{2m_0} \\
c_1^A(k_{\Gamma K}, \{p\}) &= -\Delta_{SO} E_g - \left[\Delta_{SO} (\tilde{e} - 2\tilde{\gamma}_1) + 3E_g \tilde{\gamma}_1 + \frac{2m_0}{\hbar^2} P^2 \right] \frac{\hbar^2 k_{\Gamma K}^2}{2m_0} \\
&\quad - [3\tilde{e}\tilde{\gamma}_1 - 3\tilde{\gamma}_1^2 + 3\tilde{\gamma}_2^2 + 9\tilde{\gamma}_3^2] \left(\frac{\hbar^2 k_{\Gamma K}^2}{2m_0} \right)^2 \\
c_2^A(k_{\Gamma K}, \{p\}) &= - \left[2\Delta_{SO} E_g \tilde{\gamma}_1 + \frac{2}{3} \Delta_{SO} \frac{2m_0}{\hbar^2} P^2 \right] \frac{\hbar^2 k_{\Gamma K}^2}{2m_0} \\
&\quad - [2(\tilde{e}\tilde{\gamma}_1 - \tilde{\gamma}_1^2 + \tilde{\gamma}_2^2 + 3\tilde{\gamma}_3^2) \Delta_{SO} - 3(-\tilde{\gamma}_1^2 + \tilde{\gamma}_2^2 + \tilde{\gamma}_3^2) E_g \\
&\quad + (2\tilde{\gamma}_1 - \tilde{\gamma}_2 - 3\tilde{\gamma}_3) \frac{2m_0}{\hbar^2} P^2] \left(\frac{\hbar^2 k_{\Gamma K}^2}{2m_0} \right)^2 \\
&\quad - [3\tilde{e}(\tilde{\gamma}_1^2 - \tilde{\gamma}_2^2 - 3\tilde{\gamma}_3^2) + \tilde{\gamma}_1(-\tilde{\gamma}_1^2 + 3\tilde{\gamma}_2^2 + 9\tilde{\gamma}_3^2) + 2\tilde{\gamma}_2^3 - 18\tilde{\gamma}_2\tilde{\gamma}_3^2] \left(\frac{\hbar^2 k_{\Gamma K}^2}{2m_0} \right)^3 \\
c_3^A(k_{\Gamma K}, \{p\}) &= - \left[\Delta_{SO} E_g (\tilde{\gamma}_1^2 - \tilde{\gamma}_2^2 - 3\tilde{\gamma}_3^2) + \frac{\Delta_{SO}}{3} (2\tilde{\gamma}_1 - \tilde{\gamma}_2 - 3\tilde{\gamma}_3) \frac{2m_0}{\hbar^2} P^2 \right] \left(\frac{\hbar^2 k_{\Gamma K}^2}{2m_0} \right)^2 \\
&\quad - [\Delta_{SO} \tilde{e} (\tilde{\gamma}_1^2 - \tilde{\gamma}_2^2 - 3\tilde{\gamma}_3^2) + E_g (\tilde{\gamma}_1 - 2\tilde{\gamma}_2) (\tilde{\gamma}_1 + \tilde{\gamma}_2 + 3\tilde{\gamma}_3) (\tilde{\gamma}_1 + \tilde{\gamma}_2 - 3\tilde{\gamma}_3) \\
&\quad + (\tilde{\gamma}_1 - 2\tilde{\gamma}_2) (\tilde{\gamma}_1 + \tilde{\gamma}_2 - 3\tilde{\gamma}_3) \frac{2m_0}{\hbar^2} P^2] \left(\frac{\hbar^2 k_{\Gamma K}^2}{2m_0} \right)^3 \\
&\quad - \tilde{e} (\tilde{\gamma}_1 - 2\tilde{\gamma}_2) (\tilde{\gamma}_1 + \tilde{\gamma}_2 + 3\tilde{\gamma}_3) (\tilde{\gamma}_1 + \tilde{\gamma}_2 - 3\tilde{\gamma}_3) \left(\frac{\hbar^2 k_{\Gamma K}^2}{2m_0} \right)^4
\end{aligned} \tag{17}$$

with the numerical counterpart being

$$\begin{aligned}
c_0^N(k_{\Gamma K}) &= -\epsilon_{CB}(k_{\Gamma K}) - \epsilon_{LH}(k_{\Gamma K}) - \epsilon_{SO}(k_{\Gamma K}) - \epsilon_{HH}(k_{\Gamma K}) \\
c_1^N(k_{\Gamma K}) &= \epsilon_{CB}(k_{\Gamma K})\epsilon_{LH}(k_{\Gamma K}) + \epsilon_{SO}(k_{\Gamma K})\epsilon_{LH}(k_{\Gamma K}) + \epsilon_{HH}(k_{\Gamma K})\epsilon_{LH}(k_{\Gamma K}) + \epsilon_{CB}(k_{\Gamma K})\epsilon_{SO}(k_{\Gamma K}) + \\
&\quad \epsilon_{CB}(k_{\Gamma K})\epsilon_{HH}(k_{\Gamma K}) + \epsilon_{SO}(k_{\Gamma K})\epsilon_{HH}(k_{\Gamma K}) \\
c_2^N(k_{\Gamma K}) &= -\epsilon_{CB}(k_{\Gamma K})\epsilon_{LH}(k_{\Gamma K})\epsilon_{SO}(k_{\Gamma K}) - \epsilon_{CB}(k_{\Gamma K})\epsilon_{HH}(k_{\Gamma K})\epsilon_{SO}(k_{\Gamma K}) - \epsilon_{LH}(k_{\Gamma K})\epsilon_{HH}(k_{\Gamma K})\epsilon_{SO}(k_{\Gamma K}) - \\
&\quad \epsilon_{CB}(k_{\Gamma K})\epsilon_{LH}(k_{\Gamma K})\epsilon_{HH}(k_{\Gamma K}) \\
c_3^N(k_{\Gamma K}) &= \epsilon_{CB}(k_{\Gamma K})\epsilon_{LH}(k_{\Gamma K})\epsilon_{SO}(k_{\Gamma K})\epsilon_{HH}(k_{\Gamma K})
\end{aligned} \tag{18}$$

The Γ - L direction functions are

$$\begin{aligned}
c_{HH}^A(k_{\Gamma L}, \{p\}) &= -(\tilde{\gamma}_1 - 2\tilde{\gamma}_3) \frac{\hbar^2 k_{\Gamma L}^2}{2m_0} \\
c_0^A(k_{\Gamma L}, \{p\}) &= \Delta_{SO} - E_g + [2(\tilde{\gamma}_1 + \tilde{\gamma}_3) - \tilde{e}] \frac{\hbar^2 k_{\Gamma L}^2}{2m_0} \\
c_1^A(k_{\Gamma L}, \{p\}) &= -\Delta_{SO} E_g - \left[\Delta_{SO} (\tilde{e} - \tilde{\gamma}_1 - 2\tilde{\gamma}_3) + 2E_g (\tilde{\gamma}_1 + \tilde{\gamma}_3) + \frac{2m_0}{\hbar^2} P^2 \right] \frac{\hbar^2 k_{\Gamma L}^2}{2m_0} \\
&\quad + [-2\tilde{e}(\tilde{\gamma}_1 + \tilde{\gamma}_3) + \tilde{\gamma}_1^2 + 2\tilde{\gamma}_1\tilde{\gamma}_3 - 8\tilde{\gamma}_3^2] \left(\frac{\hbar^2 k_{\Gamma L}^2}{2m_0} \right)^2 \\
c_2^A(k_{\Gamma L}, \{p\}) &= -\left[\Delta_{SO} E_g (\tilde{\gamma}_1 + 2\tilde{\gamma}_3) + \frac{2}{3} \Delta_{SO} \frac{2m_0}{\hbar^2} P^2 \right] \frac{\hbar^2 k_{\Gamma L}^2}{2m_0} \\
&\quad - \left[\Delta_{SO} \tilde{e} (\tilde{\gamma}_1 + 2\tilde{\gamma}_3) + E_g (\tilde{\gamma}_1 + 4\tilde{\gamma}_3) (\tilde{\gamma}_1 - 2\tilde{\gamma}_3) + \frac{2m_0}{\hbar^2} P^2 (\tilde{\gamma}_1 - 2\tilde{\gamma}_3) \right] \left(\frac{\hbar^2 k_{\Gamma L}^2}{2m_0} \right)^2 \\
&\quad - \tilde{e} (\tilde{\gamma}_1 + 4\tilde{\gamma}_3) (\tilde{\gamma}_1 - 2\tilde{\gamma}_3) \left(\frac{\hbar^2 k_{\Gamma L}^2}{2m_0} \right)^3
\end{aligned} \tag{19}$$

and their numerical counterpart

$$\begin{aligned}
c_{HH}^N(k_{\Gamma L}) &= -\epsilon_{HH}(k_{\Gamma L}) \\
c_0^N(k_{\Gamma L}) &= -\epsilon_{CB}(k_{\Gamma L}) - \epsilon_{LH}(k_{\Gamma L}) - \epsilon_{SO}(k_{\Gamma L}) \\
c_1^N(k_{\Gamma L}) &= \epsilon_{CB}(k_{\Gamma L})\epsilon_{LH}(k_{\Gamma L}) + \epsilon_{SO}(k_{\Gamma L})\epsilon_{LH}(k_{\Gamma L}) + \epsilon_{CB}(k_{\Gamma L})\epsilon_{SO}(k_{\Gamma L}) \\
c_2^N(k_{\Gamma L}) &= -\epsilon_{CB}(k_{\Gamma L})\epsilon_{LH}(k_{\Gamma L})\epsilon_{SO}(k_{\Gamma L})
\end{aligned} \tag{20}$$

III. 6X6 HAMILTONIAN

In the paper, we considered the 8×8 Kane Hamiltonian. However, for large gap materials or when the interest relies in effects occurring only inside the valence band, we can neglect the interaction between the conduction and valence bands, setting the parameter P to zero. In such approach, we can define two independent A classes, one for valence band (2×2) states and the other for the conduction band states (6×6), obtaining a new Hamiltonian that will be denoted as 6×6 [7].

Although the functional form of the 6×6 and 8×8 terms are the same, the different choices for the A classes requires

correction in the effective mass parameters. The Hamiltonian is given by the following matrix

$$\begin{pmatrix} Q & S & R & 0 & i\frac{S}{\sqrt{2}} & -i\sqrt{2}R & 0 & 0 \\ S^\dagger & T & 0 & R & i\frac{(T-Q)}{\sqrt{2}} & i\sqrt{\frac{3}{2}}S & 0 & 0 \\ R^\dagger & 0 & T & -S & -i\sqrt{\frac{3}{2}}S^\dagger & i\frac{(T-Q)}{\sqrt{2}} & 0 & 0 \\ 0 & R^\dagger & -S^\dagger & Q & -i\sqrt{2}R^\dagger & -i\frac{S^\dagger}{\sqrt{2}} & 0 & 0 \\ -i\frac{S^\dagger}{\sqrt{2}} & -i\frac{(T-Q)^\dagger}{\sqrt{2}} & i\sqrt{\frac{3}{2}}S & i\sqrt{2}R & \frac{Q+T}{2} + \Delta_{so} & 0 & 0 & 0 \\ i\sqrt{2}R^\dagger & -i\sqrt{\frac{3}{2}}S^\dagger & -i\frac{(T-Q)^\dagger}{\sqrt{2}} & i\frac{S}{\sqrt{2}} & 0 & \frac{Q+T}{2} + \Delta_{so} & 0 & 0 \\ 0 & 0 & 0 & 0 & 0 & 0 & E_c & 0 \\ 0 & 0 & 0 & 0 & 0 & 0 & 0 & E_c \end{pmatrix} \quad (21)$$

with the terms being

$$\begin{aligned} Q &= -\frac{\hbar^2}{2m_0} [(\gamma_1 + \gamma_2)(k_x^2 + k_y^2) - (\gamma_1 - 2\gamma_2)k_z^2] & T &= \frac{\hbar^2}{2m_0} [(\gamma_2 - \gamma_1)(k_x^2 + k_y^2) - (\gamma_1 + 2\gamma_2)k_z^2] \\ R &= \frac{\hbar^2}{2m_0} \sqrt{3} [(2i\gamma_3 k_x k_y) + \gamma_2(k_x^2 - k_y^2)] & S &= \frac{\hbar^2}{2m_0} [2\sqrt{3}i\gamma_3 k_z(k_x - ik_y)] \\ E_c &= E_g + e\frac{\hbar^2 k^2}{2m_0} & k^2 &= k_x^2 + k_y^2 + k_z^2. \end{aligned} \quad (22)$$

IV. FITTING FUNCTIONS OF THE 6X6 HAMILTONIAN

We also applied the fitting method to obtain the parameters for the 6×6 Hamiltonian (21) as described in section 3 in the paper. In this Hamiltonian, valence and conduction band are decoupled and can be treated independently. As conduction band is a diagonal block with dimension 2, we have the following polynomial equation:

$$[-\epsilon + c_0^A(\mathbf{k}, \{p\})]^2 = 0, \quad (23)$$

where the square in the expression means a the two-fold degeneracy of the eigenvalues. The analytical coefficient is then given by

$$c_0^A(\mathbf{k}, \{p\}) = E_g + e\frac{\hbar^2 k^2}{2m_0}, \quad (24)$$

and the parameter set, $\{p\}$, in this case, is $\{e, E_g\}$.

e is determined through the fitting of the conduction band to a parabolic curve (24) and E_g is extracted from the DFT-HSE band structure. For the valence band, also two-fold degenerated, we have the following secular equation

$$[\epsilon^3 + c_2^N(\mathbf{k}, \{p\})\epsilon^2 + c_1^N(\mathbf{k}, \{p\})\epsilon + c_0^N(\mathbf{k}, \{p\})]^2 = 0, \quad (25)$$

with the parameter set being $\{p\} = \{\gamma_1, \gamma_2, \gamma_3, \Delta_{so}\}$.

The sampling directions were chosen to be the same used in the 8×8 model, i. e., $\Gamma - X$, $\Gamma - K$ and $\Gamma - L$. The analytical coefficients for the $\Gamma - X$ direction are

$$\begin{aligned} c_{HH}^A(k_{\Gamma X}, \{p\}) &= -[\gamma_1 - 2\gamma_2] \frac{\hbar^2 k_{\Gamma X}^2}{2m_0} \\ c_0^A(k_{\Gamma X}, \{p\}) &= \Delta_{so} + 2[\gamma_1 + \gamma_2] \frac{\hbar^2 k_{\Gamma X}^2}{2m_0} \\ c_1^A(k_{\Gamma X}, \{p\}) &= \Delta_{so} [\gamma_1 + 2\gamma_2] \frac{\hbar^2 k_{\Gamma X}^2}{2m_0} + [\gamma_1^2 + 2\gamma_1\gamma_2 - 8\gamma_2^2] \left(\frac{k_{\Gamma X}^2}{2m_0}\right)^2 \end{aligned} \quad (26)$$

and the numerical coefficients

$$\begin{aligned} c_{HH}^N(k_{\Gamma X}) &= \epsilon_{HH}(k_{\Gamma X}) \\ c_1^N(k_{\Gamma X}) &= -\epsilon_{LH}(k_{\Gamma X}) - \epsilon_{SO}(k_{\Gamma X}) \\ c_0^N(k_{\Gamma X}) &= \epsilon_{LH}(k_{\Gamma X})\epsilon_{SO}(k_{\Gamma X}). \end{aligned} \quad (27)$$

For the $\Gamma - K$ direction we have

$$\begin{aligned}
c_0^A(k_{\Gamma K}, \{p\}) &= \Delta_{so} + 3\gamma_1 \frac{\hbar^2 k_{\Gamma K}^2}{2m_0} \\
c_1^A(k_{\Gamma K}, \{p\}) &= 2\Delta_{so}\gamma_1 \frac{\hbar^2 k_{\Gamma K}^2}{2m_0} + 3[\gamma_1^2 - \gamma_2^2 - 3\gamma_3^2] \left(\frac{\hbar^2 k_{\Gamma K}^2}{2m_0} \right)^2 \\
c_2^A(k_{\Gamma K}, \{p\}) &= \Delta_{so} [\gamma_1^2 - \gamma_2^2 - 3\gamma_3^2] \left(\frac{\hbar^2 k_{\Gamma K}^2}{2m_0} \right)^2 + (\gamma_1 - 2\gamma_2) [\gamma_1^2 + 2\gamma_1\gamma_2 + \gamma_2^2 - 9\gamma_3^2] \left(\frac{\hbar^2 k_{\Gamma K}^2}{2m_0} \right)^3
\end{aligned} \tag{28}$$

with the numerical coefficients

$$\begin{aligned}
c_2^N(k_{\Gamma K}) &= -\epsilon_{HH}(k_{\Gamma K}) - \epsilon_{LH}(k_{\Gamma K}) - \epsilon_{SO}(k_{\Gamma K}) \\
c_1^N(k_{\Gamma K}) &= \epsilon_{HH}(k_{\Gamma K})\epsilon_{LH}(k_{\Gamma K}) + \epsilon_{HH}(k_{\Gamma K})\epsilon_{SO}(k_{\Gamma K}) + \epsilon_{LH}(k_{\Gamma K})\epsilon_{SO}(k_{\Gamma K}) \\
c_0^N(k_{\Gamma K}) &= \epsilon_{HH}(k_{\Gamma K})\epsilon_{LH}(k_{\Gamma K})\epsilon_{SO}(k_{\Gamma K}) .
\end{aligned} \tag{29}$$

And for the $\Gamma - L$ direction we have

$$\begin{aligned}
c_{HH}^A(k_{\Gamma L}, \{p\}) &= -[\gamma_1 - 2\gamma_3] \frac{\hbar^2 k_{\Gamma L}^2}{2m_0} \\
c_0^A(k_{\Gamma L}, \{p\}) &= \Delta_{so} + 2[\gamma_1 + \gamma_3] \frac{\hbar^2 k_{\Gamma L}^2}{2m_0} \\
c_1^A(k_{\Gamma L}, \{p\}) &= \Delta_{so} [\gamma_1 + 2\gamma_3] \frac{\hbar^2 k_{\Gamma L}^2}{2m_0} + [\gamma_1^2 + 2\gamma_1\gamma_3 - 8\gamma_3^2] \left(\frac{k_{\Gamma L}^2}{2m_0} \right)^2
\end{aligned} \tag{30}$$

with the numerical coefficients

$$\begin{aligned}
c_{HH}^N(k_{\Gamma L}) &= \epsilon_{HH}(k_{\Gamma L}) \\
c_1^N(k_{\Gamma L}) &= -\epsilon_{LH}(k_{\Gamma L}) - \epsilon_{SO}(k_{\Gamma L}) \\
c_0^N(k_{\Gamma L}) &= \epsilon_{LH}(k_{\Gamma L})\epsilon_{SO}(k_{\Gamma L}) .
\end{aligned} \tag{31}$$

V. PARAMETER SETS FOR THE 6X6 HAMILTONIAN

Using the same procedure as for the 8×8 case, we performed the fitting for different regions around the Γ point obtaining a different set of parameters for each one of them. The definition of the best set of parameters was done using the RMSD analysis. Fig. V shows the values of RMSD for each different region enclosing the Γ point.

As expected, the lower RMSD values were obtained for fitting regions below 8%, where the band structure is almost parabolic. However, even for fitting regions beyond this limit, up to 12% of the FBZ, the RMSD values are still considerably small, indicating that the model can still be used.

An animated figure showing the comparison of the $\mathbf{k} \cdot \mathbf{p}$ fitting and the original DFT-HSE band structures is available with this text at [http:// magazine site](http://magazine.site). In this animation we vary the parameters showing emphasizing the fitting region used for their extraction.

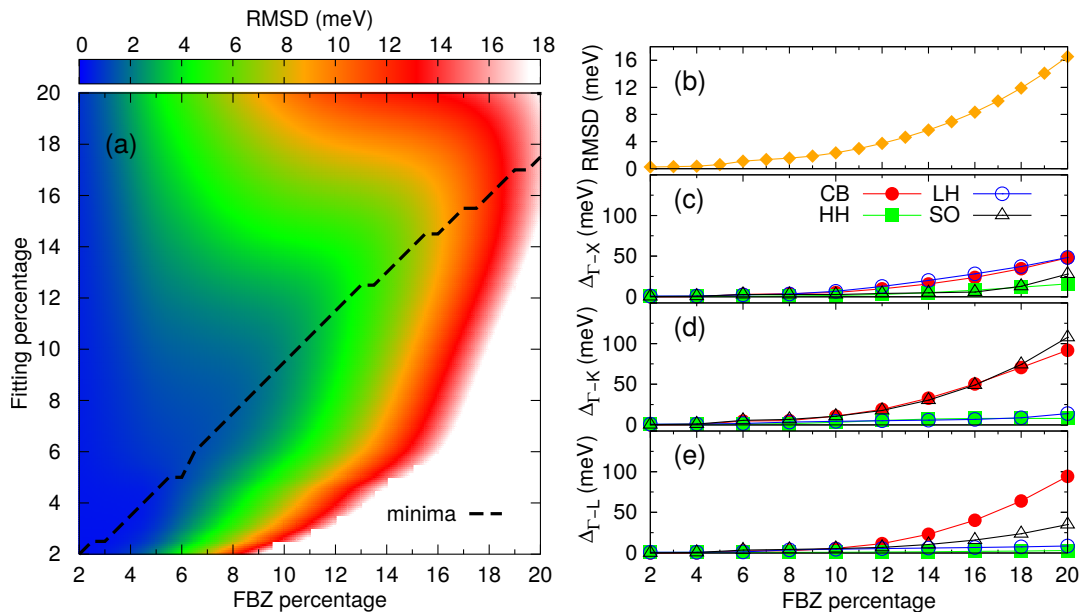


FIG. 1: (a) Root mean square deviation (RMSD) values intensity map showing the agreement of the different adjusted parameter sets against the range around the Γ -point. A dashed curve indicate the optimal parameters for each enclosed region. (b) RMSD of the optimal set of parameters for each region. (c), (d) and (e) show the maximum deviation for each optimal parameter set for the three directions.

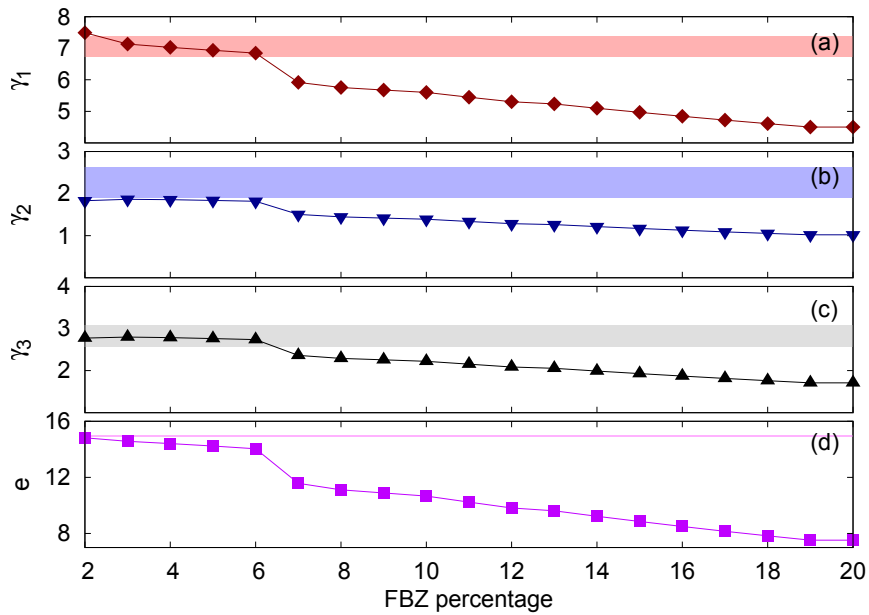


FIG. 2: Comparison of the optimal parameters with the literature. The optimal parameters are shown in the curves and the shadowed regions present the intervals of the standard deviation around the average values of the parameters, determined from 7 traditional papers [12–18] (see Table I). (a) γ_1 , (b) γ_2 , (c) γ_3 and (d) e .

Figure 2 shows the comparison of the optimal parameters with literature values. The colored regions indicate the region of one standard deviation around the average calculated with Refs. [12–18]. For small percentage of the band (up to 8%), the variation of the parameters is flat and similar the literature, i.e., for the unique set parameters

we describing this region. However, above to 8% (outside of the validity of the Hamiltonian), the parameters have variation because the developed method return the best values to describe effects non-present in the Hamiltonian.

TABLE I: Experimental data used to compute the average and standard deviation of literature parameters

	ref.[12]	ref.[13]	ref. [14]	ref. [15]	ref.[16]	ref. [17]	ref. [18]
γ_1	6.98	6.85	7.65	6.67	7.20	6.79	7.17
γ_2	2.06	2.16	2.41	1.87	2.50	1.92	2.88
γ_3	2.93	2.79	3.28	2.67	2.50	2.68	2.91
e	14.93	14.93	14.93	14.93	14.93	15.04	15.04

VI. PARAMETERS FOR REGIONS DEFINED BY DIFFERENT PERCENTAGES OF THE FBZ

TABLE II: Optimal parameter sets for different enclosing regions of the FBZ, for both Hamiltonians (6×6 and 8×8).

%	6×6 Hamiltonian				8×8 Hamiltonian				P
	γ_1	γ_2	γ_3	e	$\tilde{\gamma}_1$	$\tilde{\gamma}_2$	$\tilde{\gamma}_3$	\tilde{e}	
2	7.49	1.83	2.77	14.82	-1.26	-2.55	-1.55	-11.29	12.74
3	7.13	1.86	2.80	14.57	-0.43	-2.00	-1.02	-8.30	11.99
4	7.03	1.85	2.78	14.41	0.27	-1.55	-0.59	-5.80	11.32
5	6.93	1.84	2.76	14.24	0.64	-1.32	-0.37	-4.52	10.95
6	6.85	1.82	2.74	14.04	0.89	-1.15	-0.21	-3.68	10.69
7	5.92	1.50	2.36	11.57	1.32	-0.92	0.01	-2.33	10.22
8	5.76	1.45	2.29	11.12	1.34	-0.90	0.02	-2.22	10.16
9	5.67	1.42	2.26	10.89	1.35	-0.88	0.02	-2.19	10.12
10	5.60	1.39	2.22	10.67	1.35	-0.87	0.03	-2.17	10.09
11	5.45	1.34	2.15	10.24	1.35	-0.85	0.03	-2.17	10.06
12	5.30	1.29	2.09	9.82	1.34	-0.83	0.03	-2.18	10.03
13	5.23	1.26	2.05	9.62	1.33	-0.82	0.03	-2.19	10.00
14	5.10	1.22	1.99	9.23	1.32	-0.81	0.03	-2.20	9.99
15	4.97	1.17	1.93	8.86	1.31	-0.79	0.03	-2.22	9.96
16	4.84	1.13	1.87	8.50	1.31	-0.78	0.03	-2.24	9.94
17	4.73	1.09	1.81	8.16	1.21	-0.77	0.03	-2.27	9.91
18	4.61	1.05	1.76	7.83	1.29	-0.76	0.03	-2.29	9.90
19	4.50	1.02	1.71	7.52	1.28	-0.74	0.03	-2.32	9.86
20	4.50	1.02	1.71	7.52	1.28	-0.73	0.03	-2.34	9.85

-
- [1] P. Hohenberg, W. Kohn, Inhomogeneous Electron Gas, *Physical Review* 136 (3B) (1964) B864–B871.
- [2] W. Kohn, L. J. Sham, Self-Consistent Equations Including Exchange and Correlation Effects, *Physical Review* 140 (4A) (1965) A1133–A1138.
- [3] E. Kane, The k-p method, in: R. Willardson, A. C. Beer (Eds.), *Semiconductors and Semimetals*, Vol. 1 of *Semiconductors and Semimetals*, Elsevier, 1966, pp. 75 – 100.
- [4] J. M. Luttinger, W. Kohn, Motion of Electrons and Holes in Perturbed Periodic Fields, *Physical Review* 97 (4) (1955) 869–883.
- [5] G. Dresselhaus, Spin-orbit coupling effects in zinc blende structures, *Physical Review* 100 (2) (1955) 580–586.
- [6] R. Enderlein, J. M. N. Horing, *Fundamentals Of Semiconductor Physics And Devices*, World Scientific, Singapore, 1997.
- [7] M. Willatzen, L. C. Lew Yan Voon, *The k p Method*, Springer Berlin Heidelberg, Berlin, Heidelberg, 2009.
- [8] P.-O. Löwdin, A note on the quantum-mechanical perturbation theory, *The Journal of Chemical Physics* 19 (11) (1951) 1396.
- [9] M. S. Dresselhaus, G. Dresselhaus, A. Jório, *Group Theory - Applications to the Physics of Condensed Matter*, 1st Edition, Springer Science & Business Media, 2007.
- [10] P. Y. Yu, M. Cardona, *Fundamentals of semiconductors*, Springer-Verlag, Berlin, Heidelberg, 2005.
- [11] E. O. Kane, Band structure of indium antimonide, *Journal of Physics and Chemistry of Solids* 1 (4) (1957) 249–261.

-
- [12] I. Vurgaftman, J. R. Meyer, L. R. Ram-Mohan, Band parameters for III-V compound semiconductors and their alloys, *Journal of Applied Physics* 89 (11) (2001) 5815.
 - [13] S. Shokhovets, O. Ambacher, G. Gobsch, Conduction-band dispersion relation and electron effective mass in III-V and II-VI zinc-blende semiconductors, *Physical Review B* 76 (12) (2007) 125203.
 - [14] P. Lawaetz, Valence-Band Parameters in Cubic Semiconductors, *Physical Review B* 4 (10) (1971) 3460–3467.
 - [15] T. Ostromek, Evaluation of matrix elements of the 8×8 k.p Hamiltonian with k-dependent spin-orbit contributions for the zinc-blende structure of GaAs, *Physical Review B* 54 (20).
 - [16] Q. Vrehan, Interband magneto-optical absorption in gallium arsenide, *Journal of Physics and Chemistry of Solids* 29 (1) (1968) 129–141.
 - [17] L. W. Molenkamp, R. Eppenga, G. W. 't Hooft, P. Dawson, C. T. Foxon, K. J. Moore, Determination of valence-band effective-mass anisotropy in GaAs quantum wells by optical spectroscopy, *Physical Review B* 38 (6) (1988) 4314–4317.
 - [18] C. Neumann, A. Nöthe, N. O. Lipari, Two-photon magnetoabsorption of ZnTe, CdTe, and GaAs, *Physical Review B* 37 (2) (1988) 922–932.

Supplementary Material: A comprehensive study of g-factors, elastic, structural and electronic properties of III-V semiconductors using Hybrid-Density Functional Theory

Carlos M. O. Bastos,¹ Fernando P. Sabino,¹ Guilherme M. Sipahi,¹ and Juarez L. F. Da Silva²

¹*São Carlos Institute of Physics, University of São Paulo,
PO Box 369, 13560-970, São Carlos, SP, Brazil.*

²*São Carlos Institute of Chemistry, University of São Paulo,
POBox 780, 13560-970, São Carlos, SP, Brazil.*

I. COMPUTATIONAL DETAILS

TABLE I: HSE functional PAW VASP projectors used in this work, together with the number of valence electrons (ZVAL) and the cut-off energies recommended by VASP, used in the minimization of the stress/elastic constants tensor and in the determination of the total energy/band structures.

PAW		ZVAL	valence	cut-off energy (eV)		
				recommended	stress/elastic constants	total energy/band structure
Al	Al_GW_19Mar2012	3	3s ² 3p ¹	240.300	360.450	270.337
Ga	Ga_d_GW_06Jul2010	3	4s ² 4p ¹	134.678	202.017	151.513
In	In_d_GW_29May2007	13	4d ¹⁰ 5s ² 5p ¹	278.624	417.936	313.452
N	N_GW_10Apr2007	5	2s ² 2p ³	420.902	631.353	473.515
P	P_GW_19Mar2012	5	3s ² 3p ³	255.040	382.560	286.920
As	As_GW_20Mar2012	5	4s ² 4p ³	208.702	313.053	234.790
Sb	Sb_d_GW_22Apr2009	15	4d ¹⁰ 5s ² 5p ³	172.069	258.103	193.578

TABLE II: PBE functional PAW VASP projectors used in this work, together with the number of valence electrons (ZVAL) and the cut-off energies recommended by VASP, used in the minimization of the stress/elastic constants tensor and in the determination of the total energy/band structures.

PAW		ZVAL	valence	cut-off energy (eV)		
				recommended	stress elastic constants	total energy/band structure
Al	Al_GW_19Mar2012	3	3s ² 3p ¹	240.300	480.600	600.750
Ga	Ga_d_GW_06Jul2010	3	4s ² 4p ¹	134.678	269.356	336.695
In	In_d_GW_29May2007	13	4d ¹⁰ 5s ² 5p ¹	278.624	557.248	696.560
N	N_GW_10Apr2007	5	2s ² 2p ³	420.902	841.804	1052.255
P	P_GW_19Mar2012	5	3s ² 3p ³	255.040	510.080	637.600
As	As_GW_20Mar2012	5	4s ² 4p ³	208.702	417.404	521.755
Sb	Sb_d_GW_22Apr2009	15	4d ¹⁰ 5s ² 5p ³	172.069	344.138	430.172

II. DEPENDENCE OF PROPERTIES WITH PARAMETERS

A. Dependence of the band gap and Δ_{so} on the α parameter

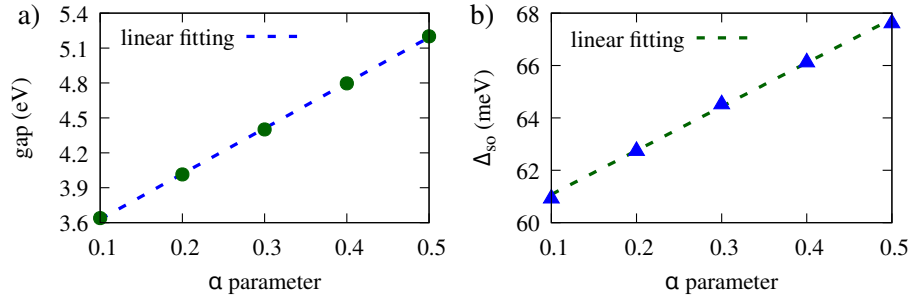


FIG. 1: Linear dependence of the band gap (right) and Δ_{so} (left) on the α parameter for AIP.

B. α parameters

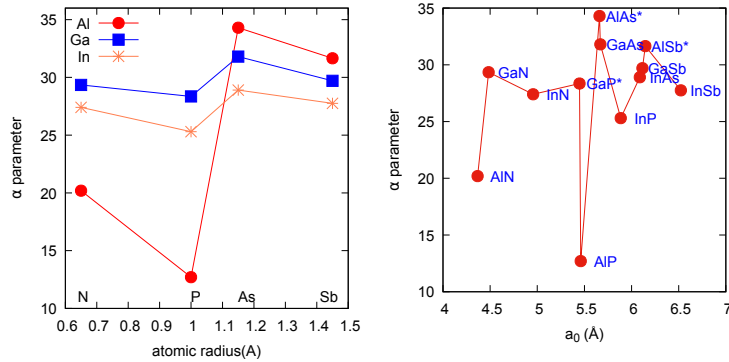


FIG. 2: Cation atomic radius (left) and lattice parameter(right) dependence on the α parameter.

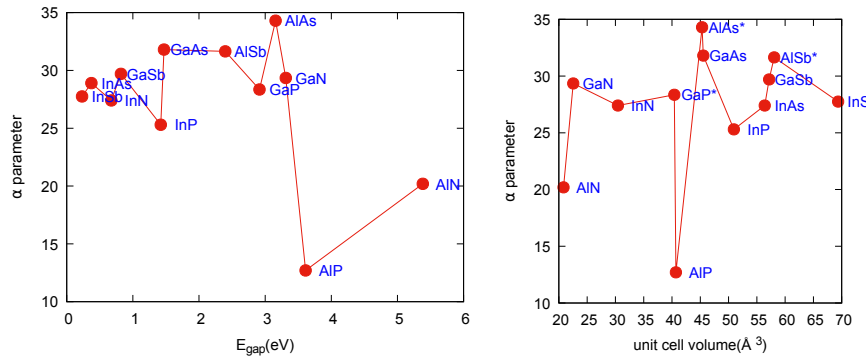


FIG. 3: Energy gap (left) and equilibrium volume (right) dependence on the α parameter.

III. BAND STRUCTURES

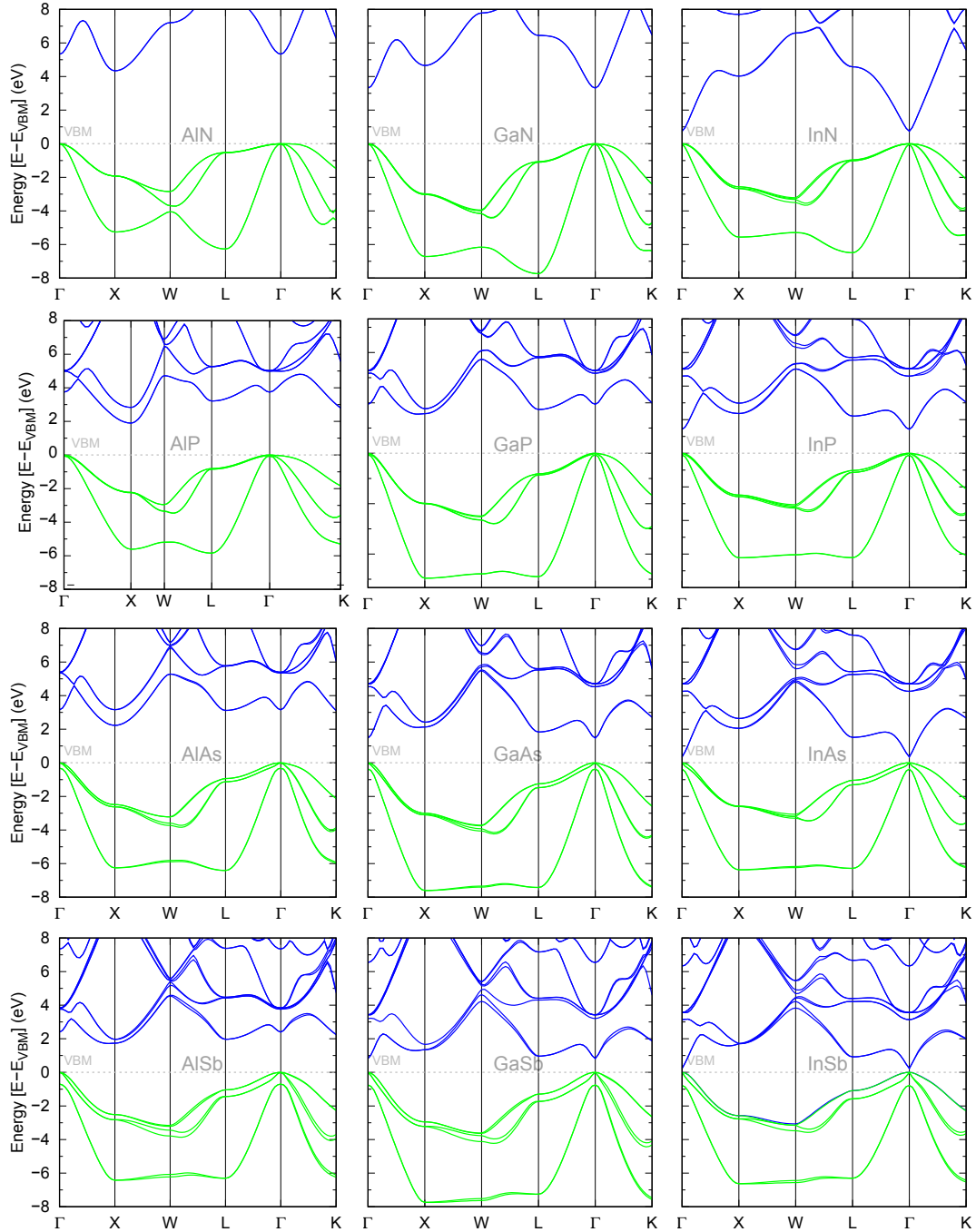


FIG. 4: HSE $_{\alpha}$ +SOC band structures obtained. Energy zero is set to the valence band maximum (VBM). Blue and green lines indicate conduction and valence bands, respectively.

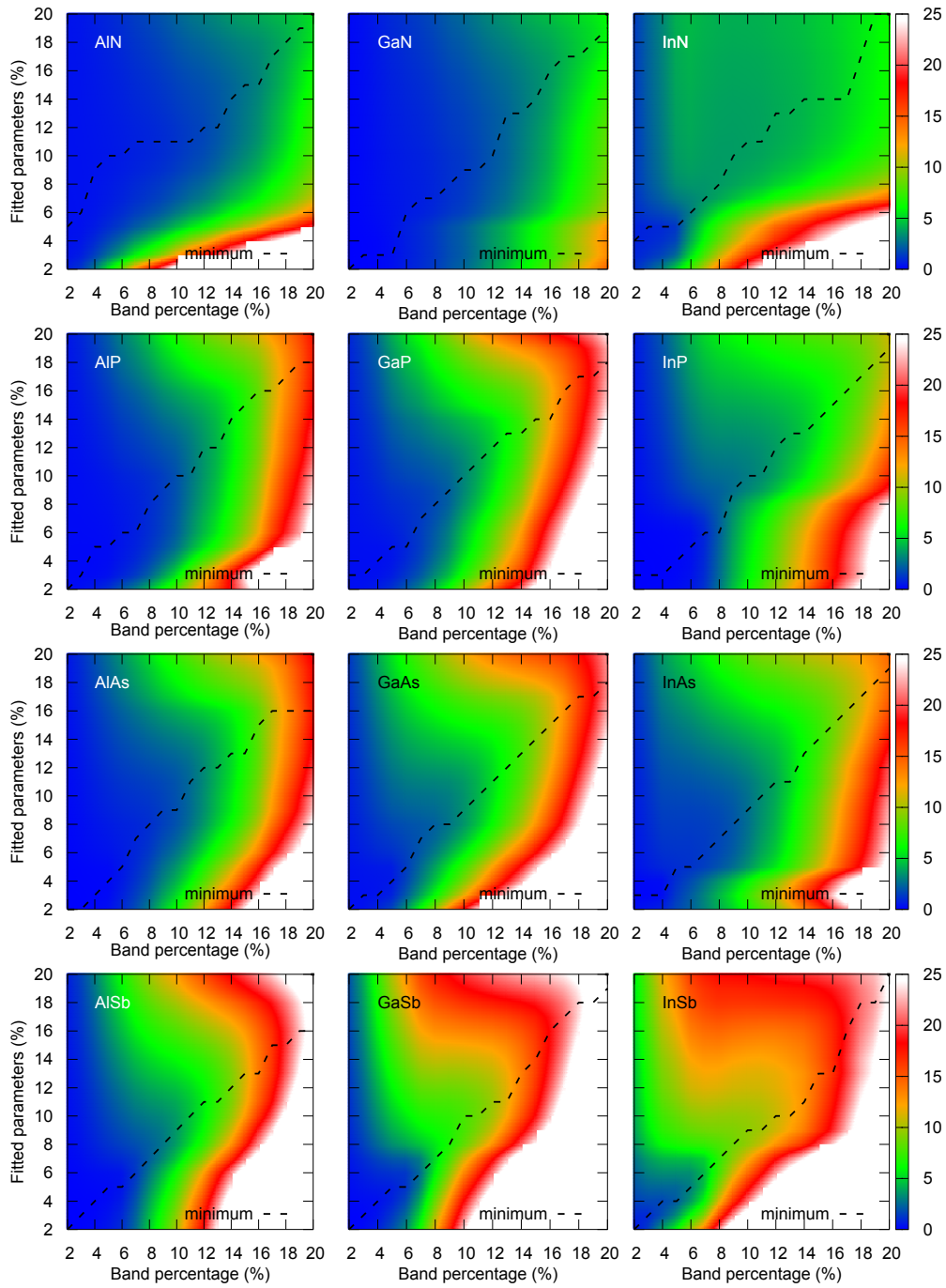
IV. $k \cdot p$ PARAMETERS

FIG. 5: Recommended Kane-Luttinger parameters for each region near to Γ point for aluminum-V compounds. In the x-axis is the percentage of the FBZ used in the fitting.

V. KANE-LUTINGER PARAMETERS

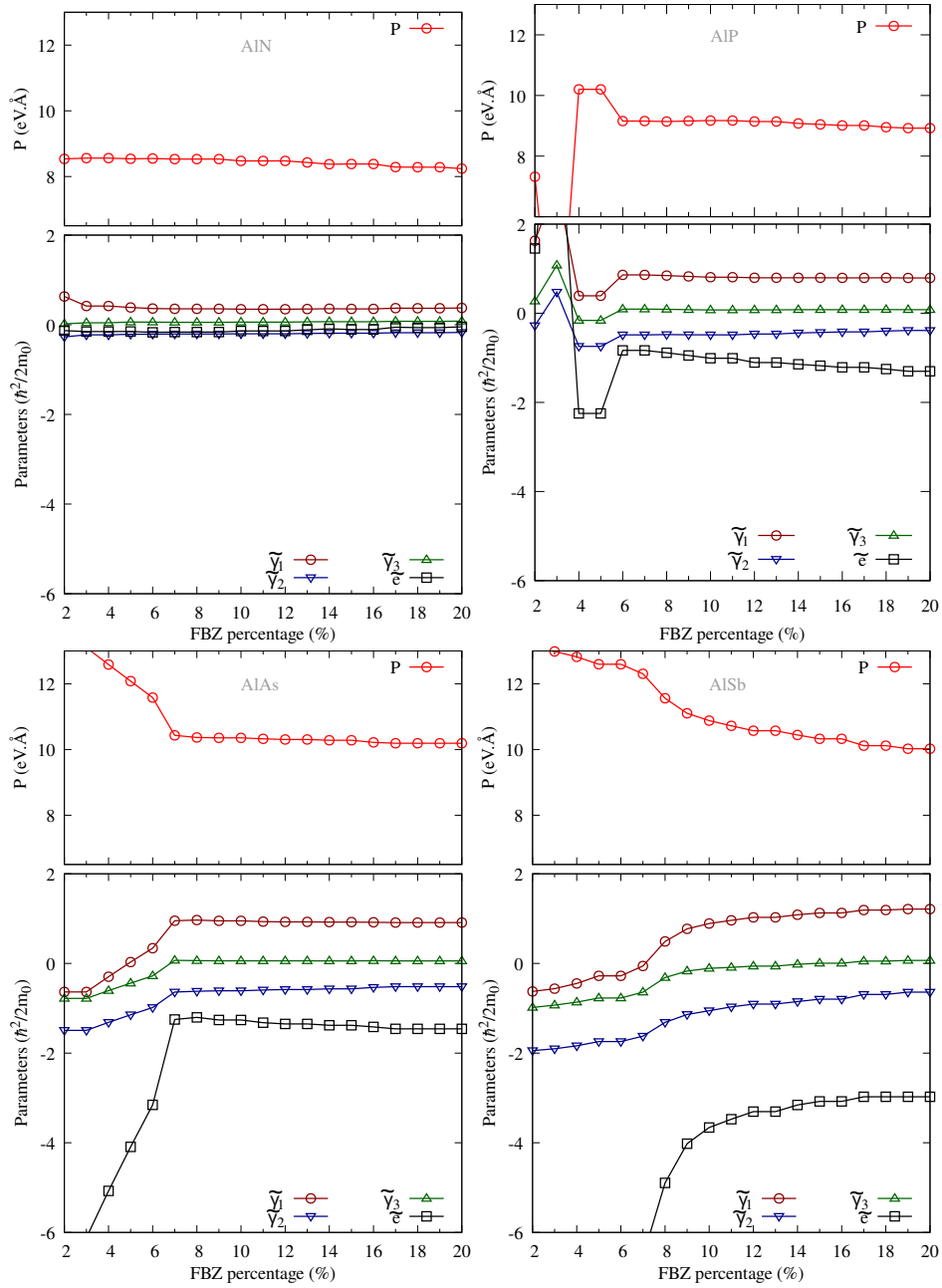


FIG. 6: Recommended Kane-Luttinger parameters for each region near to Γ point for aluminum-V compounds. In the x-axis is the percentage of the FBZ used in the fitting.

VI. KANE-LUTINGER PARAMETERS

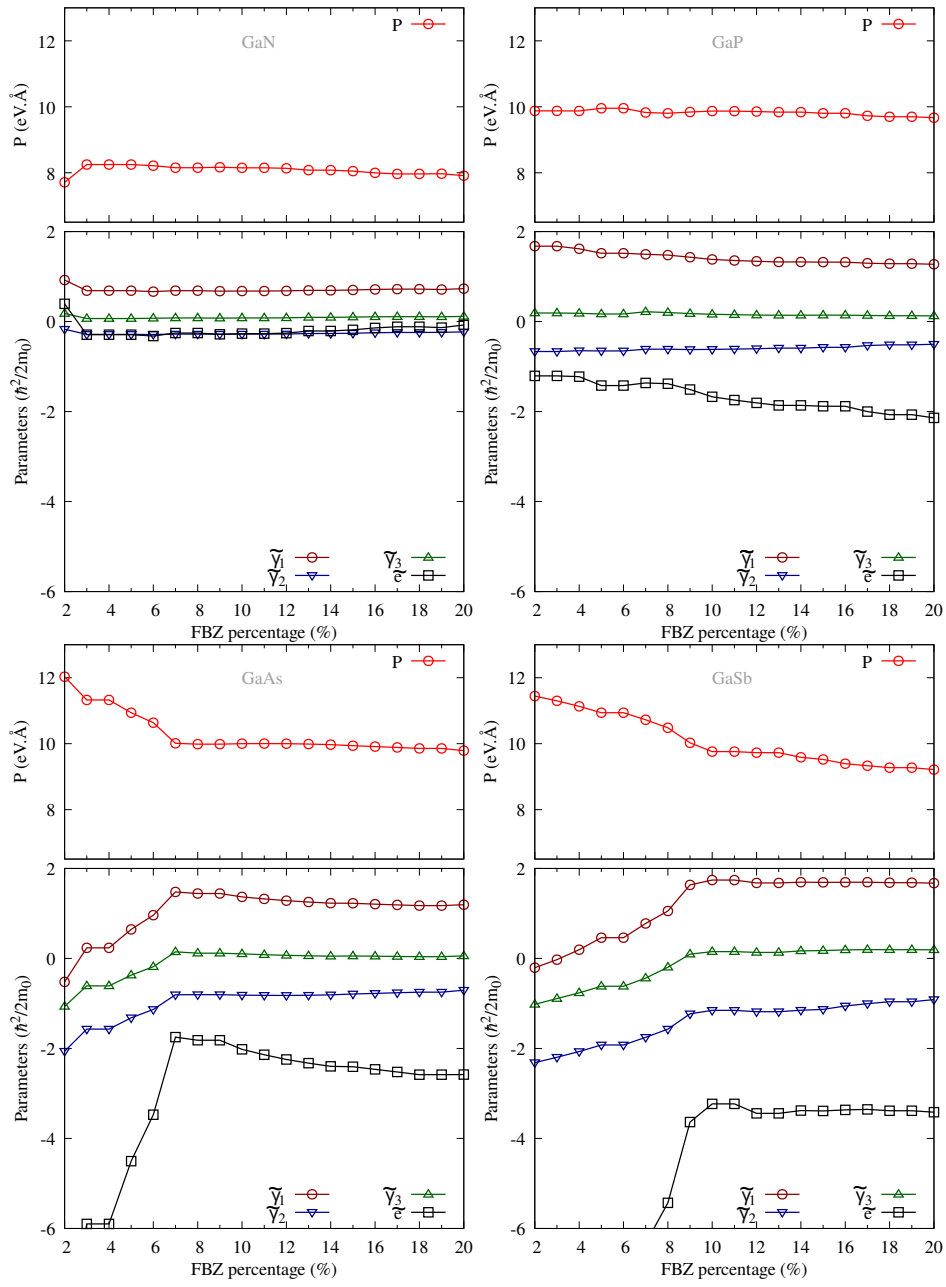


FIG. 7: Recommended Kane-Luttinger parameters for each region near to Γ point for gallium-V compounds. In the x-axis is the percentage of the FBZ used in the fitting.

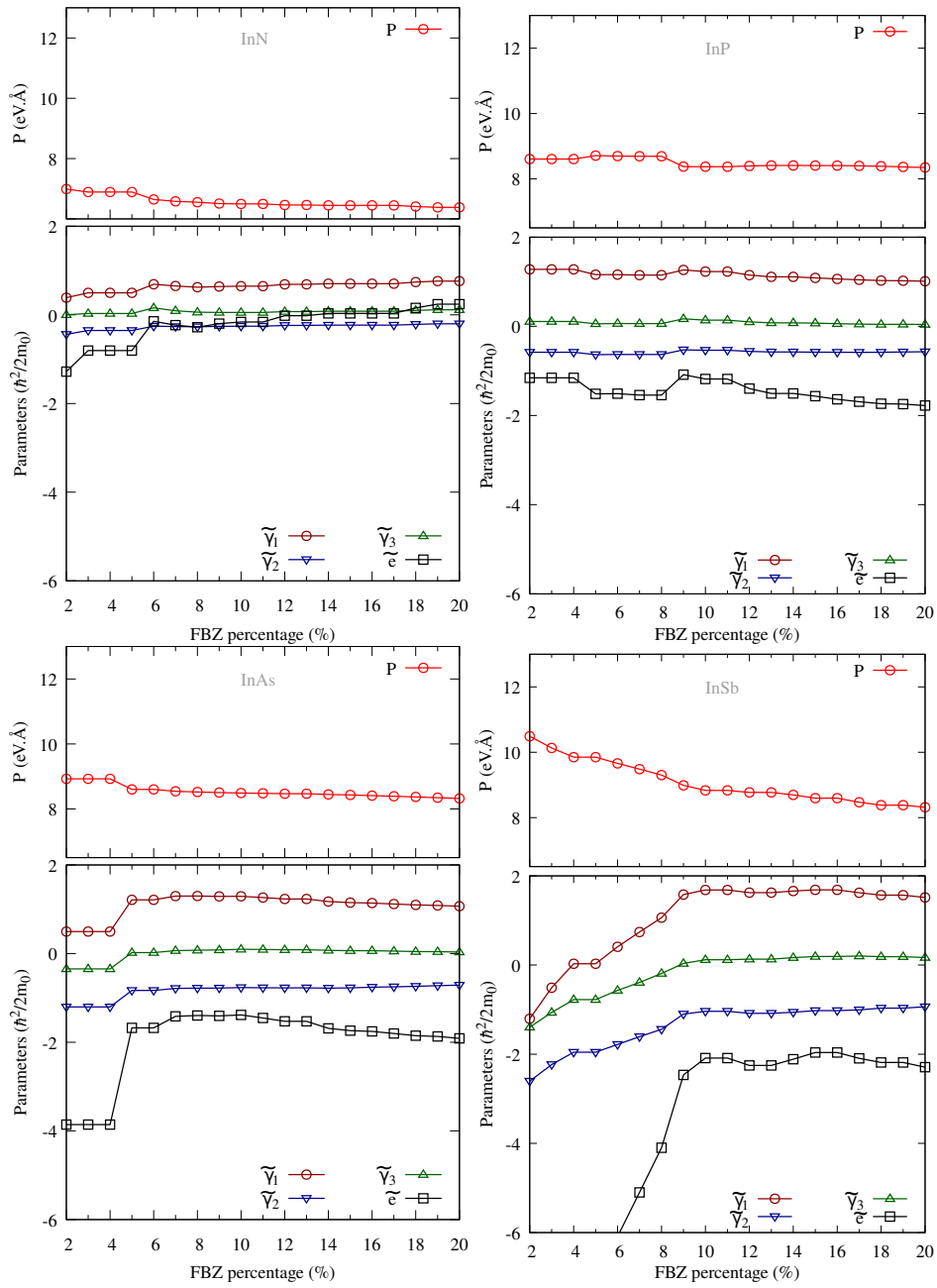


FIG. 8: Recommended Kane-Luttinger parameters for each region near to Γ point for Indium-V compounds. In the x-axis is the percentage of the FBZ used in the fitting.

TABLE III: Adjusted Kane-Luttinger parameters and E_p for AlN and AlP in function of the adjusted region. The RMSDs are also indicated.

%	AlN						AlP					
	RMSD	$\tilde{\gamma}_1$	$\tilde{\gamma}_2$	$\tilde{\gamma}_3$	\tilde{e}	P	RMSD	$\tilde{\gamma}_1$	$\tilde{\gamma}_2$	$\tilde{\gamma}_3$	\tilde{e}	P
2	0.35	0.439	-0.228	0.006	-0.049	8.44	0.19	1.627	-0.278	0.272	1.453	7.32
3	0.37	0.399	-0.221	0.022	-0.101	8.49	0.18	1.627	-0.278	0.272	1.453	7.32
4	0.44	0.365	-0.206	0.048	-0.113	8.49	0.20	0.392	-0.742	-0.161	-2.248	10.20
5	0.52	0.358	-0.204	0.051	-0.119	8.49	0.26	0.392	-0.742	-0.161	-2.248	10.20
6	0.61	0.358	-0.204	0.051	-0.119	8.49	0.49	0.861	-0.485	0.094	-0.833	9.16
7	0.75	0.362	-0.198	0.060	-0.099	8.45	0.71	0.861	-0.485	0.094	-0.833	9.16
8	0.85	0.362	-0.198	0.060	-0.099	8.45	1.01	0.846	-0.479	0.089	-0.887	9.14
9	1.00	0.362	-0.198	0.060	-0.099	8.45	1.41	0.826	-0.484	0.081	-0.946	9.16
10	1.20	0.362	-0.198	0.060	-0.099	8.45	1.89	0.810	-0.484	0.075	-1.010	9.17
11	1.45	0.362	-0.198	0.060	-0.099	8.45	2.71	0.810	-0.484	0.075	-1.010	9.17
12	1.64	0.360	-0.196	0.062	-0.097	8.44	3.55	0.796	-0.464	0.076	-1.107	9.14
13	1.99	0.360	-0.196	0.062	-0.097	8.44	4.33	0.796	-0.464	0.076	-1.107	9.14
14	2.38	0.365	-0.188	0.070	-0.076	8.39	5.49	0.797	-0.442	0.082	-1.145	9.08
15	2.72	0.358	-0.189	0.069	-0.094	8.40	6.79	0.796	-0.431	0.081	-1.177	9.04
16	3.09	0.358	-0.189	0.069	-0.094	8.40	8.31	0.795	-0.418	0.081	-1.213	9.01
17	3.65	0.376	-0.177	0.079	-0.042	8.31	10.71	0.795	-0.418	0.081	-1.213	9.01
18	4.11	0.372	-0.176	0.077	-0.053	8.31	12.84	0.795	-0.398	0.083	-1.253	8.96
19	4.73	0.379	-0.171	0.081	-0.036	8.26	14.78	0.792	-0.386	0.081	-1.301	8.92
20	5.34	0.379	-0.171	0.081	-0.036	8.26	17.36	0.792	-0.386	0.081	-1.301	8.92

TABLE IV: Adjusted Kane-Luttinger parameters and E_p for AlAs and AlSb in function of the adjusted region. The RMSDs are also indicated.

%	AlAs						AlSb					
	RMSD	$\tilde{\gamma}_1$	$\tilde{\gamma}_2$	$\tilde{\gamma}_3$	\tilde{e}	P	RMSD	$\tilde{\gamma}_1$	$\tilde{\gamma}_2$	$\tilde{\gamma}_3$	\tilde{e}	P
2	0.02	-0.636	-1.493	-0.779	-6.117	13.10	0.02	-0.625	-1.944	-0.981	-8.268	13.08
3	0.05	-0.636	-1.493	-0.779	-6.117	13.10	0.04	-0.562	-1.904	-0.929	-8.037	12.98
4	0.10	-0.295	-1.313	-0.605	-5.074	12.58	0.10	-0.445	-1.836	-0.863	-7.681	12.82
5	0.18	0.031	-1.144	-0.439	-4.090	12.08	0.24	-0.277	-1.743	-0.772	-7.193	12.59
6	0.51	0.342	-0.982	-0.277	-3.154	11.58	0.43	-0.277	-1.743	-0.772	-7.193	12.59
7	0.86	0.953	-0.638	0.070	-1.250	10.43	1.23	-0.057	-1.622	-0.639	-6.554	12.30
8	1.06	0.967	-0.621	0.064	-1.203	10.36	2.18	0.491	-1.315	-0.315	-4.895	11.56
9	1.49	0.951	-0.609	0.060	-1.262	10.35	2.78	0.772	-1.139	-0.169	-4.021	11.10
10	1.87	0.951	-0.609	0.060	-1.262	10.35	3.60	0.890	-1.054	-0.108	-3.660	10.87
11	2.49	0.935	-0.593	0.060	-1.320	10.32	4.60	0.963	-0.969	-0.087	-3.475	10.72
12	3.23	0.929	-0.581	0.058	-1.349	10.30	5.65	1.028	-0.907	-0.058	-3.305	10.57
13	4.15	0.929	-0.581	0.058	-1.349	10.30	7.16	1.028	-0.907	-0.058	-3.305	10.57
14	5.08	0.923	-0.567	0.057	-1.378	10.28	8.81	1.086	-0.851	-0.019	-3.157	10.44
15	6.43	0.923	-0.567	0.057	-1.378	10.28	10.90	1.127	-0.796	0.004	-3.076	10.32
16	8.02	0.920	-0.534	0.061	-1.415	10.21	13.64	1.127	-0.796	0.004	-3.076	10.32
17	10.35	0.913	-0.517	0.058	-1.459	10.19	16.10	1.192	-0.691	0.052	-2.973	10.11
18	12.53	0.913	-0.517	0.058	-1.459	10.19	19.36	1.192	-0.691	0.052	-2.973	10.11
19	14.77	0.913	-0.517	0.058	-1.459	10.19	22.64	1.213	-0.640	0.067	-2.973	10.02
20	17.60	0.913	-0.517	0.058	-1.459	10.19	25.94	1.213	-0.640	0.067	-2.973	10.02

TABLE V: Adjusted Kane-Luttinger parameters and E_p for GaN and GaP in function of the adjusted region. The RMSDs are also indicated.

%	GaN						GaP					
	RMSD	$\tilde{\gamma}_1$	$\tilde{\gamma}_2$	$\tilde{\gamma}_3$	\tilde{e}	P	RMSD	$\tilde{\gamma}_1$	$\tilde{\gamma}_2$	$\tilde{\gamma}_3$	\tilde{e}	P
2	0.02	0.922	-0.171	0.179	0.394	7.70	0.30	1.677	-0.665	0.190	-1.206	9.87
3	0.05	0.687	-0.285	0.067	-0.291	8.24	0.31	1.677	-0.665	0.190	-1.206	9.87
4	0.13	0.687	-0.285	0.067	-0.291	8.24	0.32	1.616	-0.648	0.183	-1.224	9.87
5	0.31	0.687	-0.285	0.067	-0.291	8.24	0.47	1.518	-0.653	0.169	-1.421	9.95
6	0.58	0.664	-0.287	0.074	-0.321	8.21	0.85	1.518	-0.653	0.169	-1.421	9.95
7	0.69	0.687	-0.278	0.080	-0.254	8.15	1.35	1.495	-0.614	0.218	-1.363	9.82
8	0.88	0.687	-0.278	0.080	-0.254	8.15	1.74	1.478	-0.615	0.201	-1.381	9.80
9	1.13	0.676	-0.281	0.076	-0.283	8.16	2.24	1.431	-0.621	0.178	-1.511	9.84
10	1.33	0.679	-0.278	0.080	-0.267	8.14	3.13	1.380	-0.618	0.163	-1.671	9.86
11	1.65	0.679	-0.278	0.080	-0.267	8.14	3.93	1.357	-0.612	0.153	-1.744	9.86
12	2.03	0.682	-0.275	0.083	-0.256	8.13	4.91	1.340	-0.602	0.146	-1.806	9.85
13	2.37	0.694	-0.265	0.094	-0.208	8.07	6.09	1.325	-0.589	0.140	-1.863	9.83
14	2.81	0.694	-0.265	0.094	-0.208	8.07	7.25	1.325	-0.589	0.140	-1.863	9.83
15	3.28	0.702	-0.259	0.099	-0.183	8.04	9.46	1.321	-0.573	0.143	-1.882	9.80
16	3.69	0.714	-0.248	0.106	-0.140	7.99	11.64	1.321	-0.573	0.143	-1.882	9.80
17	4.26	0.721	-0.241	0.110	-0.115	7.96	13.71	1.298	-0.532	0.136	-1.999	9.72
18	4.80	0.721	-0.241	0.110	-0.115	7.96	16.16	1.285	-0.518	0.131	-2.068	9.69
19	5.29	0.713	-0.240	0.106	-0.134	7.97	18.83	1.285	-0.518	0.131	-2.068	9.69
20	5.89	0.732	-0.228	0.115	-0.076	7.91	22.05	1.273	-0.504	0.127	-2.141	9.66

TABLE VI: Adjusted Kane-Luttinger parameters and E_p for GaAs and GaSb in function of the adjusted region. The RMSDs are also indicated.

%	GaAs						GaSb					
	RMSD	$\tilde{\gamma}_1$	$\tilde{\gamma}_2$	$\tilde{\gamma}_3$	\tilde{e}	P	RMSD	$\tilde{\gamma}_1$	$\tilde{\gamma}_2$	$\tilde{\gamma}_3$	\tilde{e}	P
2	0.27	-0.521	-2.062	-1.065	-8.613	12.03	0.04	-0.205	-2.315	-1.020	-9.431	11.44
3	0.34	0.236	-1.569	-0.609	-5.899	11.32	0.12	-0.027	-2.196	-0.891	-8.785	11.29
4	0.44	0.236	-1.569	-0.609	-5.899	11.32	0.32	0.195	-2.069	-0.764	-8.086	11.13
5	0.57	0.645	-1.318	-0.371	-4.504	10.93	0.71	0.461	-1.923	-0.617	-7.278	10.93
6	1.38	0.961	-1.133	-0.184	-3.472	10.63	1.18	0.461	-1.923	-0.617	-7.278	10.93
7	2.00	1.477	-0.807	0.148	-1.749	10.01	2.52	0.776	-1.754	-0.437	-6.335	10.72
8	2.25	1.443	-0.804	0.117	-1.816	9.98	5.06	1.054	-1.571	-0.195	-5.430	10.48
9	2.75	1.443	-0.804	0.117	-1.816	9.98	6.53	1.635	-1.230	0.097	-3.636	10.02
10	3.46	1.368	-0.815	0.103	-2.020	9.99	7.69	1.743	-1.154	0.150	-3.232	9.75
11	4.23	1.322	-0.821	0.084	-2.140	10.00	8.57	1.743	-1.154	0.150	-3.232	9.75
12	5.23	1.284	-0.821	0.070	-2.245	9.99	9.65	1.677	-1.183	0.134	-3.442	9.72
13	6.40	1.254	-0.817	0.059	-2.328	9.98	11.41	1.677	-1.183	0.134	-3.442	9.72
14	7.54	1.229	-0.808	0.051	-2.398	9.97	13.54	1.694	-1.150	0.168	-3.380	9.58
15	9.12	1.226	-0.789	0.056	-2.406	9.93	15.74	1.690	-1.131	0.175	-3.388	9.52
16	10.84	1.207	-0.776	0.050	-2.464	9.91	18.28	1.693	-1.056	0.190	-3.365	9.39
17	12.76	1.190	-0.762	0.044	-2.523	9.88	20.52	1.694	-1.004	0.196	-3.354	9.33
18	15.30	1.175	-0.749	0.040	-2.582	9.85	23.25	1.683	-0.961	0.194	-3.385	9.27
19	18.04	1.175	-0.749	0.040	-2.582	9.85	26.15	1.683	-0.961	0.194	-3.385	9.27
20	21.48	1.194	-0.705	0.057	-2.581	9.78	28.79	1.674	-0.915	0.193	-3.416	9.21

TABLE VII: Adjusted Kane-Luttinger parameters and E_p for InN and InP in function of the adjusted region. The RMSDs are also indicated.

%	InN						InP					
	RMSD	$\tilde{\gamma}_1$	$\tilde{\gamma}_2$	$\tilde{\gamma}_3$	\tilde{e}	P	RMSD	$\tilde{\gamma}_1$	$\tilde{\gamma}_2$	$\tilde{\gamma}_3$	\tilde{e}	P
2	0.75	0.388	-0.441	0.004	-1.280	6.99	0.03	1.277	-0.581	0.110	-1.156	8.60
3	0.86	0.498	-0.352	0.031	-0.805	6.89	0.04	1.277	-0.581	0.110	-1.156	8.60
4	0.97	0.498	-0.352	0.031	-0.805	6.89	0.07	1.277	-0.581	0.110	-1.156	8.60
5	1.27	0.498	-0.352	0.031	-0.805	6.89	0.14	1.159	-0.636	0.057	-1.515	8.71
6	2.92	0.691	-0.254	0.158	-0.145	6.64	0.29	1.160	-0.630	0.063	-1.510	8.69
7	3.51	0.651	-0.263	0.094	-0.231	6.58	0.85	1.149	-0.631	0.061	-1.541	8.69
8	3.69	0.623	-0.267	0.062	-0.279	6.55	2.13	1.149	-0.631	0.061	-1.541	8.69
9	3.74	0.639	-0.259	0.054	-0.197	6.51	2.64	1.264	-0.527	0.168	-1.085	8.37
10	3.79	0.648	-0.255	0.055	-0.161	6.50	2.95	1.227	-0.537	0.138	-1.182	8.37
11	3.87	0.648	-0.255	0.055	-0.161	6.50	3.30	1.227	-0.537	0.138	-1.182	8.37
12	4.04	0.689	-0.237	0.075	-0.019	6.46	3.74	1.149	-0.562	0.099	-1.396	8.39
13	4.17	0.689	-0.237	0.075	-0.019	6.46	4.24	1.110	-0.574	0.079	-1.507	8.40
14	4.33	0.704	-0.230	0.082	0.032	6.45	4.74	1.110	-0.574	0.079	-1.507	8.40
15	4.62	0.704	-0.230	0.082	0.032	6.45	5.49	1.087	-0.578	0.071	-1.567	8.40
16	4.85	0.704	-0.230	0.082	0.032	6.45	6.30	1.062	-0.582	0.060	-1.636	8.40
17	5.20	0.704	-0.230	0.082	0.032	6.45	7.23	1.043	-0.583	0.051	-1.690	8.39
18	5.56	0.739	-0.214	0.102	0.159	6.41	8.15	1.027	-0.582	0.044	-1.735	8.38
19	5.86	0.762	-0.201	0.114	0.241	6.38	9.40	1.023	-0.575	0.045	-1.744	8.36
20	6.29	0.762	-0.201	0.114	0.241	6.38	10.74	1.011	-0.570	0.041	-1.777	8.34

TABLE VIII: Adjusted Kane-Luttinger parameters and E_p for InAs and InSb in function of the adjusted region. The RMSDs are also indicated.

%	InAs						InSb					
	RMSD	$\tilde{\gamma}_1$	$\tilde{\gamma}_2$	$\tilde{\gamma}_3$	\tilde{e}	P	RMSD	$\tilde{\gamma}_1$	$\tilde{\gamma}_2$	$\tilde{\gamma}_3$	\tilde{e}	P
2	0.09	0.499	-1.202	-0.345	-3.857	8.92	0.29	-1.204	-2.604	-1.393	-10.959	10.48
3	0.12	0.499	-1.202	-0.345	-3.857	8.92	0.90	-0.508	-2.233	-1.062	-8.840	10.13
4	0.25	0.499	-1.202	-0.345	-3.857	8.92	1.66	0.028	-1.954	-0.775	-7.220	9.85
5	1.06	1.214	-0.831	0.022	-1.676	8.60	2.10	0.028	-1.954	-0.775	-7.220	9.85
6	1.20	1.214	-0.831	0.022	-1.676	8.60	2.93	0.410	-1.781	-0.569	-6.092	9.66
7	1.38	1.296	-0.785	0.068	-1.415	8.54	4.33	0.740	-1.607	-0.391	-5.099	9.48
8	1.64	1.299	-0.779	0.077	-1.396	8.52	7.01	1.062	-1.442	-0.187	-4.099	9.30
9	1.99	1.291	-0.776	0.082	-1.405	8.50	8.60	1.581	-1.100	0.034	-2.465	8.98
10	2.60	1.293	-0.766	0.097	-1.382	8.49	9.39	1.685	-1.037	0.120	-2.086	8.83
11	3.33	1.264	-0.770	0.093	-1.453	8.48	9.93	1.685	-1.037	0.120	-2.086	8.83
12	3.96	1.233	-0.772	0.087	-1.527	8.47	10.77	1.624	-1.082	0.132	-2.252	8.76
13	5.00	1.233	-0.772	0.087	-1.527	8.47	11.73	1.624	-1.082	0.132	-2.252	8.76
14	6.17	1.174	-0.778	0.074	-1.687	8.45	12.83	1.660	-1.058	0.168	-2.111	8.69
15	7.22	1.152	-0.772	0.066	-1.738	8.43	14.37	1.687	-1.022	0.193	-1.960	8.59
16	8.49	1.141	-0.758	0.065	-1.754	8.41	16.36	1.687	-1.022	0.193	-1.960	8.59
17	9.81	1.119	-0.749	0.056	-1.803	8.39	18.74	1.622	-1.004	0.203	-2.092	8.46
18	11.08	1.099	-0.739	0.047	-1.851	8.37	20.86	1.567	-0.966	0.188	-2.186	8.38
19	12.56	1.087	-0.723	0.043	-1.869	8.35	22.13	1.567	-0.966	0.188	-2.186	8.38
20	14.17	1.069	-0.711	0.035	-1.911	8.32	24.57	1.517	-0.936	0.169	-2.290	8.31

VII. LUTINGER PARAMETERS

TABLE IX: Adjusted Luttinger parameters and E_p for AIN and AIP in function of the adjusted region. The RMSDs are also indicated.

%	AIN						AIP					
	RMSD	γ_1	γ_2	γ_3	e	E_p	RMSD	γ_1	γ_2	γ_3	e	E_p
2	0.36	1.597	0.351	0.585	3.421	18.71	0.19	2.926	0.372	0.921	5.327	14.07
3	0.38	1.572	0.366	0.608	3.410	18.93	0.18	2.926	0.372	0.921	5.327	14.07
4	0.44	1.536	0.379	0.634	3.395	18.91	0.20	2.912	0.518	1.100	5.272	27.31
5	0.52	1.529	0.382	0.636	3.388	18.91	0.26	2.912	0.518	1.100	5.272	27.31
6	0.62	1.529	0.382	0.636	3.388	18.91	0.49	2.892	0.530	1.109	5.226	22.00
7	0.76	1.523	0.383	0.640	3.380	18.75	0.71	2.892	0.530	1.109	5.226	22.00
8	0.85	1.523	0.383	0.640	3.380	18.75	1.01	2.869	0.533	1.100	5.149	21.92
9	1.00	1.523	0.383	0.640	3.380	18.75	1.41	2.859	0.533	1.097	5.117	22.02
10	1.20	1.523	0.383	0.640	3.380	18.75	1.89	2.848	0.535	1.094	5.071	22.08
11	1.45	1.523	0.383	0.640	3.380	18.75	2.71	2.848	0.535	1.094	5.071	22.08
12	1.65	1.519	0.383	0.641	3.375	18.71	3.55	2.819	0.547	1.088	4.929	21.92
13	1.99	1.519	0.383	0.641	3.375	18.71	4.33	2.819	0.547	1.088	4.929	21.92
14	2.39	1.510	0.384	0.642	3.354	18.49	5.49	2.793	0.555	1.079	4.809	21.62
15	2.73	1.506	0.385	0.642	3.344	18.53	6.79	2.778	0.560	1.072	4.735	21.47
16	3.10	1.506	0.385	0.642	3.344	18.53	8.31	2.762	0.566	1.065	4.656	21.32
17	3.66	1.498	0.384	0.640	3.320	18.12	10.71	2.762	0.566	1.065	4.656	21.32
18	4.11	1.494	0.385	0.638	3.307	18.11	12.84	2.738	0.573	1.055	4.543	21.05
19	4.74	1.489	0.384	0.636	3.291	17.93	14.78	2.721	0.578	1.045	4.453	20.89
20	5.35	1.489	0.384	0.636	3.291	17.93	17.36	2.721	0.578	1.045	4.453	20.89

TABLE X: Adjusted Luttinger parameters and E_p for AlAs and AlSb in function of the adjusted region. The RMSDs are also indicated.

%	AlAs						AlSb					
	RMSD	γ_1	γ_2	γ_3	e	E_p	RMSD	γ_1	γ_2	γ_3	e	E_p
2	0.30	24.311	10.358	11.224	52.550	27.0	0.02	5.627	1.181	2.145	9.073	44.9
3	0.73	23.074	9.947	10.808	51.087	24.1	0.04	5.592	1.173	2.148	9.035	44.2
4	1.28	23.074	9.947	10.808	51.087	24.1	0.10	5.554	1.163	2.137	8.960	43.1
5	1.84	22.304	9.631	10.487	49.867	22.5	0.24	5.513	1.152	2.123	8.866	41.6
6	2.39	21.766	9.392	10.247	48.879	21.5	0.43	5.513	1.152	2.123	8.866	41.6
7	3.80	21.360	9.207	10.062	48.091	20.8	1.23	5.469	1.141	2.124	8.775	39.7
8	6.03	20.859	8.978	9.871	46.911	20.3	2.18	5.369	1.124	2.124	8.637	35.0
9	7.18	20.026	8.612	9.463	45.106	19.1	2.78	5.272	1.111	2.081	8.461	32.3
10	7.89	19.552	8.394	9.245	43.973	18.6	3.60	5.210	1.106	2.052	8.323	31.0
11	8.37	19.262	8.259	9.107	43.261	18.4	4.60	5.158	1.128	2.010	8.161	30.1
12	8.77	19.262	8.259	9.107	43.261	18.4	5.65	5.108	1.133	1.982	8.012	29.3
13	9.36	19.077	8.177	9.020	42.799	18.3	7.16	5.108	1.133	1.982	8.012	29.3
14	10.22	19.077	8.177	9.020	42.799	18.3	8.81	5.065	1.138	1.971	7.880	28.6
15	11.06	18.723	8.035	8.862	41.884	18.1	10.98	5.018	1.150	1.950	7.719	27.9
16	11.99	18.617	8.001	8.813	41.627	18.0	13.64	5.018	1.150	1.950	7.719	27.9
17	12.99	18.503	7.962	8.758	41.343	17.9	16.10	4.928	1.177	1.920	7.391	26.8
18	14.03	18.385	7.923	8.700	41.053	17.8	19.31	4.928	1.177	1.920	7.391	26.8
19	15.22	18.277	7.890	8.648	40.792	17.7	22.65	4.880	1.193	1.900	7.199	26.3
20	16.57	18.156	7.848	8.588	40.492	17.6	25.93	4.880	1.193	1.900	7.199	26.3

TABLE XI: Adjusted Luttinger parameters and E_p for GaN and GaP in function of the adjusted region. The RMSDs are also indicated.

%	GaN						GaP					
	RMSD	γ_1	γ_2	γ_3	e	E_p	RMSD	γ_1	γ_2	γ_3	e	E_p
2	0.02	2.491	0.614	0.963	5.090	15.5	0.30	4.604	0.799	1.654	7.483	25.5
3	0.05	2.484	0.614	0.965	5.089	17.8	0.31	4.604	0.799	1.654	7.483	25.5
4	0.13	2.484	0.614	0.965	5.089	17.8	0.32	4.542	0.814	1.646	7.460	25.5
5	0.31	2.484	0.614	0.965	5.089	17.8	0.47	4.493	0.834	1.656	7.408	26.0
6	0.58	2.447	0.604	0.965	5.014	17.7	0.85	4.493	0.834	1.656	7.408	26.0
7	0.69	2.442	0.599	0.958	5.000	17.4	1.35	4.392	0.834	1.667	7.238	25.3
8	0.88	2.442	0.599	0.958	5.000	17.4	1.74	4.362	0.827	1.643	7.180	25.2
9	1.13	2.437	0.600	0.957	4.990	17.5	2.24	4.337	0.832	1.631	7.116	25.4
10	1.33	2.433	0.599	0.956	4.981	17.4	3.13	4.303	0.844	1.624	7.006	25.5
11	1.65	2.433	0.599	0.956	4.981	17.4	3.93	4.280	0.849	1.614	6.931	25.5
12	2.03	2.430	0.598	0.957	4.975	17.3	4.91	4.255	0.856	1.604	6.849	25.4
13	2.37	2.417	0.597	0.955	4.949	17.1	6.09	4.229	0.863	1.592	6.760	25.4
14	2.81	2.417	0.597	0.955	4.949	17.1	7.25	4.229	0.863	1.592	6.760	25.4
15	3.28	2.412	0.596	0.954	4.938	16.9	9.46	4.205	0.869	1.585	6.679	25.2
16	3.69	2.403	0.596	0.951	4.916	16.7	11.64	4.205	0.869	1.585	6.679	25.2
17	4.26	2.397	0.597	0.947	4.901	16.6	13.71	4.137	0.887	1.556	6.429	24.8
18	4.80	2.397	0.597	0.947	4.901	16.6	16.16	4.108	0.894	1.542	6.311	24.6
19	5.29	2.391	0.599	0.945	4.888	16.6	18.83	4.108	0.894	1.542	6.311	24.6
20	5.89	2.386	0.599	0.942	4.874	16.4	22.05	4.078	0.899	1.529	6.186	24.5

TABLE XII: Adjusted Luttinger parameters and E_p for GaAs and GaSb in function of the adjusted region. The RMSDs are also indicated.

%	GaAs						GaSb					
	RMSD	γ_1	γ_2	γ_3	e	E_p	RMSD	γ_1	γ_2	γ_3	e	E_p
2	0.27	8.088	2.242	3.240	15.497	37.9	0.04	13.779	4.677	5.972	25.834	34.3
3	0.34	7.866	2.246	3.207	15.470	33.6	0.12	13.607	4.621	5.926	25.597	33.5
4	0.44	7.866	2.246	3.207	15.470	33.6	0.32	13.427	4.547	5.852	25.283	32.5
5	0.57	7.761	2.240	3.186	15.424	31.3	0.71	13.238	4.466	5.771	24.943	31.4
6	1.38	7.691	2.232	3.180	15.375	29.6	1.18	13.238	4.466	5.771	24.943	31.4
7	2.00	7.437	2.173	3.128	14.943	26.2	2.52	13.054	4.385	5.702	24.627	30.1
8	2.25	7.374	2.161	3.083	14.793	26.1	5.06	12.783	4.294	5.669	24.148	28.8
9	2.75	7.374	2.161	3.083	14.793	26.1	6.53	12.368	4.137	5.463	23.431	26.3
10	3.46	7.314	2.159	3.076	14.635	26.2	7.69	11.912	3.931	5.235	22.413	24.9
11	4.23	7.272	2.154	3.059	14.523	26.2	8.57	11.912	3.931	5.235	22.413	24.9
12	5.23	7.230	2.152	3.043	14.409	26.2	9.65	11.780	3.868	5.185	22.036	24.8
13	6.40	7.187	2.150	3.026	14.288	26.1	11.41	11.780	3.868	5.185	22.036	24.8
14	7.54	7.142	2.148	3.007	14.160	26.0	13.54	11.509	3.757	5.076	21.371	24.1
15	9.12	7.100	2.148	2.993	14.046	25.9	15.74	11.372	3.710	5.016	21.028	23.7
16	10.83	7.052	2.146	2.972	13.905	25.7	18.28	11.113	3.654	4.900	20.389	23.1
17	12.79	7.003	2.144	2.950	13.755	25.6	20.52	10.993	3.645	4.845	20.096	22.8
18	15.39	6.952	2.139	2.928	13.596	25.4	23.25	10.863	3.629	4.784	19.765	22.5
19	18.08	6.952	2.139	2.928	13.596	25.4	26.15	10.863	3.629	4.784	19.765	22.5
20	21.47	6.892	2.144	2.906	13.378	25.1	28.79	10.736	3.616	4.723	19.436	22.2

TABLE XIII: Adjusted Luttinger parameters and E_p for InN and InP in function of the adjusted region. The RMSDs are also indicated.

%	InN						InP					
	RMSD	γ_1	γ_2	γ_3	e	E_p	RMSD	γ_1	γ_2	γ_3	e	E_p
2	0.75	6.729	2.730	3.174	17.583	12.81	0.03	5.833	1.697	2.387	12.182	19.4
3	0.86	6.662	2.730	3.113	17.536	12.46	0.04	5.833	1.697	2.387	12.182	19.4
4	0.97	6.662	2.730	3.113	17.536	12.46	0.07	5.833	1.697	2.387	12.182	19.4
5	1.27	6.662	2.730	3.113	17.536	12.46	0.14	5.827	1.698	2.391	12.150	19.9
6	2.92	6.422	2.612	3.023	16.905	11.58	0.29	5.813	1.696	2.389	12.111	19.8
7	3.51	6.279	2.551	2.907	16.511	11.37	0.85	5.796	1.693	2.385	12.064	19.8
8	3.69	6.199	2.521	2.849	16.309	11.27	2.13	5.796	1.693	2.385	12.064	19.8
9	3.74	6.141	2.492	2.805	16.171	11.12	2.64	5.580	1.630	2.325	11.549	18.4
10	3.79	6.129	2.486	2.796	16.147	11.08	2.95	5.539	1.619	2.294	11.443	18.3
11	3.87	6.129	2.486	2.796	16.147	11.08	3.30	5.539	1.619	2.294	11.443	18.3
12	4.04	6.110	2.473	2.785	16.109	10.96	3.74	5.484	1.605	2.267	11.297	18.4
13	4.17	6.110	2.473	2.785	16.109	10.96	4.24	5.458	1.600	2.254	11.226	18.5
14	4.33	6.103	2.469	2.782	16.095	10.91	4.74	5.458	1.600	2.254	11.226	18.5
15	4.62	6.103	2.469	2.782	16.095	10.91	5.49	5.435	1.596	2.245	11.163	18.5
16	4.85	6.103	2.469	2.782	16.095	10.91	6.30	5.409	1.591	2.233	11.090	18.5
17	5.20	6.103	2.469	2.782	16.095	10.91	7.23	5.382	1.586	2.221	11.014	18.5
18	5.56	6.079	2.455	2.772	16.044	10.79	8.15	5.354	1.582	2.208	10.934	18.4
19	5.86	6.052	2.444	2.759	15.980	10.69	9.40	5.329	1.578	2.198	10.863	18.3
20	6.29	6.052	2.444	2.759	15.980	10.69	10.74	5.300	1.574	2.185	10.777	18.2

TABLE XIV: Adjusted Luttinger parameters and E_p for InAs and InSb in function of the adjusted region. The RMSDs are also indicated.

%	InAs						InSb					
	RMSD	γ_1	γ_2	γ_3	e	E_p	RMSD	γ_1	γ_2	γ_3	e	E_p
2	0.09	19.193	8.145	9.002	42.725	20.91	0.29	40.229	18.113	19.324	81.384	28.8
3	0.12	19.193	8.145	9.002	42.725	20.91	0.90	38.150	17.096	18.267	77.318	26.9
4	0.25	19.193	8.145	9.002	42.725	20.91	1.66	36.572	16.318	17.497	74.225	25.4
5	1.06	18.575	7.849	8.702	41.584	19.41	2.10	36.572	16.318	17.497	74.225	25.4
6	1.20	18.575	7.849	8.702	41.584	19.41	2.93	35.553	15.791	17.003	72.231	24.4
7	1.38	18.421	7.777	8.631	41.256	19.15	4.33	34.599	15.322	16.538	70.363	23.6
8	1.64	18.336	7.739	8.595	41.058	19.05	7.01	33.638	14.846	16.101	68.504	22.7
9	1.99	18.267	7.712	8.570	40.897	18.98	8.60	31.999	14.109	15.243	65.326	21.2
10	2.60	18.202	7.688	8.552	40.752	18.91	9.39	31.053	13.647	14.804	63.367	20.4
11	3.33	18.136	7.666	8.529	40.590	18.87	9.93	31.053	13.647	14.804	63.367	20.4
12	3.96	18.065	7.644	8.502	40.415	18.82	10.77	30.580	13.396	14.610	62.283	20.1
13	5.00	18.065	7.644	8.502	40.415	18.82	11.73	30.580	13.396	14.610	62.283	20.1
14	6.17	17.916	7.592	8.444	40.030	18.72	12.83	30.130	13.177	14.402	61.339	19.8
15	7.22	17.826	7.565	8.403	39.812	18.65	14.37	29.505	12.887	14.102	60.038	19.3
16	8.49	17.738	7.540	8.364	39.604	18.56	16.36	29.505	12.887	14.102	60.038	19.3
17	9.81	17.639	7.511	8.316	39.362	18.47	18.74	28.634	12.501	13.709	58.109	18.8
18	11.08	17.535	7.480	8.265	39.107	18.38	20.86	28.022	12.261	13.415	56.773	18.4
19	12.56	17.437	7.452	8.218	38.873	18.28	22.13	28.022	12.261	13.415	56.773	18.4
20	14.17	17.327	7.417	8.164	38.599	18.18	24.57	27.552	12.081	13.186	55.733	18.1

VIII. EFFECTIVE MASSES AND g -FACTORSTABLE XV: Optimal AlN effective masses and electronic g -factors. Heavy (m_{hh}) and light (m_{lh}) hole effective masses are presented for three different high-symmetry directions ([100], [110] and [111]), while spin-orbit splitting hole (m_{so}) and electron (m_e) effective masses are isotropic. RMSD values are also presented.

%	RMSD	[100]		[110]		[111]		m_{so}	m_e	g_e
		m_{hh}	m_{lh}	m_{hh}	m_{lh}	m_{hh}	m_{lh}			
2	0.36	1.117	0.435	2.345	0.361	1.907	0.375	0.628	0.292	1.991
3	0.38	1.190	0.434	2.820	0.359	2.193	0.372	0.638	0.293	1.991
4	0.44	1.286	0.436	3.723	0.357	2.668	0.371	0.653	0.295	1.991
5	0.52	1.306	0.436	3.898	0.357	2.757	0.371	0.656	0.295	1.991
6	0.62	1.306	0.436	3.898	0.357	2.757	0.371	0.656	0.295	1.991
7	0.76	1.320	0.437	4.123	0.357	2.858	0.371	0.659	0.296	1.991
8	0.85	1.320	0.437	4.123	0.357	2.858	0.371	0.659	0.296	1.991
9	1.00	1.320	0.437	4.123	0.357	2.858	0.371	0.659	0.296	1.991
10	1.20	1.320	0.437	4.123	0.357	2.858	0.371	0.659	0.296	1.991
11	1.45	1.320	0.437	4.123	0.357	2.858	0.371	0.659	0.296	1.991
12	1.65	1.329	0.438	4.225	0.357	2.905	0.371	0.660	0.296	1.991
13	1.99	1.329	0.438	4.225	0.357	2.905	0.371	0.660	0.296	1.991
14	2.39	1.349	0.439	4.445	0.358	3.006	0.372	0.664	0.298	1.991
15	2.73	1.360	0.439	4.519	0.358	3.043	0.373	0.666	0.299	1.991
16	3.10	1.360	0.439	4.519	0.358	3.043	0.373	0.666	0.299	1.991
17	3.66	1.370	0.441	4.574	0.360	3.074	0.374	0.669	0.301	1.991
18	4.11	1.380	0.442	4.595	0.361	3.090	0.375	0.671	0.302	1.991
19	4.74	1.387	0.443	4.610	0.362	3.102	0.376	0.673	0.304	1.991
20	5.35	1.387	0.443	4.610	0.362	3.102	0.376	0.673	0.304	1.991

TABLE XVI: Optimal AlP effective masses and electronic g -factors. Heavy (m_{hh}) and light (m_{lh}) hole effective masses are presented for three different high-symmetry directions ([100], [110] and [111]), while spin-orbit splitting hole (m_{so}) and electron (m_e) effective masses are isotropic. RMSD values are also presented.

%	RMSD	[100]		[110]		[111]		m_{so}	m_e	g_e
		m_{hh}	m_{lh}	m_{hh}	m_{lh}	m_{hh}	m_{lh}			
2	0.19	0.458	0.273	0.923	0.210	0.777	0.219	0.344	0.188	1.957
3	0.18	0.458	0.273	0.923	0.210	0.777	0.219	0.344	0.188	1.957
4	0.20	0.533	0.253	1.402	0.196	1.065	0.205	0.348	0.190	1.916
5	0.26	0.533	0.253	1.402	0.196	1.065	0.205	0.348	0.190	1.916
6	0.49	0.546	0.253	1.484	0.196	1.112	0.205	0.350	0.191	1.932
7	0.71	0.546	0.253	1.484	0.196	1.112	0.205	0.350	0.191	1.932
8	1.01	0.555	0.254	1.497	0.197	1.124	0.206	0.353	0.194	1.932
9	1.41	0.558	0.255	1.504	0.198	1.129	0.207	0.354	0.195	1.932
10	1.89	0.563	0.255	1.516	0.199	1.138	0.208	0.355	0.197	1.932
11	2.71	0.563	0.255	1.516	0.199	1.138	0.208	0.355	0.197	1.932
12	3.55	0.580	0.256	1.556	0.200	1.168	0.209	0.359	0.203	1.932
13	4.33	0.580	0.256	1.556	0.200	1.168	0.209	0.359	0.203	1.932
14	5.49	0.594	0.256	1.577	0.202	1.187	0.211	0.362	0.208	1.933
15	6.79	0.603	0.257	1.579	0.203	1.193	0.212	0.364	0.211	1.934
16	8.31	0.613	0.257	1.580	0.204	1.200	0.213	0.366	0.215	1.934
17	10.71	0.613	0.257	1.580	0.204	1.200	0.213	0.366	0.215	1.934
18	12.84	0.628	0.257	1.590	0.206	1.214	0.215	0.370	0.220	1.935
19	14.78	0.639	0.258	1.588	0.208	1.220	0.216	0.372	0.225	1.936
20	17.36	0.639	0.258	1.588	0.208	1.220	0.216	0.372	0.225	1.936

TABLE XVII: Optimal AlAs effective masses and electronic g-factors. Heavy (m_{hh}) and light (m_{lh}) hole effective masses are presented for three different high-symmetry directions ([100], [110] and [111]), while spin-orbit splitting hole (m_{so}) and electron (m_e) effective masses are isotropic. RMSD values are also presented.

%	RMSD	[100]		[110]		[111]		m_{so}	m_e	g_e
		m_{hh}	m_{lh}	m_{hh}	m_{lh}	m_{hh}	m_{lh}			
2	0.02	0.426	0.170	-0.885	0.172	1.085	0.137	0.272	0.130	1.114
3	0.05	0.426	0.170	-0.885	0.172	1.085	0.137	0.272	0.130	1.114
4	0.10	0.429	0.171	2.220	0.164	1.093	0.137	0.271	0.130	1.183
5	0.18	0.431	0.171	0.572	0.152	1.099	0.138	0.270	0.130	1.247
6	0.51	0.434	0.172	0.374	0.136	1.116	0.139	0.269	0.131	1.308
7	0.86	0.449	0.175	0.291	0.101	1.231	0.140	0.271	0.133	1.439
8	1.06	0.453	0.176	0.283	0.102	1.190	0.142	0.273	0.134	1.446
9	1.49	0.461	0.176	0.285	0.103	1.203	0.143	0.274	0.136	1.447
10	1.87	0.461	0.176	0.285	0.103	1.203	0.143	0.274	0.136	1.447
11	2.49	0.472	0.177	0.289	0.104	1.227	0.144	0.277	0.138	1.450
12	3.23	0.478	0.177	0.290	0.105	1.232	0.144	0.278	0.139	1.452
13	4.15	0.478	0.177	0.290	0.105	1.232	0.144	0.278	0.139	1.452
14	5.08	0.486	0.177	0.290	0.106	1.237	0.145	0.279	0.140	1.455
15	6.43	0.486	0.177	0.290	0.106	1.237	0.145	0.279	0.140	1.455
16	8.02	0.503	0.177	0.291	0.107	1.253	0.146	0.282	0.143	1.462
17	10.35	0.514	0.177	0.291	0.108	1.254	0.147	0.284	0.145	1.464
18	12.53	0.514	0.177	0.291	0.108	1.254	0.147	0.284	0.145	1.464
19	14.77	0.514	0.177	0.291	0.108	1.254	0.147	0.284	0.145	1.464
20	17.60	0.514	0.177	0.291	0.108	1.254	0.147	0.284	0.145	1.464

TABLE XVIII: Optimal AlSb effective masses and electronic g-factors. Heavy (m_{hh}) and light (m_{lh}) hole effective masses are presented for three different high-symmetry directions ([100], [110] and [111]), while spin-orbit splitting hole (m_{so}) and electron (m_e) effective masses are isotropic. RMSD values are also presented.

%	RMSD	[100]		[110]		[111]		m_{so}	m_e	g_e
		m_{hh}	m_{lh}	m_{hh}	m_{lh}	m_{hh}	m_{lh}			
2	0.02	0.306	0.125	-1.849	0.121	0.748	0.101	0.237	0.110	-0.827
3	0.04	0.308	0.126	-4.144	0.121	0.772	0.101	0.238	0.111	-0.783
4	0.10	0.310	0.127	3.624	0.120	0.781	0.102	0.238	0.112	-0.713
5	0.24	0.312	0.128	1.010	0.118	0.790	0.102	0.238	0.113	-0.618
6	0.43	0.312	0.128	1.010	0.118	0.790	0.102	0.238	0.113	-0.618
7	1.23	0.314	0.129	0.542	0.114	0.819	0.103	0.237	0.114	-0.499
8	2.18	0.320	0.131	0.294	0.099	0.893	0.104	0.234	0.116	-0.206
9	2.78	0.328	0.133	0.252	0.092	0.901	0.106	0.235	0.118	-0.035
10	3.60	0.334	0.135	0.240	0.089	0.904	0.107	0.236	0.120	0.047
11	4.60	0.345	0.135	0.226	0.088	0.879	0.109	0.238	0.123	0.103
12	5.65	0.352	0.136	0.220	0.087	0.874	0.110	0.239	0.125	0.155
13	7.16	0.352	0.136	0.220	0.087	0.874	0.110	0.239	0.125	0.155
14	8.81	0.359	0.136	0.219	0.086	0.890	0.111	0.240	0.127	0.201
15	10.98	0.368	0.137	0.217	0.085	0.895	0.112	0.242	0.130	0.240
16	13.64	0.368	0.137	0.217	0.085	0.895	0.112	0.242	0.130	0.240
17	16.10	0.388	0.137	0.217	0.084	0.919	0.114	0.245	0.135	0.311
18	19.31	0.388	0.137	0.217	0.084	0.919	0.114	0.245	0.135	0.311
19	22.65	0.401	0.138	0.216	0.084	0.927	0.115	0.247	0.139	0.342
20	25.93	0.401	0.138	0.216	0.084	0.927	0.115	0.247	0.139	0.342

TABLE XIX: Optimal GaN effective masses and electronic g-factors. Heavy (m_{hh}) and light (m_{lh}) hole effective masses are presented for three different high-symmetry directions ([100], [110] and [111]), while spin-orbit splitting hole (m_{so}) and electron (m_e) effective masses are isotropic. RMSD values are also presented.

%	RMSD	[100]		[110]		[111]		m_{so}	m_e	g_e
		m_{hh}	m_{lh}	m_{hh}	m_{lh}	m_{hh}	m_{lh}			
2	0.02	0.791	0.269	0.394	0.131	1.771	0.226	0.403	0.196	1.979
3	0.05	0.796	0.269	0.415	0.156	1.807	0.227	0.405	0.197	1.976
4	0.13	0.796	0.269	0.415	0.156	1.807	0.227	0.405	0.197	1.976
5	0.31	0.796	0.269	0.415	0.156	1.807	0.227	0.405	0.197	1.976
6	0.58	0.808	0.274	0.440	0.157	1.934	0.229	0.411	0.199	1.976
7	0.69	0.805	0.275	0.432	0.156	1.899	0.229	0.412	0.200	1.976
8	0.88	0.805	0.275	0.432	0.156	1.899	0.229	0.412	0.200	1.976
9	1.13	0.808	0.275	0.435	0.157	1.911	0.230	0.412	0.200	1.976
10	1.33	0.810	0.275	0.437	0.156	1.924	0.230	0.413	0.201	1.976
11	1.65	0.810	0.275	0.437	0.156	1.924	0.230	0.413	0.201	1.976
12	2.03	0.811	0.276	0.439	0.156	1.936	0.230	0.414	0.201	1.976
13	2.37	0.817	0.277	0.444	0.154	1.975	0.231	0.416	0.202	1.977
14	2.81	0.817	0.277	0.444	0.154	1.975	0.231	0.416	0.202	1.977
15	3.28	0.820	0.277	0.446	0.153	1.986	0.231	0.417	0.203	1.977
16	3.69	0.826	0.278	0.446	0.152	1.993	0.232	0.418	0.203	1.977
17	4.26	0.831	0.279	0.445	0.152	1.993	0.233	0.419	0.204	1.977
18	4.80	0.831	0.279	0.445	0.152	1.993	0.233	0.419	0.204	1.977
19	5.29	0.837	0.279	0.446	0.153	1.992	0.234	0.420	0.205	1.977
20	5.89	0.841	0.279	0.444	0.151	1.991	0.234	0.421	0.205	1.977

TABLE XX: Optimal GaP effective masses and electronic g-factors. Heavy (m_{hh}) and light (m_{lh}) hole effective masses are presented for three different high-symmetry directions ([100], [110] and [111]), while spin-orbit splitting hole (m_{so}) and electron (m_e) effective masses are isotropic. RMSD values are also presented.

%	RMSD	[100]		[110]		[111]		m_{so}	m_e	g_e
		m_{hh}	m_{lh}	m_{hh}	m_{lh}	m_{hh}	m_{lh}			
2	0.30	0.333	0.161	0.186	0.075	0.772	0.126	0.222	0.134	1.816
3	0.31	0.333	0.161	0.186	0.075	0.772	0.126	0.222	0.134	1.816
4	0.32	0.343	0.162	0.192	0.077	0.800	0.128	0.225	0.134	1.816
5	0.47	0.354	0.162	0.203	0.079	0.847	0.128	0.227	0.135	1.813
6	0.85	0.354	0.162	0.203	0.079	0.847	0.128	0.227	0.135	1.813
7	1.35	0.367	0.165	0.220	0.079	0.945	0.129	0.233	0.138	1.818
8	1.74	0.369	0.166	0.218	0.080	0.930	0.131	0.234	0.139	1.819
9	2.24	0.374	0.167	0.220	0.082	0.930	0.132	0.236	0.141	1.817
10	3.13	0.382	0.167	0.224	0.084	0.948	0.132	0.237	0.143	1.816
11	3.93	0.387	0.167	0.225	0.085	0.952	0.133	0.239	0.144	1.816
12	4.91	0.393	0.168	0.226	0.086	0.955	0.134	0.240	0.146	1.817
13	6.09	0.399	0.168	0.226	0.087	0.957	0.135	0.242	0.148	1.817
14	7.25	0.399	0.168	0.226	0.087	0.957	0.135	0.242	0.148	1.817
15	9.46	0.405	0.168	0.227	0.087	0.966	0.136	0.243	0.150	1.819
16	11.64	0.405	0.168	0.227	0.087	0.966	0.136	0.243	0.150	1.819
17	13.71	0.423	0.169	0.229	0.089	0.975	0.138	0.247	0.156	1.821
18	16.16	0.431	0.170	0.229	0.090	0.977	0.139	0.249	0.158	1.822
19	18.83	0.431	0.170	0.229	0.090	0.977	0.139	0.249	0.158	1.822
20	22.05	0.439	0.170	0.230	0.091	0.980	0.140	0.251	0.162	1.824

TABLE XXI: Optimal GaAs effective masses and electronic g-factors. Heavy (m_{hh}) and light (m_{lh}) hole effective masses are presented for three different high-symmetry directions ([100], [110] and [111]), while spin-orbit splitting hole (m_{so}) and electron (m_e) effective masses are isotropic. RMSD values are also presented.

%	RMSD	[100]		[110]		[111]		m_{so}	m_e	g_e
		m_{hh}	m_{lh}	m_{hh}	m_{lh}	m_{hh}	m_{lh}			
2	0.27	0.277	0.080	0.329	0.098	0.622	0.069	0.157	0.065	-1.433
3	0.34	0.296	0.081	0.194	0.084	0.688	0.070	0.158	0.065	-1.042
4	0.44	0.296	0.081	0.194	0.084	0.688	0.070	0.158	0.065	-1.042
5	0.57	0.305	0.082	0.179	0.074	0.720	0.071	0.158	0.065	-0.837
6	1.38	0.310	0.082	0.176	0.066	0.752	0.071	0.157	0.065	-0.683
7	2.00	0.324	0.085	0.184	0.056	0.847	0.073	0.160	0.067	-0.376
8	2.25	0.328	0.086	0.181	0.058	0.828	0.074	0.162	0.068	-0.365
9	2.75	0.328	0.086	0.181	0.058	0.828	0.074	0.162	0.068	-0.365
10	3.46	0.334	0.086	0.188	0.059	0.861	0.074	0.163	0.068	-0.371
11	4.23	0.337	0.086	0.189	0.060	0.866	0.075	0.164	0.069	-0.372
12	5.23	0.342	0.087	0.191	0.061	0.874	0.075	0.165	0.069	-0.371
13	6.40	0.346	0.087	0.193	0.062	0.881	0.076	0.167	0.070	-0.366
14	7.54	0.351	0.087	0.195	0.062	0.887	0.076	0.168	0.071	-0.358
15	9.12	0.357	0.088	0.197	0.063	0.898	0.076	0.169	0.071	-0.342
16	10.83	0.362	0.088	0.198	0.063	0.903	0.077	0.170	0.072	-0.331
17	12.79	0.368	0.089	0.199	0.064	0.908	0.077	0.171	0.073	-0.318
18	15.39	0.374	0.089	0.201	0.064	0.913	0.078	0.172	0.074	-0.303
19	18.08	0.374	0.089	0.201	0.064	0.913	0.078	0.172	0.074	-0.303
20	21.47	0.384	0.089	0.203	0.064	0.926	0.079	0.174	0.075	-0.272

TABLE XXII: Optimal GaSb effective masses and electronic g-factors. Heavy (m_{hh}) and light (m_{lh}) hole effective masses are presented for three different high-symmetry directions ([100], [110] and [111]), while spin-orbit splitting hole (m_{so}) and electron (m_e) effective masses are isotropic. RMSD values are also presented.

%	RMSD	[100]		[110]		[111]		m_{so}	m_e	g_e
		m_{hh}	m_{lh}	m_{hh}	m_{lh}	m_{hh}	m_{lh}			
2	0.04	0.226	0.043	0.133	0.053	0.545	0.039	0.141	0.039	-11.373
3	0.12	0.229	0.044	0.135	0.051	0.570	0.039	0.141	0.039	-11.038
4	0.32	0.231	0.044	0.135	0.049	0.580	0.040	0.141	0.040	-10.653
5	0.71	0.232	0.045	0.134	0.046	0.590	0.040	0.140	0.040	-10.218
6	1.18	0.232	0.045	0.134	0.046	0.590	0.040	0.140	0.040	-10.218
7	2.52	0.233	0.046	0.134	0.043	0.606	0.041	0.139	0.041	-9.741
8	5.06	0.238	0.047	0.145	0.041	0.693	0.041	0.139	0.041	-9.216
9	6.53	0.244	0.048	0.143	0.037	0.694	0.043	0.138	0.043	-8.264
10	7.69	0.247	0.051	0.143	0.038	0.693	0.045	0.142	0.045	-7.724
11	8.57	0.247	0.051	0.143	0.038	0.693	0.045	0.142	0.045	-7.724
12	9.65	0.247	0.051	0.146	0.038	0.710	0.045	0.144	0.045	-7.661
13	11.41	0.247	0.051	0.146	0.038	0.710	0.045	0.144	0.045	-7.661
14	13.54	0.250	0.053	0.151	0.039	0.737	0.046	0.147	0.047	-7.386
15	15.74	0.253	0.053	0.152	0.039	0.746	0.047	0.148	0.048	-7.258
16	18.28	0.263	0.054	0.155	0.040	0.762	0.048	0.151	0.049	-7.008
17	20.52	0.270	0.055	0.157	0.040	0.768	0.048	0.153	0.050	-6.892
18	23.25	0.277	0.055	0.158	0.040	0.772	0.049	0.154	0.051	-6.779
19	26.15	0.277	0.055	0.158	0.040	0.772	0.049	0.154	0.051	-6.779
20	28.79	0.285	0.056	0.160	0.041	0.776	0.050	0.156	0.051	-6.665

TABLE XXIII: Optimal InN effective masses and electronic g-factors. Heavy (m_{hh}) and light (m_{lh}) hole effective masses are presented for three different high-symmetry directions ([100], [110] and [111]), while spin-orbit splitting hole (m_{so}) and electron (m_e) effective masses are isotropic. RMSD values are also presented.

%	RMSD	[100]		[110]		[111]		m_{so}	m_e	g_e
		m_{hh}	m_{lh}	m_{hh}	m_{lh}	m_{hh}	m_{lh}			
2	0.75	0.788	0.082	2.624	0.076	1.692	0.078	0.152	0.057	1.685
3	0.86	0.832	0.082	2.295	0.078	1.617	0.079	0.154	0.057	1.694
4	0.97	0.832	0.082	2.295	0.078	1.617	0.079	0.154	0.057	1.694
5	1.27	0.832	0.082	2.295	0.078	1.617	0.079	0.154	0.057	1.694
6	2.92	0.834	0.086	2.669	0.080	1.755	0.081	0.159	0.059	1.716
7	3.51	0.850	0.088	2.154	0.083	1.577	0.084	0.163	0.061	1.721
8	3.69	0.864	0.089	1.999	0.084	1.522	0.085	0.165	0.061	1.723
9	3.74	0.865	0.090	1.883	0.085	1.469	0.086	0.167	0.062	1.727
10	3.79	0.864	0.090	1.862	0.085	1.459	0.086	0.167	0.062	1.728
11	3.87	0.864	0.090	1.862	0.085	1.459	0.086	0.167	0.062	1.728
12	4.04	0.860	0.090	1.854	0.086	1.452	0.087	0.167	0.062	1.731
13	4.17	0.860	0.090	1.854	0.086	1.452	0.087	0.167	0.062	1.731
14	4.33	0.858	0.091	1.854	0.086	1.451	0.087	0.168	0.062	1.732
15	4.62	0.858	0.091	1.854	0.086	1.451	0.087	0.168	0.062	1.732
16	4.85	0.858	0.091	1.854	0.086	1.451	0.087	0.168	0.062	1.732
17	5.20	0.858	0.091	1.854	0.086	1.451	0.087	0.168	0.062	1.732
18	5.56	0.856	0.091	1.870	0.086	1.458	0.087	0.168	0.062	1.735
19	5.86	0.859	0.091	1.876	0.086	1.462	0.088	0.169	0.063	1.738
20	6.29	0.859	0.091	1.876	0.086	1.462	0.088	0.169	0.063	1.738

TABLE XXIV: Optimal InP effective masses and electronic g-factors. Heavy (m_{hh}) and light (m_{lh}) hole effective masses are presented for three different high-symmetry directions ([100], [110] and [111]), while spin-orbit splitting hole (m_{so}) and electron (m_e) effective masses are isotropic. RMSD values are also presented.

%	RMSD	[100]		[110]		[111]		m_{so}	m_e	g_e
		m_{hh}	m_{lh}	m_{hh}	m_{lh}	m_{hh}	m_{lh}			
2	0.03	0.410	0.108	0.210	0.071	0.945	0.094	0.182	0.082	1.342
3	0.04	0.410	0.108	0.210	0.071	0.945	0.094	0.182	0.082	1.342
4	0.07	0.410	0.108	0.210	0.071	0.945	0.094	0.182	0.082	1.342
5	0.14	0.411	0.108	0.214	0.074	0.957	0.094	0.182	0.082	1.326
6	0.29	0.413	0.109	0.216	0.074	0.966	0.094	0.183	0.083	1.328
7	0.85	0.415	0.109	0.218	0.074	0.974	0.095	0.183	0.083	1.329
8	2.13	0.415	0.109	0.218	0.074	0.974	0.095	0.183	0.083	1.329
9	2.64	0.431	0.113	0.233	0.072	1.076	0.098	0.190	0.087	1.377
10	2.95	0.435	0.114	0.230	0.073	1.050	0.099	0.191	0.087	1.377
11	3.30	0.435	0.114	0.230	0.073	1.050	0.099	0.191	0.087	1.377
12	3.74	0.440	0.115	0.232	0.076	1.052	0.100	0.193	0.089	1.374
13	4.24	0.443	0.115	0.233	0.078	1.051	0.100	0.194	0.089	1.372
14	4.74	0.443	0.115	0.233	0.078	1.051	0.100	0.194	0.089	1.372
15	5.49	0.446	0.116	0.235	0.079	1.059	0.101	0.195	0.090	1.372
16	6.30	0.449	0.116	0.236	0.080	1.061	0.101	0.196	0.090	1.372
17	7.23	0.453	0.117	0.237	0.081	1.063	0.102	0.197	0.091	1.373
18	8.15	0.456	0.117	0.238	0.081	1.066	0.102	0.198	0.091	1.375
19	9.40	0.460	0.118	0.240	0.082	1.073	0.103	0.199	0.092	1.378
20	10.74	0.465	0.118	0.241	0.082	1.076	0.103	0.200	0.093	1.381

TABLE XXV: Optimal InAs effective masses and electronic g-factors. Heavy (m_{hh}) and light (m_{lh}) hole effective masses are presented for three different high-symmetry directions ([100], [110] and [111]), while spin-orbit splitting hole (m_{so}) and electron (m_e) effective masses are isotropic. RMSD values are also presented.

%	RMSD	[100]		[110]		[111]		m_{so}	m_e	g_e
		m_{hh}	m_{lh}	m_{hh}	m_{lh}	m_{hh}	m_{lh}			
2	0.09	0.345	0.028	0.841	0.027	0.624	0.027	0.103	0.023	-16.998
3	0.12	0.345	0.028	0.841	0.027	0.624	0.027	0.103	0.023	-16.998
4	0.25	0.345	0.028	0.841	0.027	0.624	0.027	0.103	0.023	-16.998
5	1.06	0.348	0.029	0.855	0.028	0.633	0.028	0.103	0.024	-15.643
6	1.20	0.348	0.029	0.855	0.028	0.633	0.028	0.103	0.024	-15.643
7	1.38	0.349	0.029	0.862	0.028	0.637	0.028	0.103	0.024	-15.403
8	1.64	0.350	0.030	0.873	0.028	0.642	0.028	0.103	0.024	-15.314
9	1.99	0.352	0.030	0.888	0.028	0.650	0.029	0.104	0.024	-15.253
10	2.60	0.354	0.030	0.911	0.028	0.661	0.029	0.104	0.025	-15.184
11	3.33	0.357	0.030	0.928	0.028	0.670	0.029	0.105	0.025	-15.147
12	3.96	0.360	0.030	0.943	0.029	0.679	0.029	0.105	0.025	-15.106
13	5.00	0.360	0.030	0.943	0.029	0.679	0.029	0.105	0.025	-15.106
14	6.17	0.366	0.030	0.974	0.029	0.696	0.029	0.106	0.025	-15.014
15	7.22	0.371	0.030	0.981	0.029	0.703	0.029	0.107	0.025	-14.946
16	8.49	0.376	0.030	0.990	0.029	0.711	0.029	0.107	0.025	-14.867
17	9.81	0.382	0.031	0.993	0.029	0.717	0.030	0.108	0.025	-14.789
18	11.08	0.388	0.031	0.995	0.029	0.723	0.030	0.109	0.026	-14.704
19	12.56	0.395	0.031	0.999	0.030	0.730	0.030	0.110	0.026	-14.616
20	14.17	0.401	0.031	1.002	0.030	0.736	0.030	0.110	0.026	-14.522

TABLE XXVI: Optimal InSb effective masses and electronic g-factors. Heavy (m_{hh}) and light (m_{lh}) hole effective masses are presented for three different high-symmetry directions ([100], [110] and [111]), while spin-orbit splitting hole (m_{so}) and electron (m_e) effective masses are isotropic. RMSD values are also presented.

%	RMSD	[100]		[110]		[111]		m_{so}	m_e	g_e
		m_{hh}	m_{lh}	m_{hh}	m_{lh}	m_{hh}	m_{lh}			
2	0.29	0.250	0.013	0.124	0.015	0.632	0.013	0.121	0.012	-61.915
3	0.90	0.253	0.014	0.123	0.015	0.618	0.013	0.120	0.013	-57.634
4	1.66	0.254	0.014	0.125	0.015	0.634	0.014	0.119	0.013	-54.372
5	2.10	0.254	0.014	0.125	0.015	0.634	0.014	0.119	0.013	-54.372
6	2.93	0.252	0.015	0.126	0.015	0.646	0.014	0.118	0.014	-52.211
7	4.33	0.253	0.015	0.128	0.015	0.657	0.015	0.118	0.014	-50.230
8	7.01	0.253	0.016	0.132	0.015	0.696	0.015	0.117	0.015	-48.252
9	8.60	0.264	0.017	0.130	0.015	0.661	0.016	0.117	0.015	-44.921
10	9.39	0.266	0.017	0.134	0.016	0.692	0.016	0.119	0.016	-43.303
11	9.93	0.266	0.017	0.134	0.016	0.692	0.016	0.119	0.016	-43.303
12	10.77	0.264	0.017	0.139	0.016	0.735	0.017	0.121	0.016	-42.667
13	11.73	0.264	0.017	0.139	0.016	0.735	0.017	0.121	0.016	-42.667
14	12.83	0.265	0.018	0.141	0.016	0.755	0.017	0.122	0.016	-41.917
15	14.37	0.268	0.018	0.143	0.016	0.769	0.017	0.124	0.017	-40.912
16	16.36	0.268	0.018	0.143	0.016	0.769	0.017	0.124	0.017	-40.912
17	18.74	0.275	0.019	0.151	0.017	0.823	0.018	0.128	0.017	-39.668
18	20.86	0.286	0.019	0.155	0.017	0.840	0.018	0.131	0.018	-38.808
19	22.13	0.286	0.019	0.155	0.017	0.840	0.018	0.131	0.018	-38.808
20	24.57	0.295	0.019	0.158	0.017	0.848	0.019	0.134	0.018	-38.160

Supplementary Materials: Ab-initio Investigation of Structural Stability and Exfoliation Energies in Transition Metal Dichalcogenides based on Ti-, V-, and Mo-Group Elements

Carlos M. O. Bastos,¹ Rafael Besse,¹ Juarez L. F. Da Silva,² and Guilherme M. Sipahi¹

¹*São Carlos Institute of Physics, University of São Paulo,
PO Box 369, 13560-970, São Carlos, SP, Brazil.*

²*São Carlos Institute of Chemistry, University of São Paulo,
PO Box 780, 13560-970, São Carlos, SP, Brazil.*

I. COMPUTATIONAL DETAILS

TABLE I. PAW VASP projectors used in this work, with the number of valence electrons (ZVAL) and the cut-off energies recommended by VASP, used in the minimization of the stress/elastic constants tensor and in the determination of the total energy/band structures.

specie	PAW	valence	recommended	cut-off energy (eV)	
				stress/elastic	total energy/band structure
S	PAW_PBE S 06Sep2000	6	258.689	517.378	291.025
Se	PAW_PBE Se 06Sep2000	6	211.555	423.110	237.999
Te	PAW_PBE Te 08Apr2002	6	174.982	349.964	196.854
Ti	PAW_PBE Ti 08Apr2002	5	178.330	356.660	200.621
Zr	PAW_PBE Zr_sv 04Jan2005	12	229.898	459.796	258.635
Hf	PAW_PBE Hf 20Jan2003	4	220.334	440.668	247.875
V	PAW_PBE V 08Apr2002	5	192.543	385.086	216.610
Nb	PAW_PBE Nb_pv 08Apr2002	11	208.608	417.216	234.684
Ta	PAW_PBE Ta 17Jan2003	5	223.667	447.334	251.625
Cr	PAW_PBE Cr 06Sep2000	6	227.080	454.160	255.465
Mo	PAW_PBE Mo 08Apr2002	6	224.584	449.168	252.657
W	PAW_PBE W 08Apr2002	5	223.057	446.114	250.939

II. CONVERGENCE TESTS

A. k-points density

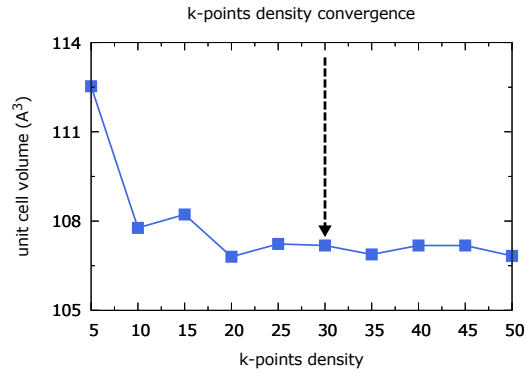


FIG. 1. Convergence test using MoS₂ in 2H phase, showing the dependence of volume unit cell with k-point density (in left) and cutoff energy (right).

B. Cut-off energy

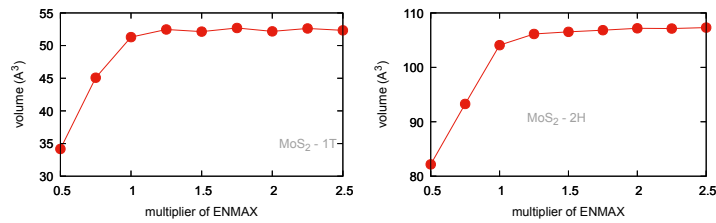


FIG. 2. Convergence test for cut-off energy using MoS₂ in 1T (left) and 2H (right) phase.

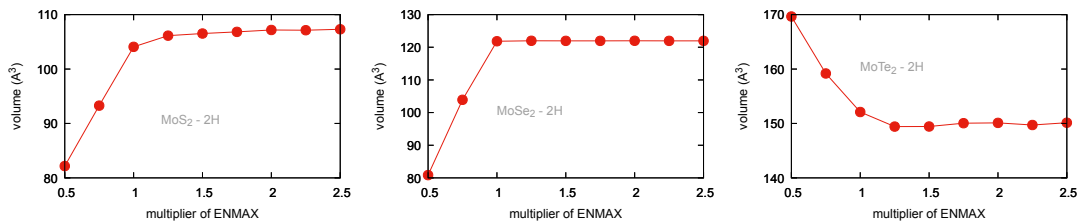


FIG. 3. Convergence test for cut-off energy for MoS₂, MoSe₂ and MoTe₂ in 2H phase.

III. INITIAL MAGNETIC CONFIGURATIONS

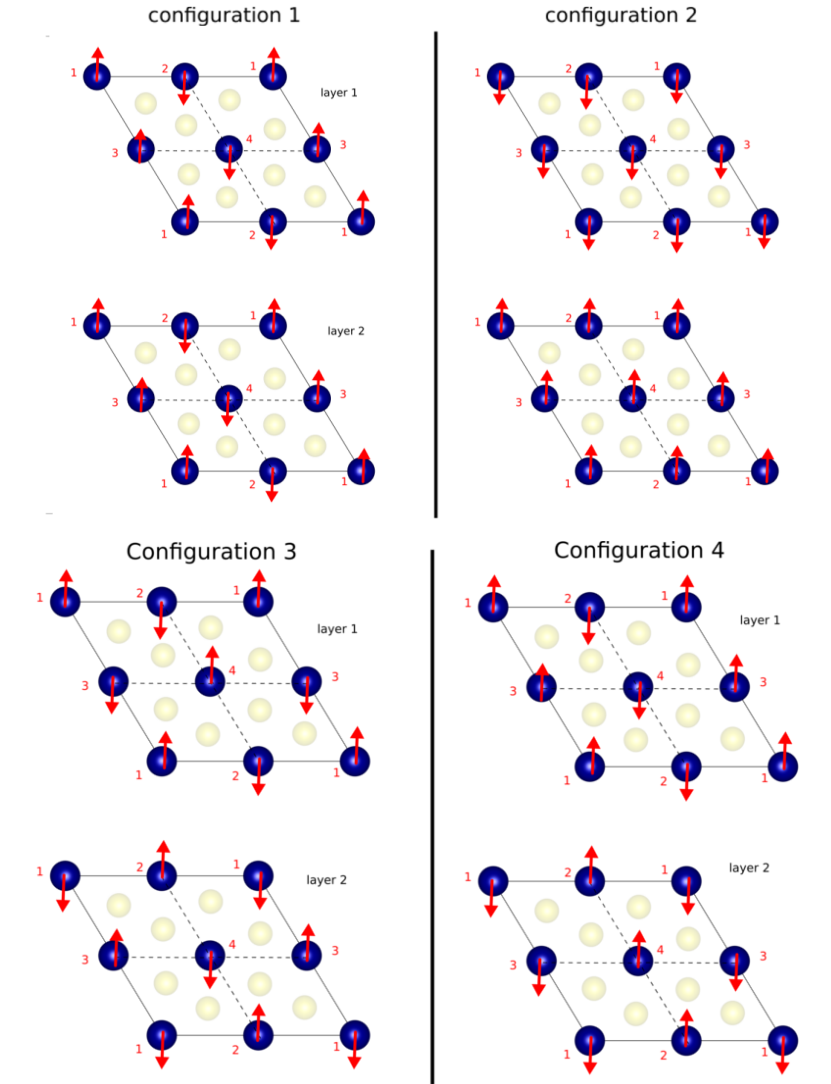


FIG. 4. Initial magnetic configurations. Arrows represent the magnetic moment in the metal element.

IV. RELATIVE ENERGY

TABLE II. Relativity energy between 1T and 1T_d in comparison with 2H phase, by atom. All energies are in meV

	energy (1T-2H)	energy (1T _d -2H)
TiS ₂	-144	-
TiSe ₂	-125	-
TiTe ₂	-112	-
ZrS ₂	-191	-
ZrSe ₂	-151	-
ZrTe ₂	-115	-
HfS ₂	-217	-
HfSe ₂	-179	-
HfTe ₂	-139	-
VS ₂	12	-
VSe ₂	8	-
VTe ₂	-4	-24.1
NbS ₂	22	-
NbSe ₂	17	-
NbTe ₂	6	-8
TaS ₂	13	-
TaSe ₂	13	-
TaTe ₂	-2	-36
CrS ₂	176	107
CrSe ₂	-32	53
CrTe ₂	-103	-
MoS ₂	271	183
MoSe ₂	227	112
MoTe ₂	170	18
WS ₂	292	178
WSe ₂	252	96
WTe ₂	188	-21

V. ELASTIC CONSTANTS

TABLE III. TMDs bulk materials elastic constants for phases 1T, 2H and 1T_d. Only the non-zero values are given according to the respective crystal symmetry. Some materials are unstable when in 1T_d phase. All values are given in GPa.

	1T							2H						1T _d									
	\bar{C}_{11}	\bar{C}_{12}	\bar{C}_{13}	\bar{C}_{14}	\bar{C}_{33}	\bar{C}_{44}	\bar{C}_{66}	\bar{C}_{11}	\bar{C}_{12}	\bar{C}_{13}	\bar{C}_{33}	\bar{C}_{44}	\bar{C}_{66}	\bar{C}_{11}	\bar{C}_{12}	\bar{C}_{13}	\bar{C}_{22}	\bar{C}_{23}	\bar{C}_{33}	\bar{C}_{44}	\bar{C}_{55}	\bar{C}_{66}	
TiS ₂	141	32	10	-3	30	12	55	140	56	13	40	5	42	unstable									
TiSe ₂	103	23	10	-3	36	13	40	115	41	15	20	4	37	unstable									
TiTe ₂	81	20	15	-7	39	19	31	76	25	19	30	1	25	unstable									
ZrS ₂	134	26	8	-3	34	9	54	138	52	10	30	4	43	unstable									
ZrSe ₂	108	22	7	-3	32	10	43	109	43	11	32	4	33	unstable									
ZrTe ₂	69	13	10	-5	35	16	28	71	24	14	27	2	23	unstable									
HfS ₂	148	29	8	-3	35	10	60	155	58	9	38	6	49	unstable									
HfSe ₂	119	24	7	-3	33	10	48	125	45	10	35	6	40	unstable									
HfTe ₂	72	13	6	-5	28	13	30	80	29	13	32	4	26	unstable									
VS ₂	171	35	11	-3	33	12	68	164	57	4	25	9	54	unstable									
VSe ₂	124	22	18	-5	34	11	51	129	42	7	12	8	43	unstable									
VTe ₂	79	28	22	-1	38	21	28	91	31	16	69	13	30	131	31	9	101	34	66	6	24	45	
NbS ₂	158	37	9	-11	36	13	61	171	56	13	51	5	58	unstable									
NbSe ₂	120	33	1	-6	26	20	44	140	46	8	46	6	47	unstable									
NbTe ₂	101	24	10	-11	17	18	39	97	34	6	44	8	31	134	24	16	85	30	74	6	28	45	
TaS ₂	178	30	11	-5	39	10	74	200	67	7	55	7	67	unstable									
TaSe ₂	123	13	4	-4	44	14	55	151	54	7	51	8	48	unstable									
TaTe ₂	107	23	13	-3	28	15	42	100	39	9	44	6	31	152	30	15	115	27	73	6	30	51	
CrS ₂	154	7	24	-6	41	11	71	204	53	11	47	12	56	206	43	28	189	26	42	5	33	87	
CrSe ₂	103	95	27	-1	97	1	39	159	46	10	42	11	39	164	40	29	148	29	34	2	26	64	
CrTe ₂	80	37	24	-5	58	18	22	108	100	30	120	15	40	unstable									
MoS ₂	197	1	27	-11	39	19	99	225	54	10	48	15	84	207	34	25	186	26	34	7	22	67	
MoSe ₂	168	9	25	-4	40	11	80	177	39	10	44	15	68	182	42	23	160	20	29	3	25	58	
MoTe ₂	131	5	18	-3	35	4	63	123	28	9	37	18	47	126	51	25	110	24	27	4	30	49	
WS ₂	198	1	22	-7	40	13	98	240	50	10	52	16	94	231	36	19	197	28	31	5	19	72	
WSe ₂	168	5	27	-2	37	8	81	195	35	10	48	17	80	206	43	18	177	19	34	3	23	64	
WTe ₂	136	-3	21	-4	34	6	70	135	21	9	40	21	57	170	41	18	96	24	27	1	24	52	

VI. EXFOLIATION ENERGY

TABLE IV. Exfoliation energy.

	energy (meV/Å ²)			energy (meV/Å ²)			energy (meV/Å ²)				
	1T	2H	1T _d	1T	2H	1T _d	1T	2H	1T _d		
TiS ₂	13	11	-	TiSe ₂	14	12	-	TiTe ₂	14	13	-
ZrS ₂	10	10	-	ZrSe ₂	11	10	-	ZrTe ₂	13	11	-
HfS ₂	10	10	-	HfSe ₂	11	11	-	HfTe ₂	13	12	-
VS ₂	15	13	-	VSe ₂	15	13	-	VTe ₂	16	15	22
NbS ₂	15	14	-	NbSe ₂	17	14	-	NbTe ₂	17	16	20
TaS ₂	15	14	-	TaSe ₂	16	15	-	TaTe ₂	17	16	21
CrS ₂	13	13	16	CrSe ₂	20	13	15	CrTe ₂	20	15	-
MoS ₂	15	14	14	MoSe ₂	16	15	14	MoTe ₂	14	15	15
WS ₂	15	14	14	WSe ₂	16	16	15	WTe ₂	15	16	15

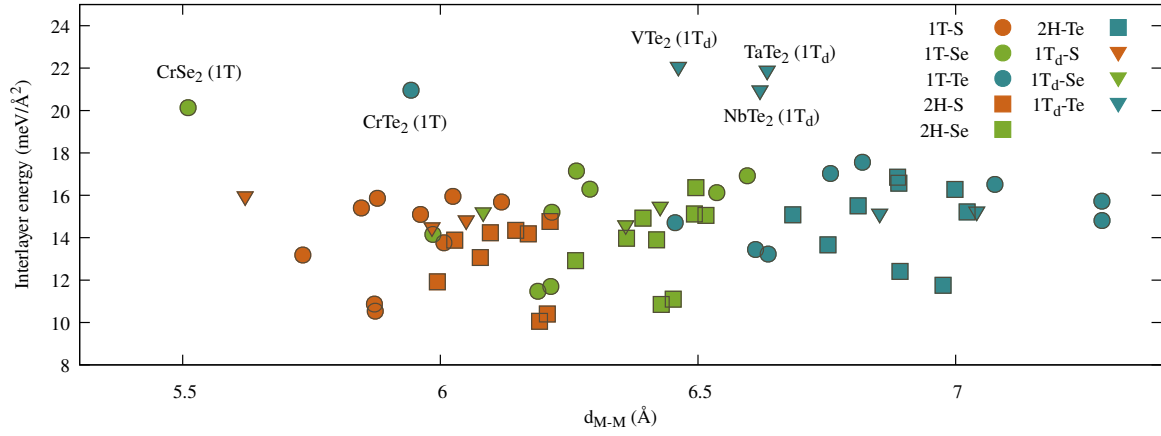


FIG. 5. Exfoliation energy. x-axis is the distance between metals in different layers

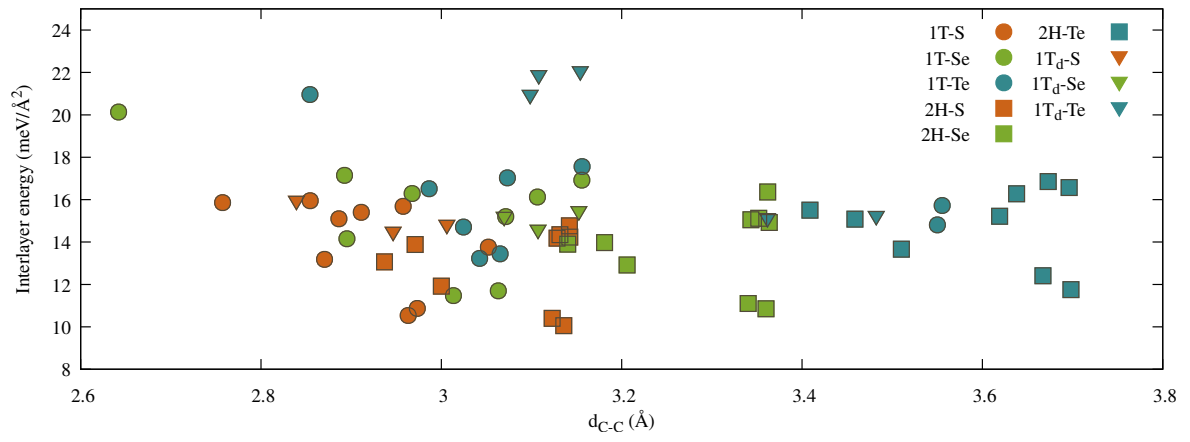


FIG. 6. Exfoliation energy. x-axis is the distance between chalcogen atoms in different layers

VII. BAND STRUCTURE AND DENSITY OF STATE FOR 2H PHASE

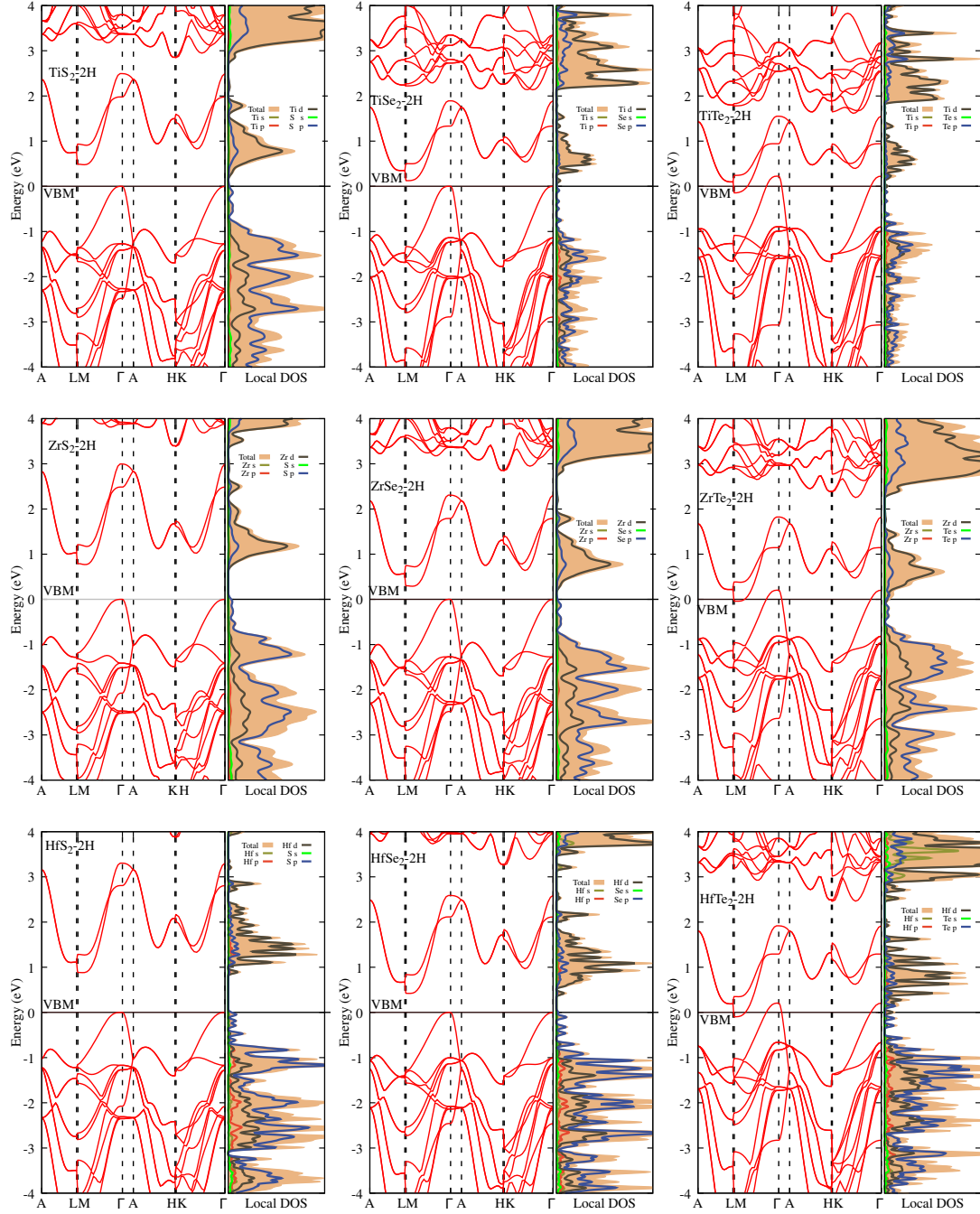


FIG. 7. 2H phase: Ti, Zr, Hf.

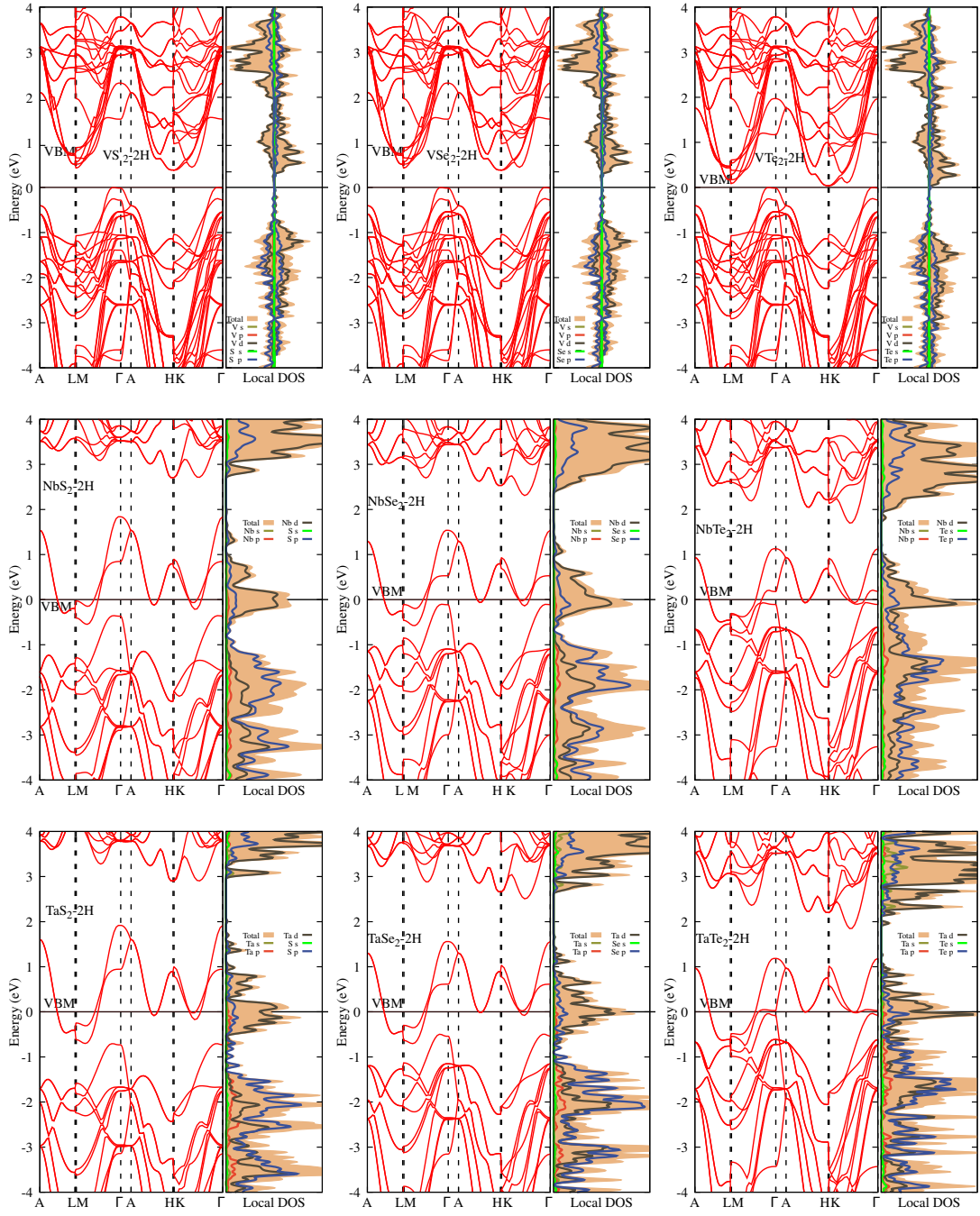


FIG. 8. 2H phase: V, Nb, Ta.

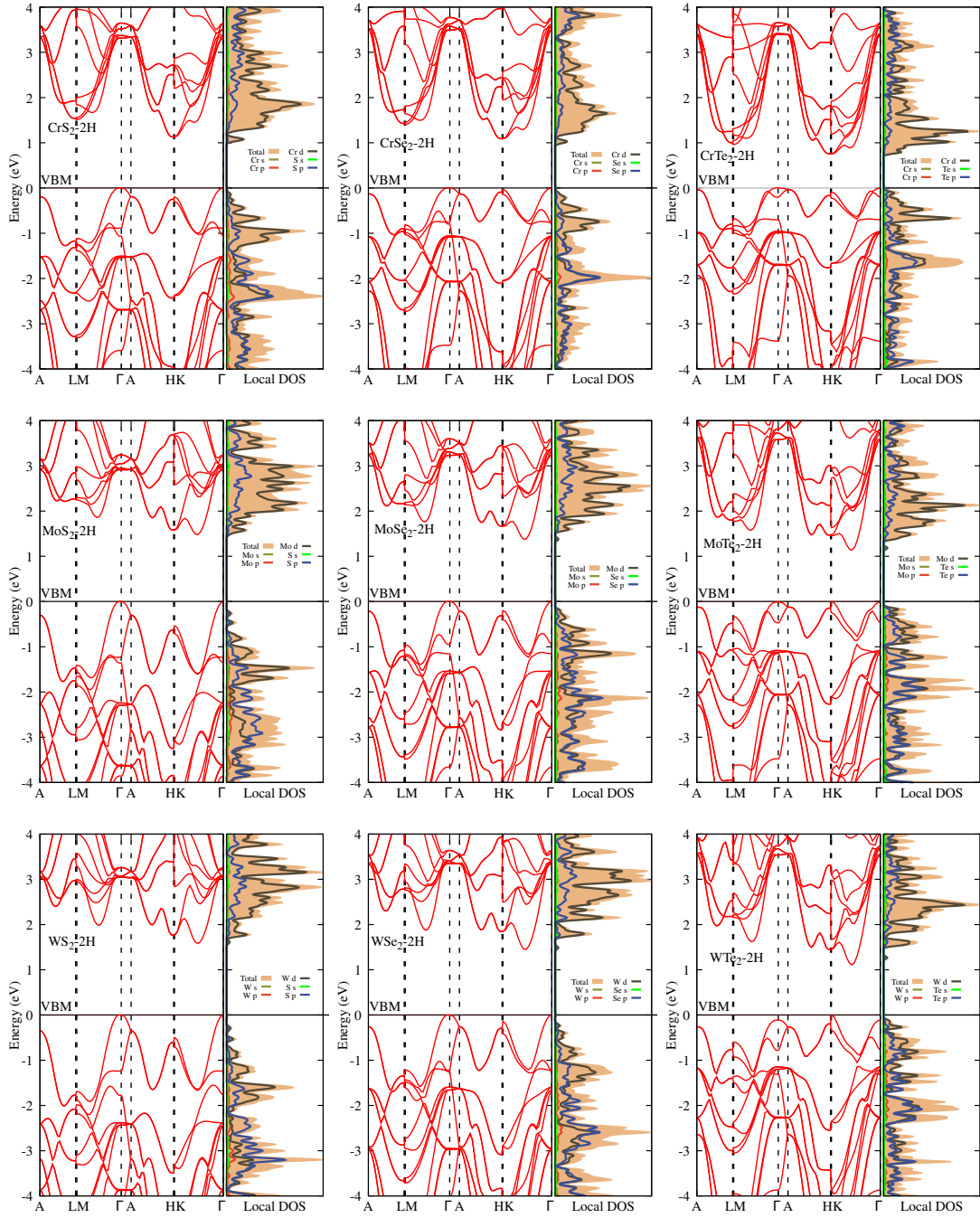


FIG. 9. 2H phase: Cr, Mo, W.

VIII. BAND STRUCTURE AND DENSITY OF STATE FOR 1T PHASE

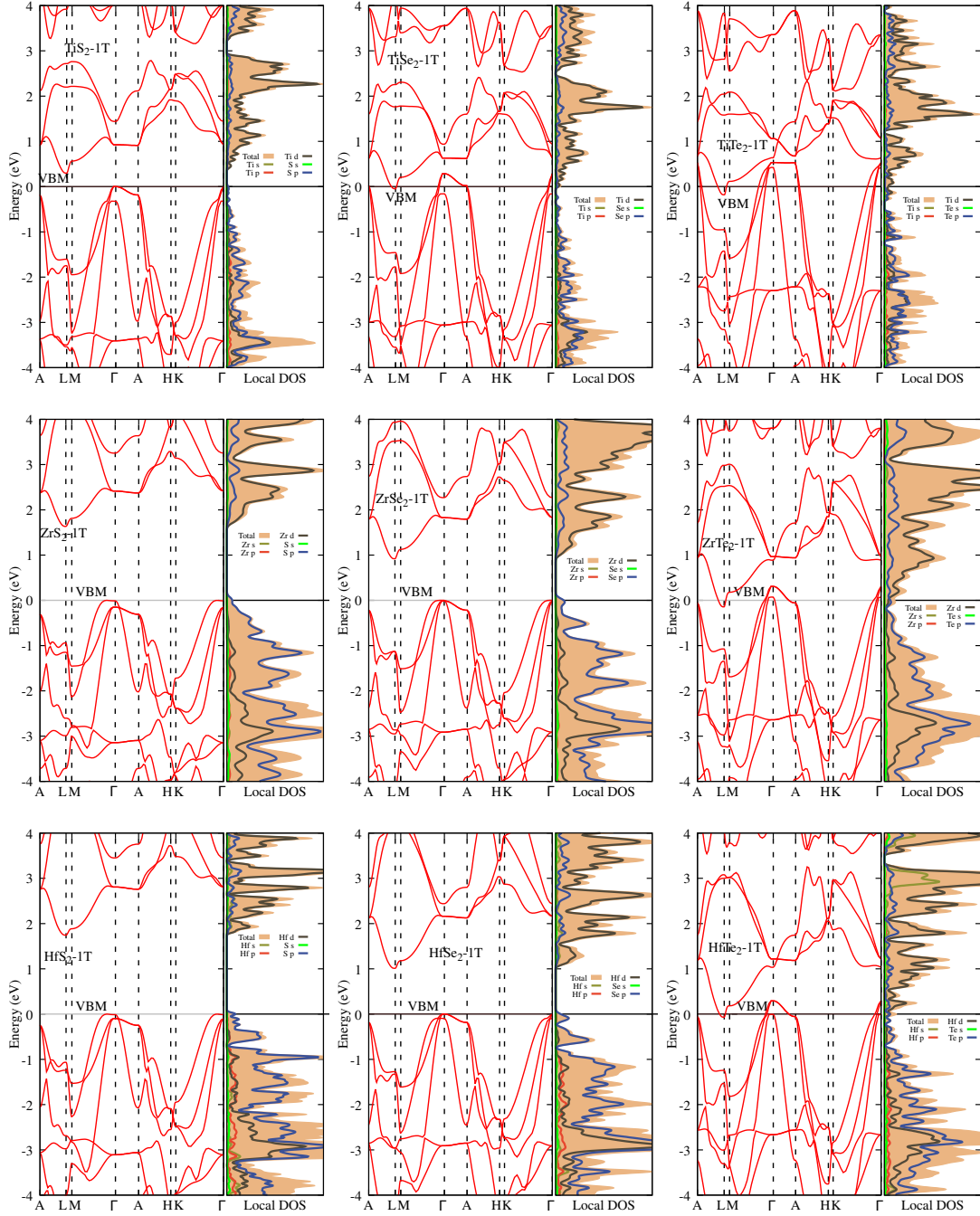


FIG. 10. 1T: Ti, Zr, Hf

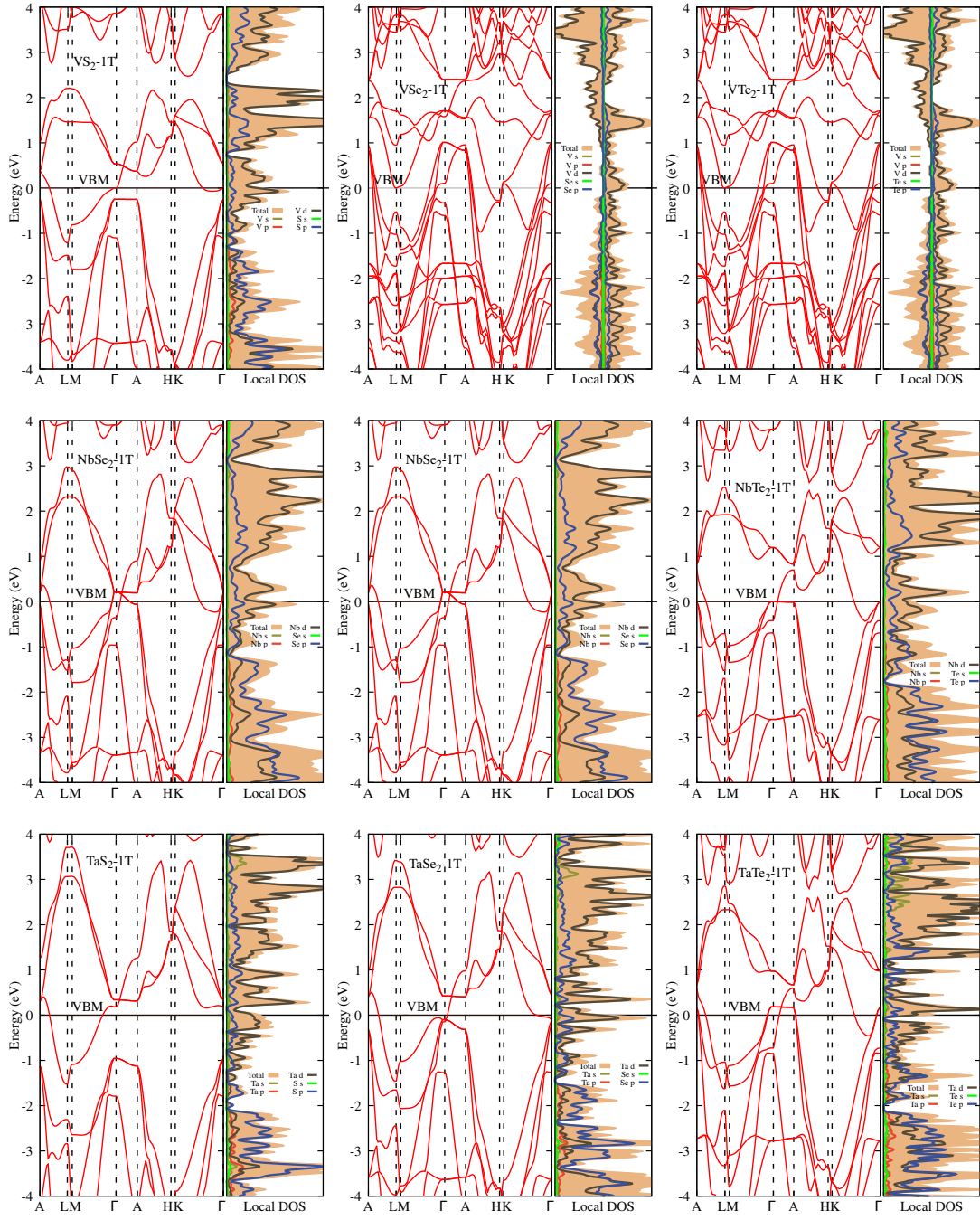


FIG. 11. 1T phase: V, Nb, Ta.

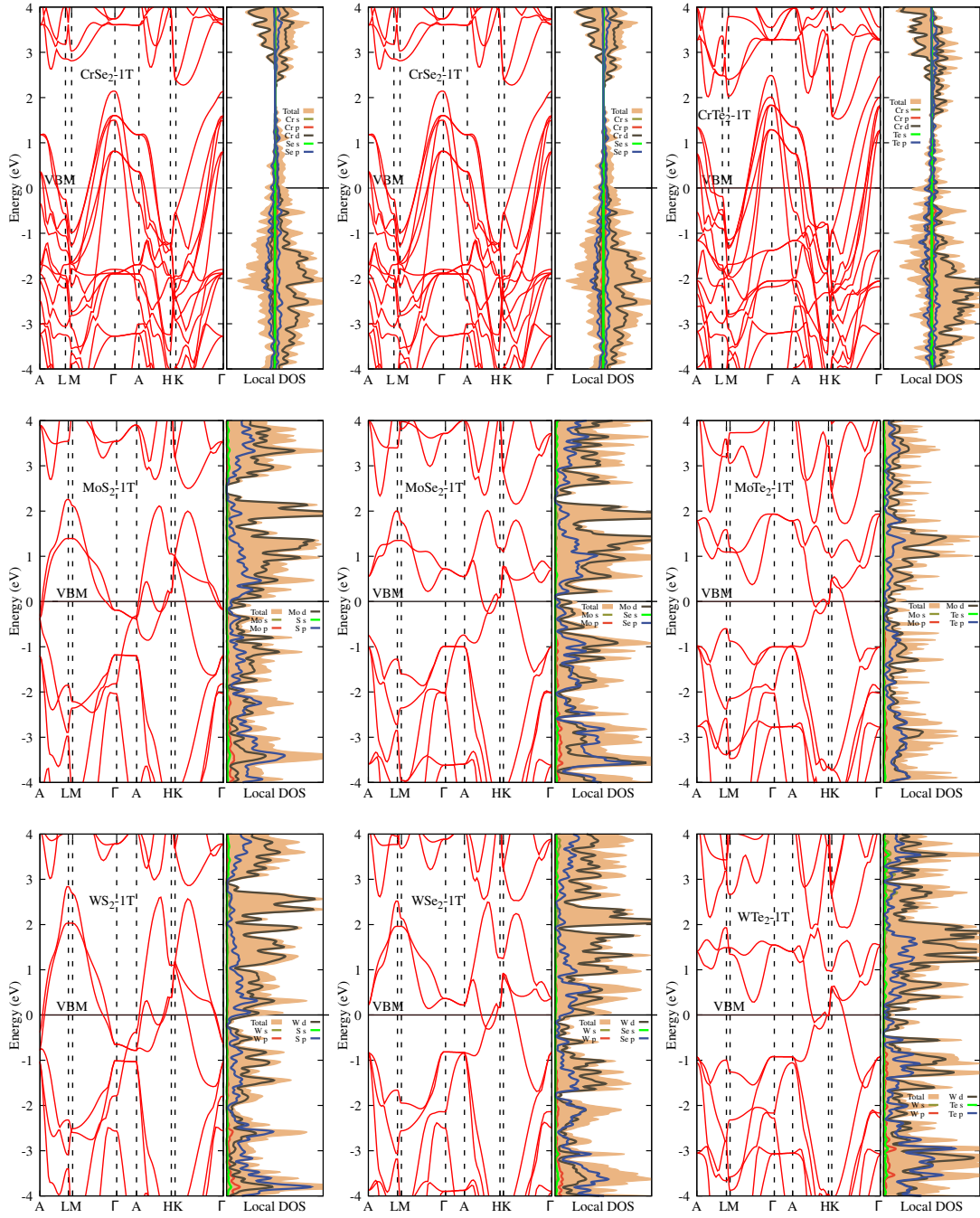
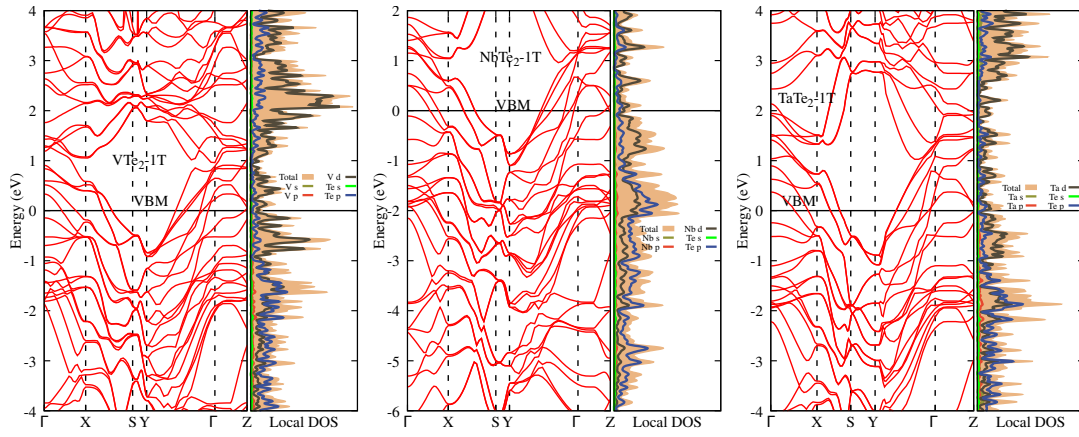


FIG. 12. 1T: Cr, Mo, W

IX. BAND STRUCTURE AND DENSITY OF STATES FOR 1T_d PHASESFIG. 13. 1T_d: V, Nb, Ta

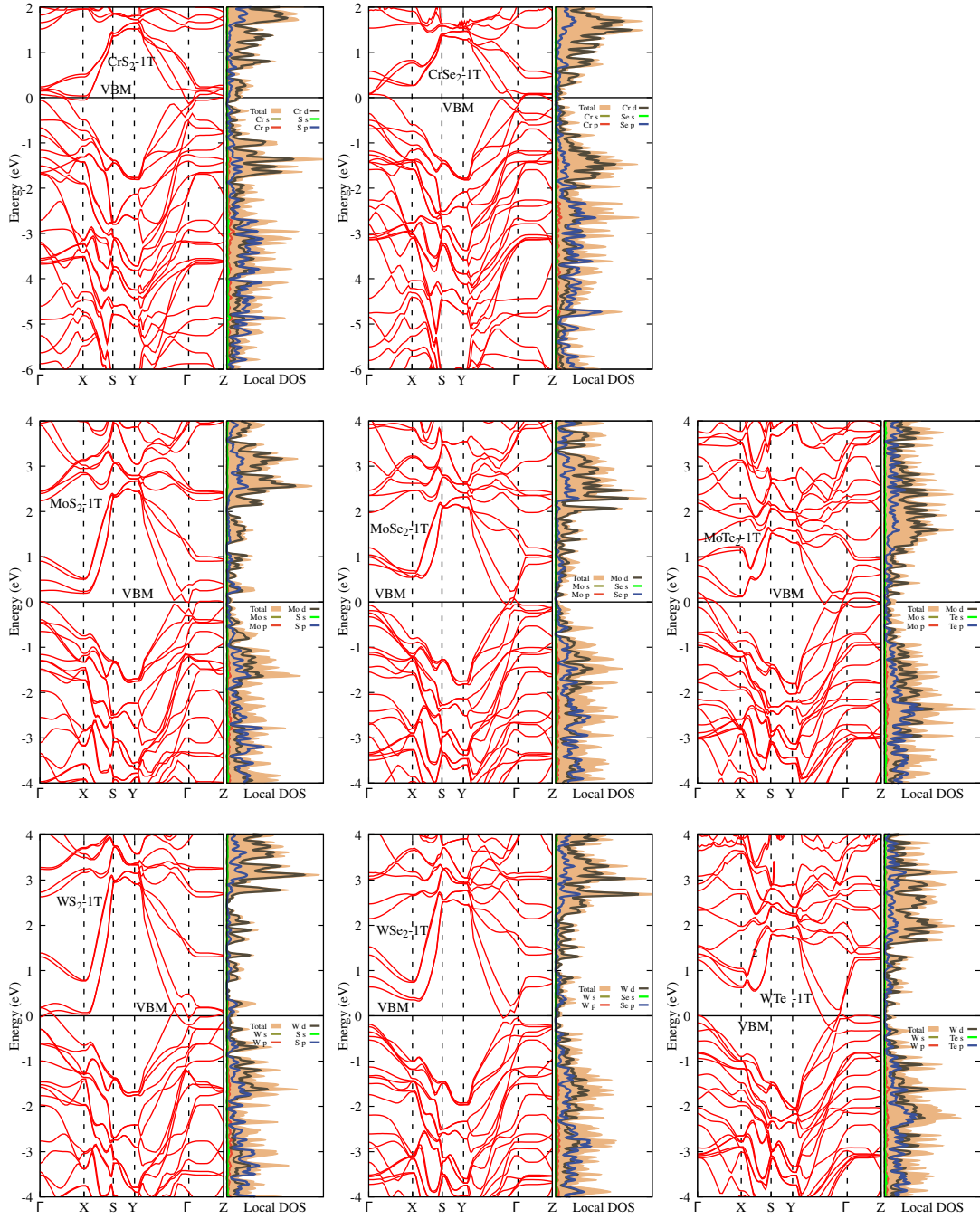


FIG. 14. 1Td: Cr, Mo, W